# Atomic Scale Studies of Thermally Aged Reactor Pressure Vessel Steels




Paul David Styman

Mansfield College

University of Oxford

A thesis submitted for the degree of

*Doctor of Philosphy*

Hilary 2013

To My Family

*The most exciting phrase to hear in science, the one that heralds new discoveries, is not 'Eureka!' but 'That's funny...'*

Isaac Asimov

# Abstract

In Pressurised Water Reactors, the reactor pressure vessel (RPV) is considered a life limiting component due to the degradation of its mechanical properties. Nano-scale Cu-enriched precipitates are known to cause embrittlement in the form of increases in hardness and the ductile-to-brittle transition temperature. The effect of irradiation on the RPV is the dominant contributor to this embrittlement. This is due to the increased mobility of Cu from the high number of vacancies, and the matrix damage providing many heterogeneous nucleation sites. However, there are also thermal effects which may be difficult to separate from the irradiation effects.

To understand the contribution of the long term thermal ageing to RPV embrittlement a series of weld and plate materials containing systematic variations of Ni and Cu has been thermally aged for times up to 100,000 hrs at 330 °C, 365 °C and 405 °C. Microstructural characterisation using Atom Probe Tomography has been performed. Complimentary Monte-Carlo simulations have been used to investigate the early stages of formation of Cu-enriched precipitates.

Thermal ageing produces a high number density of nano-scale Cu-enriched precipitates. These nanometre precipitates have a Ni-Mn-Si rich interface which was found to be wider with increased precipitate size, lower ageing temperature and higher bulk Ni content. This interface reduces the interfacial energy of the Cu-enriched precipitates through a combination of the minimising of unfavourable Fe-Cu bonds and reduction in lattice strain. The matrix Cu levels after ageing for 90,000 - 100,000 hrs were found to be around 0.06 - 0.07 at.%, close to the expected solubility limits for Cu in Fe. The Fe content of the precipitates has been characterised and found to be higher at lower ageing temperature and for smaller precipitate sizes. Cu precipitation and solute segregation at dislocations were observed, particularly in the SG steels aged at higher temperatures where the supersaturation is lowest.

Movies were produced from the Kinetic Monte-Carlo modelling (see accompanying DVD) and along with other analyses indicated that sub-critical Ni and Mn clusters may be active in the formation of Cu-enriched precipitates. This mechanism appears to occur in both the high and low Ni steels. Thus, the higher number density of larger precipitates observed with increased bulk Ni content is thought to be a consequence of the greater number of sub-critical Ni-Mn clusters providing more nucleation sites.

A small number of grain boundaries were examined. Segregation of many solute species to them was observed, which is thought to result from a multi-element co-segregation process. Ni-Mn-Si precipitates were observed at grain boundaries and dislocations in the high Ni steels with high and low Cu levels. These are consistent with similar phases in found in irradiated high Ni steels. In the high Cu steels these particles were much larger and associated with Cu-enriched precipitates.

# Preface

The work presented in this doctoral thesis has been carried out at the Department of Materials, University of Oxford from October 2009 to March 2013, under the supervision of Prof. George D. W. Smith and Prof. Jonathan M. Hyde. All of the research carried out for this thesis is original and where the work of others has been included it has been clearly referenced and acknowledged. All figures reproduced from journal articles and books have been used with permission from the respective copyright owner. No part of this thesis has been submitted for a degree at this, or any other university. Some of the work has been published in peer reviewed journals and presented at conferences and seminars as detailed below:

## Journal Articles:

J M Hyde, M G Burke, B Gault, D W Saxey, **P D Styman**, K B Wilford, and T J Williams. Atom Probe Tomography of Reactor Pressure Vessel Steels: An Analysis of Data Integrity, *Ultramicroscopy*, **111** (2011), pgs. 676 - 682.

**P D Styman**, J M Hyde, K B Wilford, A Morley and G D W Smith, Precipitation in Long Term Thermally Aged High Copper, High Nickel Model RPV Steel Welds, *Progress in Nuclear Energy*, **57** (2012), pgs. 86 - 92.

J M Hyde, R M Boothby, C A English, **P D Styman**, H Thompson, G D W Smith, K B Wilford, and T J Williams. Microstructural Characterisation of Nanometre Scale Irradiation Damage in High-Ni Weld. In *Proceedings of the 141st TMS Annual Meeting 2012*, Orlando, Florida, 2012, TMS, pgs. 489 - 502 (CD).

**P D Styman**, J M Hyde, K B Wilford and G D W Smith, Quantitative Methods for the APT Analysis of Thermally Aged RPV Steels, *Ultramicroscopy*, In press, 2013, doi:10.1016/j.ultramic.2012.12.003.

J M Hyde, M G Burke, **P D Styman**, H Thompson, K Wilford, Uncertainties and Assumptions Associated with APT and SANS Characterisation of Irradiation Damage in RPV Steels. *Submitted to: Proceedings of the 142nd TMS Annual Meeting 2013*, San Antonio, Texas, 2013, TMS.

A Morley, **P D Styman**, J M Hyde, A Cerezo, T J Williams, K Wilford, G D W Smith, The Long Term Thermal Ageing of Reactor Pressure Vessel Steels. Part 1: Atom Probe Tomography, (*In Preparation*), To be submitted to Acta Materialia.

**P D Styman**, A Morley, J M Hyde, A Cerezo, T J Williams, K Wilford, G D W Smith, The Long Term Thermal Ageing of Reactor Pressure Vessel Steels.

Part 2: Kinetic-Monte-Carlo-Modelling, (*In Preparation*), To be submitted to Acta Materialia.

A Morley, **P D Styman**, J M Hyde, A Cerezo, T J Williams, K Wilford, G D W Smith, An Integrity Analysis of a Lattice-Kinetic-Monte-Carlo Model for Ageing the Fe-Cu-Ni-Mn-Si System, (*In Preparation*), To be submitted to Computational Materials Science.

# Conferences:

**P D Styman**, J M Hyde, A Morley, K Wilford, G D W Smith, *Precipitation in Long Term Thermally Aged High Cu, High Ni Model RPV Steel Welds*, Oral Presentation, EMRS Bilateral Energy Conference, Nice, May 2011.

**P D Styman**, J M Hyde, K Wilford, G D W Smith, *Interfacial Segregation and Precipitation in Long Term Thermally Aged High Cu, High Ni Model RPV Steel Welds*, Oral presentation, Euromat 2011, Montpellier, September 2011.

**P D Styman**, J M Hyde, A Morley, K Wilford, G D W Smith, *Precipitation in Long Term Thermally Aged High Cu, High Ni Model RPV Steel Welds*, Oral presentation, IGRDM-16, Santa Barbara, December 2011.

**P D Styman**, J M Hyde, K B Wilford and G D W Smith, *Quantitative Methods for the APT Analysis of Thermally Aged RPV Steels*, Oral presentation, 53$^{rd}$ IFES, Tuscaloosa, May 2012.

**P D Styman**, J E Zelenty, J M Hyde, K Wilford, G D W Smith, *Effect of Ni on the Hardness Changes of High Cu PRV Steels*, Oral presentation, IGRDM-17, Les Embiez, May 2013.

**P D Styman**, J E Zelenty, J M Hyde, K Wilford, G D W Smith, *Influence of Ni and Mn on the Formation and Evolution of Cu-enriched Precipitates in RPV Steels Under Thermal Ageing*, Oral presentation, IGRDM-17, Les Embiez, May 2013.

# Seminars:

**P D Styman**, J M Hyde, K B Wilford and G D W Smith, *Atomic Scale Studies of Long Term Thermally Aged RPV Steels*, Los Alamos National Laboratory, Los Alamos, May 2012.

# Acknowledgements

Without the help and assistance of a number of people the work presented in this thesis would not have been possible. Firstly, I would like to express my deepest gratitude to my supervisors Prof. Jonathan M Hyde and Prof. George D W Smith. I thank you both for passing on some of your encyclopaedic knowledge of materials, the literature and atom probe. Your fruitful discussions, scientific guidance and motivation throughout my time here have been invaluable. I am also grateful for the free time both of you have given up to read through and improve the quality of this thesis. George, I would also like to thank you for giving me the opportunity back in early 2009 to pursue this DPhil.

I would also like to acknowledge the contribution of Dr. Daniel Haley. Without his help and vast knowledge of C, Shell and Python the Monte-Carlo modelling in this project would be nowhere near as advanced. I also thank him for the use of his posgen software and rdf programs and for adding additional features I needed and fixing bugs. These programs have made my life so much easier in this project.

I also would like to acknowledge my colleagues in the Department of Materials. I thank Mr. Bob Lloyd for keeping the furnaces containing these samples running for the past 10 years, and Mr. Laurie Walton for maintaining the workshop facilities. Also thanks to Dr. Gareth Hughes for help and training on the FIB. I also thank Dr. David Saxey and latterly Dr. Paul Bagot, for maintaining the LEAP and lab facilities.

I would also like to acknowledge Dr. Keith Wilford, Mr. Tim Williams, Dr. Dave Parfitt and Dr. Nick Riddle at Rolls-Royce for their contribution to this work and for fruitful discussions. I thank Dr. Andy Morley for help and advice with the C programming and in locating some of older data and Prof. John Titchmarsh for his advice and contributions.

I am also grateful for the financial support received from Rolls-Royce Plc who have sponsored this research, and without whom I would not have been able to undertake my doctoral studies. I would also like to thank The Worshipful Company of Founders, The Worshipful Company of Tin Plate Workers and Los Alamos National Lab for financial support to attend conferences and lab visits.

Finally, I would like to thank all members of the FIM group, both past and present for helpful discussions over the years. Particular thanks goes to Karen, Ceri and Josie Smith for their supply of cakes and to Dan for the climbing! Thanks must also go to James Douglas for proof reading the final draft. I thank my friends from Mansfield College, Devon and Swansea for their support, funtimes and banter! Lastly, I thank my family for their encouragement and support throughout my time in Oxford.

# Acronyms

*3DAP* 3-Dimensional Atom Probe.

*AKMC* Atomistic Kinetic Monte-Carlo.

*AP-FIM* Atom Probe Field Ion Microscopy.

*APT* Atom Probe Tomography.

*CEC* Cu-enriched Cluster.

*CRP* Cu-rich Precipitate.

*DBSCAN* Density Based Spatial Clustering of Applications with Noise.

*DBTT* Ductile to Brittle Transition Temperature.

*dpa* Displacements per atom.

*ECOPoSAP* Energy Compensated Optical Position Sensitive Atom Probe.

*EDX* Energy Dispersive X-Ray.

*EFTEM* Energy Filtered Transmission Electron Microscopy.

*FIB* Focussed Ion Beam.

*FIM* Field Ion Microscopy.

*HSLA* High Strength Low Alloy.

*ICF* Image Compression Factor.

*IVAS* Imago Visualisation and Analysis Software.

*KMC* Kinetic Monte-Carlo.

*LBP* Late Blooming Phase.

*LEAP* Local Electrode Atom Probe.

*LKMC* Lattice Kinetic Monte-Carlo.

*MD* Molecular Dynamics.

*MFVIC* Mean Field Vacancies and Interstitial Clustering.

*MMC* Metropolis Monte-Carlo.

*PAS* Positron Annihilation Spectroscopy.

*PISA* Phosphorus Influence on Steel Ageing.

*PWR* Pressurised Water Reactor.

*RDF* Radial Distribution Function.

*RPV* Reactor Pressure Vessel.

*SANS* Small Angle Neutron Scattering.

*SIA* Self Interstitial Atom.

*SSS* Solid Solution Strength.

*UTS* Ultimate Tensile Strength.

*VVER* Vodo-Vodyanoi Energetichesky Reactor.

# Contents

*1. Introduction* . . . 1

*2. Literature Review* . . . 3
2.1 Introduction . . . 3
2.2 General RPV Microstructure . . . 5
2.3 Precipitation of Alloy Elements in RPV Steels . . . 5
2.3.1 Intragranular Precipitation in Thermally Aged Steels . . . 6
2.3.1.1 The Composition of Cu Precipitates . . . 6
2.3.1.2 Structure of Cu Precipitates . . . 10
2.3.1.3 Alloy Element Effects on the Formation of Cu Precipitates . . . 12
2.3.1.4 Segregation of Alloy Elements to CRP Interfaces . . . 14
2.3.2 Intragranular Precipitation in Irradiated Steels . . . 16
2.3.2.1 Differences Between Clusters Formed Under Irradiation and Thermal Ageing . . . 17
2.3.2.2 The Composition of Precipitates . . . 18
2.3.2.3 Formation of Precipitates . . . 19
2.3.2.4 Segregation of Alloy Elements to CRP Interfaces . . . 22
2.3.2.5 Clustering in Low Cu/Cu Free Alloys . . . 22
2.3.3 Intergranular Precipitation and Segregation . . . 25
2.3.3.1 Thermally Aged Steels . . . 26
2.3.3.2 Irradiated Steels . . . 27
2.4 Summary of the Precipitation of Alloy Elements in RPV Steels . . . 28
2.5 Concluding Remarks . . . 29

*3. Experimental Methods and Materials* . . . 31
3.1 Materials . . . 31
3.2 Hardness Testing . . . 33
3.3 APT Sample Preparation . . . 34
3.3.1 Electropolishing . . . 34
3.3.2 Focussed Ion Beam Milling . . . 36
3.4 Atom Probe Tomography . . . 37
3.4.1 Data Reconstruction . . . 39
3.4.2 Atom Probe Artefacts Affecting Solute Clusters . . . 45
3.4.2.1 Local Magnification Effects . . . 46
3.4.2.2 Trajectory Overlaps . . . 46
3.4.3 Mass Spectrum and Ranging . . . 47
3.4.4 Atom Probe Data Analysis . . . 48

3.4.4.1 Tests for Solute Non-Randomness in Atom Probe Datasets . . . 49
3.4.4.1.1 Frequency Distributions . . . 49
3.4.4.1.2 Contingency Tables . . . 50
3.4.4.1.3 Auto-correlations . . . 51
3.4.4.1.4 Local Chemistry Method . . . 52
3.4.4.2 Cluster Search Algorithms . . . 52
3.4.4.2.1 Maximum Separation Method . . . 52
3.4.4.2.2 Chemistry Based Methods . . . 54
3.4.4.2.3 Density Based Methods . . . 55
3.4.4.2.4 Other Methods . . . 56
3.4.4.3 Compositional Analysis . . . 57
3.4.4.3.1 Composition of Clusters/Precipitates . . . 57
3.4.4.3.2 Planar Composition Profiles . . . 57
3.4.4.3.3 Radial Composition Profiles . . . 58
3.4.4.3.4 Isoconcentration Surfaces . . . 59
3.4.4.3.5 Proximity Histograms . . . 60

*4. Experimental Conditions and Analysis Techniques for LEAP Data* . . . 61
4.1 Effects of Experimental Parameters on Data Quality . . . 61
4.1.1 Voltage Pulsing . . . 62
4.1.2 Laser Pulsing . . . 65
4.1.3 Summary of the Comparison Between Voltage and Laser Pulsing. 70
4.2 Microstructural Characterisation of RPV Steels . . . 70
4.2.1 Quantification of RPV Microstructural Features . . . 70
4.2.1.1 Cluster Size, Number Density and Volume Fraction . . 70
4.2.1.2 Cluster Search Parameters . . . 72
4.2.1.3 Method for the Removal of Background Clusters . . . 76
4.2.1.4 Composition . . . 84
4.2.1.5 Interfaces . . . 85
4.3 Comparison of Data of WV Aged at 365 °C Obtained With LEAP and ECOPoSAP . . . 87
4.4 Summary . . . 90

*5. Atom Probe Tomography of Thermally Aged Materials* . . . 92
5.1 Hardness Changes . . . 92
5.2 Microstructural Evolution in the High Cu Materials . . . 96
5.2.1 WV Material . . . 96
5.2.1.1 Precipitate Size, Number Density and Volume Fraction 97
5.2.1.2 Matrix Composition . . . 101
5.2.1.3 Precipitate Solute Composition . . . 102
5.2.1.4 Fe Content of Precipitates . . . 108
5.2.1.5 Precipitate/Matrix Interface . . . 114
5.2.2 SG Material . . . 120
5.2.2.1 Precipitate Size, Number Density and Volume Fraction 121
5.2.2.2 Matrix Composition . . . 123
5.2.2.3 Precipitate Composition . . . 124
5.2.2.4 Matrix/Precipitate Interface . . . 127

5.2.2.5 Presence of Sn . . . 129
5.3 Microstructural Evolution in the Low Cu Materials . . . 131
5.3.1 WF Materials . . . 132
5.4 Precipitation and Segregation to Grain Boundaries and Dislocations . . 135
5.4.1 High-Angle Grain Boundaries . . . 135
5.4.1.1 Solute Segregation . . . 136
5.4.1.2 Precipitation . . . 138
5.4.2 Low-Angle Grain Boundaries . . . 140
5.4.3 Dislocations . . . 142
5.4.3.1 WV Material . . . 142
5.4.3.2 SG Material . . . 145
5.4.4 Comparison of Ni-Mn-Si Precipitation at Grain Boundaries and Dislocations . . . 146
5.5 Summary . . . 148

*6. Lattice Kinetic Monte Carlo Simulations of RPV Steels* . . . 150
6.1 Introduction and Overview of Previous Work . . . 150
6.1.1 New Features and Aims of This Study . . . 153
6.2 Microstructural Evolution . . . 156
6.2.1 Precipitate Size and Number Density . . . 156
6.2.2 Nucleation and Growth . . . 159
6.3 Influence of Solute Elements on Precipitate Formation . . . 161
6.3.1 Isolated Solute Atoms . . . 162
6.3.2 Environment Around Cu Atoms . . . 164
6.3.3 Environment Around the Nucleation Sites of Precipitates . . . 166
6.3.4 The Evolution of Ni-Mn Clusters . . . 178
6.3.5 Cu-enriched Precipitate Nucleation Mechanisms . . . 182
6.3.6 Visualisation of Cluster Formation . . . 187
6.4 Summary . . . 189

*7. Discussion* . . . 191
7.1 Relation of Microstructural Data to Hardness Changes . . . 191
7.1.1 High Cu Materials, WV and SG . . . 193
7.1.2 Softening of WF During Thermal Ageing . . . 195
7.2 Effects of Long Term Thermal Ageing on RPV Microstructure . . . 196
7.2.1 Effect of Alloy Ni Content in the Presence of Mn . . . 196
7.2.2 Matrix Cu Concentration . . . 197
7.2.3 Matrix-Precipitate Interfaces . . . 198
7.2.3.1 Effect of Precipitate Size . . . 199
7.2.3.2 Effect of Ageing Temperature . . . 199
7.2.3.3 Interface Composition . . . 200
7.3 Non-Equilibrium Clustering Effects on Cu-enriched Precipitate Formation . . . 200
7.4 Fe Content of Precipitates . . . 202
7.4.1 SANS vs APT . . . 202
7.4.2 Could Fe be in Precipitates? . . . 203
7.5 Ni-Mn-Si Precipitates . . . 205
7.5.1 Observations of Ni-Mn-Si Precipitates . . . 205

7.5.1.1 Matrix . . . 205
7.5.1.2 Grain Boundaries and Dislocations . . . 205
7.5.2 Kinetics of Formation of Ni-Mn-Si Precipitates . . . 206

*8. Conclusions* . . . 208

*9. Future Work* . . . 212

*Appendix* 230

*A. Selection of Appropriate Image Regions for APT Reconstruction* . . . 231

*B. Hardness Evolution of Each Alloy with Ageing Temperature* . . . 234

*C. Noise Correction of Sn Peaks* . . . 238

*D. Values Used for Monte-Carlo Modelling Parameters* . . . 241

*E. Monte-Carlo Simulation and Analysis Code* . . . 244
E.1 LKMC Code . . . 244
E.2 Additional Analysis Code . . . 286
E.2.1 Linked Clustering . . . 286
E.2.2 Cluster Formation Videos . . . 306

# 1. Introduction

In the UK and worldwide, particularly in India and China there is increased interest in nuclear power as a viable long term source of low carbon energy. Across the world there are 484 new reactors either proposed or planned, nearly half of these are in India and China, while another 62 reactors are currently under construction[1]. In recent years there has also been considerable drive to extend the lifetime of existing plants beyond their original design lifetime. Additionally, since the Fukushima disaster there has been increased attention on the safety and integrity of the Reactor Pressure Vessel (RPV). This requires in depth studies of the component materials to ensure the end of life properties are within acceptable limits. In the most common type of reactor, the Pressurised Water Reactor (PWR) the majority of this work revolves around the RPV. This is subject to embrittlement from fast fission neutrons and thermal ageing and is considered a life-limiting component. Atomic scale characterisation of representative parts of the RPV microstructure is a critical input to predictive models for the end of life properties.

This project is the continuation of a long standing collaboration between Rolls-Royce Plc and the University of Oxford. The aim of this thesis is to investigate the effects of the long term thermal ageing on a series of RPV steel weld and plate materials. Primarily the focus is on the understanding of the effects of alloy element additions on the precipitation of Cu, a well known impurity in older reactors arising from the use of Cu coated welding rods. In this project the weld materials have been characterised experimentally with APT after 90,000 - 100,000 hrs of ageing at temperatures of 330 °C to 405 °C. Complimentary studies have been performed with Monte-Carlo

modelling to investigate the early stages of formation of Cu-enriched precipitates.

The work presented in this thesis is laid out in 9 chapters beginning with a critical overview of the current understanding of Cu precipitation in RPV steels and model alloys in Chapter 2. Chapter 3 details the materials, experimental techniques and associated analysis methods used. Chapter 4 explores the optimal conditions for the analysis of these materials. This ensures optimal data quality and consistency with the work that has gone before. It also presents some new developments in analysis methods for the characterisation of solute clustering. The results of the APT investigation and hardness evolution of the thermally aged materials are presented in Chapter 5. This extends the work on the evolution of matrix Cu precipitation to 100,000 hrs and presents the results of precipitation and solute segregation to grain boundaries and dislocations. In addition, Ni-Mn-Si precipitates have been observed in thermally aged RPV steels for the first time. Complimentary Monte-Carlo modelling results are detailed in Chapter 6. These results show the development of individual Cu-enriched precipitates at the atomic scale through a number of videos which are available on the attached DVD. Furthermore, these simulations highlight the synergistic effects of Ni and Mn and their effect on the precipitation of Cu. The results are discussed in detail with reference to the outstanding issues raised in the literature review in Chapter 7. Finally, a brief summary of the main results and conclusions is detailed in Chapter 8 and important directions for future research are outlined in Chapter 9.

# 2. Literature Review

## 2.1 Introduction

In 2011 there were 436 nuclear reactors in service throughout the world, of these 60 % were Pressurised Water Reactors (PWRs) generating 270.4 GW of electricity[2]. In addition, PWRs are widely used for submarine propulsion. Most nuclear power plants were originally designed with an operational lifetime of 25 - 40 years. However, there are programs to extend the operational lifetimes of many nuclear power plants, particularly in the USA, Russia and Japan to up to 60 years[2]. To ensure the safe operation of these reactors it is crucial that the long term effects of thermal ageing and neutron irradiation to embrittlement are understood.

One of the main life limiting factors of PWRs is the embrittlement of the Reactor Pressure Vessel (RPV) caused by a combination of neutron irradiation and thermal ageing[3]. This is partly due to Cu precipitation[4]. In addition, fast neutrons from fission reactions cause displacement cascades[5] which generate an array of matrix damage which can act as nucleation sites for Cu-enriched precipitates[1]. The matrix damage caused by neutron irradiation is beyond the scope of this literature review but has been reviewed elsewhere[6–8]. At typical reactor operating temperatures ($\sim$290 °C) RPV impurity Cu levels are sometimes well above the solubility limit of Cu in Fe ($< 0.1$ wt.%), thus there is a large driving force for Cu precipitation. This is of particular concern in older reactors where Cu was introduced through the use of Cu-coated welding rods.

[1] In this thesis the terms cluster/precipitate/particle are all used interchangeably to describe a small solute rich second phase region.

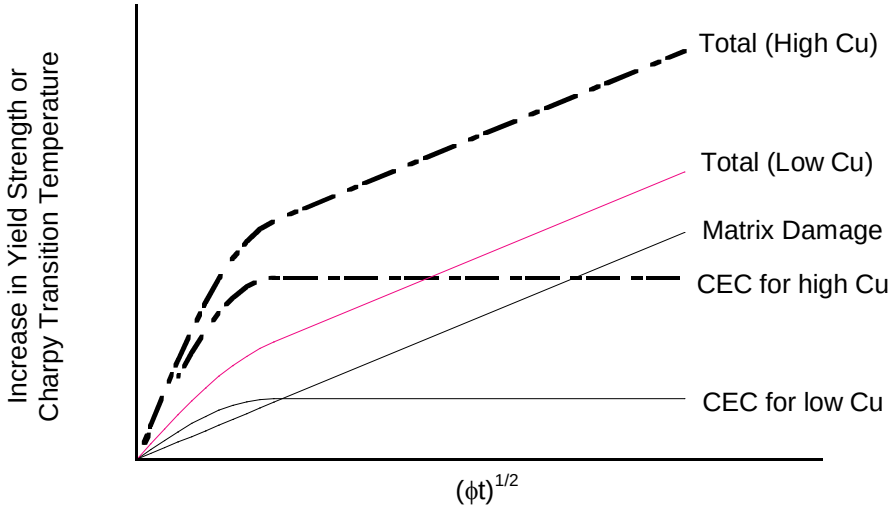


*Figure 2.1:* Example showing the contribution to the hardness/yield strength change and DBTT shift from Cu-enriched Clusters (CECs) and matrix damage, in a typical high and low Cu RPV steel with the neutron fluence. Fluence is given by neutron flux, $\phi$ multiplied by time, $t$. Image from English and Hyde[3].

The effects on the mechanical properties of RPV steels due to the precipitation of Cu have been well documented. It is well known that the formation of 1 - 2 nm radius Cu-enriched precipitates causes an increase in the hardness of RPV steels and model alloys[9–11], although matrix defects caused by irradiation also contribute to hardening[12, 13], as shown in Figure 2.1. Cu precipitation also causes increases in the yield stress[12, 14] and the Ductile to Brittle Transition Temperature (DBTT)[6, 15].

The binary Fe-Cu system has been studied for many years and consequently is relatively well understood. However, in real engineering steels it is found that there are strong synergistic effects between Cu and the alloying elements, particularly Ni, Mn and Si as well as trace impurities. These synergistic effects are less well understood. This review focuses mainly on the current understanding of the effect of these alloying additions, mainly Ni, Mn and Si on the precipitation of Cu during thermal ageing and neutron irradiation.

## 2.2 General RPV Microstructure

The majority of studies of Cu precipitates in steels have been carried out on A533B type steel welds and A302B steel plate which are typical of those used in many British and American reactors. Other studies involve samples from the French and Russian surveillance programs, which are generally higher in Ni and Mo, in addition to studies of Fe-Cu(-Ni-Mn) model alloys.

Typically the reactor vessel is constructed from two or more forgings welded together using multi-pass submerged arc welds to produce a sealed vessel. The forgings usually undergo an initial annealing followed by a temper and then a post weld stress relief heat treatment. These heat treatments typically result in a tempered bainite microstructure.

These heat treatments cause some precipitation of Cu during the slow cooling after the tempering and stress relief heat treatments. Typically this results in some large $\epsilon$-Cu precipitates mainly at grain boundaries and dislocations. Furthermore, this will reduce the matrix Cu levels slightly, but in steels where Cu precipitation is of concern this will still result in the matrix Cu being well above the solubility limit. During these heat treatments some initial solute segregation, particularly of C and P will occur at grain boundaries.

## 2.3 Precipitation of Alloy Elements in RPV Steels

Whilst there have been many studies concerned with the effect of irradiation on Cu precipitation[16–18], there have been relatively few studies of the effects of long term thermal ageing (greater than $\sim$1 - 2 years) on the precipitation of Cu in RPV steels in the absence of neutron irradiation[19, 20]. There are however, many more studies where ageing has been carried out for shorter times at higher temperatures[21–23].

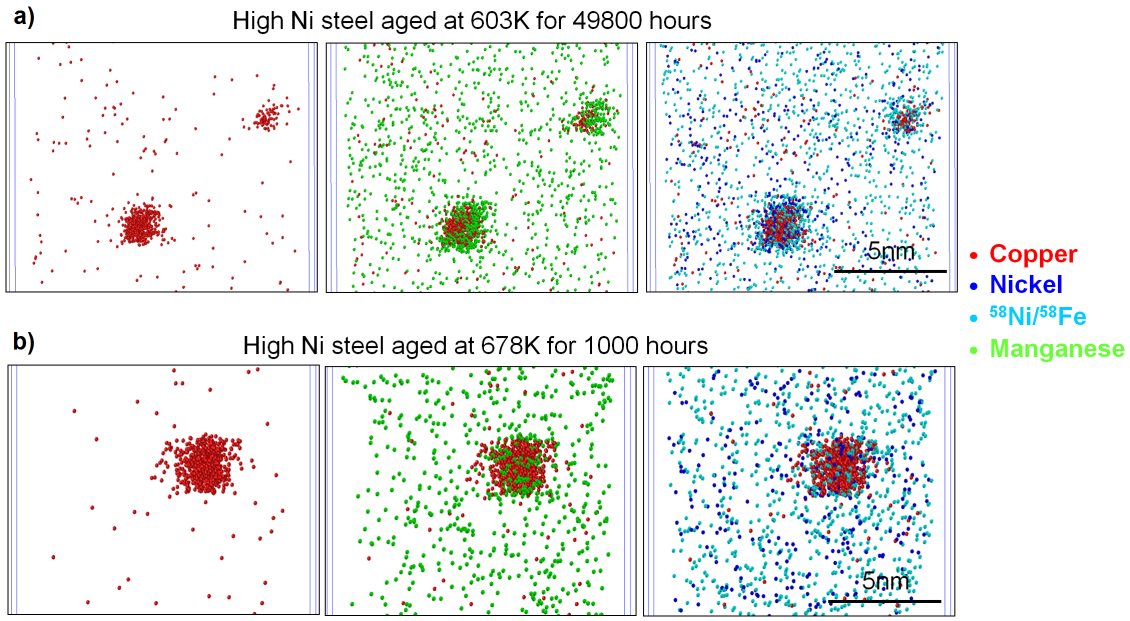


*Figure 2.2:* An example of CRPs formed under thermal ageing in a high Cu model RPV steel weld aged at (a) 330 °C for 49,800 hrs and (b) 405 °C for 1000 hrs. Image from Morley[19].

### 2.3.1 Intragranular Precipitation in Thermally Aged Steels

It is common for thermal ageing studies to be carried out at temperatures above typical reactor operating temperatures to accelerate the ageing process given the slow diffusion of Cu at 290 °C[24]. This allows predictions to be made about the contribution of thermal ageing to the embrittlement of the RPV during the reactor lifetime (around 40 years). The following sections detail some of the effects of solute elements on the precipitation of Cu which have been observed in thermally aged steels. This includes their influence on the formation and growth of Cu-rich Precipitates (CRPs) (also referred to in the literature as Cu-enriched Clusters (CECs)) and possible effects in very low Cu steels. An example of CRPs formed under thermal ageing in a model RPV steel weld is shown in Figure 2.2.

#### 2.3.1.1 The Composition of Cu Precipitates

Accurate determination of the Fe content of CRPs in Fe-Cu based systems has been a long running issue. Typically Small Angle Neutron Scattering (SANS) data are interpreted to give near pure CRPs, whereas Atom Probe Tomography (APT) suggests

they contain significant quantities of Fe. Wirth et al.[25] note that positioning errors in APT data of only 0.5 nm would incorporate large amounts of Fe into CRPs, which would artificially inflate the Fe content of the smaller CRPs. APT also suffers from poorer statistics than SANS due to the much smaller sampled volume. The identification and quantification of precipitates and the location of a matrix-precipitate interface is a non-trivial process in APT datasets. This interface is often not well defined and is therefore open to subjective interpretation by the researcher. Selection of appropriate methods and their parameters is needed to give the most accurate estimates of CRP composition. Numerous methods for identifying and determining the composition of clusters in APT datasets have been developed and are discussed in more detail in Section 3.4.4.

Wirth et al.[25] also note that interpretation of SANS data relies on assumptions regarding the magnetisation of CRPs. A paper by Fine et al.[26] attributes these discrepancies to the fact that Cu-enriched precipitates are magnetic. Previously only particles with Fe concentrations above 30 % were thought to be magnetic. This is in agreement with Schober et al.[27, 28] who used a combination of SANS, APT and Density Functional Theory modelling to compare the measured SANS $A$ ratio (proportional to the ratio $(N + M)/N$ of Magnetic, $M$, and Nuclear, $N$, scattering contrast) to the theoretical $A$ ratio calculated from CRPs observed with APT. They observe the best fit between the two only when CRPs are assumed to be magnetic and contain significant proportions of Fe (around $\sim$50 %). In contradiction to Fine et al.[26] and Schober et al.[27, 28], Asoka-Kumar et al.[29] calculated that precipitates are non-magnetic and contain at most 10 % Fe using data from Positron Annihilation Spectroscopy (PAS).

Both SANS and PAS use assumptions and models which give compositions consistent with the presence of vacancies within Cu-enriched precipitates, which are not possible to detect with APT. In SANS experiments precipitate compositions are obtained from the magnetic to nuclear scattering ratio, $A$. This often yields results where several compositions are consistent with a given $A$ ratio, which makes determining the exact

composition almost impossible. The problem is further complicated if the assumption that precipitates are non-magnetic is not valid, although self consistent interpretation with other techniques is possible.

The composition of the alloy, the ageing time and temperature all affect the composition of precipitates. Early Atom Probe Field Ion Microscopy (AP-FIM) work by Goodman[30, 31] on a Fe-1.4 at.% Cu alloy aged at 500 °C reported Cu contents of 50 % - 100 % albeit with a large scatter. They found higher Cu contents in materials aged for longer times. However, Auger and co-workers[16, 32] report 'quasi-pure' CRPs with Cu contents in the region of 95 - 100 % in a binary Fe-0.7 wt.% Cu alloy after thermal ageing for 70 hrs at 500 °C. This result appears to come from a small volume through the precipitate, rather than an average over the whole precipitate. Auger et al.'s result is in agreement with Cu contents reported by Cerezo et al.[33]. Monte-Carlo modelling by Soisson, Martin and Barbu[34, 35] also report virtually pure Cu precipitates.

Pareige et al.[21] thermally aged a ternary Fe-Cu-Ni alloy at 400 °C, 500 °C and 550 °C for times from 1 hr to 100 hrs. They report near pure Cu particles after 10 hrs of ageing at 500 °C, up from 40 % Cu after ageing for 1 hr. At 400 °C no clusters were observed until 21 hrs of ageing where the Cu content was 10 % increasing to 40 % after 100 hrs. The Ni content of the precipitates was below 3 % in all cases, giving Fe contents greater than 50 %, except for CRPs in the specimens aged for 10 hrs and 100 hrs at 500 °C where Fe contents were of the order of 1 - 2 %.

An Energy Filtered Transmission Electron Microscopy (EFTEM) study by Lozano-Perez et al.[36] reports that the Fe content of precipitates over 3 nm in size in a model RPV weld containing 0.44 at.% Cu aged for 10,000 hrs at 405 °C fall into two distinct groups, one which is virtually Fe free and one which contains around 25 - 40 % Fe. In their study they make no distinction between differing concentrations of other solute elements in the precipitates instead calling everything which is not Fe, Cu. In addition, they make no comment as to any link between size and Fe content.

It is known that precipitates undergo a series of transformations from coherent bcc particles to incoherent fcc/fct particles via intermediate 9R and 3R stages[37, 38] (see Section 2.3.1.2). Lozano-Perez et al. propose that differing crystal structures of precipitates are able to accommodate different amounts of Fe, it appears that they think the transformed precipitates are those which contain Fe. However, the EFTEM technique cannot be used to determine crystal structure and therefore the authors could not determine it. If crystal structure does influence Fe content then it seems logical when considering other work that the bcc (untransformed) precipitates would be the ones containing the most Fe, given that Fe has a bcc structure at low temperatures. This is supported by the work of Kozeschnik who produced a thermodynamic model at a temperature of 500 °C to predict the composition of Cu precipitates in binary Fe-Cu alloy for different bulk Cu contents[39]. The model incorporates both the Gibbs energy and interfacial energy which has significant effect on small clusters[40]. The model predicts that small Cu precipitates, formed in the early stages of ageing contain large proportions of Fe, especially at higher Cu concentrations. In addition, the model predicts 'larger' precipitates contain very little Fe. The paper contains very little information on the quantitative size of features but implies the 'larger' near pure Cu precipitates are around 1 - 2 nm in size (using the free energy and interfacial energy graphs presented, the "size" appears to be "diameter"). Kozeschnik's model also implies that the Cu content of the critical nucleus depends on the bulk Cu level and ageing temperature, with higher Cu contents at lower supersaturation and higher temperatures.

A more recent study using APT by Morley[19] looked at the amount of Fe in Cu precipitates in low alloy steel welds similar to those of Lozano-Perez[36] above. Using the Cu concentration of large fcc CRPs as a benchmark, he developed a method to minimize the effects of trajectory overlaps on the composition of small bcc CRPs. He reported Fe contents of 7 % and 17 % for ageing temperatures of 405 °C and 330 °C respectively, with no change in Fe content with precipitate size, although this could be a feature of his correction method. This is in agreement with the results of

Pareige[21]; that ageing temperature has an effect on the Fe content of CRPs.

The results shown here are an illustration of some of the compositional data obtained on Fe-Cu alloys. Quantitative comparison of composition between different studies, even by the same author, is difficult since different studies use different algorithms to define precipitates. In the published papers, the algorithm used for the analysis is often unclear or key parameters are not specified, and when these are specified there is often little or no fundamental justification of them.

#### 2.3.1.2 Structure of Cu Precipitates

As noted earlier Cu precipitates undergo a series of structural transformations from being coherent with the bcc Fe matrix to a more stable fcc structure via intermediary 9R and 3R stages[37, 38, 41]. In a binary Fe-1.5 wt.% Cu alloy aged at 550 °C Monzen et al.[42] reported that the critical nucleus size for the bcc to 9R transformation is approximately 12 nm diameter, with the critical size decreasing with decreasing temperature. Other authors have suggested the transformation may occur at radii down to ∼3 nm[41, 43]. This large difference could be explained by variations in the temperature at which the transformation occurred. The transformation is believed to occur via a martensitic process, which is highly temperature dependent thus the transformation could, in some cases occur during cooling after the heat treatment and not at the ageing temperature.

Molecular Dynamics (MD) simulations by Harry and Bacon[44] and Bacon and Osetsky[45, 46] suggest that dislocations passing through Cu precipitates could induce their transformation from bcc to 9R. Lozano-Perez et al.[47] attempted to demonstrate this with *in situ* straining experiments on an Fe-1.3 wt.% Cu alloy aged at 550 °C for 3 hrs to produce a high density of Cu precipitates but could not observe the transformation directly, noting only that precipitates became easier to see after straining. This suggests a change in coherency with the matrix and/or an increase in strain around the particles both indicating precipitates have transformed.

They utilised the method of Monzen et al.[42] to identify precipitates which had transformed when straining was performed *ex situ* on the same alloy as used for the *in situ* experiments. They showed that in the unstrained material 9R precipitates are only observed above ∼5 nm, whereas in the deformed material no untransformed precipitates were observed (in both cases it was only possible to detect precipitates greater than 3 nm). This suggests, in agreement with the MD simulations of Harry and Bacon[44] and Bacon and Osetsky[45, 46], that dislocations can trigger the transformation of precipitates from the coherent bcc phase to the 9R phase. This has been observed in the reciprocal Cu-Fe system. TEM analysis by Easterling and co-workers[48–50] observed that the martensitic transformation of coherent fcc Fe precipitates to incoherent bcc precipitates can be induced by dislocations.

Wang et al.[51] used the carbon extraction replica technique to extract Cu precipitates from a model RPV steel with 0.6 wt.% Cu aged at 400 °C for 2000 hrs. They observed diffraction spots from one 20 nm diameter precipitate consistent with spots from the expected 9R structure but with additional spots arising from a 2H (ABAB.. type) structure. They explain these additional spots as arising from the precipitate having the 9R structure superimposed on a structure which has a longer periodicity.

Modelling by Wang and Zhao[52] suggests that the bcc to 9R transformation is reversible. They postulate this since for certain mean field concentrations of the matrix they observe shrinking of the smaller 9R particles in their simulations. Since no sub-critical ($\lesssim$4 nm diameter) particles are observed in the experimental material they conclude that these sub-critical 9R precipitates transform back to bcc. To be energetically favourable this must form part of a coarsening process. Whilst the larger precipitates are growing, the smaller ones are shrinking and once they shrink below the critical radius they transform back to a bcc structure. They divide the progression of Cu precipitation into three stages, initial bcc precipitates transforming to 9R followed by a stage where no transformations take place, finally a stage where sub-critical 9R particles transform back to bcc. This progression is also consistent with a growth and coarsening process. Hence, the number density of bcc precipitates initially increases,

with initial nucleation of Cu particles, then starts to decrease as particles transform to 9R, then as ageing progresses shows an increase as the sub-critical 9R precipitates transform back to bcc, finally decreasing to almost zero. Their simulations also show that the bcc to 9R transformation may lead to a bi-modal size distribution just prior to the transformation.

A key and as yet unresolved question is the role of Fe in structural transformations. Does it diffuse away prior to the transformation due to the increasing Cu content or does it diffuse away after the transformation? Another point of note is the temperature at which transformation occurs. In Monzen et al.'s work[42] it appears transformation occurs fully at the ageing temperature of 550 °C for precipitates larger than 12 nm, whereas they note that 9R precipitates in the range 4 - 12 nm are likely to have been induced by cooling.

#### 2.3.1.3 Alloy Element Effects on the Formation of Cu Precipitates

Ni and Mn are known to influence the formation of CRPs in steels. The number density of CRPs is often found to be higher in steels containing higher Ni contents indicating an influence of Ni on the precipitation process. Seko et al.[53] concluded that Ni increases the formation of bcc Cu precipitates through lowering the activation energy for the formation of a critical Cu nucleus by segregating to the matrix-precipitate interface. This is in agreement with Metropolis Monte-Carlo (MMC) simulations of Al-Motasem et al.[54] who show the effect to be greater for smaller clusters. This is likely to be due to surface area effects, larger clusters will require more Ni atoms to cover the surface of the cluster.

Cerezo et al.[55] used a combination of APT and a dynamic Ising model simulation to study the effects of Ni and Mn on the formation of CRPs. Their results show that increasing the Ni content from 0.3 at.% to 1.5 at.% in an Fe-Cu-Ni-Mn alloy aged at 365 °C for 3000 hrs produces a greater increase in hardness which they relate to a higher number density of larger CRPs. They propose that Ni and Mn

are non-randomly distributed after the initial stress relief heat treatments and this is confirmed by their Monte-Carlo simulations. This non-randomness is then thought to act as nucleation sites for CRPs as seen from their Ising model simulations. An additional paper by Cerezo et al.[56] presents a 3D Kinetic Monte-Carlo (KMC) model, which also demonstrates the effect of Ni and Mn on Cu precipitation. This seems to present many of the results of the preceding paper, although it does provide a better description of the simulated atoms maps showing what is believed to be heterogeneous nucleation.

Miller and Pareige[21] conducted studies of model Fe-Cu-Ni steels after both thermal ageing (1.13 at.% Cu, 1.36 at.% Ni) and neutron irradiation (0.22 at.% Cu, 0.70 at.% Ni). They report that in the thermally aged steels (aged for up to 100 hrs at temperatures of 400 °C and 500 °C) the Ni enrichment factor in the Cu clusters is not significantly above the matrix levels. The maximum Ni content measured was 2.7 at.% in the specimen aged at 400 °C for 100 hrs. They conclude that Cu particles grow in the Fe-Ni matrix and that in the early stages of formation Fe and Ni are present in the particles. This is then rejected from the Cu clusters during growth and coarsening indicated by the presence of Ni at the interface. They conclude that Ni does not play a role in CRP formation in the early stages of nucleation as it is not significantly enriched (enrichment factor of 1.5) above matrix composition. However, an enrichment factor of 1.5 represents a 50 % increase in solute concentration above bulk concentration. For the irradiated samples, they report a cluster composition of 37.5 % Cu, 5 % Ni with the balance Fe, giving Ni enrichments of a factor of 7, significantly higher than in the aged specimens indicating the presence of Ni in, or around, Cu clusters is more favourable under neutron irradiation.

It seems reasonable that the same effects are at play in both the irradiated and aged cases. Miller and Pareige's interpretation of the thermally aged data seems to be contrary to what would be expected from nucleation theory. Ni segregation to the interface from the matrix would lower the interfacial energy and thus increase the nucleation rate. It is also possible that transient Ni clusters formed here but

the analysis approach by Pareige was not sensitive enough to detect fine scale non-randomness.

#### 2.3.1.4 Segregation of Alloy Elements to CRP Interfaces

Koyama and Onodera[57, 58] produced a simulation of the precipitation of Cu in Fe-Cu-Ni, Fe-Cu-Mn and Fe-Cu-Ni-Mn alloys. Their simulation predicts that in the Fe-Cu-Ni alloy, Cu and Ni precipitate from the matrix, followed by Ni segregation to the matrix/precipitate interface. They predict the same behaviour of Cu and Mn in the Fe-Cu-Mn alloy and of Ni, Mn and Cu in the Fe-Cu-Ni-Mn alloy. In the simulation Ni segregation to the interface is shown to occur much faster than Mn segregation. In the latter paper they extend the simulation to include structural phase transformations of Cu precipitates (it appears they assume a direct bcc to fcc transformation, whereas the consensus is that it occurs via a 9R and 3R stage). They report similar results to their previous simulation. However, now Mn only appears to segregate to interfaces after the CRPs have transformed to an fcc structure. How much influence inclusion of the 9R and 3R stages would have on these simulations remains to be seen. Al-Motasem et al.[54] simulated Cu-Ni-Vacancy, Cu-Ni and Ni-Vacancy clusters in a Fe matrix. They show that the Cu-Ni and Cu-Ni-Vacancy clusters exhibit a core shell structure with Ni at the interface and in the case of the Cu-Ni-Vacancy cluster Cu between the Ni at the interface and vacancies at the core. They show this is due to Ni reducing the interfacial energy of the cluster. For Ni-Vacancy clusters their simulations show that they form two distinct regions, a vacancy region and a Ni region, with no intermixing. Ni atoms were not closer than a $2^{nd}$ neighbour site to a vacancy or another Ni atom. This they attribute to the weak attraction between 2 Ni atoms and between Ni and vacancies. They note that only the second neighbour interaction in their potential is attractive, whilst the first and third are repulsive. This could lead to this peculiar arrangement. Either way these clusters must contain Fe at all the $1^{st}$ neighbour sites of Ni atoms for this configuration to be possible.

The segregation of Ni and Mn to CRP interfaces has also been reported experimentally. Buswell et al.[59] observed that Ni segregated to CRP interfaces in an aged Fe-Cu-Ni alloy. Isheim et al.[60] aged Cu containing low carbon steels at 500 °C for times up to 100 hrs. They report that Ni and Mn form a shell around a Cu rich core. In addition, they report a sharpening of the interface and increasing Ni and Mn concentration with ageing time. Kolli and Seidman[23] studied the evolution of Cu precipitates in a Cu containing High Strength Low Alloy (HSLA) steel thermally aged at 500 °C for times up to 1024 hrs. It should be noted that their steel contains much higher Cu, Ni and Al levels than would be found in RPV steels. Their results clearly show segregation of Ni, Mn and Al to the matrix/precipitate interface, which increases with increasing ageing time. They calculate using the Gibbs adsorption isotherm that Ni, Mn and Al reduced the interfacial energy of a CRP in a steel aged for 1024 hrs at 500 °C by 625.6 mJ $m^{-2}$, 99.4 mJ $m^{-2}$ and 620.3 mJ $m^{-2}$ respectively. These values seem large when compared to estimates of the interfacial energy reported by others, which are in the region of 250 - 400 mJ $m^{-2}$[31, 53, 61]. Seko et al.[53] imply that Ni reduces the interfacial energy by 40 mJ $m^{-2}$, Morley observes a reduction of 40 - 80 mJ $m^{-2}$ due to segregation of Ni, Mn and Si (actual value dependent on bulk Ni content) and Ishiem et al.[22] observed a reduction of 27 mJ $m^{-2}$ due to Ni and Mn. The differences are possibly due to precipitate morphology. Kolli and Siedman's figures are for a rod shaped precipitate, whereas the other work relates to spherical precipitates. Work by Cerezo et al.[56] showed Ni and Mn segregation to CRP interfaces in a complex RPV weld aged for times up to 18,620 hrs. They, like Kolli and Siedman, attribute this to a reduction in interfacial energy and calculate the expected Mn composition at the interface using a MacLean isotherm. They obtained Mn concentrations consistent with their observed data when an energy difference of 12.5 kJ $mol^{-1}$ was used. Monzen et al.[62] used Energy Dispersive X-Ray (EDX) analysis on binary Fe-Cu and ternary Fe-Cu-Ni alloys aged at 650 °C and 700 °C and also report small enrichments of Ni at the CRP/matrix interface, which is in keeping with their calculations and those of others that Ni reduces the interfacial energy. Furthermore, Osamura et al.[63]

used a combination of SANS and APFIM to study an Fe-Cu-Ni-Mn alloy aged at 500 °C and 550 °C for times up to 100 hrs. They found that, for precipitate sizes above 2.1 nm SANS measurements of the Guinier radii obtained from the nuclear and magnetic scattering ratio differed between a binary Fe-Cu and an Fe-Cu-Mn-Ni alloy. They associate this with interfacial segregation of Ni and Mn to precipitates which have transformed from bcc to fcc. Their atom probe results suggest some interfacial segregation, but they make no comment on the crystal structure of the observed precipitates.

Sha et al.[64] show that Sn, present as a trace impurity in a model RPV weld segregates to CRP interfaces. Interfacial segregation was only observed at a large CRP which was no longer coherent with the matrix, Sn segregation to smaller ($< 4$ nm) coherent CRPs was observed, although this was present in the core of the precipitate and not at the interface. Sha et al. report the segregation of Sn to the interface is not driven by a reduction of elastic strain, as is the case for Ni and Mn, since Sn would increase this. Instead they propose that this segregation is due to the high number of special sites for large solute atoms present at the interface.

### 2.3.2 Intragranular Precipitation in Irradiated Steels

The effect of irradiation on RPV steels has been studied using model alloys containing various alloying elements, from the simple binary Fe-Cu alloy to complex multi-component systems and test specimens from RPV surveillance programs. There are significant differences between clusters formed in irradiated and thermally aged materials which will be summarised in Section 2.3.2.1. The following sections cover the same topics as for thermal ageing, with the addition of a discussion on predicted 'Late Blooming Phases' which may occur in low Cu steels under irradiation to high fluence. An example of copper precipitation in an irradiated KS-01 weld is shown in Figure 2.3.

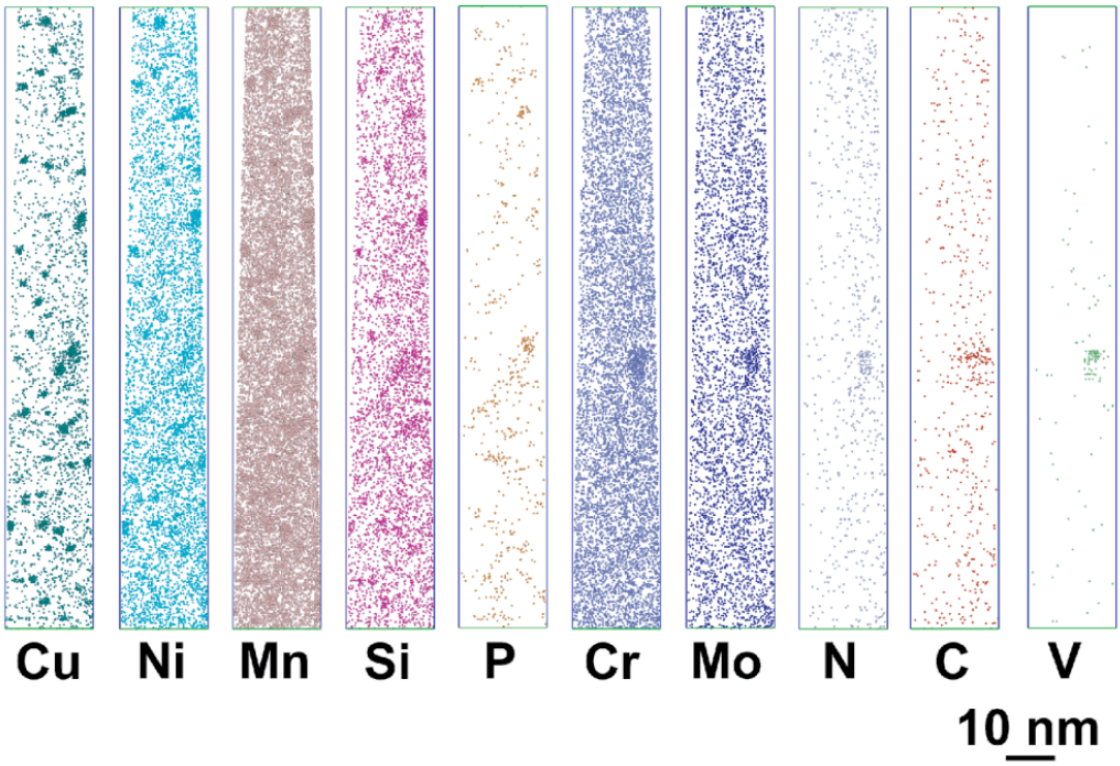


*Figure 2.3:* An example of Cu precipitates formed in a high Cu KS-01 weld neutron irradiated at a temperature of 288 °C to a fluence of 0.8 x $10^{23}$ neutrons $m^{-2}$. Image from Miller et al.[65]. [Reprinted from Philosophical Magazine, Volume 85, M K Miller et al., Atom probe tomography of radiation-sensitive KS-01 weld, pgs. 401 - 408, Copyright (2005), with permission from Taylor & Francis.]

#### 2.3.2.1 Differences Between Clusters Formed Under Irradiation and Thermal Ageing

Features produced by irradiation often occur much more quickly than in thermally aged materials since irradiation increases the concentration of vacancies and point defects which greatly increase the diffusivity of solutes. Odette terms this radiation enhanced diffusion and it is discussed in more detail in Ref.[66].

Clusters formed thermally and those formed under irradiation differ in their size and number density. Under thermal ageing precipitation occurs via nucleation followed by growth and coarsening[67]. Initially there will be a high number density of smaller precipitates, which, as precipitates grow and coarsen are replaced with a lower number density of larger precipitates. This leads to overageing of the materials[68]. In irradiated steels there is very little evidence for overageing of precipitates[69]. In

addition, the number density of features tends to be considerably higher and the features smaller in size. The composition of irradiated clusters also differs and will be discussed in more detail in the next section.

A review by Ghoneim and Hammad[70] provides a summary of the influence of some other solute elements (most notably P) on RPV embrittlement after neutron irradiation, in addition to Cu, Ni and Mn. They briefly discuss the influence of other elements such as Si and Mo on the radiation sensitivity. Furthermore, they note that the Cu, Ni and P content are the most important solute species determining the radiation sensitivity of the material. However, Burke et al.[71] suggest that Mn is the most important element in terms of the development of solute hardening features.

#### 2.3.2.2 The Composition of Precipitates

On the whole, the same discrepancies between APT, SANS and PAS studies of the Cu content of CRPs are evident in the irradiated materials as in the thermally aged materials. In aged steels the only major variables are ageing time, temperature and alloy composition, whilst in irradiated steels there are also additional variables of fluence (total number of neutrons per unit area) and flux (total number of neutrons per unit area per unit time). Displacements per atom (dpa) is often used as an alternative to fluence to describe the total irradiation damage since it allows for easier comparison of the damage done by different irradiation studies on different materials.

Irradiation induced clusters exhibit a much wider range of compositions than thermally induced clusters. They often contain elements such as P, which are not often associated with clusters formed under ageing[65, 72]. The Cu content of irradiated precipitates is also generally lower than those found in aged material.

Hyde et al.[73] compared the composition of a high Ni and a low Ni weld containing $\sim$0.4 at.% Cu after a series of thermal ageing temperatures and irradiation doses. The authors note some differences in composition of clusters between irradiation and ageing, particularly in the low Ni materials, where the clusters formed after irradiation

contained less Cu and more Mn than those after thermal ageing. They found no evidence for any differences in solute distribution within the clusters formed under irradiation or ageing, in both cases clusters exhibited a Cu-enriched core, with Ni, Mn and Si around the edges of these Cu cores.

Buswell et al.[59] compared irradiated and aged Fe-Cu and Fe-Cu-Ni alloys using a combination of SANS, TEM and APT and reported that the CRPs in the irradiated Fe-Cu-Ni alloy contained more Ni than the aged alloy. They made no estimate of the Fe content in the clusters in the Fe-Cu-Ni alloys. For both alloys after irradiation the authors interpreted SANS data to give multiple possible compositions consistent with a given magnetic $A$ ratio. Many of these compositions were consistent with at least some proportion of vacancies.

Wirth et al.[25] report that positron lifetimes of a thermally aged and a neutron irradiated model Fe-Cu-Mn alloy are very similar. This indicates that the compositions of the clusters are similar in irradiated and aged material for this model alloy. In addition, they report Cu vacancy complexes in an Fe-Cu alloy studied with SANS and PAS. In an RPV steel clusters will be more complex and exhibit much more compositional variation.

APT work by Hasegawa et al.[74] showed that the Cu content in the core of CRPs (as defined by the normalised radius of gyration) exhibited only minor variation with neutron dose of around 35 - 45 %, with higher Cu contents observed at higher dose. They observed that concentrations of P, Ni and Si were around 1 - 2 %, whilst Mn concentrations were slightly higher at 4 - 5 %. Variations with dose were shown to be around one percent, again with higher contents at higher doses.

#### 2.3.2.3 Formation of Precipitates

Pareige et al.[75] proposed that the mechanism behind solute precipitation in irradiated steels is not driven by Cu due to its very small concentration but by other solute elements such as Ni and Mn which are present in much higher quantities. In

high Cu steels the underlying mechanism is likely to be driven by Cu given the other common alloy elements are much more soluble in Fe than Cu, although Ni and Mn may have some influence on Cu precipitation. In low Cu steels the thermodynamic driving force for Cu precipitation is less, thus the influence of Ni and Mn may be enhanced since radiation assisted clustering can still occur. However, in a recent paper Radiguet and co-workers[76] studied clustering in electron and Fe-ion irradiated Cu-containing and Cu-free steels and suggested the mechanism behind irradiation induced clusters was point defect clusters (point defect clusters are thought to be interstitial loops, vacancy clusters/microvoids and vacancy loops[77]). Using Mean Field Vacancies and Interstitial Clustering (MFVIC)[78] calculations, they found that there are a high number of point defect clusters formed after ion irradiation. There were substantially fewer point defect clusters after electron irradiation. This led them to the conclusion that Cu, Ni and Mn clustering occurs via heterogeneous nucleation on small point defect clusters. However, in their experiments electron irradiation was performed to a dose of $10^{-3}$ dpa (at a flux of $10^{-9}$ dpa $s^{-1}$) whereas ion irradiation was carried out to doses in the range 0.035 - 0.4 dpa (at a flux of $1.7x10^{-4}$ dpa $s^{-1}$) so the damage caused by each irradiation is not comparable. This mechanism is unlikely in thermally aged materials given that the number of point defects and vacancies will be much less. Instead it is proposed that Ni and Mn sub-critical embryos provide heterogeneous nucleation sites (see Section 2.3.1.3).

Further to this Radiguet et al.[76] compare the experimental results of an ion irradiated Cu free Fe-Ni-Mn-P alloy with the neutron irradiated studies of a similar alloy by Meslin et al.[69], drawing the conclusion that the kinetics of precipitation decrease with increasing radiation flux. When the Fe-Ni-Mn and Fe-Ni-Mn-Cu-P alloys were compared to a binary Fe-Cu alloy previously studied by the same authors[79] they report that Ni, Mn and P slow the formation of clusters since clusters are smaller and less numerous than in the binary alloy. This explanation could well be due to interface stabilisation by those additional elements, making it harder for precipitates to grow.

Glade et al.[80] performed SANS and PAS analyses of Fe-Cu and Fe-Cu-Mn alloys which show that clusters in the Fe-Cu-Mn alloy are greater in number density and smaller in size, which is in agreement with the SANS and APT studies of Miller et al.[81] and APT measurements of Hyde et al.[82]. Glade also reports that Mn interacts with vacancies and point defects which slow the kinetics of CRP formation.

Work by Odette[66] suggests that Cu precipitation is accelerated by the increased diffusivity of Cu resulting from radiation induced defects. He also reports that given the low solubility of Cu at reactor operating temperatures "all but the smallest Cu clusters are expected to be stable" however, it is unclear what the author defines as the smallest size for a stable precipitate. The studies carried out since suggest clusters are stable down to 1 - 2 nm in diameter. Further work by Odette[6] proposes a mechanism in which CRPs form due to radiation enhanced diffusion. Odette calculates that the radiation enhanced diffusion coefficient can be several orders of magnitude higher than for thermal diffusion. Pareige and co-workers[21] compare the results of a ternary Fe-Cu-Ni alloy after thermal ageing and neutron irradiation and find Ni enrichments in CRPs much higher in the irradiated alloy than the aged alloy. They attribute this to the segregation of Ni to CRPs being favourable under neutron irradiation, this is possibly due to Odette's irradiation enhanced diffusion mechanism.

The results of Meslin and co-workers[69] showed the effect of dose (fluence) on solute precipitate formation was limited, in Fe-Cu, Fe-Mn-Ni, Fe-Cu-Mn-Ni alloys. Their results suggest that a lower flux promotes slightly larger clusters, although this is based on a comparison of only one dose and their analysis statistics appear poor. However, there is other evidence which also shows that lower flux irradiations produce larger clusters[83, 84]. Miller et al.[4] presents the matrix Cu levels from several studies after neutron irradiation. According to Miller et al. this shows that for low fluences matrix Cu levels decrease with increasing fluence. For the lower fluences listed ($\lesssim$1 x $10^{23}$ neutrons $m^{-2}$) matrix Cu levels are reasonably constant at around 0.1 at.%. At higher fluences than this matrix Cu levels decrease to around 0.05 at.%. The absolute value does not appear to change with nominal Cu content or fluence (for fluences

above 1 x $10^{23}$ neutrons $m^{-2}$), indicating the solubility limit of Cu in Fe after neutron irradiation is around 0.05 at.%. This is to be expected as diffusion rates would be expected to increase with increasing levels of damage thus increasing the precipitation rate and reducing the matrix solute concentration more quickly. It would be expected that the matrix solute concentration would approach the solubility limit faster with increasing flux.

#### 2.3.2.4 Segregation of Alloy Elements to CRP Interfaces

Interfacial segregation of solute to the matrix precipitate interface is also observed in irradiated alloys. APFIM work by Miller et al.[85] revealed segregation of Ni to the CRP/matrix interface in Fe-Cu alloys containing Ni. Miller et al.[81] have also observed similar effects of Mn in a Fe-Cu-Mn alloy after neutron irradiation studied with SANS and APT. Both Hyde and English[82] and Miller et al.[86] report Ni and Mn to be associated with CRPs and that their enrichments extend over a wider spatial range than Cu, suggesting that there is some form of interfacial segregation occurring. Furthermore, simulations by Odette[6] and experimental SANS and PAS studies by Glade et al.[80] suggest that, as in the case of thermal ageing, Mn lowers the interfacial energy of the coherent (early stage bcc) CRPs reducing the driving force for coarsening whilst decreasing the barrier to nucleation.

#### 2.3.2.5 Clustering in Low Cu/Cu Free Alloys

The so-called "Late Blooming Phase" (LBP), is principally a proposed Ni-Mn(-Si) rich phase predicted by Odette[14] from computational simulations and interpretation of SANS data. Odette predicts these features will be most prominent in low Cu steels with high Ni contents. In addition, his model predicts a greater volume fraction of Ni/Mn precipitates at lower irradiation temperatures and at higher neutron fluence. Odette catagorizes these LBPs as irradiation enhanced phases, due to their slow formation kinetics in thermally aged material. It is possible LBPs could form

thermally although no evidence of LBPs in purely thermally aged materials has been published. However, there are very few studies of materials thermally aged for the very long times which would be necessary for LBP formation.

Possible experimental evidence of Ni-Mn-Si rich precipitates has been published by Miller et al.[86–90] mainly concerning VVER type steels. Ref.[89] presents the preliminary results of the more detailed study of Ref.[90] and will not be discussed further. Refs.[87] and [88] present essentially the same results of neutron irradiation and thermal ageing of low Cu and low Ni/Ni free VVER weld and base metal surveillance specimens. Spherical and cylindrical Mn- and Si-rich features were observed in the irradiated material but not in the thermally aged material, which correlated to an increase in UTS and yield strength for the neutron irradiated materials. As with Cu rich features these Mn- and Si-rich features contain significant (>50 %) amounts of Fe.

Miller et al.[87, 88] propose a mechanism of nucleation of these features either on dislocations (cylindrical features) or dislocation loops (spherical features), in addition to possible nucleation on small Cu clusters (∼5 atoms). This second mechanism is similar to the method of CRP nucleation on sub-critical Ni-Mn clusters discussed earlier (Section 2.3.1.3).

In Miller et al.[90] the authors report nanoscale (1 - 2 nm in diameter) Ni-Mn-Si clusters in low Cu, high Ni weld and plate RPV steels after irradiation to a high fluence. These features are smaller in size than those from Ref.[88], where spherical features have reported diameters of 3 - 4 nm indicating a possible influence of Ni on cluster size. The number density of features correlated with an increase in fluence (most notably in the higher Ni weld specimen) and with increased Ni and Mn content. Average compositions were reported not to be statistically different with changes in fluence or between weld and base metal. This is broadly consistent with Takeuchi et al.[91] who report 1 - 2 nm radius Mn-Ni-Si(-Cu) rich features in steels containing 0.04 wt.% and 0.19 wt.% Cu, with only small variations in solute contents with fluence.

There are significant quantities of Fe in these precipitates, around in 80 % to 85 % in Miller et al.[87, 88] and Takeuchi et al.'s[91] work respectively whereas in Miller et al.[89, 90] Fe contents are around 10 %. These apparent differences, as well as the slight differences in size are probably due to the analysis methods chosen. A further discussion of cluster analysis techniques and analysis parameters is provided in Sections 3.4.4.2.1 and 4.2.1.2. Takeuchi et al. use the maximum separation method with a $d_{max}$ parameter of 0.7 nm, along with an $L$ parameter of 0.7 nm and an erosion distance of 0.5 nm. A $d_{max} = 0.7$ nm is very large (more than two lattice spacings) and will include many matrix atoms in the precipitate. The large difference between $L$ and $e$ will also mean many matrix atoms are added by the $L$ parameter but not eroded, again skewing the composition towards that of the matrix, i.e towards higher Fe content. In Miller et al.[87, 88] analysis parameters are not specified whilst in Miller et al.[90] the envelope method[92] was used with a grid spacing of 0.1 nm and $d_{max} = 0.6$ nm, although a $d_{max}$ of 0.6 nm is still a little high.

Meslin et al.[93] irradiated a Fe-0.7Ni-1.1Mn alloy at 300 °C to doses between 0.026 and 0.2 dpa. They observed a high number density of Ni-Mn and Mn-rich clusters for material irradiated at high flux to 0.1 and 0.2 dpa and at low flux to 0.03 dpa. The authors attribute this to a kinetic effect induced by irradiation. Corresponding simulations by Ngayam-Happy et al.[94] also show the formation of these Ni-Mn and Mn only precipitates, but at much lower doses than in the experimental work of Meslin et al.[93]. This is probably due to the limitations of the APT technique, whereby only a proportion of the evaporated atoms are detected, reducing the sensitivity to small clusters.

Ngayam-Happy et al.'s modelling also suggests the clusters are associated with Self Interstitial Atoms (SIAs), which they propose are involved in the nucleation of these clusters, whereby Ni and Mn atoms segregate to SIAs. They note Mn forms very stable mixed dumbbells (two atoms sharing the same lattice site), which then diffuse by self interstitial migration leading to local accumulation of Mn. In the same simulations, but with the presence of 0.18 % Cu, they see the presence of both Cu clusters and

Ni-Mn clusters. These are also seen by Hyde et al.[73] who present evidence of Ni-Mn-Si clusters in a high Cu steel irradiated to a high dose (353 mdpa), suggesting these features can form in high Cu steels as well as low Cu materials. Ngayam-Happy et al.'s simulations suggest that Cu clusters contain very few vacancies or SIAs due to recombination with Mn dumbbells. They suggest a differing kinetic mechanism for the formation of Ni-Mn precipitates and those containing predominantly Cu. Ni-Mn clusters nucleate at low dose, via the fast SIA mechanism, and their number density increases slowly with dose. Cu clusters nucleate slowly, via substitutional diffusion, with their number density increasing steadily with increasing dose. They combine these two mechanisms to postulate a process for the formation of Ni-Mn clusters or LBPs in Cu containing alloys. The authors propose that LBPs nucleate in the early stages of the irradiation. After a while Cu precipitation starts to dominate, as the increase in number density of Ni-Mn precipitates is slow (presumably slow growth is also a factor here). Thus at low doses Cu precipitates are by far the most dominant population of clusters. However, as the dose increases, Cu becomes exhausted from the matrix. They suggest that at this point, when no more Cu clusters are forming, that the density of Ni-Mn precipitates would increase.

### 2.3.3 Intergranular Precipitation and Segregation

Several elements for example, P, C, Mo, Ni and Mn are known to segregate to grain boundaries in RPV steels[65, 72, 95]. Figure 2.4 shows an example from a VVER-400 weld. This section presents an overview of the studies conducted into precipitation of solute elements at grain boundaries in RPV steels. The majority of the work on segregation has been observed with atom probe and Field Ion Microscopy (FIM). A study by Burke et al.[96] has shown similar results using EDX.

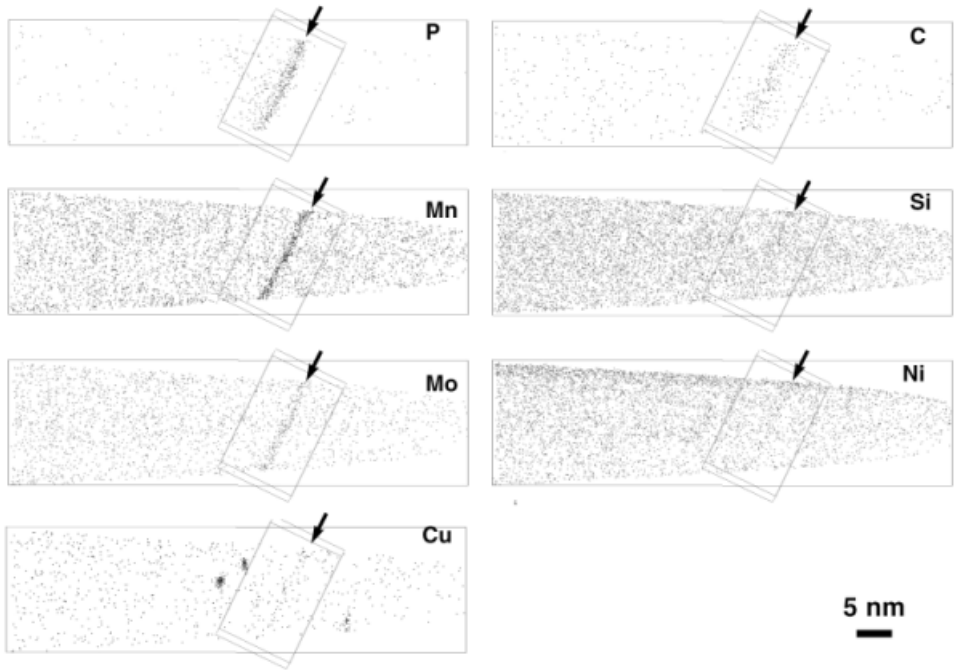


*Figure 2.4:* An example of solute segregation to a grain boundary in a VVER 400 weld. Image from Miller et al.[72]. [Reprinted from MRS Proceedings, Volume 650, M. K. Miller and P. Pareige, Atomic Level Characterization of Neutron Irradiated Pressure Vessel Steels, pgs R6.1.1-12, 2000. Copyright (2001), with permission from Cambridge University Press.]

#### 2.3.3.1 Thermally Aged Steels

Carbides, nitrides and carbo-nitrides are commonly observed at grain boundaries in both thermally aged[97] and irradiated[98] materials.

Charleux et al.[99] observed Cu precipitation at both grain boundaries and within grains. They report that precipitates are larger at grain boundaries than in the matrix. The composition of these precipitates is not given. In a HSLA steel aged at 500 °C for 100 hrs Vaynman et al.[100] observed a Ni-Al rich precipitate with small (<10 at.%) amounts of Fe, Mn, Cu and Si at a grain boundary. They report that the boundary is enriched with C, B and P but these elements are not present in the precipitate observed. Segregation of C, B and P is consistent with the observations of Isheim et al.[60].

#### 2.3.3.2 Irradiated Steels

Segregation of P to grain boundaries has been observed[98, 101, 102]. Miller et al.[4] showed that the level of P at grain boundaries increased with neutron fluence. However, whilst Faulkner et al.[103] also saw that P segregation to grain boundaries was sensitive to the dose received, they found it was dependent on the material. The level of grain boundary P was observed to be inversely proportional to the C content at the boundary. The highest levels of P segregation were found in VVER type steels. It is possible that this may be related to the overall levels of C and P present in the steel, since P and C are thought to have a repulsive interaction with one another[104] and a higher C content would likely give a lower P content at the boundary. They also observed a reduction in C segregation with irradiation dose. P segregation is also observed by Miller and Burke[95], who note that irradiation has little effect on the concentrations of Ni and Mn at the boundary. It is also worth noting that P is already enriched well above the nominal bulk composition at grain boundaries even prior to irradiation. Simulations by Ebihara et al.[105] showed no influence of dose rate on grain boundary P coverage in the range $10^{-11} - 10^{-7}$ dpa $s^{-1}$ to a total dose of 0.11 dpa. From their simulations they concluded that P atoms are transported to grain boundaries by interstitial dumbbells as opposed to vacancy diffusion.

Miller and Burke [95] observed coarse carbides and a Cu-Mn precipitate in an irradiated A533B weld. These coarse precipitates will form during the stress relief heat treatments and are not a feature of irradiation. In addition, Miller et al.[106] observed enrichments of Ni, Mn and P as well as Mo carbides and nitrides in an irradiated A533B type submerged arc weld.

Toyama et al.[107] observed segregation of P, C, Mo along with small amounts of Si and Mn to dislocation lines forming part of a low angle boundary in an irradiated RPV weld. In addition, they observed Cu precipitates with almost no other associated elements (it is not clear if these also contain Fe or are pure Cu) along the dislocations, in contrast to those in the matrix which contained Mn, Ni, P and Si. No quantitative

information is given regarding the comparative sizes but visual inspection suggests the difference is minimal. It is important to note that some precipitation of Cu will occur at both grain boundaries and dislocations during the post weld heat treatment.

## 2.4 Summary of the Precipitation of Alloy Elements in RPV Steels

Thermally aged and neutron irradiated RPV steels show slightly different effects. Features in irradiated materials tend to develop more quickly than they do thermally. In addition, they are often smaller and more numerous than in aged material and exhibit a broader range of compositions.

There is some evidence from both experiments and simulations which suggest Ni and Mn play a role in the initial formation of the CRPs, particularly in thermally aged materials. The mechanism in irradiated steels is more difficult to determine given the large numbers of vacancies and point defects present in these materials and also the difficulty in separating the influence of the thermal ageing from that of irradiation. However, it is important to remember that, in nearly all cases, the overriding driving force for Cu precipitation is the low solubility of Cu in Fe.

Although observations of Ni-Mn-Si rich clusters have recently been published for both Cu containing and Cu free alloys it would be premature to describe them as hard and fast evidence of "Late Blooming Phases", based on only a few publications. Furthermore, the evidence suggests these nucleate in the early stages of irradiation and as such, growth of these features later on should be more concerning rather than their formation. Hence, it might be more prudent to call them "slowly blooming phases". In addition, there is little agreement on the Fe content of these clusters.

The segregation of solute elements to grain boundaries is commonly observed in both aged and irradiated material. Studies suggest that segregation of P is enhanced after

neutron irradiation. Coarse carbides, formed during stress relief heat treatments are also frequently observed at boundaries along with smaller sized carbides which are probably induced by ageing and/or irradiation. In depth studies of Cu precipitation at grain boundaries appears limited.

This review also highlights the difficulties faced when comparing compositions of solute clusters. For instance SANS data, which relies on assumptions regarding the magnetisation of clusters and can yield several compositions consistent with a given $A$ ratio, can give contradictory results to atom probe. The classic example of this is the amount of Fe present in Cu-enriched precipitates. There are no standard procedures for analysing atom probe data and different analysis methods can lead to widely varying results, even between analyses on the same dataset. Likewise, whilst it is accepted that bcc Cu-enriched precipitates transform to fcc via 9R and 3R stages, there is still some disagreement as to the precise size at which this occurs. In addition, the role of Fe in this transformation remains unclear.

## 2.5 Concluding Remarks

Significant progress has been made in the understanding of the precipitation of solute elements in RPV steels particularly since the advent of the 3 dimensional atom probe. However, several outstanding issues remain.

- There remain relatively few studies on the influence of long term ageing on the microstructural and mechanical property evolution of RPV materials at temperatures close to reactor operating temperatures.
- The debate over the quantity of Fe in CRPs is ongoing, although recent work by Morley et al.[10] has made some progress in this area.
- The size at which precipitates undergo the bcc to 9R transformation and whether this effects/is affected by the Fe content of the precipitate is not well understood.

- The early stages of CRP formation are still not clear, particularly in the case of neutron irradiated specimens. Evidence for the formation of sub-critical Ni-Mn embryos acting as nucleation sites for CRPs is sparse.
- There is still doubt over the existence of 'Late Blooming Phases'[14] and the microstructural evolution in low Cu materials. Some recent progress in this area has been made by Miller et al.[86, 87] mainly on Russian VVER type steels.
- There are relatively few studies (for example the EU program PISA, Phosphorus Influence on Steel Ageing) of grain boundary evolution in both thermally aged and irradiated materials, which could have an influence on 'non-hardening embrittlement', that is embrittlement which does not contribute to hardening such as intergranular fracture.
- There are numerous methods to analyse atom probe data and the next chapter highlights the relative strengths and weaknesses of some of the more common methods.

# 3. Experimental Methods and Materials

The steels in this project are broadly in line with an A533B and A302B type weld and plate steel as used in most British and American reactors. They have a ferritic/bainitic microstructure with grain sizes of the order of 10 $\mu$m.

## 3.1 Materials

A series of eight submerged-arc weld and two reference plate specimens with systematic variations of Ni and Cu have been thermally aged for times up to 100,000 hrs at temperatures of 330 °C, 365 °C and 405 °C. The 8 weld specimens form two groups. The 'S' series, containing four steels of different Cu content, with low Ni contents and the 'W' series, also containing four welds with Cu contents broadly similar to the 'S' series but with a higher Ni content. These two groups of welds allow ageing to be studied as a function of both Cu and Ni content. The composition of all ten specimens is detailed in Table 3.1. Specimen materials were provided by Rolls-Royce Plc and heat treatments up to 50,000 hrs were performed by Dr. S. Hirosawa and Dr. A. Morley. With the exception of the WV materials aged at 365 °C, APT analysis of materials aged for times up to 50,000 hrs, were, in general, performed on the Energy Compensated Optical Position Sensitive Atom Probe (ECOPoSAP) by Hirosawa and Morley and have been reported in Ref.[19]. Some of this data is reported again here for comparison between with the newer data obtained for this thesis from longer ageing times to show trends with ageing time.

Prior to ageing all specimen blocks underwent a standard post weld heat treatment

| | Cu | Ni | Mn | Si | C | Mo | S | P | Cr | Al | V | Sn | As | Sb |
|---|---|---|---|---|---|---|---|---|---|---|---|---|---|---|
| SP | 0.06 | 0.06 | 1.58 | 0.73 | 0.27 | 0.31 | 0.026 | 0.043 | 0.013 | 0.010 | 0.0055 | 0.007 | 0.0074 | 0.0023 |
| SD | 0.13 | 0.08 | 1.76 | 1.19 | 0.28 | 0.31 | 0.031 | 0.045 | 0.069 | 0.012 | 0.0054 | 0.007 | 0.0074 | 0.0023 |
| SF | 0.21 | 0.24 | 1.48 | 0.95 | 0.22 | 0.28 | 0.042 | 0.041 | 0.043 | 0.010 | 0.0055 | 0.007 | 0.0074 | 0.0023 |
| SG | 0.43 | 0.29 | 1.52 | 0.81 | 0.24 | 0.28 | 0.043 | 0.043 | 0.047 | 0.010 | 0.0055 | 0.007 | 0.0074 | 0.0023 |
| WF | 0.02 | 1.63 | 1.43 | 1.05 | 0.18 | 0.20 | 0.012 | 0.016 | 0.100 | 0.010 | 0.0055 | 0.007 | 0.0074 | 0.0023 |
| WK | 0.12 | 1.55 | 1.47 | 0.95 | 0.24 | 0.22 | 0.009 | 0.020 | 0.046 | 0.006 | 0.0055 | 0.007 | 0.0074 | 0.0023 |
| WG | 0.20 | 1.60 | 1.22 | 1.19 | 0.17 | 0.20 | 0.012 | 0.014 | 0.100 | 0.010 | 0.0055 | 0.007 | 0.0074 | 0.0023 |
| WV | 0.44 | 1.66 | 1.38 | 0.75 | 0.19 | 0.24 | 0.016 | 0.018 | 0.054 | 0.010 | 0.0055 | 0.007 | 0.0074 | 0.0023 |
| PD | 0.06 | 0.60 | 1.28 | 0.40 | 0.90 | 0.25 | 0.021 | 0.027 | 0.11 | 0.041 | 0.0054 | 0.007 | 0.0074 | 0.0023 |
| PE | 0.19 | 0.56 | 1.46 | 0.46 | 1.09 | 0.30 | 0.019 | 0.013 | 0.12 | 0.041 | 0.0054 | 0.007 | 0.0074 | 0.0023 |
| | Cu | Ni | Mn | Si | C | Mo | S | P | Cr | Al | V | Sn | As | Sb |

*Table 3.1:* Composition of the weld and plate specimens in at.%, bal. Fe.

of annealing at $920 \pm 20$ °C for 6 hrs followed by a water quench, then tempering at $600 \pm 15$ °C and stress relief at $650 \pm 15$ °C for 42 hrs and 6 hrs respectively followed by slow cooling ($\leq$ 50 °C $hr^{-1}$) after each treatment stage. Samples were aged in sealed quartz tubes under Ar atmosphere or vacuum to limit the effects of oxidation and were water quenched upon removal from the furnace.

The ageing temperatures used in this study are higher than the typical in service operating temperature experienced by an RPV of around 290 °C. The temperatures of 330 °C, 365 °C and 405 °C were chosen so that whilst the kinetic processes which underpin the precipitation of alloy elements would take place on a faster timescale, the underlying thermodynamic regime was not too dissimilar to that experienced by an in service reactor. This allows conclusions to be made about what might be expected to occur at 290 °C with reasonable confidence. In addition, solid solubilities of Ni[108] and Mn[109], the main elements thought to affect the precipitation of Cu, are reasonably constant over this range of temperatures (290 °C - 405 °C) which allows the effect of these elements on Cu precipitation to be investigated.

## 3.2 Hardness Testing

Cu precipitation is known to cause changes in the mechanical properties of these steels. In order to relate the microstructural information with the change in macroscopic properties, hardness testing was carried out on all large specimen blocks after ageing and removal of 0.1 $\mu$m of material to remove any affects of surface oxidation or de-carburisation. Tests were carried out on the as-ground faces (excluding the end faces), with two indents made on each face using the same Vickers indenter as has been used for all previous indents of these materials, with a load of 20 kg applied for 10 s. Indents were made at a distance of at least three times the indent diagonal away from each other to negate any effects of work hardening caused by the formation of the indents. The largest and smallest readings from the 8 indents were discarded and the average of the remaining 6 indents taken to be the hardness. Hardness changes are reported since

tests have been carried out on a number of different blocks with subtle variations in initial hardness which would otherwise distort the true hardness changes. Variations in hardness data, as given by the standard deviation of the 6 measurements were, in the majority of cases less than the error of the tester (±3 Hv), which corresponds to an overall error of ±4 Hv when the hardness changes are considered.

To ensure consistency between the new measurements and those made by others a number of blocks previously tested by others were retested and compared. The re-measured values were within error of the existing results indicating that the new hardness measurements are consistent with the previously measured values on the materials aged to 50,000 hrs.

## 3.3 APT Sample Preparation

Two methods of sample preparation were used to make specimens for atom probe analysis. All specimens were cut into 0.5 x 0.5 x 0.5 mm matchsticks from the larger specimen blocks using a Buehler Isomet 5000 diamond wafering saw and then electrochemically thinned into needle shaped specimens (see Section 3.3.1). For specimens where site specific analysis was of interest, for example, grain boundaries, the electrochemically polished needles were further thinned using Focussed Ion Beam (FIB) milling to ensure the feature of interest was within the analysis volume of the atom probe (see Section 3.3.2).

### 3.3.1 Electropolishing

All specimens were thinned from matchsticks using the standard two stage electropolish method described by Miller et al.[110]. Matchsticks were thinned using a solution of 25 % perchloric acid (60 %) in acetic acid with an applied voltage of 16 V with the final stages at 8 V to produce two needle shaped specimens, see Figure 3.1a.

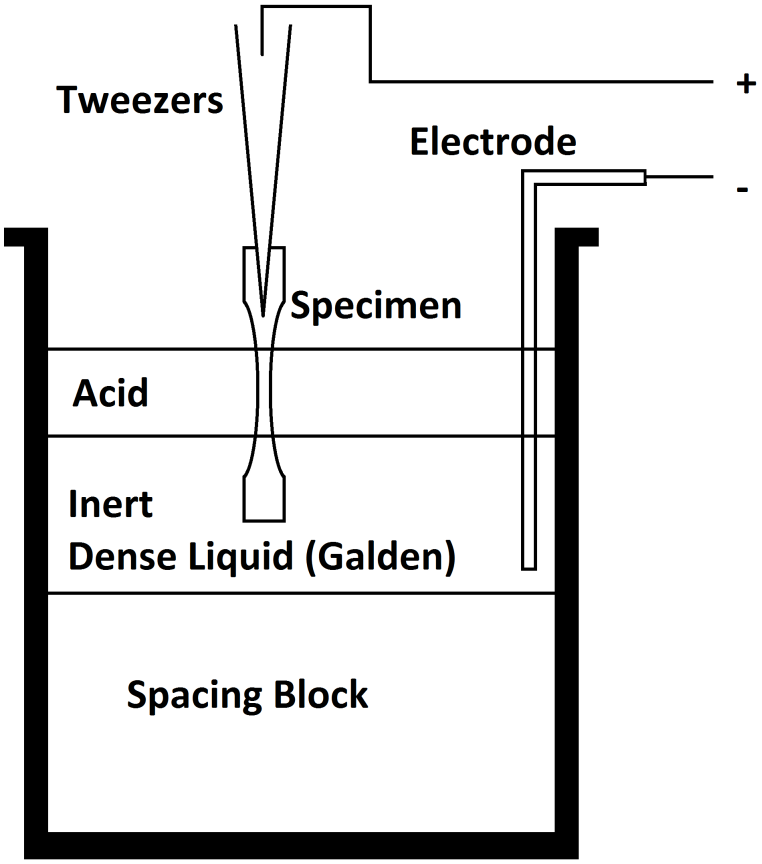


*(a)* Stage one polish set-up.

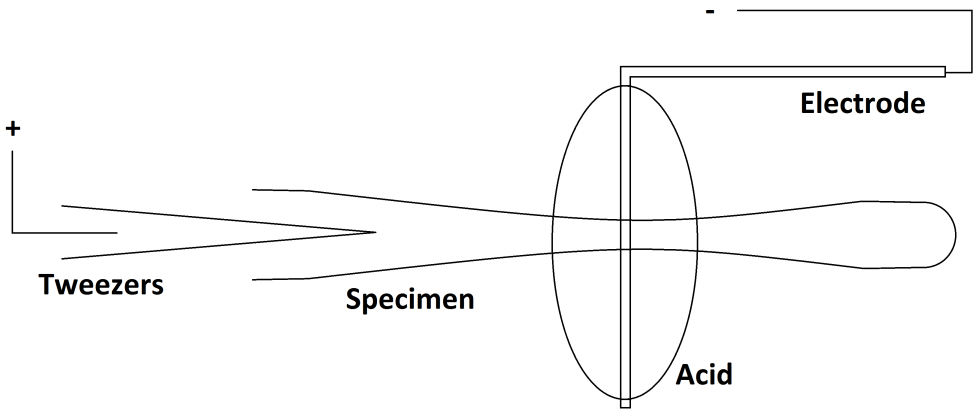


*(b)* Stage two polish set-up.

*Figure 3.1:* Set-up for electropolishing of atom probe specimens. (a) Stage one polishing and (b) stage two polishing.

These specimens were too blunt for atom probe analyses and were more finely polished using a solution of 2 % perchloric acid (60 %) in 2-butoxy-ethanol to produce specimens with an end radius of ∼100 nm, as shown in Figure 3.1b. Specimens for which FIB was to be used were intentionally left slightly blunt in order to make preparation easier in the FIB. Specimens which fractured during LEAP analysis without yielding significant volumes of analysis were re-polished using the final stage polishing solution to produce a new sharp tip for analysis. This new tip was polished so as to be at least 1 mm behind the original specimen tip to ensure a significantly different area of the specimen was analysed.

### 3.3.2 Focussed Ion Beam Milling

As previously mentioned some specimens were selected for grain boundary analysis. The grain size of these materials is of the order of 10 $\mu$m, hence an annular milling method similar to that described by Larson et al.[111] could be used as, in general, grain boundaries would be less than 10 $\mu$m from the specimen apex. This method of grain boundary specimen preparation has advantages and disadvantages over the lift out method where small sections are cut from a portion of a boundary and atom probe needles produced from this section (see, for example, Thomson et al.[112] for more details). With the lift out method it is possible to easily select boundaries of known mis-orientation and to also control the orientation of the boundary within the specimen (traditionally parallel to the analysis direction) as well as make several samples from the same boundary. Using pre-prepared needles it is much harder to control the orientation of the boundary within the analysis volume. Likewise, it is harder to select boundaries of known mis-orientation. Recent advances in APT data analysis using Hough transformations has enabled calculation of grain boundary mis-orientations from APT datasets[113]. Production of specimens from electropolished needles is considerably less time consuming and complex, so for the preliminary studies of grain boundary features in this work it was deemed the best option.

## 3.4 Atom Probe Tomography

APT[114, 115] has been used extensively to study copper clustering in RPV steels. It combines near atomic scale resolution with time-of-flight mass spectrometry to produce a 3-dimensional map of atomic species and is thus an excellent technique for studying nanoscale solute clustering. Numerous statistical techniques have been developed which allow for identification and characterisation of these nanoscale clusters within APT datasets and these are discussed in more detail in Section 3.4.4.

The atom probe technique works on the principle of having a needle shaped specimen with an extremely sharp tip. Specimens typically have a radius at the tip apex of the order of 100 nm. Application of an electric field to this tip stimulates field emission of ions from the end of the tip. With such a sharp tip the applied voltages need only be of the order 3 - 8 kV to obtain the field required for evaporation (for pure Fe this is around 33 V $nm^{-1}$ at 70 K[116]). As the analysis progresses the specimen gradually becomes blunter as ions are removed, thus a higher voltage is required to continue evaporation. A schematic of a Local Electrode Atom Probe (LEAP)[117] is shown in Figure 3.2.

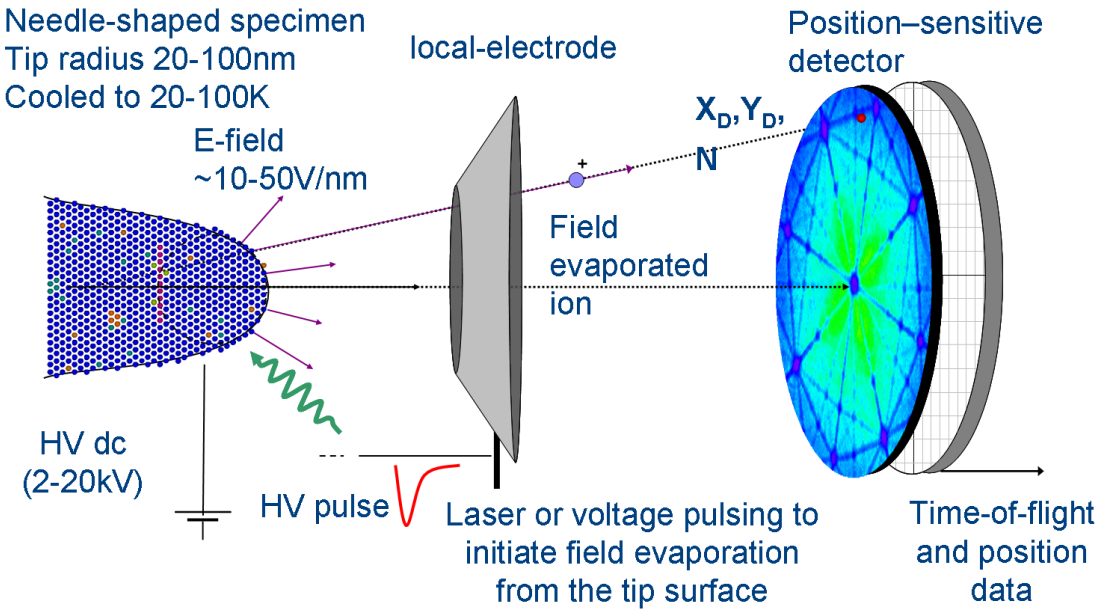


*Figure 3.2:* Schematic of a Local Electrode Atom Probe. Based on [118].

In practice, as chemical information is required, a standing voltage is applied such

that it is below the threshold for field evaporation. A series of pulses are then applied, either in the form of an additional voltage which takes the field over the threshold for evaporation or a laser pulse which heats the specimen, again triggering evaporation. This allows time-of-flight information to be recorded between the application of the pulse and the time an ion hits the detector allowing identification of the chemical species evaporated, assuming evaporation and acceleration are virtually instantaneous. The time-of-flight, $t_{flight}$, can be related to the mass to charge ratio, $m/n$ of the evaporated ion through

$$\frac{m}{n} \approx 2eV \left( \frac{t_{flight}}{L} \right)^2 \tag{3.1}$$

where $e$ is the charge of an electron, $V$ the total applied voltage (standing voltage plus pulse voltage) and $L$ the specimen to detector distance.

Ideally, atoms with the same mass to charge ratio should have the same time-of-flight, in practice there is a small energy spread which causes the broadening of mass peaks in the mass spectrum. To combat this, most modern instruments are fitted with an energy compensating lens or reflectron. This consists of a region in the flight path between the specimen and detector with opposing electric field to that on the specimen, such that ions which enter this region are slowed and reflected back out towards the detector. Ions with the same mass to charge ratio but a higher energy travel further into this region and take a slightly longer path, whilst lower energy ions travel a slightly shorter distance. The result is a narrower range of flight times and a sharper mass peak. This is particularly important for steels where there are as many as 20 peaks with mass to charge ratios in the range 25 - 33. The use of a reflectron causes some loss of ions due to ions hitting the wire mesh used to establish the equipotentials inside the electrostatic lens. Additionally, the mesh causes some slight distortion of ion trajectories resulting in a small loss of lateral resolution (around 0.1 - 0.2 nm[92]).

A position sensitive detector is used to determine the position on the tip from which the evaporated ions originated. Data reconstruction is discussed in more detail in the

next section. Ions which arrive at the same time on the detector can be distinguished provided they are spatially well separated on the detector (not within the same 1.5 x 1.5 mm area[119]). Conversely, ions which arrive at the same position can be distinguished if they arrive more than 1.5 ns apart[119]. Microchannel plate detectors are typically used as they have low noise and a high sensitivity to single ion hits. However, they are not perfect and have an overall detection efficiency of around 50 - 60 %. When coupled with the losses due to the reflectron less than 50 % of the ions evaporated from the tip are detected depending on the instrument, typically ∼37 % in the current work.

### 3.4.1 Data Reconstruction

Data reconstruction has been carried out using the IVAS$^{TM}$ software. Suitable regions from the hitmap ($x$ and $y$ limits) were selected to remove edge effects from the electrode (see Appendix A). The voltage curve was used to select an appropriate depth region, so as to exclude the ions evaporated at the beginning which will be mainly oxides and select regions of uniform evaporation (free of microfractures) also shown in Appendix A. All datasets were reconstructed using the same mass range file to ensure consistency in ranging. The specimen radius evolution was constructed from the change in specimen voltage across the run as these are inter-related (see Equation 3.7).

There are a number of equations which are used to turn the positions of the ion hits from the detector co-ordinates ($x_d$ and $y_d$) into the co-ordinates of the atoms on the tip ($x$ and $y$). In this thesis the $xy$ plane is that perpendicular to the analysis direction defined as $z$. The tip $x$ and $y$ co-ordinates are calculated using

$$x = \frac{x_d}{\eta} \tag{3.2}$$

$$y = \frac{y_d}{\eta} \tag{3.3}$$

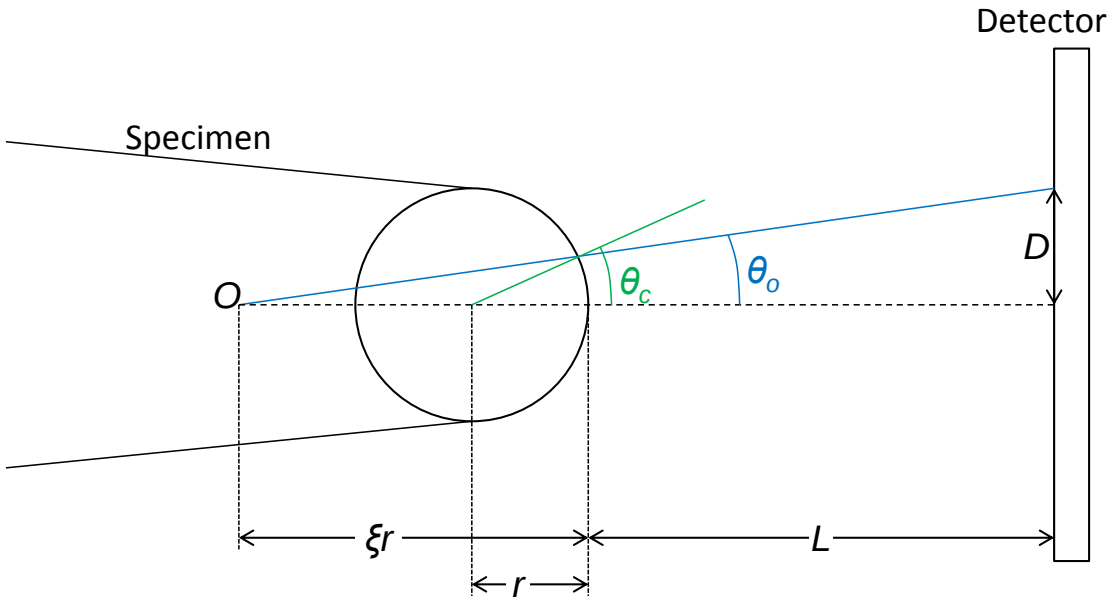


*Figure 3.3:* Diagram showing the origins of the image compression factor, $\xi$, based on Figure 4 from Ref.[120].

Where $\eta$ is the magnification, given by

$$\eta = \frac{L}{\xi r} \tag{3.4}$$

with $L$, the specimen to detector distance and $r$ the specimen radius. $\xi$, the Image Compression Factor (ICF) arises from the fact ion trajectories are bent towards the detector by the presence of the electric field and the specimen shank. In principle, for a straight flight path atom probe, $\xi$ can be calculated from[120]

$$\xi = \frac{\theta_o}{\theta_c} \tag{3.5}$$

where $\theta_c$ and $\theta_o$ are the actual angles between two crystallographic directions and the angle observed on the detector respectively, as shown in Figure 3.3.

$\theta_o$ can be calculated from[120]

$$\theta_o = \tan^{-1}\left(\frac{D}{L}\right) \tag{3.6}$$

with $D$ the distance between the centre of the two poles on the detector. The radius of the tip at any given moment can be estimated from the applied voltage using

$$r = \frac{V}{kE} \tag{3.7}$$

where $V$ is the total specimen voltage (standing plus pulse), $k$ a constant arising from specimen geometry and $E$ the evaporation field, which for pure Fe is 33 V nm$^{-1}$ at 70 K[116].

For each ion hitting the detector the $z$ co-ordinate is incremented by $dz$ which is given by

$$dz = \frac{\Omega}{\eta^2 x_d y_d \zeta} \tag{3.8}$$

where $\Omega$ is the atomic volume (since these materials are $> 95$ % Fe, this is taken to be the atomic volume of Fe, 1/85 nm$^3$) and $\zeta$, the detection efficiency, which for the LEAP instrument is taken to be 0.37 or 37 %. Since the specimen endform has some curvature (assumed to be hemi-spherical) a small correction, $z_c$ needs to be applied to $dz$. Taking this into account gives the $z$ co-ordinate as

$$z = dz + z_c = dz + \left(r - \sqrt{r^2 - (x^2 + y^2)}\right) \tag{3.9}$$

From these equations there are essentially three parameters which can be changed which alter the $x$, $y$, $z$ positions of the atoms, and hence the quality of the reconstruction, namely the ICF, $\xi$, the geometric factor from Equation 3.7, $k$ and the initial radius, $r$. Although it is possible to calculate the ICF value from Equation 3.5, in practice with a reflectron instrument where the exact flight path length is not known this is not possible. Likewise, it is difficult to calculate the exact value of $k$, since this will change slightly from run to run and requires knowledge of the specimen radius. Hence, the values for the ICF and $k$ were left as the default values in IVAS (these were 1.6 for the ICF and 3.3 for $k$). Values of the initial radius were chosen such that the plane spacing around the major pole in the dataset was correct, typically

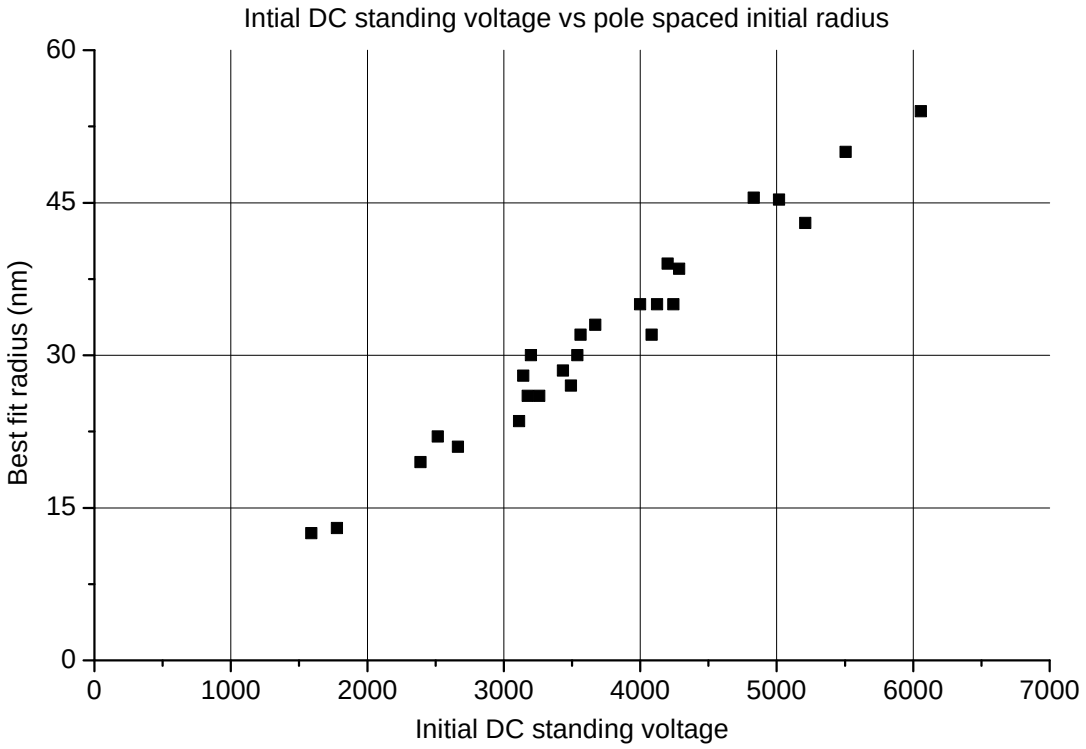


*Figure 3.4:* Correlation between the initial radius giving the correct plane spacing and the initial DC voltage for all WV reconstructions.

this calibration was performed on (110), (200) or (020) poles. It was not possible to perform the calibration if one of these poles was not present, since other plane spacings are too close together to be easily resolved, in this case the best fit radius was calculated based upon the radii used previously (see Figure 3.4).

Plane spacings were calculated using the rdf-kd program, courtesy of Dr. D. J. Haley[121]. Radial Distribution Functions (RDFs) calculate the frequency of ions at a given distance from one another. The rdf-kd program allows this to be visualised in three dimensions, where the strongest signal will correspond to the plane spacing (since this corresponds to the most frequent spacing of atoms). Adjusting the initial radius changes the plane spacing such that the correct spacing can be achieved, increasing the radius, reduces the plane spacing and vice-versa. The following procedure was used to perform data reconstructions:

1. An appropriate region of data was selected based upon the detector hit map and voltage curve.

2. Ranging applied.
3. An initial value for the specimen radius was chosen.
4. Visible poles were indexed based upon the detector hitmap, atom density plots and any segregated solutes.
5. A small region (∼8 x 8 x 20 nm) down the major pole in the dataset was selected, where planes were most visible and the rdf-kd program run on this region with a nearest neighbour distance of 1.5 nm and a bin size of 0.05 nm.
6. The plane spacing was calculated from the distance between neighbouring peaks in the 3D RDF.
7. Steps 3 - 6 were repeated until the planes had the expected spacing.

Figure 3.5 shows a comparison between the reconstruction using the default IVAS values (ICF, $k$, initial $r$) compared with the reconstruction with the correct plane spacing and the corresponding 3D RDFs for a WV steel aged for 3000 hrs at 365 °C. Using the default parameters with an initial radius of 35 nm and looking at the spacing of planes down the (011) pole gives a spacing of 0.11 nm, which is around half the expected value of $a_0/\sqrt{2} = 0.203$ nm. Decreasing the initial radius (akin to increasing the $k$ value) causes the plane spacing to increase. With an initial radius of 26 nm, the (011) plane spacing is 0.201 nm, which is very close to the expected value. The increase in the quality of the reconstruction is also seen from the shape of the Cu-enriched precipitates. In Figure 3.5a the precipitates appear to be "pancake shaped" i.e squashed in the $z$ direction, in the correct reconstruction (Figure 3.5d) the precipitates have a much more spherical shape consistent with what would be expected. Likewise, Figures 3.5b and 3.5e show that the planes are more widely spaced and more easily discernible in the correct reconstruction.

The default values in IVAS for $k$ and $\xi$ are based upon CAMECA simulations of evaporation of ions from a tip in a set-up identical to that in the LEAP. This allows computation of the values for $k$ and $\xi$ for the simulated set up. However, for real APT

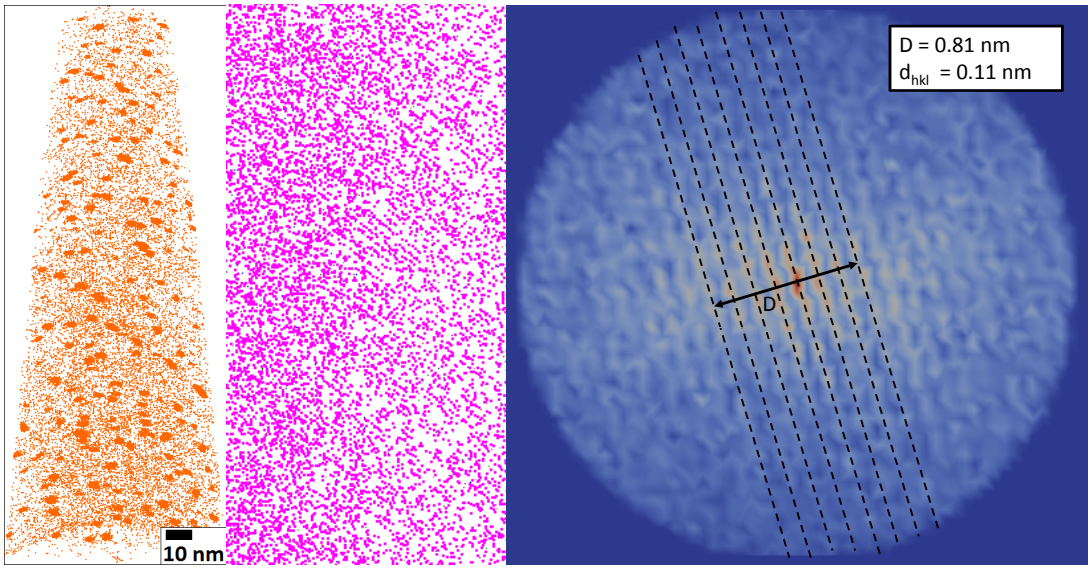


*(a)* Default Reconstruction.

*(b)* Section showing planes from atom map in (a).

*(c)* 3D RDF corresponding to (a).

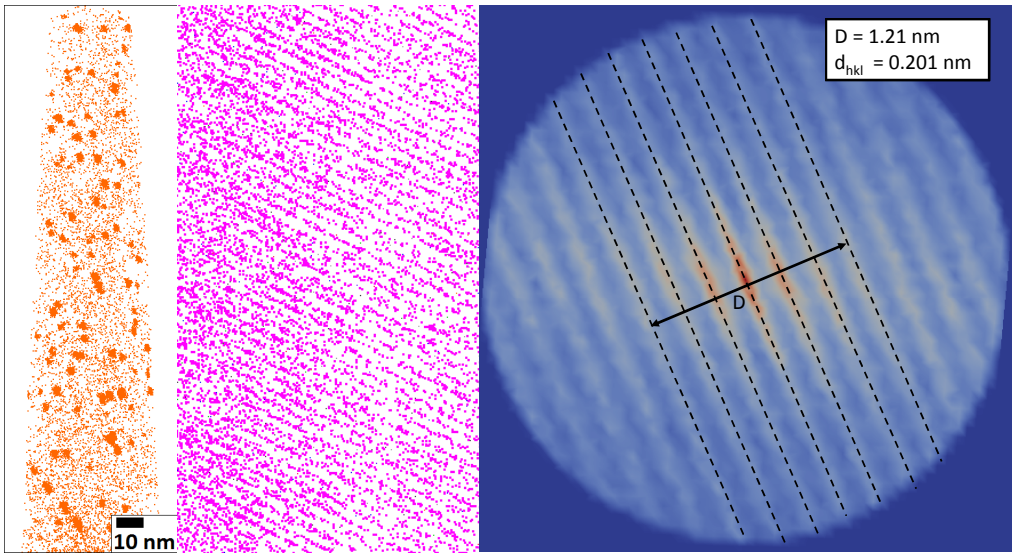


*(d)* Correct Reconstruction.

*(e)* Section showing planes from atom map in (d).

*(f)* 3D RDF corresponding to (d).

*Figure 3.5:* (a) Atom map showing the reconstruction of a WV steel aged for 3000 hrs at 365 °C with default reconstruction parameters, (b) 5 x 10 nm section from the (011) pole from the atom map in (a) showing lattice planes, (c) 3D RDF used to calculated the plane spacing of the (011) pole in (a), (d) Atom map showing the reconstruction of the sample in (a) with the initial radius chosen to give the correct plane spacing down the (011) pole, (e) 5 x 10 nm section from the (011) pole from atom map in (d) showing lattice planes, (f) 3D RDF showing the plane spacing of the reconstruction in (d) very close to the expected value of 0.203 nm.

specimens $k$ and $\xi$ are not constant and will vary from specimen to specimen. IVAS estimates the radius based upon Equation 3.7, so if the $k$ value is too small then the radius will be overestimated as is the case here. Hence adjusting $k$ alters the radius or as has been done here $r$ has been adjusted which alters $k$.

### 3.4.2 Atom Probe Artefacts Affecting Solute Clusters

As with any technique there are inherent limitations to APT. The books by Miller et al.[110], Miller[92] and Gault et al.[122] provide detailed information on the principles of the atom probe technique including information on these limitations. There are two effects which warrant description here since they are directly related to some of the problems discussed earlier regarding fine scale solute clustering (Section 2.3.1.1). These are local magnification effects and trajectory overlaps. Also, the imperfect detection efficiency means that clusters detected by APT appear to contain fewer atoms than they actually do, since only a portion of the ions evaporated are detected. This is a particular issue for clusters containing very few atoms, which consequently may not be detected by cluster search algorithms. The detection efficiency has no influence on composition since the detection of a given atom occurs randomly.

Combining Equation 3.4 for the magnification with Equation 3.7 for the radius, gives

$$\eta = \frac{LEk}{V\xi} \tag{3.10}$$

Hence, the magnification of the tip at the detector is a function of the applied voltage (proportional to the tip radius) and evaporation field among other things. In practice, the assumption of a hemispherical tip with uniform evaporation field is not strictly valid. Firstly, regional variations in curvature, for example due to crystal orientation lead to variations in magnification[110]. In addition, in the case of alloys, different phases have different evaporation fields. This effect is prominent in the case of precipitates, where the Fe-Cu system is a good example. Cu requires a lower field for

evaporation than Fe and this results in local magnification and potentially trajectory overlaps.

#### 3.4.2.1 Local Magnification Effects

Differences in local curvature between the matrix and the second phase, cause an apparent difference in the density of atoms in the associated regions of the reconstructed volume[123]. In the case of the Fe-Cu system the Cu-enriched regions appear more dense than the Fe matrix. De Geuser et al.[124] and Vurpillot et al.[125] show this using simulated data. This has also been observed experimentally[19]. In the paper by De Geuser et al. they proposed a method to try and remove some of the effects of local magnification due to precipitates by using separate reconstruction parameters for matrix and precipitate atoms. They apply this method to simulated and real data and whilst the results are not perfect, they are an improvement.

#### 3.4.2.2 Trajectory Overlaps

Simulations have shown that local magnification effects can lead to overlaps in ion trajectories[125]. This can result in one phase appearing to contain atoms from another phase. The discrepancy between the amount of Fe in CRPs between 3DAP and SANS/PAS data is probably partly due to this.

Camus et al.[126] proposed a method to try to reduce the effects of trajectory overlaps using Fourier transforms and pattern matching to find the statistically best fit for repositioning of atoms to their lattice sites. The applicability of this technique to real datasets was not determined. An alternative method by Vurpillot et al.[127] also uses the Fourier transform technique to reposition atoms affected by trajectory overlaps onto their nearest lattice plane in the reconstructed volume. They estimate that this can be done with around 85 % efficiency. There are some important limitations to this method. Firstly, the method has only been applied to pure W and not alloys where other problems arise due to differences in evaporation field between different

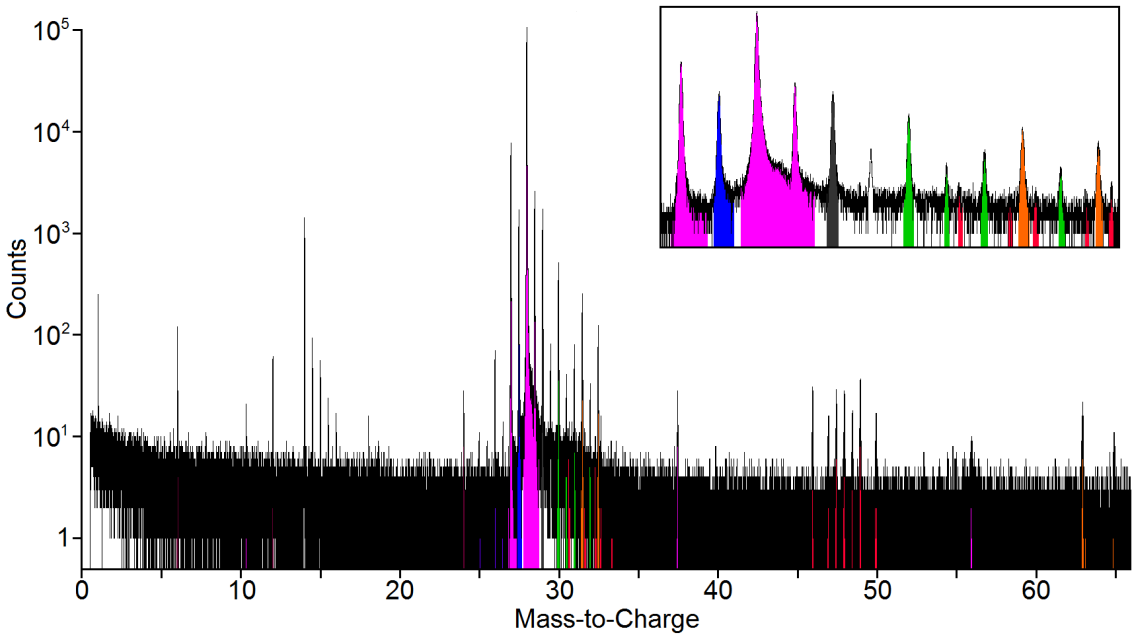


*Figure 3.6:* Typical mass spectrum obtained with voltage pulsing at 50 K and 20 % pulse fraction. Inset, magnified section of the peaks in 27 - 33 region.

atomic species. Furthermore, the method can only replace atoms to the nearest lattice plane(s) which is not necessarily the correct lattice site, it can also result in multiple atoms at a given lattice site. The authors quantify this, taking into account detection efficiency (60 %), as occurring at no more than ∼8 % of lattice sites. Application of this procedure to LEAP data, where the detection efficiency is only 37 %, is even more difficult.

### 3.4.3 Mass Spectrum and Ranging

A typical mass spectrum obtained with voltage pulsing from the high Cu, high Ni WV steel is shown in Figure 3.6.

The spectrum shows that the majority of the peaks are well separated and that it is possible to see the presence of P at levels around 0.018 at.%. Since the atomic species is inferred from the time-of-flight data, if two or more atomic species have the same time-of-flight they appear in the same peak in the mass spectrum. This could arise from two atomic species having isotopes of the same mass, such as $^{58}Fe^{2+}$ and $^{58}Ni^{2+}$. Alternatively, two different atomic species could have the same mass-to-charge ratio

| Species 1 | Species 2 | Mass-to-charge ratio | Treatment |
|---|---|---|---|
| $^{14}N^{+}$ | $^{28}Si^{2+}$ | 14 | Considered to be Si |
| $^{54}Cr^{2+}$ | $^{54}Fe^{2+}$ | 27 | Considered to be Fe |
| $^{28}Si^{+}$ | $^{56}Fe^{2+}$ | 28 | Considered to be Fe |
| $^{58}Fe^{2+}$ | $^{58}Ni^{2+}$ | 29 | Treated separately |
| $^{31}P^{+}$ | $^{62}Ni^{2+}$ | 31 | Considered to be Ni |
| $^{96}Mo^{3+}$ | $^{64}Ni^{2+}$ | 32 | Considered to be Ni |
| $^{12}C^{+}$ | $^{12}C_2^{2+}$ | 12 | Considered to be $^{12}C^{+}$ |

*Table 3.2:* Treatment of the main peak overlaps observed in the mass spectrum.

and thus the same time-of-flight, for example, $^{28}Si^{+}$ and $^{56}Fe^{2+}$. In these cases it is not possible to discern the atoms of one species from the others which constitute the peak overlap. The main peak overlaps of concern in these materials are listed in Table 3.2.

Most of the overlaps listed in Table 3.2 are considered to be one atomic species. In each case the species which makes up only a very minor portion of the peak is ignored. However, this is not the case for the $^{58}Fe^{2+}/^{58}Ni^{2+}$ peak overlap. This peak consists of significant proportions of both Fe and Ni. In general, this will be treated as the hypothetical element Fn and treated accordingly. In the high Ni steels this can be considered as Ni when determining cluster compositions, since the peak will only contain approximately 1 % Fe (based upon a precipitate containing 15 % Ni, 40 % Fe). For the matrix composition this can be de-convoluted by calculating the expected amounts of each element in the peak based upon the counts and isotopic abundances of the other isotopes of Ni and Fe. In the low Ni steels this peak will in general be reported as Fn.

### 3.4.4 Atom Probe Data Analysis

Since the invention of the 3-Dimensional Atom Probe (3DAP) there have been many methods developed to analyse the acquired data sets. Delargy showed that clustering in atom probe data is difficult to identify in atomic "dot maps" with the naked eye[128] and thus demonstrated the need for computerised methods, which were not susceptible

to the bias of the human eye. The increased computer power available today has made the process of cluster characterisation a much quicker process and enabled more complex algorithms to be used. Books by Miller[92] and Miller et al.[110] present an overview of some of the different analysis methods developed up to the year 2000 and provide a good starting point for further information on characterisation techniques. More recent analysis techniques are discussed in Gault et al.[122] and Marquis and Hyde[129]. The sections below provide an overview of some of the more common methods which can be used to characterise clusters/interfaces in atom probe datasets. More details on each of the methods mentioned below can be found in the appropriate references.

#### 3.4.4.1 Tests for Solute Non-Randomness in Atom Probe Datasets

There are several methods which can be used to detect non-randomness in the distribution of atomic species in atom probe datasets. Several methods discussed later in this section build on these basic techniques and so they will discussed briefly here.

##### 3.4.4.1.1 Frequency Distributions

A frequency distribution analysis[110] involves dividing the dataset into blocks with a fixed number of atoms. This is done without reference to spatial location and thus some spatial resolution is lost. The frequency of blocks containing a given number, or concentration, of a particular atomic species is plotted. This can be compared to the binomial distribution, which would be expected if the dataset were entirely random. Comparison between the two distributions allows non-randomness or ordering to be detected. If ordering has occurred the experimental distribution will be narrower than the binomial distribution, if there is non-randomness in the dataset then the distribution will be broader. The statistical significance of any deviation from randomness can be found using the chi-squared test, see page 326 in Ref.[110].

The drawback of using the chi-squared test is that it requires careful choice of block size. If the block size is too big then the compositional variation will be of the order of the block size and statistical significance will not be detected. Conversely, if the block size is too small blocks will need to be combined together since the number of blocks containing $i$ solute atoms should be larger than some minimum, usually 5. This removes the influence of single observations which have a disproportionally large contribution to chi-squared.

#### 3.4.4.1.2 Contingency Tables

Contingency tables[110] involve dividing the data set up into equally sized blocks containing a fixed number of atoms, as with the frequency distribution technique, but now there are two variables, A and B. If a system contains more than 2 elements then blocks must contain a fixed number of atoms of the elements not being used in the contingency table to avoid systematic error[122]. The number of blocks, $n_{rc}$ containing a given number of A and B atoms is plotted in a table, like that shown in Table 3.3.

| | | Number of B atoms in a block | | | | | | |
|---|---|---|---|---|---|---|---|---|
| | | 1 | 2 | 3 | 4 | . | c | Total |
| Number of A atoms in a block | 1 | $n_{11}$ | $n_{12}$ | $n_{13}$ | $n_{14}$ | $n_{1.}$ | $n_{1c}$ | $t_{1.}$ |
| | 2 | $n_{21}$ | $n_{22}$ | $n_{23}$ | $n_{24}$ | $n_{2.}$ | $n_{2c}$ | $t_{2.}$ |
| | 3 | $n_{31}$ | $n_{32}$ | $n_{33}$ | $n_{34}$ | $n_{3.}$ | $n_{3c}$ | $t_{3.}$ |
| | 4 | $n_{41}$ | $n_{42}$ | $n_{43}$ | $n_{44}$ | $n_{4.}$ | $n_{4c}$ | $t_{4.}$ |
| | . | $n_{.1}$ | $n_{.2}$ | $n_{.3}$ | $n_{.4}$ | $n_{..}$ | $n_{.c}$ | $t_{..}$ |
| | r | $n_{r1}$ | $n_{r2}$ | $n_{r3}$ | $n_{r4}$ | $n_{r.}$ | $n_{rc}$ | $t_{r.}$ |
| | Total | $t_{.1}$ | $t_{.2}$ | $t_{.3}$ | $t_{.4}$ | $t_{..}$ | $t_{.c}$ | $t_{..}$ |

*Table 3.3:* An example of a contingency table showing the number of blocks containing a given number of A and B atoms. Based on Table 5.1 in Ref.[110].

This can then be compared to the estimated expected number, $e_{rc}$, given by

$$e_{rc} = \frac{t_{r.}t_{.c}}{t_{..}} \tag{3.11}$$

A final table can then be constructed detailing whether the observed number is more or less than the expected number, with the significance again given by a chi-squared test. The sum of the number of blocks in each row and column should be the same in both the observed and expected cases.

#### 3.4.4.1.3 Auto-correlations

The 1-dimensional autocorrelation function is defined in Equation 3.12.

$$R_k = \frac{1}{\sigma^2} \sum_{i=1}^{n_b-k} (c_i - c_0)(c_{i+k} - c_0) \tag{3.12}$$

It can be easily calculated from a composition profile with $n_b$ blocks (see Sections 3.4.4.3.2 and 3.4.4.3.3). $c_0$ is the mean concentration, $c_i$ and $c_{i+k}$ are the compositions of the $i^{th}$ and $(i+k)^{th}$ block respectively and $\sigma^2$ the variance. $k$ is the lag and defines the length over which correlation is being investigated. If there is no correlation on the length scale of $k$, i.e the data is random the number of positive and negative correlations will balance out and $R_k$ will be zero. A positive value of $R_k$ indicates correlation between atoms of the same kind at a distance of $k$ blocks apart. Whereas a strong negative correlation signals there is an inverse correlation. Positive correlations could indicate clustering, spinodal decomposition or even ordering on the scale of lattice planes, for example in a superlattice. It is obvious that the sensitivity of this method is highly dependent on the lag, $k$. This technique was developed for the original one dimensional atom probe and was extended to APT data with the three dimensional autocorrelation function by Cerezo and Hetherington[130].

Analogous to the auto-correlation functions are cross-correlations. These can be used to identify differences in auto-correlation functions of two solute species for example. These are of some use when studying co-segregation, but contingency table analysis would, in general, provide more useful information[110].

#### 3.4.4.1.4 Local Chemistry Method

The local chemistry method[131] is a technique developed by Hyde et al. to detect fine scale solute clustering/non-randomness in atom probe datasets. The technique combines the contingency table analysis and frequency distribution techniques by considering the mean concentration around a given solute atom and comparing it to what would be expected from a random distribution. The ratio of the observed number of 'B' atoms in the vicinity of 'A' atoms to the expected number is calculated, with a value of 1 representing a random distribution, a value less than 1 indicating depletion of 'B' in the region of 'A' and a value greater than 1 indicating clustering of 'A' and 'B'. This technique keeps the spatial information which is lost with contingency tables. However, both techniques are subject to uncertainties due to positioning errors and imperfect detection efficiency. Hyde et al. show this method detects non-randomness between Mn and Si, and Ni and Si which was not evident using a contingency table analysis. The authors also demonstrate that the method successfully reproduces results from frequency distribution and contingency table analyses where clustering/non-randomness was detectable using those techniques.

### 3.4.4.2 Cluster Search Algorithms

#### 3.4.4.2.1 Maximum Separation Method

The maximum separation method is one of the more commonly used cluster identification algorithms[10, 132]. The original algorithm was first published by Hyde and English[82]. Later, Heinrich et al.[133] proposed a similar, more basic method than the one of Hyde and English. The maximum separation method identifies all solute atoms within a distance, $d_{max}$ of another solute atom. Two solute atoms which are within this distance are said to be in the same cluster. This process is repeated for all solute atoms in the dataset. It is usual for a parameter $N_{min}$, the minimum number of atoms in a cluster, to be introduced to remove the contributions of clusters

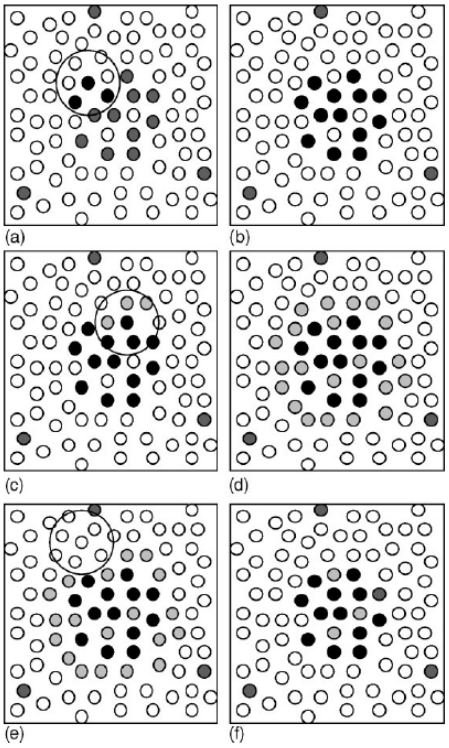


*Figure 3.7:* Schematic of the maximum separation method. (a) and (b) Solute atoms within a distance $d_{max}$ of another solute atom are selected. (c) and (d) Atoms within a distance $L$ of solute atoms in the cluster are added. (e) Erosion. Atoms within a distance $e$ of a matrix atom are removed. (f) Final cluster. Selected solute atoms are black, unselected solute is dark grey, other atoms are white/light grey. [Reprinted from Surface and Interface Analysis, Volume 39, A Cerezo and L Davin, Aspects of the observation of clusters in the 3-dimensional atom probe, pgs. 184 - 188, Copyright (2007), with permission from John Wiley and Sons.]

which occur due to random processes. The next step in the algorithm has several variations. It was proposed by Hyde and English[82] that in order to include any additional atoms which may form part of the cluster, which have not been identified previously, all neighbouring atoms to those characterised by the $d_{max}$ parameter should be included. This has the undesirable affect of introducing a shell of matrix atoms around the cluster which can then be removed. Vaumousse et al.[134] explain the method for the addition of these atoms and the removal of the shell of matrix atoms more clearly than in the paper by Hyde and English. According to Vaumousse et al. all atoms within a distance $L$ of atoms classified as being in a cluster are also considered part of that cluster. An erosion process is then used to remove the undesired matrix atoms. The method is shown schematically in Figure 3.7.

The erosion process removes atoms systematically from the cluster based on the distance from the nearest atom not identified as being part of the cluster. Plotting the composition of the eroded particles shows that a sharp change in the composition is observed at the cluster matrix boundary[134]. The erosion process is explained more clearly by Morley[19].

It is clear this method relies heavily on selecting suitable parameters for $d_{max}$, $N_{min}$, $L$ and the erosion parameter, $e$. Too small a value of $d_{max}$ means large clusters are characterised as many smaller clusters, whilst too large a $d_{max}$ parameter can mean all solute atoms are selected as being part of a single cluster or very few large clusters[134]. Papers by Vaumousse et al.[134], Cerezo and Davin[135] and Vaumousse[136] have all suggested ways for optimising the parameters used in the algorithm.

#### 3.4.4.2.2 Chemistry Based Methods

An alternative to the maximum separation method for identifying solute clusters is one based upon the local chemistry of different regions. Kolli and Seidman[132] use a method based upon isoconcentration surfaces (see Section 3.4.4.3.4). They identify precipitates as regions with a concentration greater than some threshold, termed $C^{threshold}$, since the concentration of particular atomic species will be enhanced in a cluster. The authors note however, that this method is highly sensitive to the value chosen for $C^{threshold}$ and that small precipitates close to the edge of larger ones may be considered part of the same feature. They propose that the value chosen for $C^{threshold}$ is such that small changes do not significantly alter the number or size.

Lefebvre et al.[137] present an alternative method, which is also based on the local chemical environment. In this method they move a sphere of radius, $R$ over all atoms in the dataset and calculate, for example, the concentration of a species within this sphere. If the concentration of a given species is above some threshold this atom is designated a being part of a cluster. Atoms which are within the distance $R$, are considered part of the same cluster if the concentration measured in the sphere is

above the threshold in both cases.

#### 3.4.4.2.3 Density Based Methods

In addition to the maximum separation method and concentration based methods there are density based algorithms. Stephenson et al.[138] propose a density based method, named core-linkage, which is based upon the DBSCAN[139] algorithm. Essentially this is the maximum separation method when only the first nearest neighbour is considered, but with the core-linkage method higher order nearest neighbours can be considered. The method is divided into two steps, a core step and a linkage step. In the core step solute atoms are identified as being core atoms if they adhere to some condition, such as having a local density greater than some characteristic minimum density. The linkage stage adds all atoms within a distance $d_{link}$ of a core atom, referred to by the authors as border atoms. This method does not appear to implement an erosion step, which if $d_{link}$ is not chosen correctly could lead to a shell of matrix around clusters.

Lefebrve et al.[140] demonstrate the application of Delaunay tessellation to identify clusters in APT datasets. This method essentially works by linking atoms of a particular element together with vertices. These vertices must be wholly contained within an empty sphere whose surface passes through 3 atoms (2d case as shown in the example in Figure 3.8) or 4 atoms (3d case) which form a series of small enclosed volumes or cells.

In the case of a random solute distribution the lengths of the vertices of these cells, $R_C$ approximately follows a Poisson type distribution. If the lengths of the cell edges are less than some threshold $R_T$ then Lefebvre considers the atoms at the vertices of the cell to be in a clustered cell. To remove cells which are incorrectly characterised as part of the wrong phase (clustered cells considered as matrix cells and vice-versa) an erosion-expansion algorithm is employed, which considers the environment around such clustered cells. Clustered cells must be attached to at least one other clustered

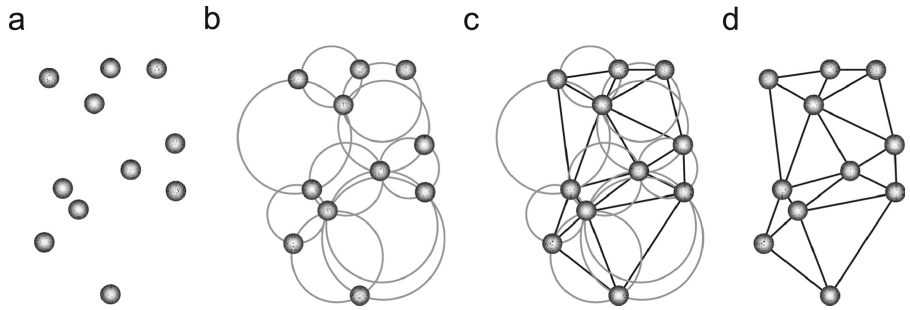


*Figure 3.8:* Example of the application of the Delaunay tessellation to a distribution of solute atoms in a 2d dataset. (a) 2d distribution of solute atoms, (b) Circles drawn such that each circle contains only three atoms on its border and no other atoms are contained within it, (c) triangles constructed to link the atoms within the circle and (d) the completed Delaunay Tessellation. [Reprinted from Ultramicroscopy, Volume 111, W Lefebvre, T Phillipe and F Vurpillot, Application of Delaunay tessellation for the characterisation of solute-rich clusters in atom probe tomography, pgs. 200 - 206, Copyright (2010), with permission from Elsevier B.V]

cell, likewise matrix cells attached to three clustered cells are also considered clustered cells. The erosion-expansion algorithm is considered complete when the identities of the cells (matrix or clustered) no longer change. Clusters are then given by all the atoms which are contained within these clustered cells.

In principle, density based cluster search methods could be used to exploit the higher local density of Cu-enriched precipitates compared to the surrounding matrix due to local magnification. In practice, the two algorithms presented are likely to be more time consuming than the standard maximum separation method. Additionally, the algorithms are not easily available and hence less widely used, making comparative analysis with other results more difficult. This is also true of the concentration based methods presented in Section 3.4.4.2.2.

#### 3.4.4.2.4 Other Methods

The previous three sections have highlighted some of the methods and algorithms which have been developed and applied to APT datasets. This is by no means an exhaustive list and there are many other methods which have been used including those based upon Nearest-Neighbours e.g Phillipe et al.[141] and those using 3d Markov chains e.g Ceguerra et al.[142].

#### 3.4.4.3 Compositional Analysis

It is generally of interest to know the chemical composition of localised regions within a large dataset for instance across a grain boundary or of clusters identified using a cluster identification tool such as those in Section 3.4.4.2.

##### 3.4.4.3.1 Composition of Clusters/Precipitates

The simplest method of measuring the composition of a feature is to define a region of interest around the cluster, usually a sphere and work out the concentration of each element contained in this volume. This can then be taken as the composition of the given feature. Whilst easy to apply, this method can include a contribution from the matrix atoms if the feature deviates from a spherical geometry. In addition, it can be difficult to determine the exact position of the matrix/precipitate interface within the dataset, thus under- or over-estimating the extent and thus composition of the feature. A better way is to use a cluster search algorithm to determine which atoms belong to a feature, the composition of the feature is then given in the usual way. The ratio of the concentration of an element in a feature to its concentration in the matrix can be used to define an enrichment factor for a given element within the feature.

##### 3.4.4.3.2 Planar Composition Profiles

1 and 2 dimensional composition profiles are a useful analysis tool for viewing the compositional change across an interface, for example, at a grain boundary. They are less suited to radial features like clusters/precipitates. One-dimensional composition profiles are usually obtained by defining a small region of interest within the larger volume of the dataset, typically in the form of an elongated cuboid or cylinder. The composition profile is then generated by subdividing the region of interest into small subsections of equal width (voxels) perpendicular to the desired direction of analysis. The concentration of each element in each of these small volumes is then calculated

and plotted on a graph resulting in a one dimensional composition profile. This can be extended to two dimensions by creating small cuboid volumes, perpendicular to the analysis plane. These cuboids should have equal cross sectional area in the plane of the analysis direction. This results in a contour map of the concentration for a given region of interest.

Both one and two dimensional profiles require careful consideration of voxel size since too small a voxel size can introduce large statistical errors from the low number of atoms in the voxel. Too large a voxel size can mask subtle variations in concentration over the region of interest but have lower statistical error.

#### 3.4.4.3.3 Radial Composition Profiles

It is often the case that the composition profile of a very small cluster or precipitate within a dataset is desired. In this case the method described above is inadequate, since it will include large proportions of matrix atoms in the profile, distorting the concentration profile, especially if the desired feature is spherically or near spherically symmetric. This problem can be solved using a radial composition profile. Instead of defining a cube or cylindrical region of interest, one can define a spherical region and apply the same method as before but now the thin sections are replaced with thin shells emanating from a central point, often defined at the centre of mass of the precipitate. This method will henceforth be referred to as the shell method. It is obvious that this method can only be applied to spherical or cylindrical precipitates since for other shapes there will be significant matrix contribution in the outermost shells. It is also important to define the centre of the precipitate as accurately as possible, since this can also lead to significant matrix contribution to the composition profile. Radial composition profiles suffer from large statistical error at their centres where compositions are calculated from very small numbers of atoms, whilst there are many more atoms in the outer shells. For one and two dimensional profiles, since each voxel will contain roughly similar numbers of atoms, the error is roughly constant

between each voxel, however the relative error may be much higher since there may be only a few atoms in each voxel.

An alternative method of determining the composition profile of clusters, proposed by Vaumousse et al.[134] is a simple extension of the erosion process used in the maximum separation method. By continuing the erosion process until all the atoms in the cluster have been removed, an erosion profile of the cluster is generated. This method has two advantages over the shell method above in that it requires no prior knowledge of the centre of the precipitate, thus reducing the susceptibility to uncertainties from incorrect definition of the precipitate centre. It can also be applied to non spherical precipitates. Morley further extends this method to remove the effects of trajectory aberrations from the composition profile[10].

#### 3.4.4.3.4 Isoconcentration Surfaces

Isoconcentration surfaces can be thought of as the three dimensional extension of a composition profile and are an excellent technique for visualising the interface between two regions, whether this be a precipitate or grain boundary. Isoconcentration surfaces are generated by linking regions of a given concentration of an element together using the marching cubes algorithm[143]. This requires the data to be divided into voxels, typically these are square with length of the order of 0.5 nm. The average concentration of an element in this voxel is calculated. This is turned into a lattice of points representing the average concentration of a given element within the voxel, with each point spatially correlated with the position of the corresponding voxel. Neighbouring points on this lattice with the same concentration are then linked together to give the isoconcentration surface. It is common for these surfaces to be smoothed, since with small voxels there can be large variation from voxel to voxel giving very rough surfaces.

#### 3.4.4.3.5 Proximity Histograms

Proximity histograms[144, 145] allow 1 dimensional/radial concentration profiles to be built up over an arbitrarily shaped interface. The interface is defined by an isoconcentration surface produced by forming a 3 dimensional grid of concentration values using the method described by Hellman et al.[144]. They note that the interface, as defined by the isoconcentration surface, will depend on the concentration of solute chosen to produce it, but note this effect can be minimised if the interface is taken to be the point of steepest concentration gradient. The proximity histogram is then produced by plotting the concentration of a given element as a function of distance from the interface. The authors add that since the composition profile is based on distance from an interface, results from many interfaces can be easily combined together to reduce statistical error. However, this is susceptible to error introduced from incorrectly setting the concentration defining the isoconcentration surface. Conversely, it has an advantage over radial composition profiles produced by the shell method since it requires no prior knowledge of precipitate centres and, much like the method of Vaumousse, can be applied to arbitrarily shaped precipitates.

# 4. Experimental Conditions and Analysis Techniques for LEAP Data

This chapter explains the choice of analysis conditions for the atom probe analysis of the RPV materials in this project. In addition, the chapter reports some of the methods used to analyse data obtained and describes the methods used to analyse the interfaces between Cu-enriched precipitates and the surrounding matrix and to remove the influence of background clusters from the results of the cluster search. A comparison between the results obtained from the ECOPoSAP by Morley, Hirosawa and Sha[19] and the new data from the LEAP has also been performed to demonstrate consistency between the two sets of data.

## 4.1 Effects of Experimental Parameters on Data Quality

It is important to select appropriate values for experimental parameters for atom probe analysis, such as voltage or laser pulsing, specimen temperature etc. to ensure optimal data quality. In order to investigate these effects a series of calibration experiments were performed on a homogenised sample of the same composition as the WV weld material (see Table 3.1). The specimen was solution treated at 950 °C for 2 hrs followed by a water quench. This produced a visually random distribution of solute as shown in Figure 4.1. This sample was used to select appropriate analysis conditions for the specimens in this study by comparing between specimens run with voltage

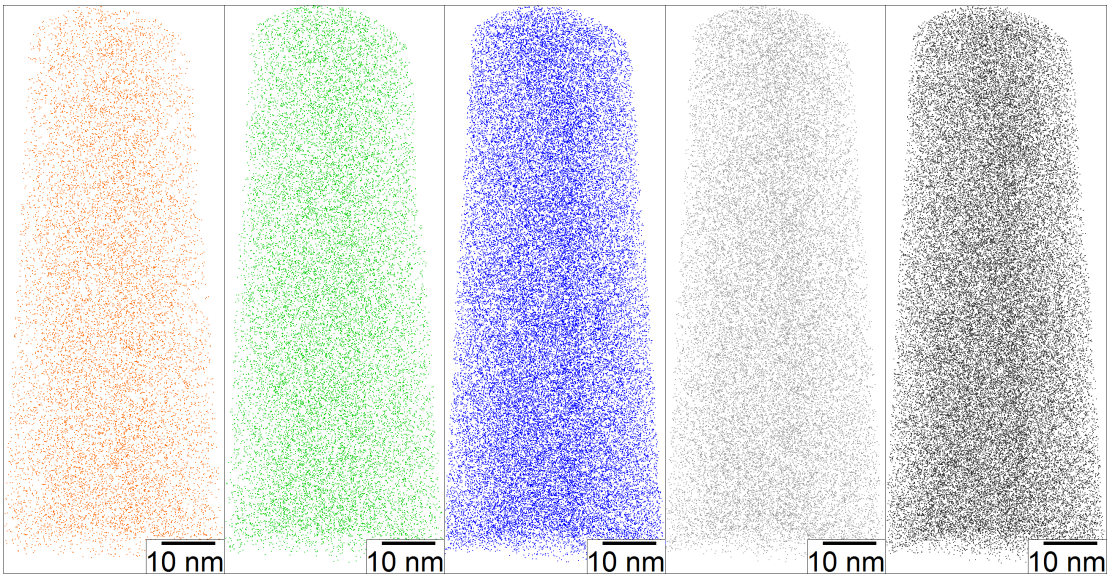


*(a)* Cu. *(b)* Ni. *(c)* Mn. *(d)* Si. *(e)* Fn.

*Figure 4.1:* Typical atom maps of (a) Cu, (b) Ni, (c) Mn, (d) Si and (e) Fn in the solution treated WV sample.

pulsing and laser pulsing using a variety of specimen temperatures and laser energies.

### 4.1.1 Voltage Pulsing

Traditionally, RPV materials have been analysed using voltage pulsing with specimen temperatures of around 40 - 60 K. Low temperatures are used to minimise the evaporation of Cu between pulses. Hyde et al.[146] showed that the optimal conditions for atom probe analysis of RPV materials were voltage pulsing with a pulse fraction of 20 % and a specimen temperature of 50 K. These are also the conditions used for the analysis of specimens previously analysed by Morley and Hirosawa. For this reason these conditions were used as a baseline to compare with data obtained using laser pulsing. Laser pulsing is advantageous since it reduces the chance of specimen fracture and often leads to much larger volumes of data. Three things are of particular interest: the quality of the mass spectra, the bulk composition of the alloy as measured with atom probe and the distribution of solutes in the data set i.e whether there is segregation to major poles and zone lines. Figures 3.6 and 4.2 show a typical voltage pulsed mass spectrum and 2-dimensional concentration profiles of Cu, Ni, Mn and Si

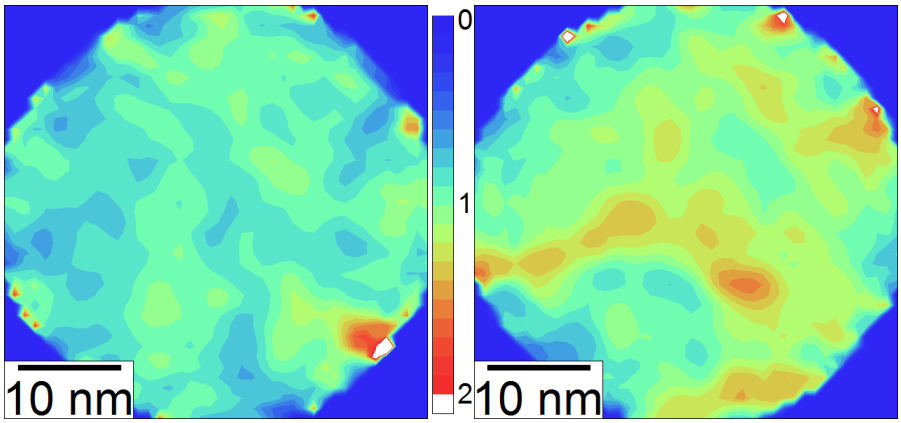


*(a)* Cu distibution. *(b)* Ni distibution.

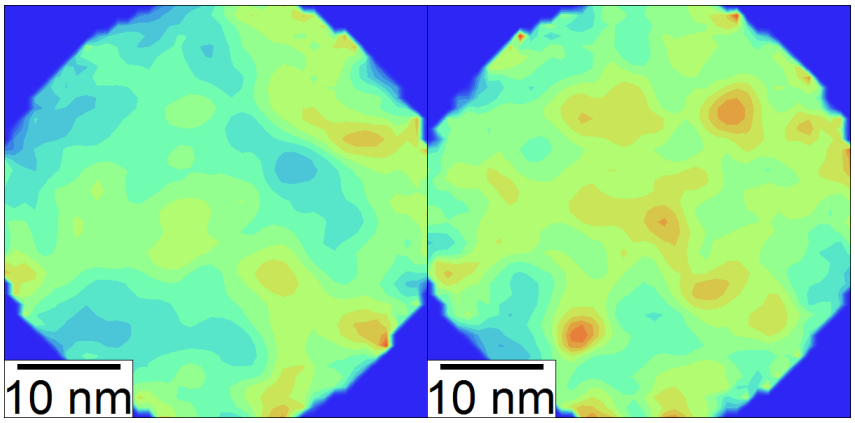


*(c)* Mn distibution. *(d)* Si distibution.

*Figure 4.2:* Typical 2d concentration profiles taken perpendicular to the analysis direction for (a) Cu, (b) Ni, (c) Mn, (d) Si in the solution treated WV sample analysed with voltage pulsing with a specimen temperature of 50 K and a pulse fraction of 20 %. Scale set such that the expected bulk concentration is 1 and the upper and lower bounds are 0 and twice the expected concentration. Bins are 1 $nm^2$ in the $xy$ plane.

taken along the direction perpendicular to the analysis direction i.e in the $xy$ plane. Table 4.1 shows the overall composition of the homogenised sample along with the expected values for comparison.

Voltage pulsing results in sharp peaks in the mass spectrum making it possible to resolve the $Cu^{2+}$ and $Mo^{3+}$ peaks, which are separated by just 0.3 Da. In addition, the tail of the main $Fe^{2+}$ peak at 28 does not significantly influence the peaks of Ni or Cu. The majority of the species are evaporated in 2+ or 3+ charge states.

There is significant surface migration of Si to the major poles, which Miller and Smith[147] and Gault et al.[148] attribute to Si being retained on the specimen surface

| | Measured (at.%) | Expected (at.%) |
|---|---|---|
| Si | 0.79 ± 0.003 | 0.75 |
| Cu | 0.41 ± 0.002 | 0.44 |
| Ni | 0.58 ± 0.003 | 0.53 |
| Fn | 1.44 ± 0.005 | 1.40 |
| Mn | 1.39 ± 0.004 | 1.38 |
| Mo | 0.24 ± 0.002 | 0.24 |
| C | 0.09 ± 0.001 | 0.19 |
| Cr | 0.08 ± 0.001 | 0.054 |
| P | 0.02 ± 0.001 | 0.018 |
| As | 0.03 ± 0.001 | 0.0074 |
| V | 0.004 ± 0.0002 | 0.0055 |
| Fe | 94.94 ± 0.008 | 94.99 |

*Table 4.1:* Composition of the alloy as measured by atom probe and the expected bulk composition of the main alloy elements in the homogenised WV sample. Data obtained with voltage pulsing with a specimen temperature of 50 K and a pulse fraction of 20 %.

due to its higher evaporation field than Fe. According to Miller and Smith this retention is thought to arise from Si being attached to step-edges and rolling towards the centre of the pole. Distributions of Ni, Mn and Cu appear reasonably uniform across the specimen surface.

The measured bulk composition of the alloy as determined from the atom probe (shown in Table 4.1) compares reasonably well with the expected bulk composition, however a number of values lie outside of errors. The lower than expected levels of C will primarily be due to the formation of carbides which will significantly deplete it from the matrix, as will its segregation to dislocations and grain boundaries. The slightly lower Cu content than expected could be due to small loss of Cu between pulses. The increase in Ni and Fn may be due to some small increase in the background noise arising from the small Fe peak tail. Si is often retained on the specimen surface due to its high evaporation field[147] and so the increase in Si observed here could arise from small losses of other matrix atoms with lower evaporation fields between pulses. This would artificially inflate the Si concentration. It also is worth mentioning here that the errors are small because they are dominated by a $1/\sqrt{N}$ term (see Equation 4.5) in reality specimen-to-specimen variance is probably larger than that

quoted here.

### 4.1.2 Laser Pulsing

Specimens were run using a variety of laser energies from 0.1 - 0.6 nJ and specimen temperatures of 40 K and 50 K, with pulse repetition rates of 200,000 Hz so as to be comparable with the voltage results. In most cases two datasets were obtained, one where laser power was increased and one with decreasing laser energy. There was no noticeable difference between the two cases. Where possible, these runs were carried out on one specimen for each condition (increasing/decreasing laser energy) except in the case of a few specimens which fractured before all laser energies had been studied.

Figure 4.3 shows sections of the mass spectra from 20 - 60 Da obtained with laser pulsing with laser energies of 0.1 nJ, 0.3 nJ and 0.5 nJ at 50 K and 0.3 nJ at 40 K. It is clear that when laser pulsing is used there is a more significant tail to the $^{28}Fe^{2+}$ peak which increasingly impacts on the $Ni^{2+}$ and $Cu^{2+}$ peaks as the laser energy is decreased. This effect is slightly reduced by lowering the specimen temperature, however the tail is still more significant than with voltage pulsing. In addition, changing the laser energy changes the charge states of field evaporated species, typically towards lower values[149, 150] as the probability of a given charge state (1+, 2+, etc) is dependent on the applied field. Zhou et al.[150] propose this to be a thermally activated process as opposed to that of post-ionisation[149, 151]. Post-ionisation will dominate for the high charge states (greater than 2+) whereas for 2+ charge states both mechanisms may be active, but it is likely that post ionisation will be the dominant mechanism. Both methods suggest higher charge states at lower laser energies as was observed here. This can be seen from the presence of peaks in the 50 - 60 range which are not present in the spectrum obtained with voltage pulsing and at low laser energy, where the fields are highest. Potentially this causes problems with peak overlaps which are not an issue with voltage pulsing, for example $^{28}Si^{+}$ and $^{56}Fe^{2+}$ and thus could impact on the observed composition.

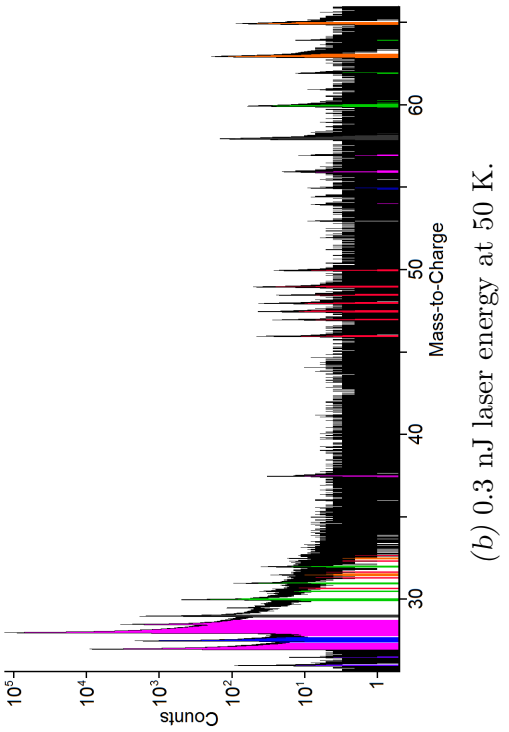


(a) 0.1 nJ laser energy at 50 K.




(b) 0.3 nJ laser energy at 50 K.

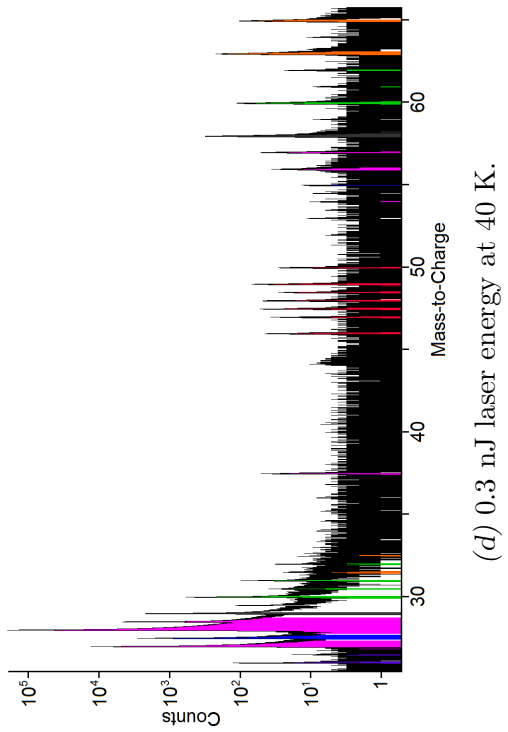


(c) 0.5 nJ laser energy at 50 K.




(d) 0.3 nJ laser energy at 40 K.

*Figure 4.3:* Typical mass spectra observed with laser pulsing with laser energies and specimen temperatures of (a) 0.1 nJ and 50 K, (b) 0.3 nJ and 50 K, (c) 0.5 nJ and 50 K, (d) 0.3 nJ and 40 K for the homogenised WV sample.

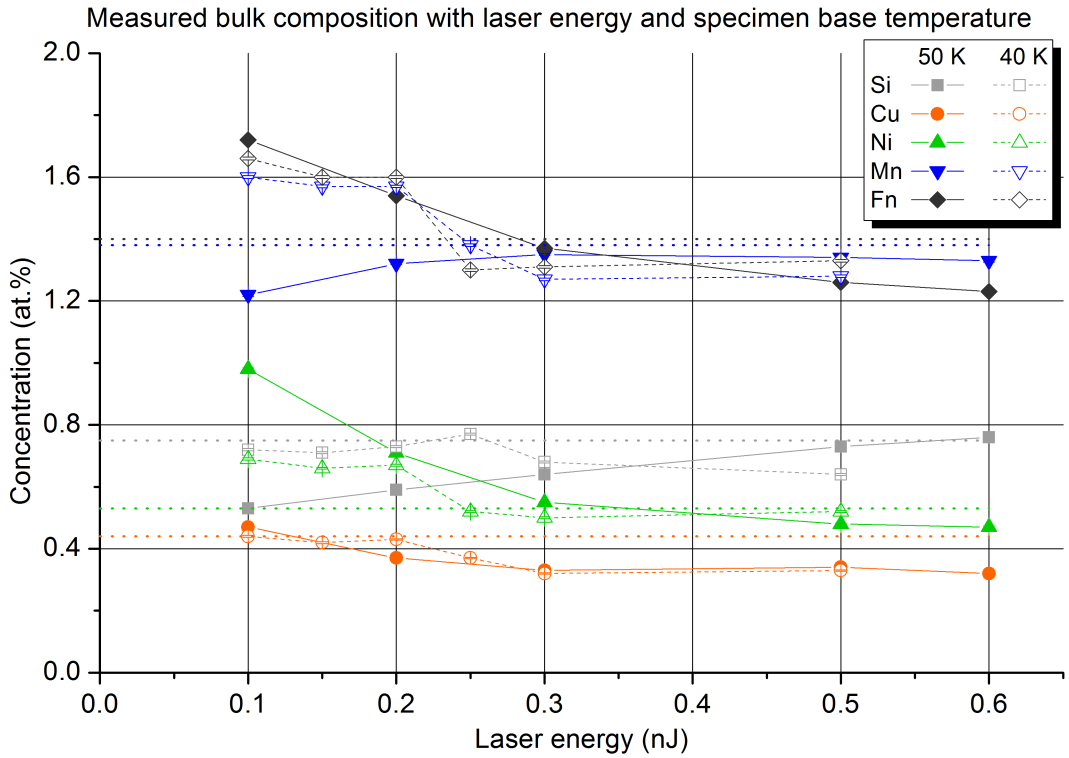


*Figure 4.4:* Comparison between the measured bulk concentration of the main solute elements of the homogenised WV sample analysed with different laser energies and specimen base temperatures. Corresponding dashed lines indicated expected bulk composition.

The bulk concentration of the main alloy elements observed over the range of laser energies studied is shown graphically in Figure 4.4. To highlight the effects of the Fe peak tails on composition the quoted values have not been corrected to take this into account.

For laser energies above around 0.3 nJ the observed bulk composition is close to what is expected at both 40 K and 50 K. There is slight loss of Cu at these laser energies, thought to be due to loss of Cu between pulses[146]. This is likely to be occurring at all laser energies since there is a significant contribution from the Fe tail on the $Cu^{2+}$ peaks at 31.5 and 32.5, but the measured concentration is not significantly above the expected value. The measured concentration of Si increases to its expected value with increasing laser energy with a specimen temperature of 50 K. This is in contradiction to what may be expected, since if it shifted from a 2+ charge state to a 1+, as seen with Fe, Ni and Mn, then less Si would be expected with higher laser energies. At 40 K it is broadly consistent with the expected value. Ni and Fn decrease towards

the expected bulk values with increasing laser energy at both 40 K and 50 K. The influence of the Fe peak tails significantly effects these elements at low laser energies artificially inflating the counts. Mn is overestimated with a specimen temperature of 40 K, whilst it is underestimated at 50 K for laser energies less than 0.2 nJ. Above 0.3 nJ at both 40 K and 50 K, bulk Mn is slightly underestimated, as with Cu probably due to losses between pulses, as it too has a lower evaporation field than Fe.

Perhaps the most significant issue with laser pulsing is the diffusion of atomic species along the surface of the tip, particularly Si, although this phenomenon occurs with many other atomic species[148] including C and P which are also of relevance to RPVs. As for the data obtained with voltage pulsing 2d concentration profiles of Cu, Ni, Mn and Si were plotted perpendicular to the analysis direction for the laser energies and temperatures studied, these are shown in Figure 4.5.

From these figures it can be seen that there is significant surface diffusion of some species, which changes with specimen analysis conditions. Cu is slightly segregated to poles and zone lines with low laser energy (Figure 4.5a), likewise for Ni (Figure 4.5b). Figure 4.5c shows no visible segregation of Mn with low laser energy, whereas Si is segregated to poles (Figure 4.5d). At higher laser energies there is no real change in the distribution of Mn, it remains reasonably uniform across all laser energies studied. Both Ni and Cu behave similarly, as laser energy is increased there is no significant segregation to either poles or zone lines. For Si however, there is significant change in behaviour, at higher laser energies there is significant segregation to zone lines as shown in Figure 4.5l, which shifts from pole segregation at low laser energies (Figure 4.5d). Specimen temperature does not seem to influence the segregation behaviour, except perhaps for Si. From Figures 4.5h and 4.5p at 40 K there appears to be slightly more surface migration of Si, this could be a feature of the fact that there is a pole in the middle of this zone line. At lower temperatures the field is higher, which promotes more migration to poles (this is evident from the low laser energy data).

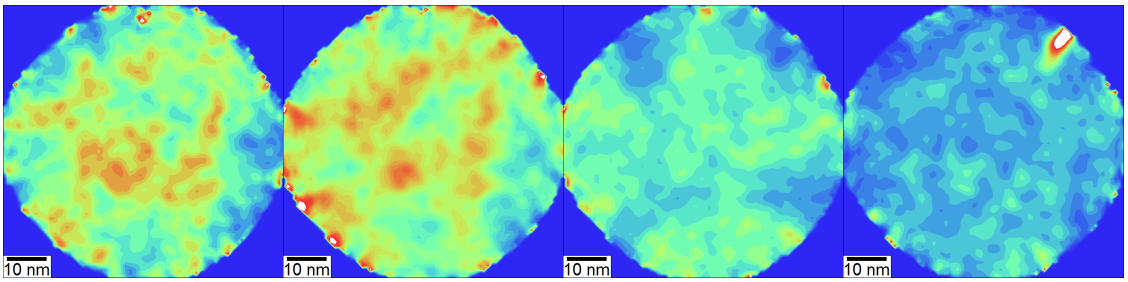


*(a)* Cu distibution 50 K, 0.1 nJ. *(b)* Ni distibution 50 K, 0.1 nJ. *(c)* Mn distibution 50 K, 0.1 nJ. *(d)* Si distibution 50 K, 0.1 nJ.

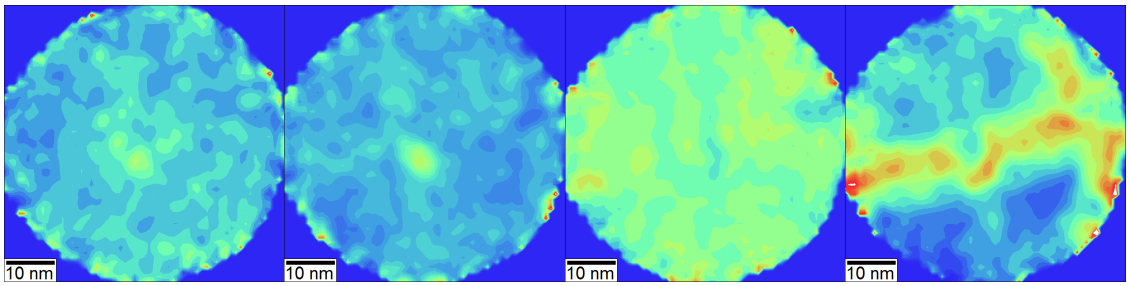


*(e)* Cu distibution 50 K, 0.3 nJ. *(f)* Ni distibution 50 K, 0.3 nJ. *(g)* Mn distibution 50 K, 0.3 nJ. *(h)* Si distibution 50 K, 0.3 nJ.

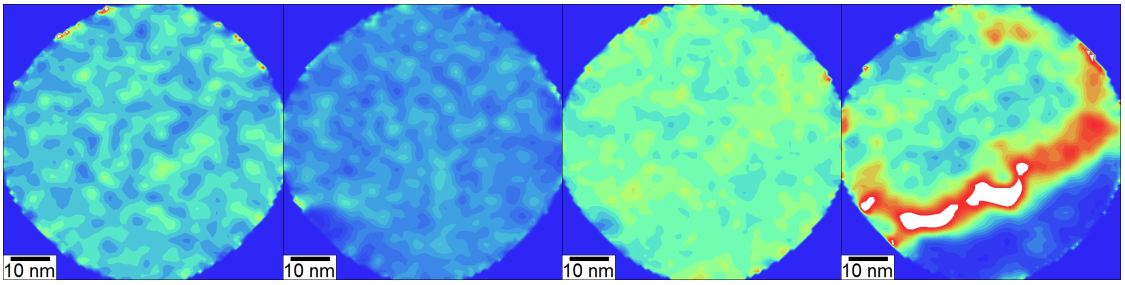


*(i)* Cu distibution 50 K, 0.5 nJ. *(j)* Ni distibution 50 K, 0.5 nJ. *(k)* Mn distibution 50 K, 0.5 nJ. *(l)* Si distibution 50 K, 0.5 nJ.

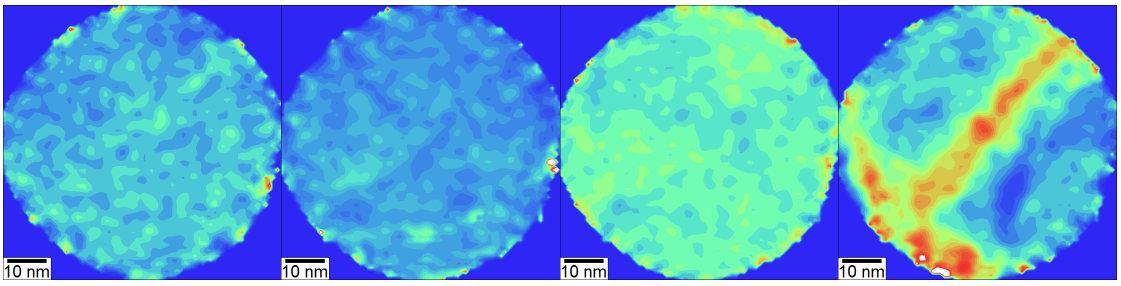


*(m)* Cu distibution 40 K, 0.3 nJ. *(n)* Ni distibution 40 K, 0.3 nJ. *(o)* Mn distibution 40 K, 0.3 nJ. *(p)* Si distibution 40 K, 0.3 nJ.

*Figure 4.5:* Typical 2d concentration profiles of Cu, Ni, Mn and Si from the solution treated WV sample taken perpendicular to the analysis direction. For laser energies and specimen temperatures of (a) - (d) 0.1 nJ at 50 K, (e) - (h) 0.3 nJ at 50 K, (i) - (l) 0.5 nJ at 50 K and (m) - (p) 0.3 nJ at 40 K. Scale set to the same as in Figure 4.2, such that the expected bulk concentration is 1 (lime green colour) and the upper and lower bounds are 0 (dark blue) and twice the expected concentration (red).

### 4.1.3 Summary of the Comparison Between Voltage and Laser Pulsing.

It is clear that there are significant issues when studying RPV materials with laser pulsing at both high and low laser energies.

At low laser energies there is significant noise in the mass spectrum arising from the tails to the Fe peaks which affect the measured bulk compositions of Ni, Mn and Cu. These tails are much smaller with voltage pulsing and as such have only a very small influence on the observed compositions. With laser pulsing there appears to be loss of Cu atoms between pulses, which is significantly reduced with voltage pulsing.

The diffusion of solutes across the specimen surface is similar between voltage pulsing and laser pulsing with low laser energies ($< 0.3$ nJ), as seen from the distributions of the elements taken perpendicular to the analysis direction (Figures 4.2 and 4.5). At high laser energies, there is significant surface segregation of Si to zone axes, whereas at low laser energies and with voltage pulsing it is segregated to major poles.

For these reasons, in the rest of this project specimens were analysed using voltage pulsing with a pulse fraction of 20 %, a pulse repetition rate of 200 kHz at a temperature of 50 K.

## 4.2 Microstructural Characterisation of RPV Steels

### 4.2.1 Quantification of RPV Microstructural Features

#### 4.2.1.1 Cluster Size, Number Density and Volume Fraction

In order to ensure consistency with the previous work, the same methods of reporting the cluster size, number density and volume fraction will be used. They are summarised here. In general, cluster sizes will be given as the number of detected atoms, to remove assumptions used to convert these to radii. Errors are given by the

standard error of the mean, $\Delta f$ (Equation 4.1), where $\sigma$ is the standard deviation and $N$ the sample size.

$$\Delta f = \frac{\sigma}{\sqrt{N}} \tag{4.1}$$

Clusters observed in the LEAP will appear smaller due to the lower detection efficiency when compared directly to those from the ECOPoSAP. Hence, when comparing between results from the LEAP and ECOPoSAP the simple approximation of dividing the number of detected atoms in the clusters observed with the LEAP, by the ratio of the two detection efficiencies (0.74) is used[1]. In some cases conversion to a radius is necessary, in which case this is taken as the radius of an equivalent sphere, $r_{es}$, calculated from

$$r_{es} = \left(\frac{3N_A\Omega}{4\pi\zeta}\right)^{1/3} \tag{4.2}$$

where $\Omega$ is taken to be the atomic volume of pure Fe, 1/85 nm$^3$, $N_A$ is the number of detected ions in the cluster and $\zeta$ the detection efficiency (0.5 for ECOPoSAP data, 0.37 for LEAP data).

Feature number density is simply given by the number of features, $N_C$, in a given volume, $V$, calculated from

$$N_d = \frac{N_C}{V} = \frac{N_C\zeta}{N_T\Omega} \tag{4.3}$$

where $N_C$ is the total number of clusters across all datasets, and $N_T$ the total number of atoms making up those datasets. As with the cluster sizes the atomic volume, $\Omega$, is taken to be that of pure Fe. Errors are reported as the standard error in the mean number density from each dataset.

Precipitate volume fraction is calculated as the ratio of the number of atoms in clusters to the total number of atoms. Errors are quoted as the standard error in the mean volume fraction of each of the constituent datasets, which gives an estimate of the run-to-run variation in the volume fraction. There is a second source of error arising

[1] In reality Stephenson et al.[152] show that efficiency degraded cluster sizes are drawn from a distribution. Since this conversion is only done on average sizes, where an efficiency degraded cluster will, on average, be smaller the resulting error is expected to be small.

from counting the number of atoms in clusters, essentially a $1/\sqrt{N}$ type counting error. For the large number of atoms in clusters this error will be small and can be neglected.

#### 4.2.1.2 Cluster Search Parameters

Careful consideration is needed to choose suitable parameters for cluster searching. Due to the differences between the LEAP and 3DAP instruments, different cluster search parameters are needed. The following parameters were used by Morley et al. to analyse the work performed on the ECOPoSAP:

- Solutes - Cu, Ni (including $^{58}Fe^{2+}/^{58}Ni^{2+}$ for the high Ni steels) and Mn.
- $d_{max} = 0.4$ nm
- $N_{min} = 10$ atoms
- $L = e = 0.3$ nm

Whilst it is important to ensure the analysis of data from the LEAP is consistent with that from the ECOPoSAP, cluster search parameters for the LEAP should not be chosen to exactly replicate the ECOPoSAP data as this may not yield the best parameters for LEAP data. Instead the ECOPoSAP data should be used as a verification tool to show that the two instruments give consistent data, this is discussed in more detail in Section 4.3.

The lower detection efficiency of the LEAP instrument means that a larger $d_{max}$ is required[153]. In addition, Si was not included as a solute atom for cluster searches of the ECOPoSAP data. In this study, and as noted from the literature, Si is often associated with the interface of particles and, as such, has been included as a solute atom in the cluster search with the LEAP data. As will be discussed in Section 4.3 this is found not to have a significant effect on the overall results.

The choice of $N_{min}$ is inherently linked to the chosen value of $d_{max}$, a larger $d_{max}$ requires a larger $N_{min}$ and vice-versa. Selecting an appropriate $d_{max}$ value is difficult, but it should be chosen such that larger clusters are not identified as several small clusters ($d_{max}$ too small), nor are many smaller clusters mistakenly identified as being part of a few large clusters ($d_{max}$ too large). To identify suitable values of $d_{max}$ it is useful to use a sample which contains very few "background clusters", that is clusters which are due to random occurrences rather than from ageing. The heavily overaged WV material is suitable for this as a large proportion of the solute will be contained in clusters. Thus the matrix of this material will be a useful reference material to identify a suitable $d_{max}$ value.

An approach to select a suitable value of $N_{min}$ for a given $d_{max}$ is to choose a value such that no, or very few clusters with size larger than $N_{min}$ are observed in a randomised dataset of the same composition. Randomised datasets corresponding to a given $d_{max}$ and $N_{min}$ combination were created using the matrix ions of a given dataset, i.e those ions not selected as part of a cluster with that combination of $d_{max}$ and $N_{min}$. This removes the high density regions corresponding to Cu-enriched precipitates. The chemical identities of matrix ions were then randomly exchanged with one another without altering the position information. The resulting dataset has a random distribution of solute with overall composition and density fluctuations of the matrix. Cluster searches were carried out on 20 randomised datasets to give good statistical significance.

Cluster search parameters were chosen using the WV material, the most solute rich of all the alloys listed in Table 3.1. A large dataset ($>$ 20 million ions) of a WV sample aged for 90,000 hrs at 365 °C was used to perform a series of cluster searches using different values of $d_{max}$ between 0.40 nm and 0.60 nm. For consistency, for each $d_{max}$ value the values of $L$ and $e$ were set to be $d_{max} - 0.10$ nm. For example, for a $d_{max} = 0.30$ nm, $L$ and $e$ were set to 0.20 nm.

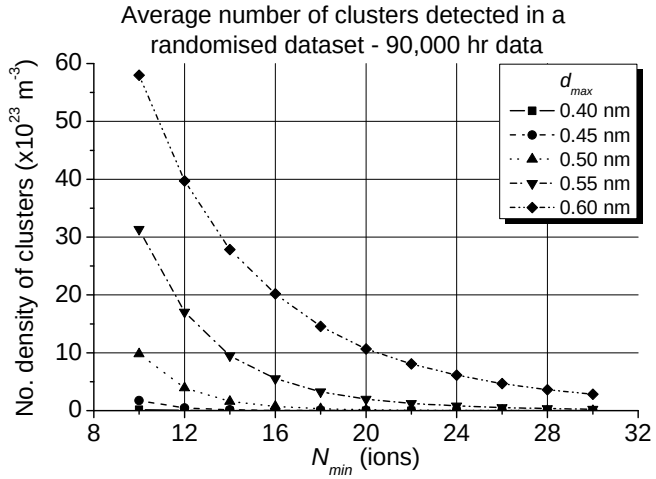


*(a)* Number density of features in the randomised 90,000 hr dataset.

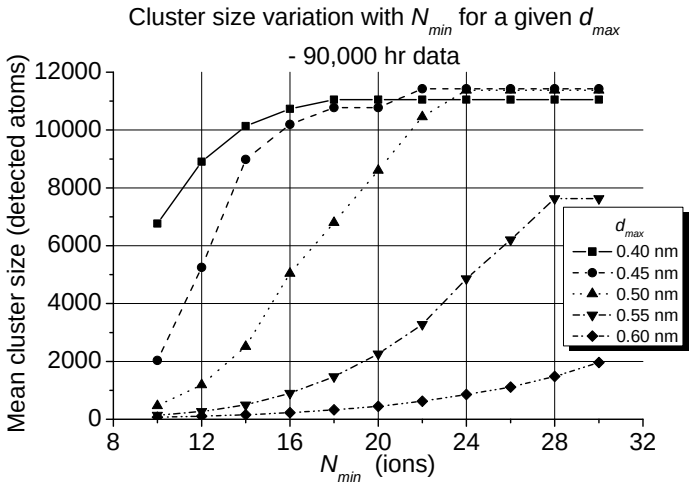


*(b)* Mean size of features in the 90,000 hr dataset.

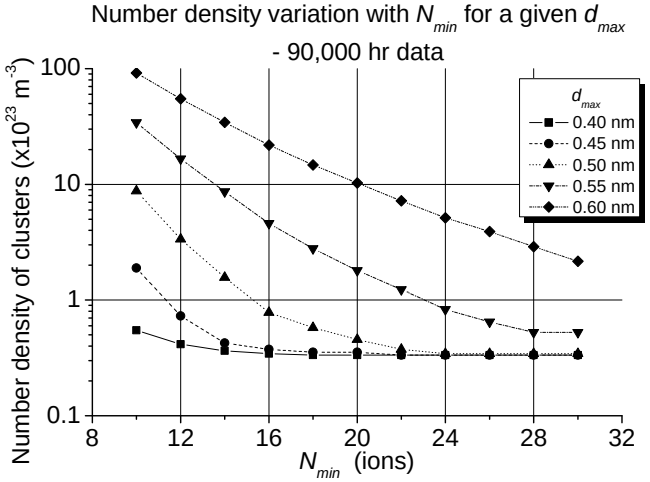


*(c)* Number density of features in the 90,000 hr dataset.

*Figure 4.6:* (a) Cluster number density in the matrix of a randomised dataset. Variation in the (b) mean cluster size and (c) cluster number density observed for a given combination of $d_{max}$ and $N_{min}$, for a WV steel aged to 90,000 hrs at 365 °C.

Figure 4.6a shows the mean number density of clusters observed in the randomised datasets. From the graph in Figure 4.6a it is clear that a $d_{max} > 0.50$ nm requires an $N_{min}$ larger than 30 to give an insignificant (almost zero) number of features in the randomised dataset. As such there are still significant background clusters contributing to the mean size and number density. This results in the mean size and number density being under- and over-estimated respectively for these values of $d_{max}$ in Figure 4.6. For a $d_{max} = 0.40$ nm the number of clusters observed in a randomised dataset falls to an insignificant level above an $N_{min}$ of 12, however looking at the mean size (Figure 4.6b) suggests an $N_{min}$ of 18 would be better as this gives the largest mean size. The need to increase $N_{min}$ from 12 to 18 for $d_{max} = 0.40$ to give the largest cluster size is likely to be due to some of the larger clusters having been broken into several smaller clusters due to an insufficiently large $d_{max}$. Similarly this is also likely to be occurring with $d_{max} = 0.45$ nm, requiring $N_{min}$ to be increased from 18 to 22. With a $d_{max} > 0.50$ nm a significant number of background clusters are detected across a large range of $N_{min}$ values, hence a $d_{max} > 0.50$ nm is not suitable.

Using the graphs in Figure 4.6, the most appropriate $N_{min}$ for the $d_{max}$ values outlined were identified. These are detailed in Table 4.2.

| $d_{max}$ (nm) | $N_{min}$ (atoms) |
|---|---|
| 0.40 | 18 |
| 0.45 | 22 |
| 0.50 | 24 |
| 0.55 | $> 30$ |
| 0.60 | $> 30$ |

*Table 4.2:* Best values for $N_{min}$ for a given $d_{max}$ for the 90,000 hr dataset.

For their simulated data Hyde et al.[153] recommend an $N_{min}$ of 13 for a $d_{max} = 0.50$ nm. However, when the experimental data from this work are used, which have present local variations in density due to the inherent APT artefacts, a larger $N_{min}$ is required, nearly double the value Hyde et al. recommend[2]. This is a

[2] The solute content of the alloy in this work is also slightly larger than that in Hyde's simulations, which will also increase $N_{min}$.

concern particularly in the case of irradiated materials and the early stages of phase decomposition in thermally aged materials where the clusters can be of the order of only a few nm in size. Using such a large $N_{min}$ is effectively discarding all clusters which have a physical size below around 65 atoms, since due to imperfect detection efficiency, observed clusters in APT datasets contain fewer atoms than their original physical size.

A $d_{max} = 0.50$ nm was selected as being the most suitable $d_{max}$ value, which is in agreement with Hyde et al.[153].

#### 4.2.1.3 Method for the Removal of Background Clusters

Choosing $N_{min}$ such that no clusters are observed in a randomised dataset (Figure 4.6a) relies on the assumption that only the size of the feature is important in determining whether or not a cluster is the result of ageing. This is effectively saying that because, for example, a 10 atom cluster was observed in a randomised dataset then most 10 atom clusters in the real dataset are also suspected to be random statistical co-incidences. It is not the case that all these clusters will be random coincidences[154, 155]. This is because the composition of the clusters in the experimental data may be unlikely to occur in the statistically random case and therefore the cluster is a feature of ageing. For example, a cluster of 10 Cu atoms might occur in the experimental dataset but be very unlikely to occur in a random distribution of solute. In addition, these clusters may be present in much higher number densities than found in the random case.

A method to identify clusters in APT datasets which are typical of those in a randomised dataset has been developed. Application of this method to APT data increases the sensitivity to small clusters, which allows for a more accurate determination/characterisation of clustering over and above background clusters from random statistical fluctuations.

When relating microstructural data to mechanical properties, particularly in alloys

containing clusters, it is useful to identify clustering which has occurred over and above those which form from random statistical fluctuations. Marceau et al.[156] used an approach whereby they subtracted the number of clusters of a given size in a randomised dataset from those observed in the experimental data. In their approach it is not possible to identify the specific clusters in the experimental dataset which are typical of those in the randomised one, thus it gives information on how many background clusters there are but not which ones. The method presented here is able to identify and remove background clusters typical of those in a randomised dataset based upon a comparison between the clusters in a randomised dataset with those in the aged material. If the features are the same, in terms of size and composition, then it is concluded that the cluster in the aged data is typical of those in a randomised dataset (i.e a "background cluster"). Likewise, if they are different then it is concluded that it is a feature of ageing, i.e an "ageing induced cluster". This method essentially expands the criteria upon which we do this comparison from being purely based on the number of ions (applying $N_{min}$ such that no clusters are observed in a randomised dataset), to something based on the number of ions and the cluster composition. This reveals features which would be discarded based purely on a size cut off, but are distinct from the clusters in a randomised dataset in that their composition is different, thus they are likely to be a feature of ageing.

The method for this correction is outlined below:

1. The dataset of interest is cluster-searched using the appropriate maximum separation method parameters. $d_{max}$ and $N_{min}$ can be determined from plots similar to Figure 4.6.

2. The clusters identified in step 1 are recorded and a file exported containing only the ions identified as belonging to the matrix.

3. The masses of the ions in the matrix are randomly swapped whilst the position information is left unchanged. This creates a file with a random distribution of solute.

4. This randomised dataset is then cluster searched using the same parameters as in step 1 and any identified clusters recorded.

5. From the clusters identified in step 4 a threshold can be selected to determine which clusters are to be considered as part of the background. The threshold will be a size and a particular concentration of solute, determined by examining the distributions of cluster compositions in the randomised data.

6. Identify the clusters in step 1 with similar compositions to those in the randomised dataset and in the same size range (typically equivalent to 0 - 1 nm). These are the "background clusters". An example is shown in Table 4.3. Suppose the threshold Cu content is 10 % and the size threshold is 130 atoms. Clusters 1, 3 and 4 meet either the size threshold or the composition threshold and are classified as being the result of ageing. Cluster 2 on the other hand is deemed to be a background cluster as it meets neither of the criteria. Under a purely $N_{min}$ based cut-off all clusters would be deemed the result of ageing. The size, size distribution, number density, volume fraction and composition of the remaining cluster population can now be adjusted to remove the influence of these background clusters.

| Cluster number | Size (atoms) | Cu concentration (%) | Result |
|---|---|---|---|
| 1 | 500 | 30 | Result of ageing |
| 2 | 30 | 3 | Background cluster |
| 3 | 150 | 6 | Result of ageing |
| 4 | 75 | 20 | Result of ageing |

*Table 4.3:* Example of the application of step 6 of the background cluster correction assuming a threshold Cu value of 10 % Cu and a threshold size of 130 atoms.

7. A final check should be made to verify that the number of clusters identified as background is consistent with expectations, for example their number density is comparable to the number density of clusters in a randomised dataset with the same parameters (Figure 4.6).

In the first instance it is recommended that graphs such as those in Figure 4.6 are produced to compare results before and after correction from which a new value of $N_{min}$ can be determined. Once the revised $N_{min}$ has been chosen it is then possible simply to apply steps 1 to 7 to any given dataset of that material.

To demonstrate the method, an in depth analysis was carried out using the 90,000 hr data which has large clusters present, and the 1000 hr data which has a population of much smaller clusters, using the optimum $d_{max}$ value of 0.50 nm found in Section 4.2.1.2. It is much harder to determine an appropriate $N_{min}$ after background correction for the 1000 hr data than the 90,000 hr data, hence the best values of $N_{min}$ found for the 90,000 hr data were used to compare between the clusters observed with and without correction in the 1000 hr data.

In this demonstration a simple threshold was used for determining the background clusters based upon only the concentration of one specific element, Cu and the feature size. More specifically, the criteria used to identify a "background cluster" was that clusters must contain above a certain concentration of Cu. This threshold was set as the mean plus two standard deviations of the Cu concentration observed in the clusters in the randomised dataset. Since very few clusters above ∼130 ions (equivalent to ∼1 nm radius) were observed in randomised datasets, the Cu threshold was only applied to clusters below this size. In practice the concentration of two (or more) elements could be used.

Applying steps 1 to 7 to the 90,000 hr dataset allows Figures 4.6b and 4.6c to be re-calculated, corrected for the presence of "background clusters". The results for mean cluster size and number density for a $d_{max} = 0.50$ nm are shown in Figure 4.7. For comparison the original uncorrected data are also shown.

These graphs clearly show that this method is able to reproduce the data in the case where $N_{min}$ is high enough to remove all "background clusters", i.e for $N_{min}$ larger than 24 ions. However, it is possible to recreate the observed number densities and sizes with much lower values of $N_{min}$ for $d_{max} = 0.50$ nm when correction for "background

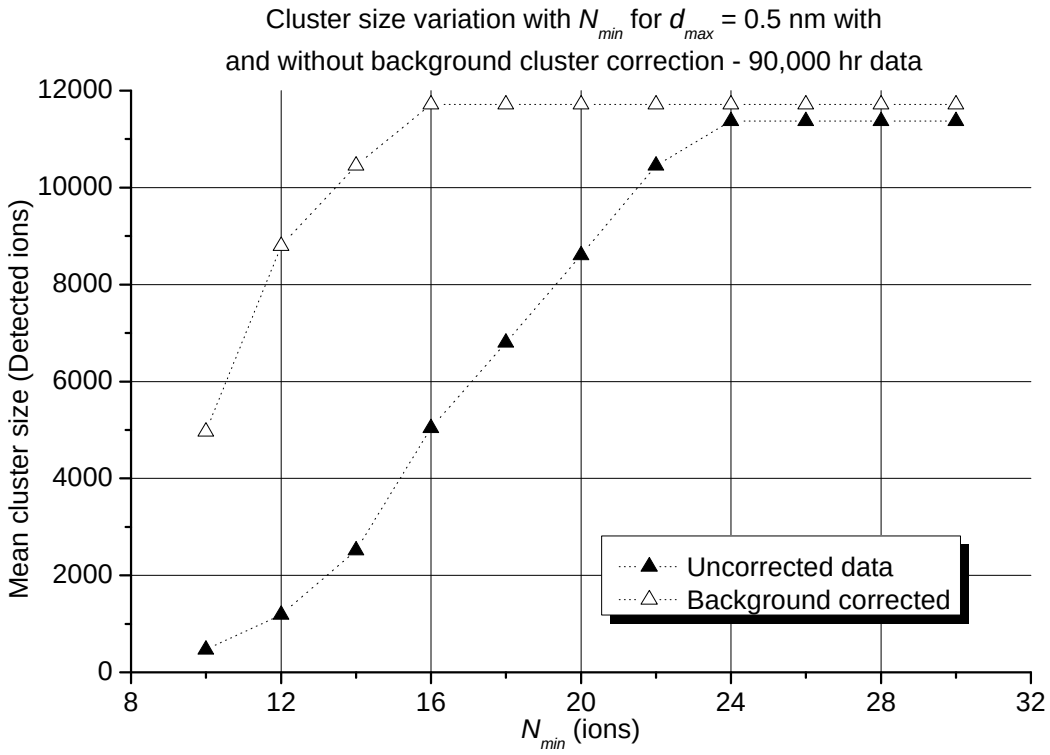


*(a)* Mean cluster size with and without background correction.

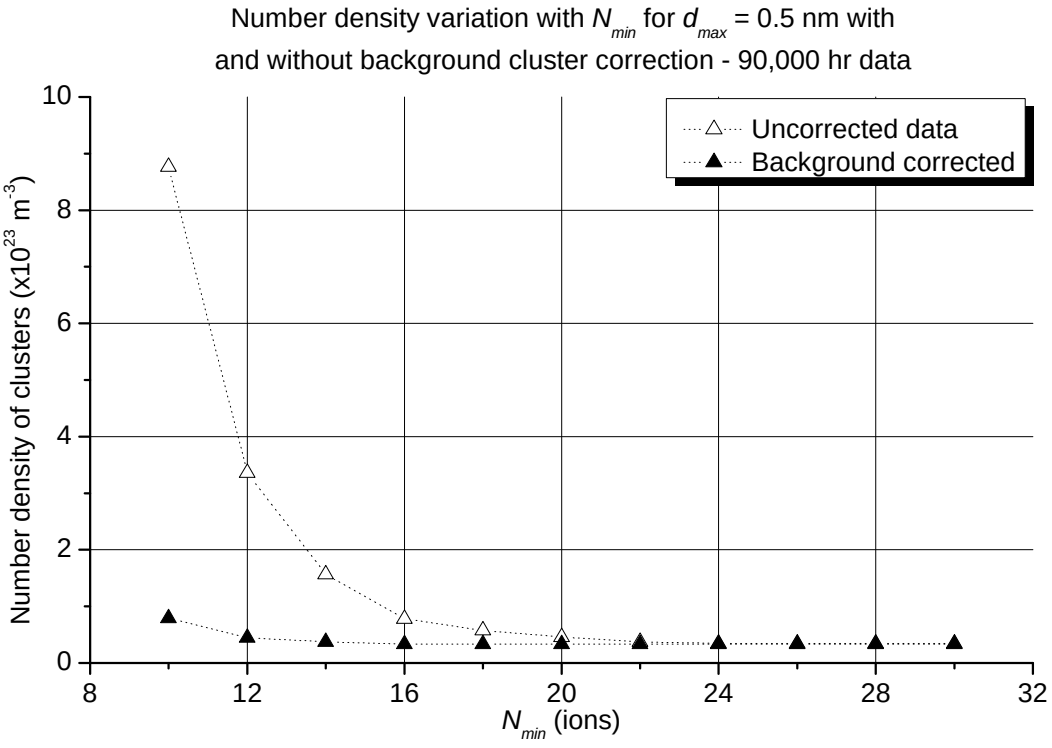


*(b)* Cluster number density with and without background correction.

*Figure 4.7:* Graph showing the variation in (a) cluster size and (b) number density with $N_{min}$ for $d_{max} = 0.50$ nm for the 90,000 hr dataset with (unfilled shapes) and without (filled shapes) correction for "background clusters".

clusters" is applied. The slightly higher mean size obtained with background cluster correction is due to the new algorithm identifying some clusters as being background clusters which the older method just based upon $N_{min}$ did not.

So far only large overaged clusters have been considered, which are comparatively easy to characterise compared to smaller clusters observed at shorter ageing times. Using the methods described earlier graphs of the mean size and number density were plotted for the 1000 hr data. These are shown in Figure 4.8 along with the uncorrected data for the case of $d_{max} = 0.50$ nm.

The average number density of clusters in the randomised datasets show much the same trend as for the 90,000 hr data, with similar points where the number of clusters becomes insignificant. For a $d_{max} = 0.50$ nm, using $N_{min} = 24$ calculated using the method from Figure 4.6a results in an overestimate of the mean cluster size and underestimates their number density by around 15% when compared to the data using an $N_{min} = 16$ and applying the correction for background clusters. These differences can be highlighted in a little more detail by looking at the composition of the clusters.

A ternary diagram showing the ratio of solute elements (Cu:Ni+Mn:Si) in each individual cluster can be used to compare the composition of the clusters observed in a randomised dataset to those observed in the experimental data. Figure 4.9 shows such ternary plots with each point on the graphs representing one cluster. Since the focus here is on small clusters only clusters containing $< 130$ ions are shown. Figures 4.9a and 4.9b show the composition of all the detected clusters with an $N_{min}$ of 24 and 16 respectively, along with those observed in a randomised dataset using the same parameters. Figure 4.9c shows the clusters which remain after correction for background clusters with $N_{min} = 16$. Finally, Figure 4.9d shows the clusters containing 16 - 23 ions which are compositionally different to those in a randomised dataset but are discarded if an $N_{min} = 24$ is used (ageing induced clusters). In addition, it shows features which contain 24 - 130 ions but have compositions similar to clusters in a randomised dataset (background clusters).

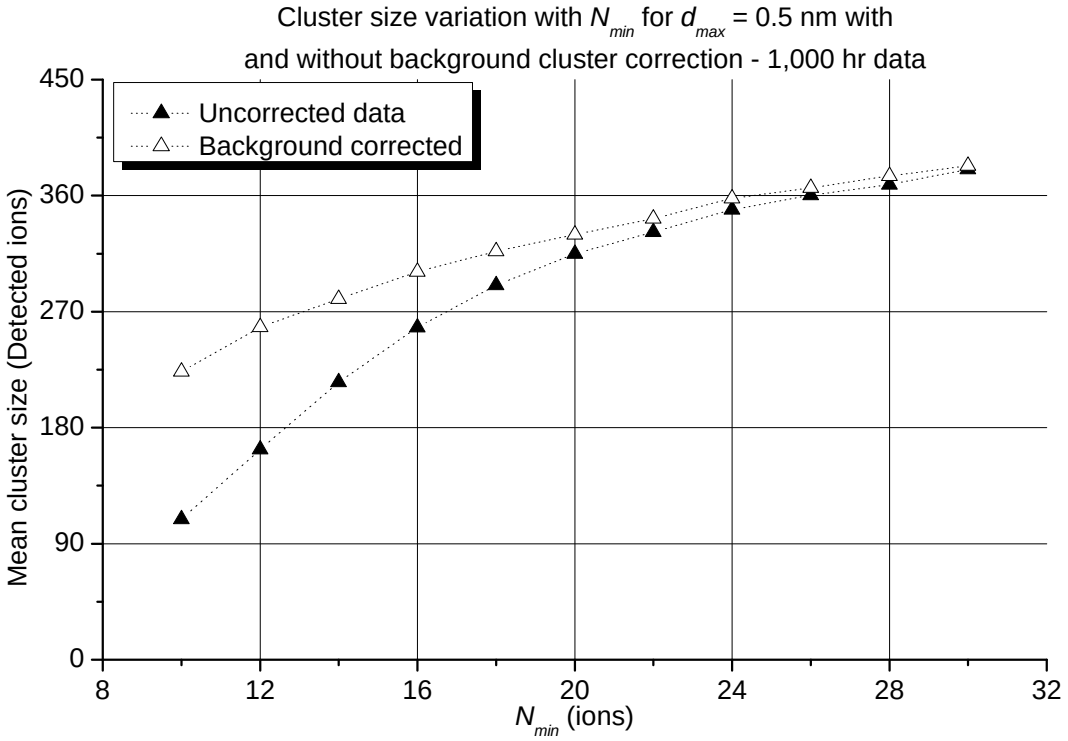


*(a)* Mean cluster size with and without background correction.

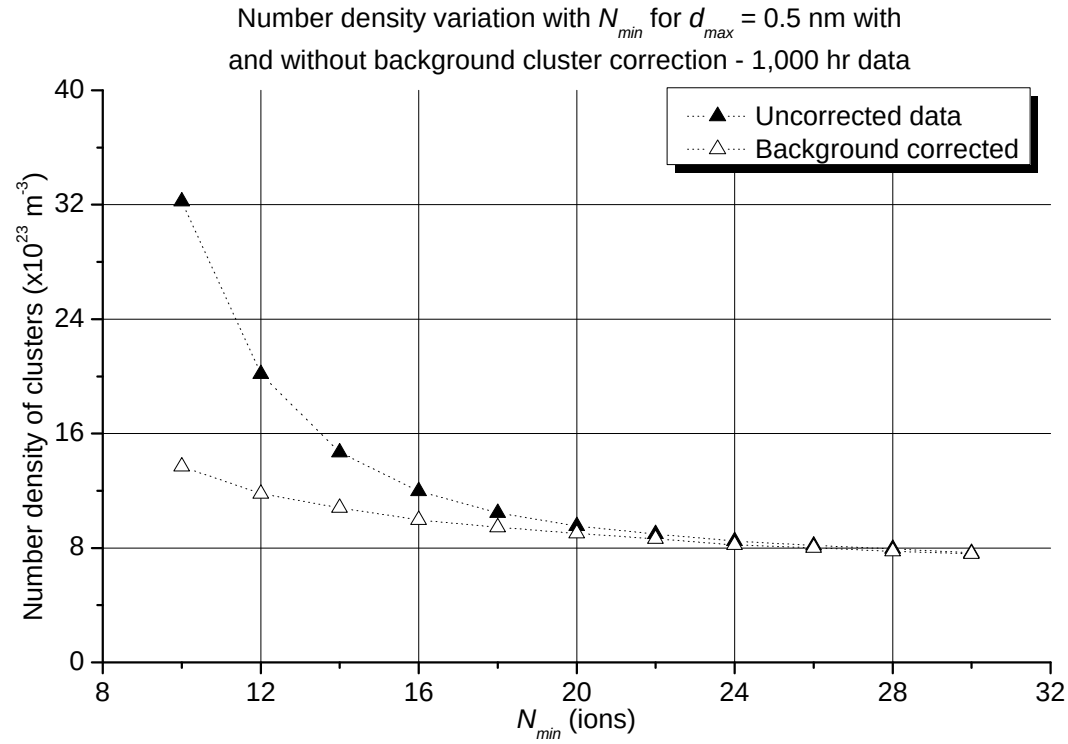


*(b)* Cluster number density with and without background correction.

*Figure 4.8:* Graph showing the variation in (a) cluster size and (b) number density with $N_{min}$ for $d_{max} = 0.50$ nm for the 1,000 hr dataset with (unfilled shapes) and without (filled shapes) correction for "background clusters".

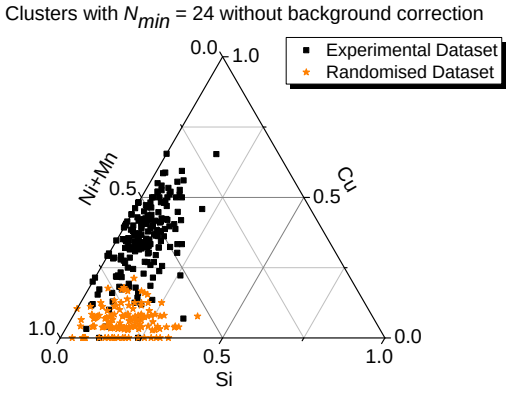


*(a)* Clusters observed in the experimental and randomised datasets with $N_{min} = 24$.

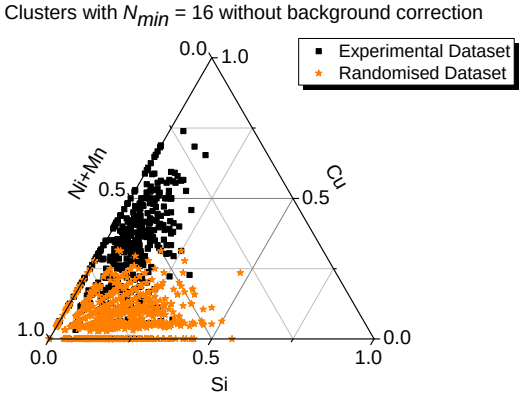


*(b)* Clusters observed in the experimental and randomised datasets with $N_{min} = 16$.

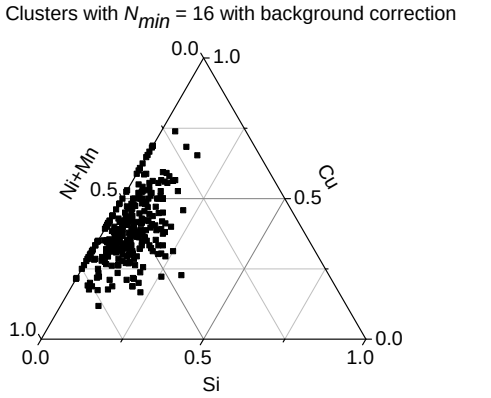


*(c)* Clusters observed with $N_{min} = 16$ after background correction.

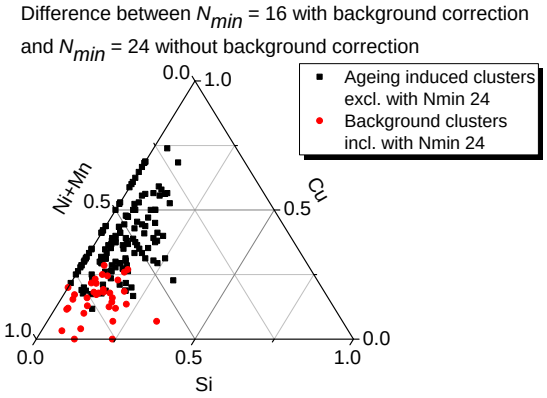


*(d)* Comparison between uncorrected $N_{min} = 24$ and corrected $N_{min} = 16$.

*Figure 4.9:* Ternary plots showing 0 - 1 nm radius clusters in the 1000 hr datasets with (a) $N_{min} = 24$ without background cluster correction and clusters observed in a randomised dataset, (b) $N_{min} = 16$ without background correction and clusters observed in a randomised dataset, (c) $N_{min} = 16$ with background correction and (d) ageing induced clusters not detected with an $N_{min} = 24$ and those which are not identified as "background clusters" with an $N_{min} = 24$, but are typical of clusters in a randomised dataset.

With $N_{min} = 24$ (Figure 4.9a) there are very few clusters with compositions which overlap with those observed in a randomised dataset. There are substantially more when $N_{min} = 16$ is used (Figure 4.9b) however, these have been successfully identified and corrected for (Figure 4.9c). Figure 4.9d shows there are ageing induced clusters which are not detected if an $N_{min} = 24$ is used (black squares in Figure 4.9d) but are compositionally different to those in a randomised dataset. In addition, it also highlights several clusters which have sizes and compositions typical of clusters in a randomised dataset (red circles in Figure 4.9d) but are not removed based on only using an $N_{min}$ cut off.

As demonstrated in Figures 4.7 and 4.9 using the example case of $d_{max} = 0.50$ nm applying a background correction allowed the reduction of $N_{min}$ from 24 ions to 16 ions which enabled some ageing induced clusters to be detected, which were not detected when a larger $N_{min}$ was used. The method also identified clusters which were typical of those in a randomised dataset which were previously classified as features of ageing when only an $N_{min}$ cut off was used. This was observed in both the 90,000 hr data, from the increased mean size after background cluster correction (Figure 4.7a), and in the 1000 hr data also from the increased size and from Figure 4.9d.

This method of background cluster correction was applied to all datasets obtained from the LEAP. An $N_{min} = 16$ ions was used with a $d_{max} = 0.50$ nm as these were found to be the optimum parameters for these materials.

#### 4.2.1.4 Composition

Cluster composition is calculated using the standard methods which were previously used in this project. The mean composition is calculated by simply treating all the atoms identified as being in a cluster as a single dataset of $N_A^{tot}$ atoms and then working out the fraction of atoms of each species $i$ in the usual way, i.e:

$$C_i = \frac{N_A^i}{N_A^{tot}} \tag{4.4}$$

Where $C_i$ is the atomic fraction of species $i$ and $N_A^i$ the combined number of atoms of type $i$. Errors are given by the standard error in the mean, which is given by[110]

$$\Delta C_i = \sqrt{\frac{C_i(1 - C_i)}{N_A^{tot}}} \tag{4.5}$$

This has been applied to calculate the bulk composition, where the dataset is made up of all the ranged ions, the cluster composition, where the dataset contained only ions identified as being part of clusters and the matrix composition, in which case the dataset contained only ions which were not identified as being part of a cluster. In all

cases in this work compositions are given in at.%.

#### 4.2.1.5 Interfaces

The following method has been used to characterise the interfaces between precipitates and the matrix, which has been used to estimate the following:

- Cluster core radius
- Interface width
- Core composition
- Interface composition

The method is shown schematically in Figure 4.10. The first step (Figure 4.10(a)) is to search the dataset to identify the clusters present using a cluster search algorithm. In the high Cu steels SG and WV the clusters are typically made up of a core and an interface represented in Figure 4.10 by the ideal case of a pure Cu core, with a Ni, Mn and Si interface. The resulting cluster, Figure 4.10b, is then cluster searched (see below) to identify the atoms in the core, Figure 4.10c. This allows the core sizes and compositions to be calculated in the same way as for the whole clusters. The whole clusters (core plus interface) are matched with their respective cores based upon the position of their respective centres and the number of ions in the core, since the number of cluster core ions cannot be larger than the number in the whole cluster. Once this matching is complete, it is a trivial exercise to work out the interface size and composition since this is given by a subtraction of the number of atoms in the core from the number in the whole cluster. Interface widths are given by the difference in radius of the whole cluster and core of the cluster, as calculated from the radius of an equivalent sphere (Equation 4.2). The resulting atoms identified as being in the cluster core and interface regions are shown in Figures 4.10(d) and 4.10(e).

The process of cluster searching and identifying and matching cores with their original cluster has been automated, along with the calculation of the individual and average

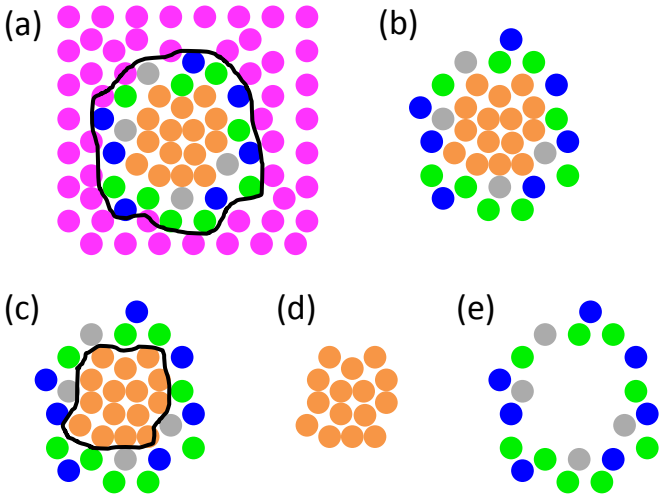


*Figure 4.10:* Schematic showing the process of identifying the interface around Cu clusters. (a) Whole cluster identified using maximum separation method, (b) cluster identified from (a), (c) Whole cluster is searched again to identify the core atoms, (d) and (e) resulting core and interface atoms. In this example matrix atoms are pink, interface atoms green, blue and grey and core atoms orange.

cluster compositions and sizes. The example shown in Figure 4.10 demonstrates an ideal case where the core and interface are distinct and are easily separable. In practice this is not the case and there is some blurring of the interface region. Cluster search parameters for identifying the core atoms have to be carefully chosen to avoid incorporating atoms from the interface into the core and to avoid splitting the cluster core into several pieces. The parameters chosen for the initial search are discussed in Section 4.2.1.2. Since the cores of the precipitates are expected to be mainly Cu rich, only Cu is used for the stage 2 cluster search, with a $d_{max} = 0.5$ nm, $L = e = 0.4$ nm and an $N_{min} = 10$ atoms. These parameters minimise the amount of interface classified as part of the core and limit the number of cases of the core being split into multiple clusters. Where splitting is observed, this is usually one very large cluster and one of a handful of atoms and these are matched back together manually, hence the error arising from cluster splitting is negligible.

## 4.3 Comparison of Data of WV Aged at 365 °C Obtained With LEAP and ECOPoSAP

Since the previous results obtained by Morley, Sha and Hirosawa were obtained using the ECOPoSAP instrument and the results from this study were obtained on the LEAP instrument it was important to ensure consistency between the results obtained between the two. There are a few differences between the two instruments which could affect the results obtained. Firstly, the LEAP instrument has a much larger field of view. This has the major advantage in that it is possible to analyse much greater volumes of material, thus statistics are better and it is possible to see features which are lower in number density than in the ECOPoSAP. However, it can cause a larger number of poles to be present in the analysed region, which can cause significant density variation and surface diffusion of solute towards them as highlighted in Section 4.1. Perhaps the most significant difference is the lower detection efficiency of the LEAP instrument which will affect the ability to detect smaller clusters. In the ECOPoSAP the detection efficiency is around 50 %, whereas in the LEAP this is 37 % which equates to around 26 % fewer atoms for the same analysed volume.

To demonstrate consistency between the new and old data, the WV materials aged at 365 °C were analysed using the LEAP and the data compared with that obtained by Morley and Hirosawa with the ECOPoSAP. The size, number density, volume fraction and composition were all compared between the two for ageing times of 1000 hrs, 3000 hrs, 10,000 hrs, 18,500 hrs and 50,000 hrs. Figure 4.11 shows the comparison between the size, number density and volume fraction of clusters observed in the LEAP data and that obtained from the ECOPoSAP.

The graphs in Figure 4.11 show that there is reasonable agreement between the data obtained with the LEAP and ECOPoSAP instruments. The cluster sizes agree well, with the exception of the datapoint at 10,000 hrs which appears as an outlier in the ECOPoSAP data and is more in line with the trend in the LEAP data. For

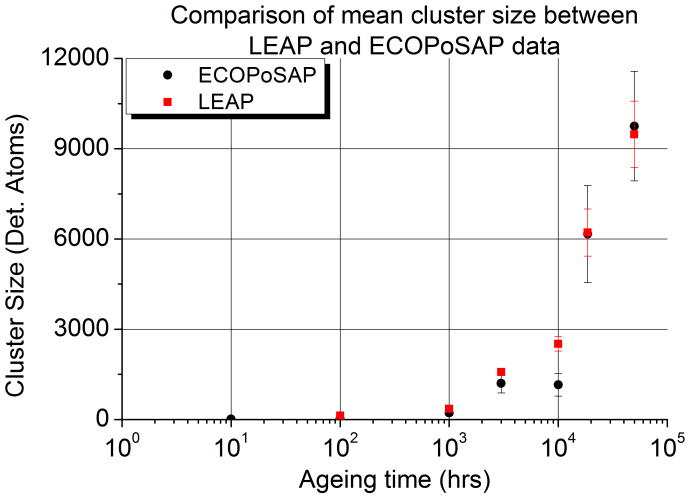


*(a)* Mean cluster size.

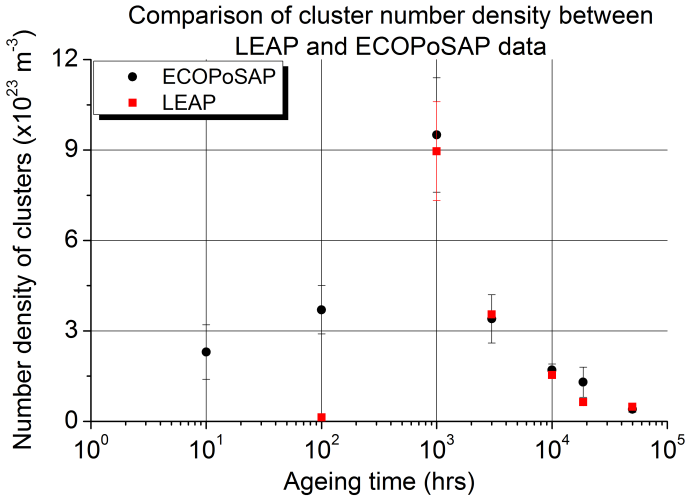


*(b)* Number density.

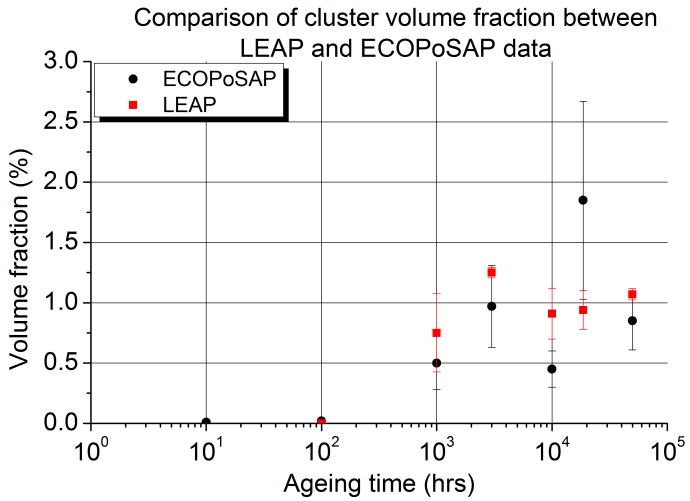


*(c)* Volume fraction.

*Figure 4.11:* Comparison of (a) mean cluster size, (b) number density and (c) volume fraction from the LEAP and ECOPoSAP data.

| Time (hrs) | Instrument | Cu (%) | Ni (%) | Mn (%) | Si (%) | Fe (%) |
|---|---|---|---|---|---|---|
| 10 | ECOPoSAP | 8 ± 2.4 | 36 ± 6.8 | 16 ± 3.3 | 1 ± 0.8 | 39 ± 4.4 |
| | LEAP | - | - | - | - | - |
| 100 | ECOPoSAP | 13 ± 1.5 | 25 ± 2.9 | 15 ± 1.7 | 2 ± 0.6 | 44 ± 2.3 |
| | LEAP | 19 ± 2.1 | 15 ± 4.5 | 10 ± 2.2 | 4 ± 2.3 | 52 ± 1.6 |
| 1,000 | ECOPoSAP | 21 ± 0.4 | 13 ± 0.5 | 10 ± 0.3 | 3 ± 0.2 | 52 ± 0.5 |
| | LEAP | 16 ± 0.2 | 13 ± 0.4 | 8 ± 0.2 | 3 ± 0.2 | 60 ± 0.1 |
| 3,000 | ECOPoSAP | 23 ± 0.2 | 14 ± 0.3 | 11 ± 0.2 | 2 ± 0.1 | 49 ± 0.3 |
| | LEAP | 19 ± 0.1 | 13 ± 0.2 | 9 ± 0.1 | 3 ± 0.1 | 57 ± 0.1 |
| 10,000 | ECOPoSAP | 20 ± 0.4 | 16 ± 0.5 | 13 ± 0.3 | 2 ± 0.1 | 48 ± 0.5 |
| | LEAP | 24 ± 0.2 | 13 ± 0.4 | 10 ± 0.2 | 3 ± 0.2 | 50 ± 0.1 |
| 18,500 | ECOPoSAP | 26 ± 0.2 | 19 ± 0.3 | 14 ± 0.2 | 3 ± 0.1 | 37 ± 0.2 |
| | LEAP | 25 ± 0.2 | 18 ± 0.4 | 14 ± 0.2 | 3 ± 0.2 | 40 ± 0.1 |
| 50,000 | ECOPoSAP | 27 ± 0.2 | 17 ± 0.2 | 14 ± 0.1 | 3 ± 0.1 | 38 ± 0.2 |
| | LEAP | 27 ± 0.1 | 16 ± 0.3 | 13 ± 0.1 | 3 ± 0.1 | 41 ± 0.1 |

*Table 4.4:* Comparison of the composition of the main solute elements and Fe of the clusters as measured with the LEAP and ECOPoSAP for WV aged at 365 °C. N.B Percentages may not total 100 % since minor elemental species are not included here.

the number density there is good agreement at and beyond peak number density. However, agreement is poor below this, probably due to the fact it is much harder to detect the smaller features with the LEAP, which results in a much lower number density. In addition, LEAP data were corrected for background clusters, whereas this was not done for the ECOPoSAP data. This may also explain some of the difference observed. The results for the volume fraction show less scatter with the LEAP data and are reasonably consistent with where a trend line would fall through the ECOPoSAP datapoints.

The composition of the features has also been compared. This is likely to show slightly more variation between the two instruments due to slight differences in the cluster search parameters and subtle changes in instrument resolution and aberrations. The mean composition of the clusters across the range of ageing times studied is shown in Table 4.4.

For the longer ageing times (18,500 hrs and 50,000 hrs) the compositions agree well,

as here the features are larger and better defined. The smaller clusters observed in the ECOPoSAP data at ageing times less than 10,000 hrs contain about 8 % more Fe than those observed in the LEAP, and correspondingly they contain less Cu, Ni and Mn. At the shorter ageing times ($< 10,000$ hrs), in general there is variation of a few percent between the concentrations of Si, Ni and Mn. Slightly larger variations exist between the Cu and Fe concentrations observed. These variations will be due to the slightly different cluster search parameters used. There is little difference in the measured concentration of Si between the LEAP and ECOPoSAP data, despite the fact that Si was not included as solute for the cluster search of the ECOPoSAP data. It can be concluded that the cluster search parameters identified in Section 4.2.1.2 give results which are acceptably consistent with the existing results from Hirosawa and Morley obtained on the ECOPoSAP instrument.

## 4.4 Summary

The comparison between voltage pulsing and laser pulsing highlighted that there was significant loss of data quality when laser pulsing over a range of laser energies and specimen temperatures. Significant diffusion of species was observed along with significant Fe peak tails which degraded the accuracy of the measured composition. In addition, there appeared to be systematically less Cu observed with laser pulsing suggesting loss of Cu ions between pulses. For this reason specimens were run using voltage pulsing with a specimen temperature of 50 K, pulse fraction of 20 % at a pulse repetition rate of 200 kHz. Data acquisition rates were generally set to be between 0.001 and 0.002 ions/pulse.

The best parameters for cluster searching of obtained data were identified, specifically:

- Solutes - Cu, Ni, Fn, Mn and Si[3]

[3] Within the matrix of the high Ni steels the Fn peak is approximately 20 % Fe, whilst in the low Ni steels the Fn peak is approximately 60 % Fe. Even so if the $^{58}Fe^{2+}/^{58}Ni^{2+}$ peak is not included in the low Ni searches significant quantities of Ni atoms are not detected in the clusters.

- $d_{max} = 0.50$ nm
- $N_{min} = 16$ ions
- $L = e = 0.40$ nm

A method for distinguishing between clusters which were features of ageing and clusters which are typical of random statistical fluctuations was developed, which enabled a lower $N_{min}$ to be used for the cluster search, increasing the sensitivity to small clusters. This method has been applied to all datasets obtained with the LEAP in this study. The criteria for determining a background cluster was applied to the clusters containing less than 130 ions ($\sim$1 nm) with a Cu concentration less than the average Cu concentration of the clusters in the corresponding randomised data plus two standard deviations.

There is good agreement between the data obtained with the LEAP and ECOPoSAP instruments. Mean cluster size, number density and volume fraction agree well except for times less than 100 hrs where significantly more clusters are observed with the ECOPoSAP due to its higher detection efficiency and thus greater sensitivity to small features. Slight variations in composition are observed but this is to be expected given the slightly different parameters used for the cluster search and the different instruments used.

# 5. Atom Probe Tomography of Thermally Aged Materials

This chapter presents the APT results of the thermally aged materials. The chapter is divided into four main sections. One summarises the hardness evolution of all the materials, the second investigates the microstructural evolution in the high Cu materials, WV and SG, and is followed by a section on the low Cu WF material. The high Ni WF and WV welds are both candidate materials for the formation of Ni-Mn-Si precipitates. Finally, the results of precipitation and solute segregation to grain boundaries and dislocations are presented.

## 5.1 Hardness Changes

Hardness measurements were performed on all specimen blocks as detailed in Section 3.2. Hardness changes are reported rather than absolute hardness values. Since several different specimen blocks were used, reporting hardness changes removes the effects of small variations in initial hardness appearing as hardness gains or losses after ageing. Measurements were taken on all blocks after ageing for 100,000 hrs at the three ageing temperatures, 330 °C, 365 °C and 405 °C. Some blocks were also tested after 90,000 hrs of ageing. These new measurements, along with those obtained and reported previously by Morley are shown in Figure 5.1. More detailed graphs showing the hardness change with time for each alloy at the three ageing temperatures are shown in Appendix B.

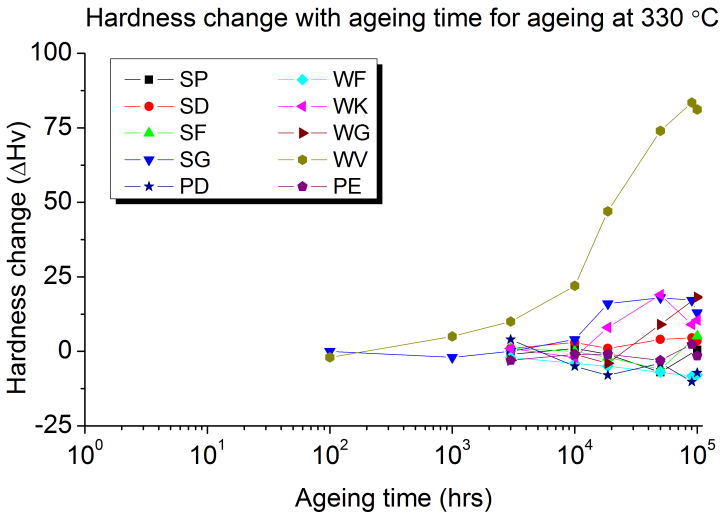


*(a)* Hardness change with ageing time at 330 °C.

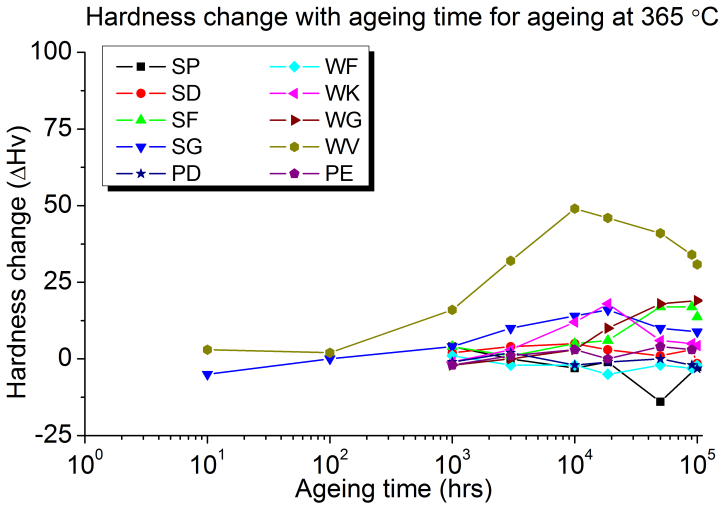


*(b)* Hardness change with ageing time at 365 °C.

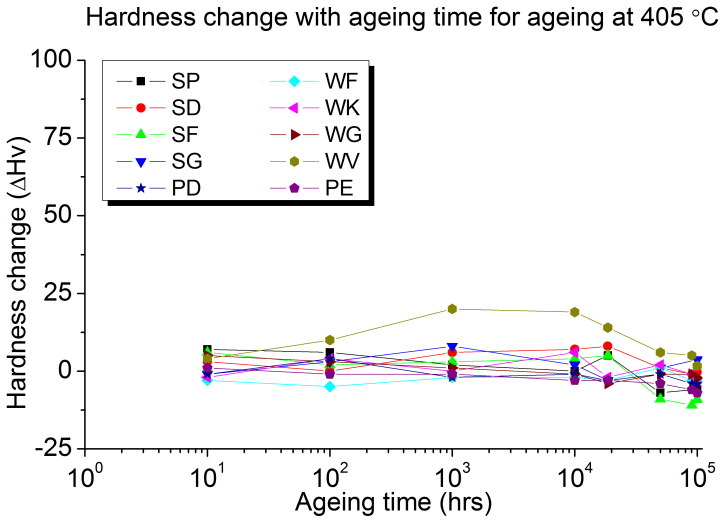


*(c)* Hardness change with ageing time at 405 °C.

*Figure 5.1:* Hardness changes with ageing time for ageing temperatures of (a) 330 °C, (b) 365 °C and (c) 405 °C. Errors are ±4 Hv and are not shown for clarity.

As noted in Section 3.2 the error in the hardness change measurements are ±4 Hv, so only hardness changes larger than 4 Hv are statistically significant. Notwithstanding this, there are a number of alloys which, in most cases, have hardened and in a few cases softened by more than 4 Hv.

As would be expected, the most significant hardening is seen in the high Cu materials, particularly those with high Ni contents. In the WV material aged at 330 °C peak hardness must occur after 100,000 hrs or more of ageing, since no significant decrease in hardness due to overageing is observed. Since the start of ageing the hardness of this material has increased by 50 %. After 100,000 hrs of ageing at 365 °C the hardness of the WV material decreased from its peak value of $49 \pm 4$ Hv at 10,000 hrs as it overaged. For the WG material aged at 330 °C and 365 °C, the hardness increase is smaller, at just less than $20 \pm 4$ Hv. The low Cu material, WK, aged at 330 °C has begun to overage, reaching peak hardness between 50,000 hrs and 90,000 hrs. In the high Ni, lowest Cu, WF material, one of the most likely candidates for formation of "Late Blooming Phases", there is no evidence of the onset of rapid hardening for times up to 100,000 hrs. This might be expected if "Late Blooming Phases" were forming. In fact, at the lowest temperature the material is continuing to soften, whereas the material aged at 365 °C and 405 °C has shown no significant change in hardness.

In the low Ni materials, the highest Cu material, SG, again shows the largest increase in hardness. The SG material aged for 100,000 hrs at 330 °C has begun to overage, with the maximum hardness increment around a quarter of that in the equivalent high Ni material, WV. At 365 °C the latest hardness measurement is consistent with continued overageing. In the SF material significant hardening is only observed in the material aged at 365 °C. This shows no significant change between 50,000 hrs and 90,000 hrs indicating peak hardness may have occurred at some point between these two measurements. However, given the measurement uncertainty this could still be increasing. At 330 °C and 405 °C the SF material showed no significant changes in hardness. A maximum increase of only $8 \pm 4$ Hv is observed in the SG steel aged at 405 °C which has twice the Cu content, hence any increase may have been lost

in the data scatter. Conversely, at 330 °C significant increases in hardening may only start to occur after 50,000 hrs, which is consistent with the slower kinetics at this temperature. For the SP and SD materials which contain very low Ni levels ($< 0.1$ at.%) no significant changes in hardness outside of a few Hv are observed with the exception of the SP material aged to 50,000 hrs at 365 °C, which at face value appears to have softened before recovering to its original hardness. It is suspected this may simply be an anomalous reading since if this was 4 Hv higher then it would not be noticed. Due to the block upon which this measurement was taken being put back into the furnace it was not possible to retest this block.

Very little hardening or softening outside of a couple of Hv is observed in the two plate materials. The one result worth noting is the comparison of the hardening between the PE and SF materials aged at 365 °C. In the SF material after 100,000 hrs of ageing the hardness change is around $12 \pm 4$ Hv whereas the PE plate material shows no significant change in hardness. These two materials have similar Cu levels (0.21 and 0.19 at.% respectively) yet they show differing hardness changes. If this was related to the different Ni contents (PE has around twice the Ni content of SF, 0.56 at.% and 0.24 at.% respectively) then it would be expected that the changes in hardness would be opposite to that observed.

In general, ageing at 405 °C produces very small changes in hardness in all the materials studied. When significant hardening has been observed as in the SG and WV materials, the materials overage relatively quickly. For this reason the high Cu materials aged at 405 °C (SG and WV) have not been investigated experimentally in this project. The precipitates will be very large and present at a low number density, hence they will be difficult to observe in a typical analysis run and APT is unlikely to yield any quantitative information on precipitation. In essence the interesting features of these materials have already been observed.

The APT work focuses on the two high Cu materials WV and SG aged at 330 °C and 365 °C. The low Cu WF material has also been analysed with atom probe to

investigate the difference in hardening at 330 °C and 405 °C after ageing for 90,000 - 100,000 hrs. In this case the 405 °C material provides a reference to study the differences with the material aged at 330 °C which has shown signs of softening.

## 5.2 Microstructural Evolution in the High Cu Materials

In order to relate the underlying microstructural progression to the change in mechanical properties, in this instance the change in hardness, APT analysis has been used to characterise the high and low Ni steels with high Cu contents. The early evolution of these microstructures was discussed in detail by Morley[19] using data from the ECOPosAP. For this reason, the focus of this section will be on comparison of features observed at the very long ageing times, 90,000 hrs and 100,000 hrs at temperatures of 330 °C and 365 °C. Some new data obtained with the LEAP from the WV material aged at 365 °C for times up to 50,000 hrs are also reported where new analyses have been performed and to compare with the data from the longer times using datasets from the same instrument.

### 5.2.1 WV Material

Typical atom maps of the WV material after 90,000 hrs of ageing at 330 °C and 365 °C are shown in Figures 5.2 and 5.3. Also shown in Figures 5.2 and 5.3 are maps showing the density of atoms in the reconstructed volume with the lowest density regions dark blue and the highest density regions red.

It is clear from the atom maps that the features at 330 °C are much smaller and are present at a much higher number density than in the material aged at 365 °C. Furthermore, there is clear association of Ni, Mn and Si with the Cu precipitates. These atom maps will be useful for comparison later on with the low Ni, SG welds

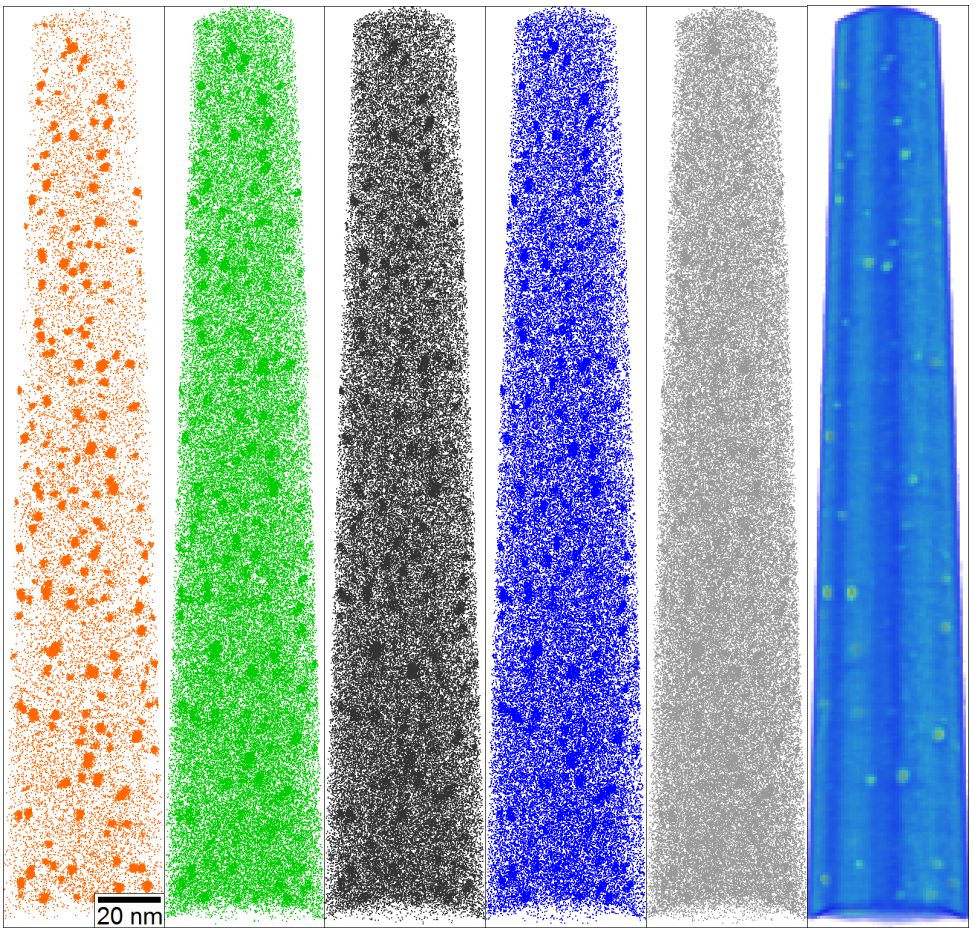


*(a)* Cu. *(b)* Ni. *(c)* Fn. *(d)* Mn. *(e)* Si. *(f)* Atom density.

*Figure 5.2:* Atom maps showing the typical distribution of (a) Cu, (b) Ni, (c) Fn ($^{58}Fe^{2+}$ and $^{58}Ni^{2+}$), (d) Mn, (e) Si atoms and (f) the density of atoms in the reconstructed volume (regions of high density appear red) in the WV weld aged for 90,000 hrs at 330 °C. For clarity only 50 % of the Fn and Mn atoms are shown.

in Section 5.2.2. The atom density maps show that the Cu-enriched precipitates correspond to regions of higher atomic density. This is due to local magnification caused by the different evaporation fields of Fe and Cu. This is thought to be at least partly responsible for the high Fe contents of these precipitates.

#### 5.2.1.1 Precipitate Size, Number Density and Volume Fraction

Aside from the simple visual inspection that the precipitates are smaller and more numerous in the 330 °C material, it is important to quantify this data. Typically the precipitates have a Cu enriched core with an associated Ni, Mn, Si rich

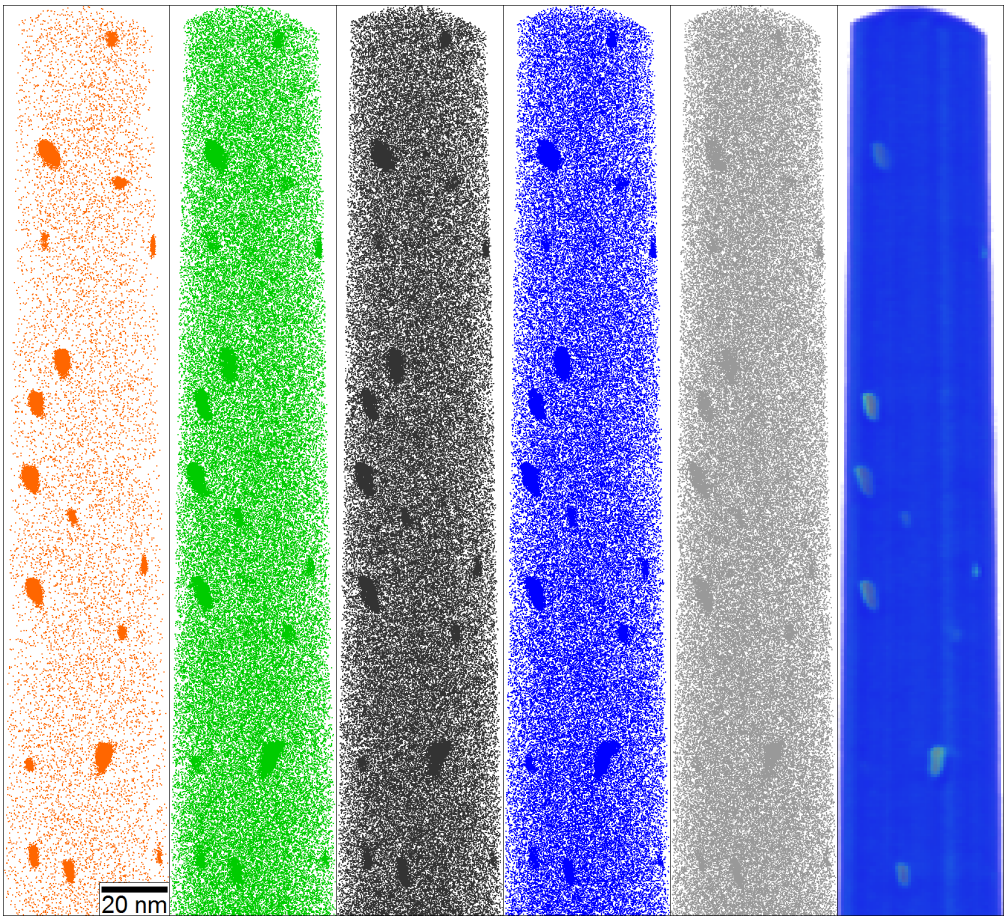


*(a)* Cu. *(b)* Ni. *(c)* Fn. *(d)* Mn. *(e)* Si. *(f)* Atom density.

*Figure 5.3:* Atom maps showing the typical distribution of (a) Cu, (b) Ni, (c) Fn ($^{58}Fe^{2+}$ and $^{58}Ni^{2+}$), (d) Mn, (e) Si atoms and (f) the density of atoms in the reconstructed volume (regions of high density appear red) in the WV weld aged for 90,000 hrs at 365 °C. For clarity only 50 % of the Fn and Mn atoms are shown.

interface. Determination of "size" poses the question of whether or not to include this interface (see Section 4.2.1.5 for details on how the core and interface sizes are calculated). When talking about the relation between features and mechanical properties then clearly the size of the whole feature is important, since the core and interface could have differing elastic moduli and hence a different ability to pin dislocations. However, when comparing between particles formed after ageing at different temperatures, it makes sense to compare between precipitates with the same core size (see Section 4.2.1.5). This removes the effects of interface segregation which may well be ageing temperature and/or precipitate size dependent. Hence, both the size of the core and that of the core plus interface are given here. Figures 5.4a, 5.4b

and 5.4c show the average precipitate size (core and core plus interface), number density and volume fraction respectively after thermal ageing for 90,000 hrs at 330 °C and 365 °C.

As was seen from the atom maps in Figures 5.2 and 5.3 ageing at 330 °C has produced a higher number density of smaller precipitates after ageing for 90,000 hrs. At this ageing time a precipitate in the material aged at 365 °C contains, on average, an order of magnitude more atoms than one in the material aged at 330 °C. The core size for the material aged at 365 °C (dashed line in Figure 5.4a) shows the same trend as that of the core plus interface, albeit with the difference increasing with increased ageing time. This indicates that these particles are growing/coarsening through both addition of atoms at the interface and to the core. The decreasing number density and increasing particle size at both ageing temperatures is indicative of precipitate coarsening after the long ageing times studied. As expected with ageing at lower temperatures, given slower diffusion rates, peak precipitate number density occurs around 10 times later at 330 °C. The volume fraction of the precipitate phase observed after ageing at 365 °C is also consistent with a coarsening population of precipitates. After a sharp initial increase, the volume fraction would be expected to plateau in a pure coarsening regime. However, Figure 5.4c shows that after the initial steep increase the volume fraction appears to continue to increase, although the errors are large here. This is consistent with growth of a precipitate-matrix interface region. The peak at 3000 hrs is not thought to be significant as it is only slightly outside of errors of the surrounding points. After 90,000 hrs of ageing at 330 °C the volume fraction is still increasing, indicating that there is either additional growth of precipitates, a growing interface region or a combination of the two. In addition, some precipitates must be coarsening which is evident from the decreasing number density.

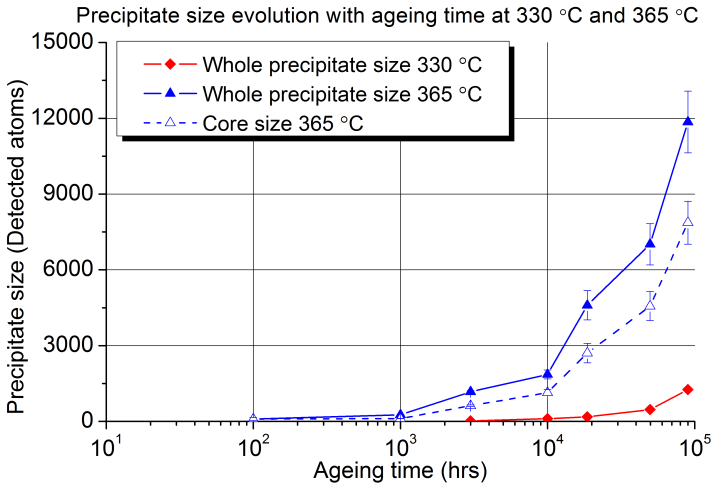


*(a)* Precipitate size.

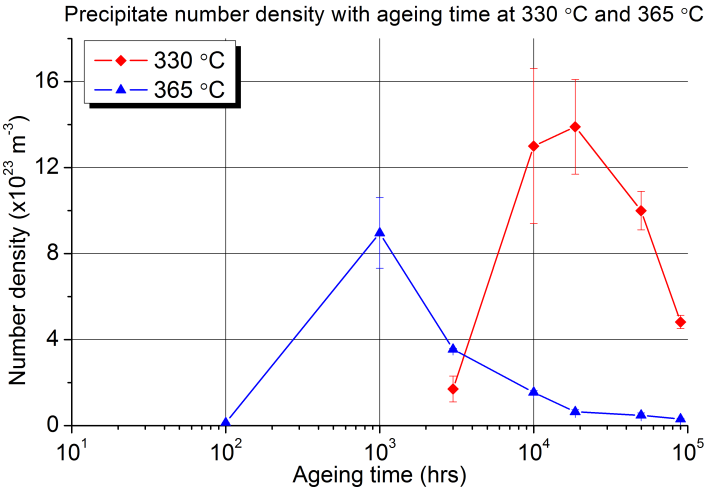


*(b)* Precipitate number density.

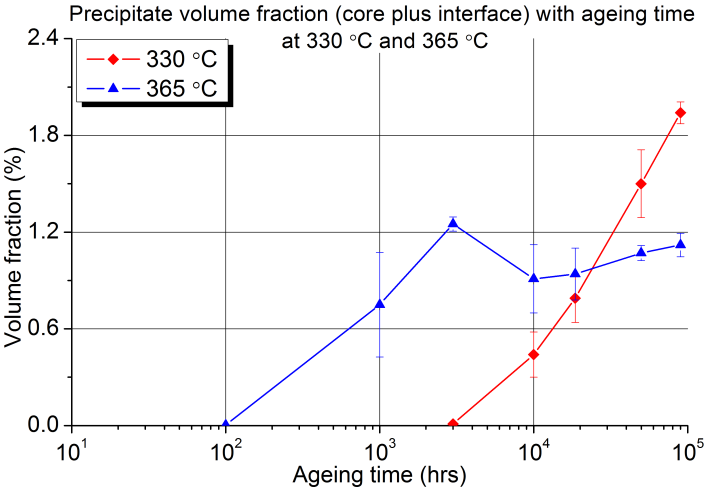


*(c)* Volume fraction.

*Figure 5.4:* (a) Precipitate size, (b) Number density and (c) Volume fraction of the WV specimen aged for times up to 90,000 hrs at 330 °C and 365 °C. 330 °C data for 3,000 hrs - 50,000 hrs from ECOPoSAP.

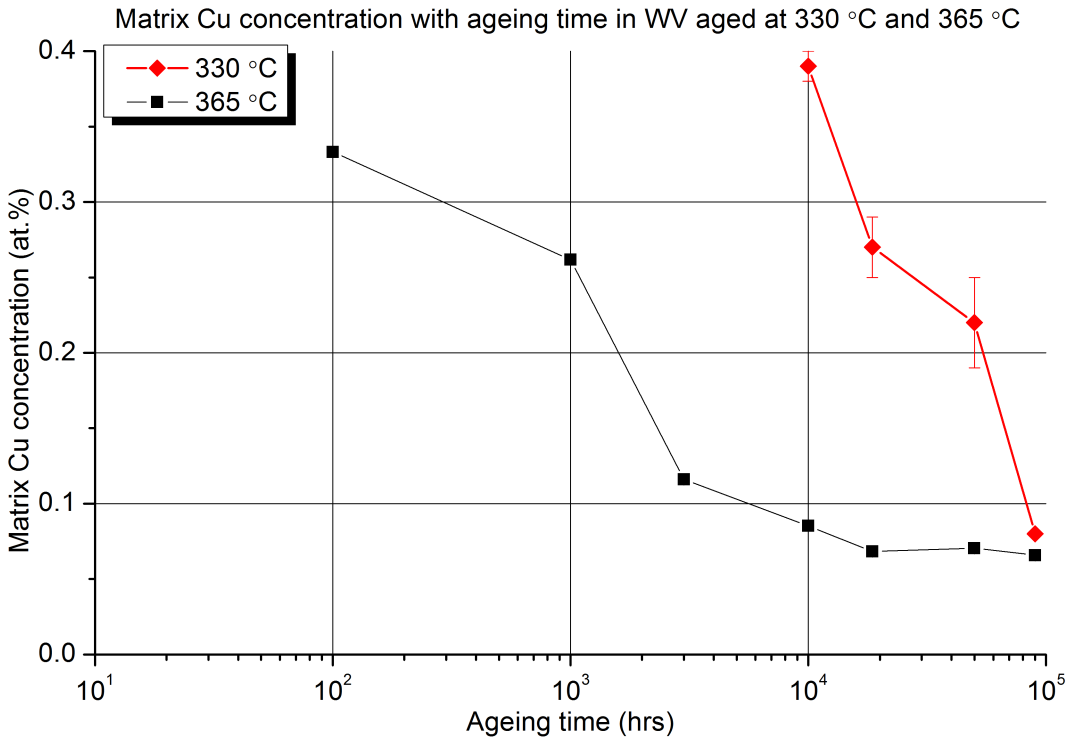


*Figure 5.5:* Measured matrix Cu content in the WV steels aged for times up to 90,000 hrs at 330 °C and 365 °C. Errors for the LEAP data are negligibly small. 330 °C data for 10,000 hrs - 50,000 hrs from the ECOPoSAP.

#### 5.2.1.2 Matrix Composition

The low temperature solubility of Cu in Fe and Fe alloys is of importance since it is a key parameter for KMC models which are used to predict the end of life mechanical properties of the RPV. Given the slow diffusion of Cu in Fe it takes considerable time to approach the equilibrium matrix concentration. Given the very long ageing times in this project the long term evolution of the matrix Cu concentration can be studied. The effect of Ni on the Cu solubility will be discussed in Section 5.2.2.2. The Cu concentration of the matrix in the WV steels aged at 330 °C and 365 °C is shown in Figure 5.5.

Figure 5.5 shows that the matrix Cu content at 365 °C has plateaued at 0.07 at.% after 18,000 hrs of ageing, indicating that the equilibrium level has been reached. Furthermore, this gives the solubility of Cu in Fe at 365 °C for this alloy system as around 0.07 at.%. At 330 °C the Cu level in the matrix falls rapidly after 10,000 hrs,

reaching almost the same level as at 365 °C after 90,000 hrs. It is not possible to say whether this is the equilibrium level for this temperature as the concentration has yet to plateau. Hence, all that can be said for the solubility at 330 °C is that it is equal to or less than 0.08 at.%. It would be expected that the solubility at 330 °C would approach a lower value than at 365 °C given the Fe-Cu phase diagram.

#### 5.2.1.3 Precipitate Solute Composition

Section 5.2.1.1 detailed the size, number density and volume fraction of the precipitates but it is also interesting to study the evolution of their composition. The composition of the interface will be discussed later. To compare like-for-like particles between different ageing temperatures/times the composition and size of the core was used (see Section 4.2.1.5). Figure 5.6 shows the core composition of the precipitates from the WV material aged at 330 °C and 365 °C for 90,000 hrs.

For precipitates larger than 2 - 3 nm in core radius the composition is similar for the two ageing temperatures. The Cu concentration increases with increasing size whereas the concentration of Ni, Fn, Mn and Si are roughly constant over this range of sizes. At sizes above 2 - 3 nm the precipitates at the higher ageing temperature contain more Ni, Fn and Mn. There is no real difference between the Si content with ageing temperature. Below 2 - 3 nm precipitates exhibit a very different composition with ageing time. The precipitates in the steel aged at 365 °C contain significantly less Cu than their counterparts from the material aged at 330 °C. Conversely, they contain more Ni, Fn, Mn and Si. The trends exhibited by these elements with precipitate size is also opposing. At 330 °C, with the exception of Si which is constant, the Ni, Fn and Mn concentrations increase with size up to 2 - 3 nm. In the 365 °C material, the Ni, Fn, Mn and Si concentrations decrease, having initially been higher than at 330 °C.

There are a number of possible reasons for this difference. Firstly, there is the influence of partial features, these are features which are intersected by the boundary of the

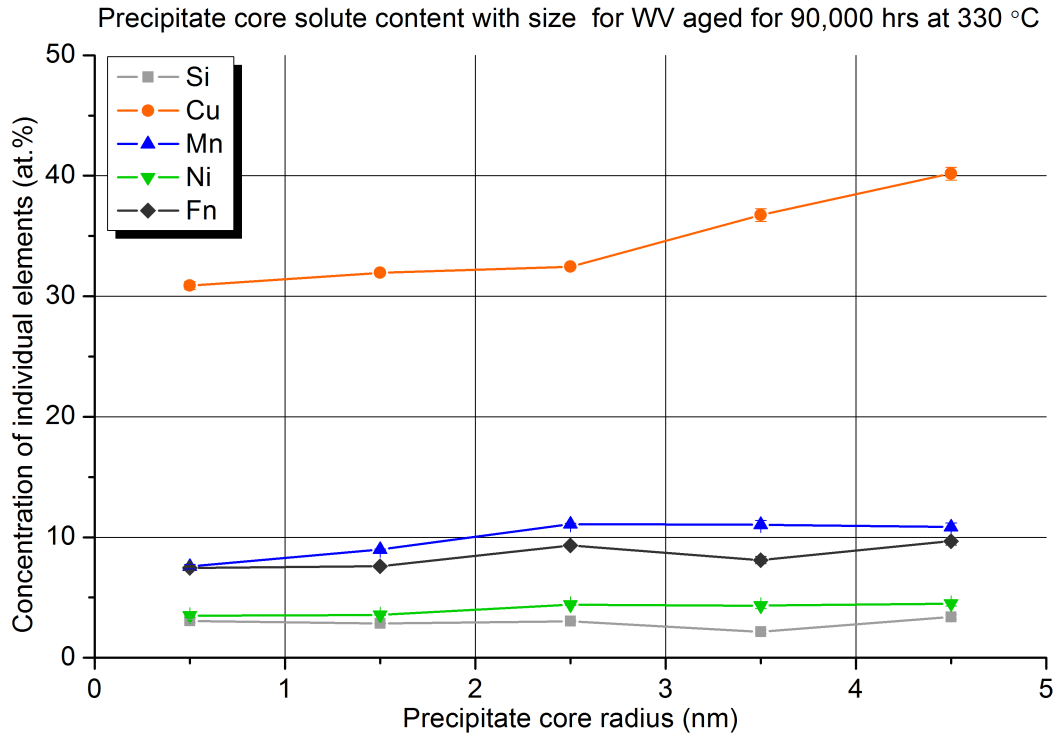


*(a)* Precipitate compositions with core radius after ageing for 90,000 hrs at 330 °C.

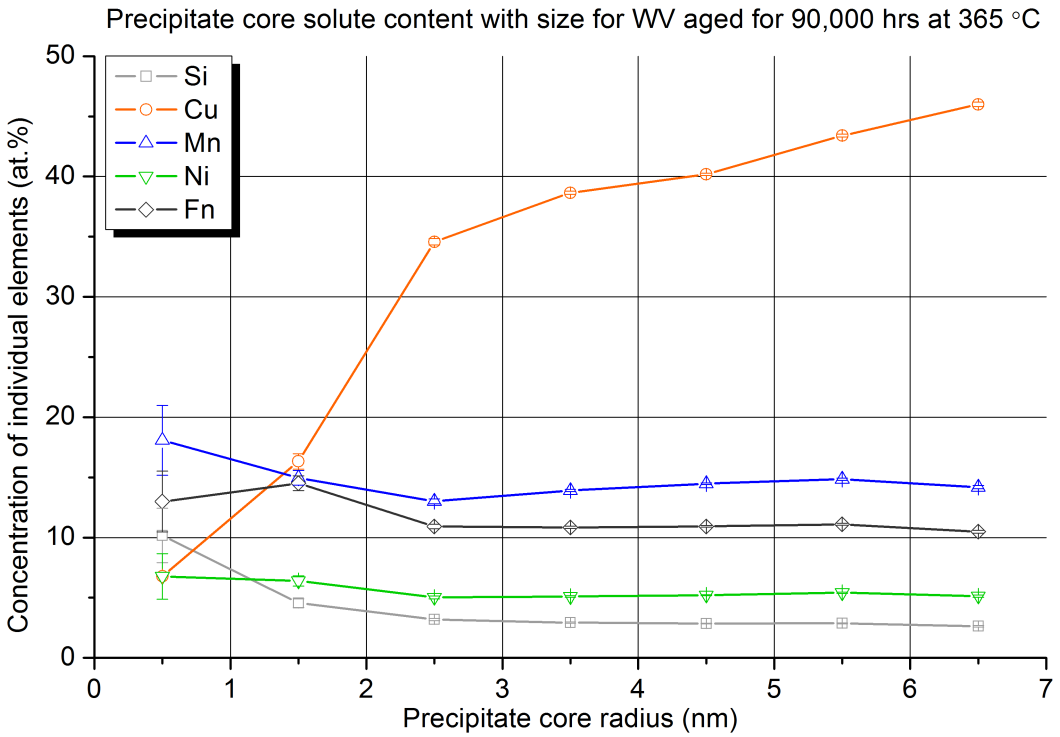


*(b)* Precipitate compositions with core radius after ageing for 90,000 hrs at 365 °C.

*Figure 5.6:* Mean precipitate core solute concentrations observed in the WV steel aged for 90,000 hrs at (a) 330 °C and (b) 365 °C.

analysis volume. These precipitates will be larger than they appear and could contain disproportionately more interface atoms but these would not be identified as so. A number of partial features are observed in the 1 - 2 nm range so the results for this size range should be treated with some caution. For the other size ranges partial features were not observed to have any significant effect on the observed results. It should be noted that correction for partial features has not been performed due to the number of precipitates observed (both whole and partial) and the lack of an automated method for identifying the partial features.

Additionally, it is possible that there is a different mechanism involved in the nucleation of features, with particles at the higher temperatures nucleating from a more Ni, Mn, Si rich cluster but this seems unlikely given the small change in temperature. Alternatively, the relative number of other atoms could be changing i.e a change in the number of Fe atoms, which could result in a higher Cu concentration for the same total number of Cu atoms. One way to investigate this is to plot the number of atoms of a given solute in the precipitate core versus the total number of atoms in the precipitate core for all the detected precipitates at each ageing temperature. The gradient of this plot gives the concentration of a given solute. Plotting this for each of the solute elements for the two temperatures will show any differences in the relative number of solutes with size. These plots are shown in Figures 5.7a - 5.7d. The inset plots on these figures show the region of 0 - 1000 total atoms, which is approximately equivalent to the 0 - 2 nm size range, allowing comparison with Figure 5.6.

For precipitates containing more than a few 1000 atoms, there is very little difference in the number of solute atoms of each element for an equivalently sized precipitate with ageing temperature, as the plots for 330 °C and 365 °C lie on top of one another. As the size increases the number of particles becomes less and hence there is more scatter. Likewise there will be some scatter from particles which are intersected by the boundaries of the analysis volume and are thus larger than they appear. The inset to the plots in Figure 5.6 indicate that the lower Cu content and higher Ni, Mn and Si concentrations with higher ageing temperature are also observed in these

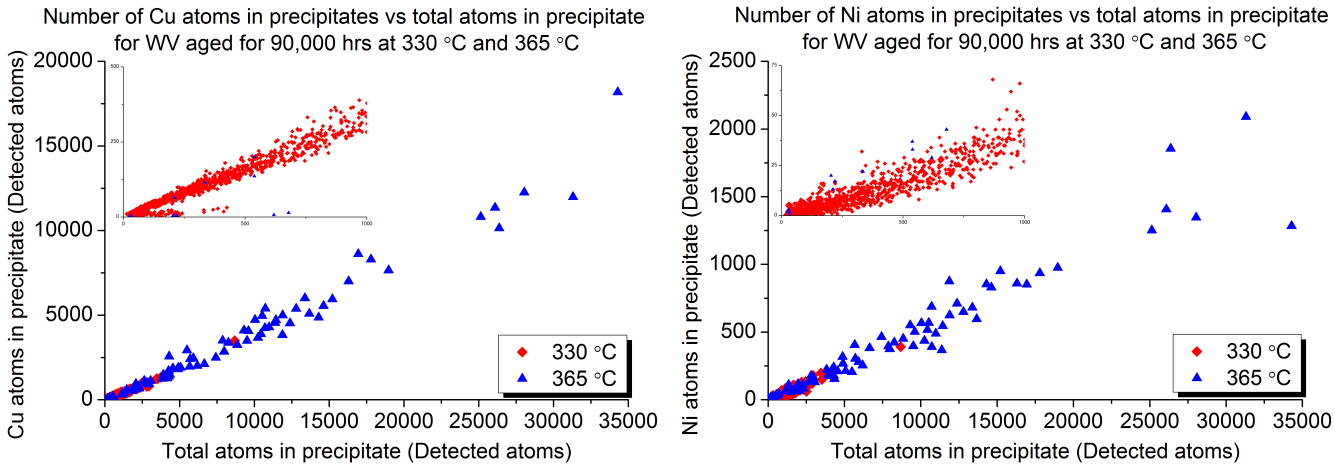


*(a)* Cu atoms.

*(b)* Ni atoms.

*(c)* Mn atoms.

*(d)* Si atoms.

*Figure 5.7:* Plots of the number of solute atoms of (a) Cu, (b) Ni, (c) Mn and (d) Si versus the total number of atoms in the precipitate core for the WV steel aged for 90,000 hrs at 330 °C and 365 °C. Insets show a zoomed in portion of the main images detailing the region from 0 to 1000 total atoms.

plots. The inset to Figure 5.7a shows the presence of some features at 365 °C which contain around 500 atoms but very few Cu atoms, these are partial features which only capture a small proportion of the Ni-Mn-Si interface. The difference between the 0 - 1 nm features at the two ageing temperatures does not appear to be related to partial features.

As mentioned earlier it is possible that the changes in concentration observed in Figure 5.6 could be due to differences in the Fe content at the two temperatures, either from actual effects or artefacts (this will be discussed in more detail in Section 5.2.1.4). This can be investigated by plotting the composition of the precipitates excluding the Fe atoms, as shown in Figure 5.8. This will reveal any subtle changes in precipitate solute concentration with size.

From Figure 5.8a there appears to be very little variation in the Cu content with size in the material aged at 330 °C. Likewise, there is little variation in the Mn or Si content with size. The dip in the Cu content at 2 - 3 nm coincides with a small increase in Ni (plus Fn) and Mn, which appears to peak around this value. At 365 °C the Cu content in precipitates above 2 - 3 nm slowly increases with the concentration around 5% less than at 330 °C. The Fn, Mn and Si concentrations all show no change with size above 2 - 3 nm, and are comparable with the concentration at 330 °C. The Ni content is slightly higher at 365 °C, again showing little change with size. Below 2 - 3 nm the precipitates are predominantly Ni, Mn and Si rich, which is also observed when the Fe atoms are included. As noted previously the 1 - 2 nm features are influenced by partial features which could explain the differences observed in this size range. This is not a viable explanation for the 0 - 1 nm precipitates, and from Figure 5.8b this also cannot be explained by differences in the Fe content. This suggests that this is a real effect and these precipitates are genuinely richer in Ni, Mn and Si. It is possible that these features may be a precursor to the formation of Ni-Mn-Si rich features in the matrix.

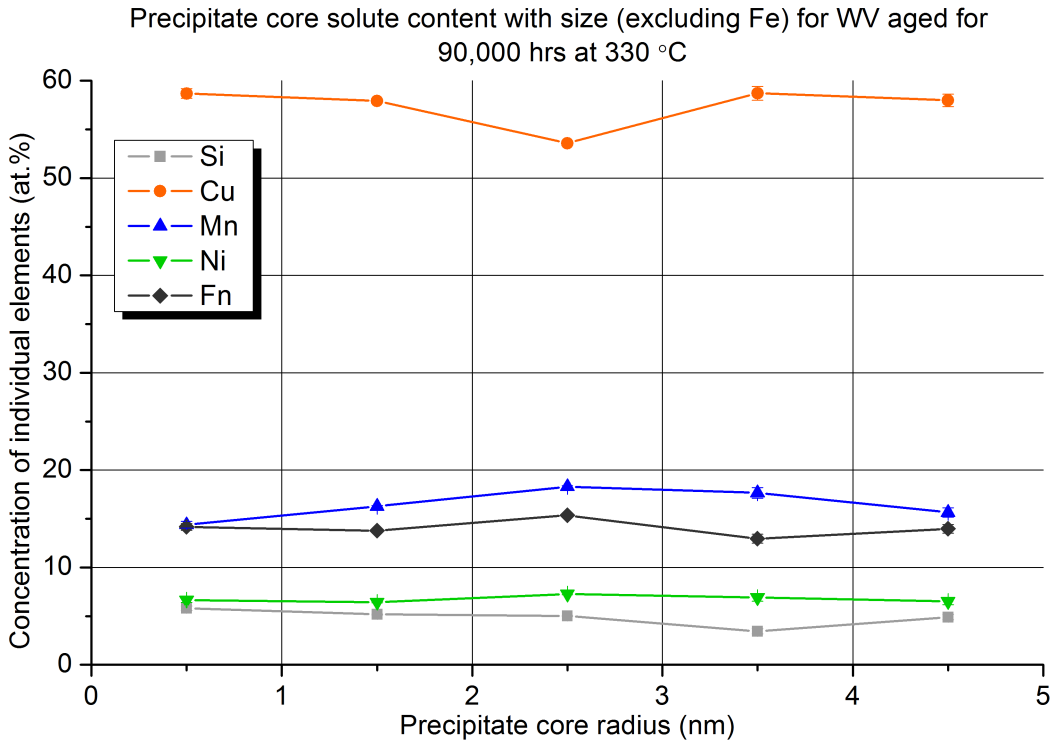


*(a)* Precipitate solute content with core radius after ageing for 90,000 hrs at 330 °C.

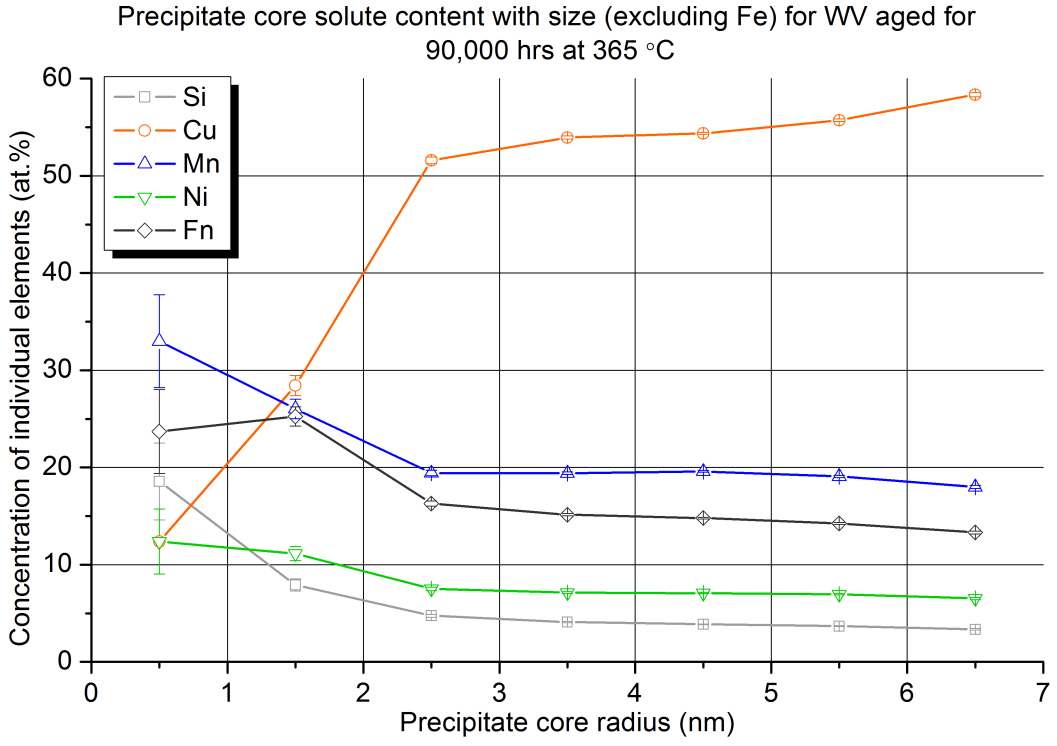


*(b)* Precipitate solute content with core radius after ageing for 90,000 hrs at 365 °C.

*Figure 5.8:* Variation in the solute content of the precipitates with core radius in the material aged for 90,000 hrs at (a) 330 °C and (b) 365 °C. Fe atoms excluded from precipitate to calculate compositions.

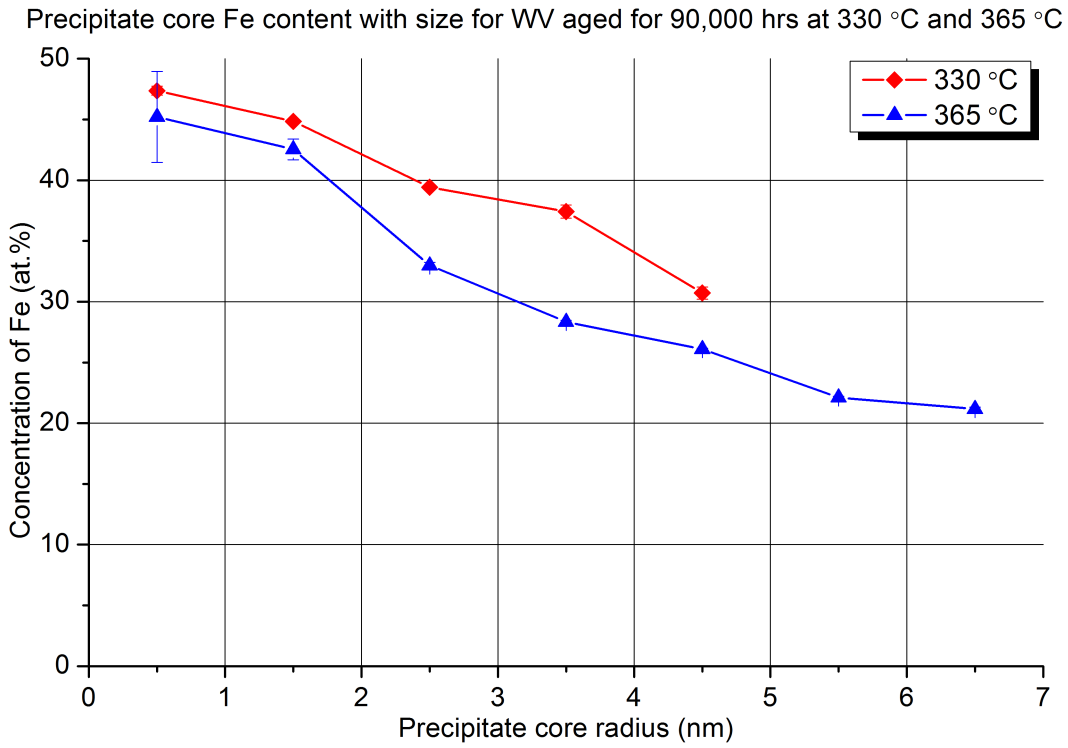


*Figure 5.9:* Mean Fe content of the precipitates observed in the WV material aged for 90,000 hrs at 330 °C and 365 °C.

#### 5.2.1.4 Fe Content of Precipitates

The Fe content of Cu precipitates was discussed in Chapter 2 and is the source of much debate. Again the focus will be on the precipitate core region, as this should, to some extent at least, reduce the effect of trajectory overlaps and any Fe included from the cluster search algorithm. These artefacts will cause an increase in the apparent Fe content of the precipitates. However, by comparing features of similar size it should be possible to see trends between the two ageing temperatures, as artefacts will be comparable. As with the solute content, it is logical to start with the average concentration with core radius at the two ageing temperatures, this is shown in Figure 5.9.

It is clear from Figure 5.9 that for all precipitate sizes above 0 - 1 nm the Fe content is less in the precipitates aged at the higher temperature. This indicates that the precipitates must contain some Fe, at least at the lower temperature, since the artefacts should be comparable here as precipitates are of roughly similar sizes. It

is much harder to comment on (a) the absolute magnitude of the Fe content in these precipitates and (b) the Fe content with size. This is because it is difficult to quantify how much Fe is incorrectly positioned in precipitates since this will depend on the local curvature around the edges of the particle and may well be different for different size precipitates.

A number of approaches could be used to limit the influence of Fe from trajectory overlaps on the composition by selectively removing Fe atoms from the precipitates. One method, used by Morley[19] used larger precipitates to "correct" the Fe content of smaller precipitates. This method took the Fe content in the core of very large (>10 nm) precipitates which, in theory, should be free of Fe from trajectory overlaps and then set the Fe content of the smaller particles to this value. This however, will mask any changes in the Fe content with size, but it does allow comparison of similar sized precipitates with ageing temperature.

Liddle et al.[157] used an alternative method to remove Fe from carbides present in a Fe-14wt.%Co-10%Ni-2%Cr-1%Mo-0.16%C alloy based on the number of Co and Ni atoms observed in the carbides. The authors thought it unlikely that the carbides contained these two elements and hence removed them. This also required the removal of an equivalent proportion of Fe, corresponding to the overall matrix composition. Hence, the number of Fe atoms to remove for each Co or Ni atom removed was given by %Fe/(%Co + %Ni) where all percentages refer to the matrix composition. For the Cu-enriched precipitates in these steels the obvious candidate elements which are unlikely to be present are C, Mo, Cr. Precipitates on dislocations or grain boundaries (see Section 5.4) will be found associated with regions enriched in these elements and may contain small proportions of these elements. In general, precipitates in the matrix are unlikely to contain these elements. Using these elements to identify the amount of Fe to remove does not give satisfactory results in the majority of cases. This is because the number of Fe atoms identified for removal generally exceeds the actual number of Fe atoms in the precipitate. The main reason for this is that the number of Fe atoms to remove is given, as with the Ni and Co case by, %Fe/(%Mo + %C + %Cr)

= ∼300 (whereas for Liddle's case of Co-Ni the corresponding ratio is 3) so very few C, Mo and Cr atoms are required before several 1000 Fe atoms need to be removed. Part of the reason why this does not work could come from the noise in the mass spectrum. Mo for example, has 7 isotopes and often evaporates in two charges states (2+ and 3+) meaning the Mo atoms are spread over as many as 14 different mass peaks, thus there is potential for significant noise in the Mo counts. Likewise, the levels of C and Cr are small and so can also be adversely affected by noise. Even after correcting the counts of C, Cr and Mo for background noise in both the matrix and clusters this method does not work. In Liddle's case the much higher matrix levels of Co and Ni means that noise is much less of an issue and each noise count of Ni or Co would only involve the removal of 3 additional Fe atoms. Additionally, C, and due to co-segregation effects Mo and Cr, are unlikely to be homogeneously distributed within the matrix, which was the case for Co and Ni in Liddle's work. Also evaporation artefacts lead to an inhomogeneous solute distribution within the APT dataset (C tends to be observed at low index poles). Hence, Liddle's method is unlikely to give consistent results in this case.

Finally, there is the following approach, which is based on removing atoms based on the extent and density of atoms from trajectory overlaps in a precipitate. This idea is based on the principle that the precipitate, as seen in the reconstruction, is a superposition of the atoms from the precipitate with atoms from trajectory overlaps. The simplest case of spherical particles with trajectory overlaps extending over a fixed region, $d_{traj}$, results in a shell of width, $d_{traj}$ which is affected by overlap atoms. It is possible to derive expressions for the number of atoms from trajectory overlaps in the precipitate core ($N_{traj}^{core}$) and interface ($N_{traj}^{int}$). These are given by

$$N_{traj}^{core} = \begin{cases} \frac{4\pi\zeta}{3\Omega_{traj}}[R_c^3 - (R_c - \{d_{traj} - d_{int}\})^3] & \text{for} \quad 0 \leq d_{int} < d_{traj} \\ 0 & \text{for} \quad d_{int} \geq d_{traj} \end{cases} \tag{5.1}$$

$$N_{traj}^{int} = \begin{cases} N_{traj}^{int} = \frac{4\pi\zeta}{3\Omega_{traj}}[R_w^3 - (R_w - d_{int})^3] & \text{for} \quad d_{int} \leq d_{traj} \\ N_{traj}^{int} = \frac{4\pi\zeta}{3\Omega_{traj}}[R_w^3 - (R_w - d_{traj})^3] & \text{for} \quad d_{int} \geq d_{traj} \end{cases} \tag{5.2}$$

Where $\Omega_{traj}$ is the density of trajectory overlap atoms in the shell, $R_c$ and $R_w$ are the radii of the core and whole precipitate (core plus interface) respectively. The extent of the overlap region in the core will be affected by the presence of the precipitate-matrix interface, the width of which is given by $d_{int}$. This is taken into account with the $(d_{traj} - d_{int})$ term in Equation 5.1. These equations require values for both $\Omega_{traj}$ and $d_{traj}$. The extent of trajectory overlaps is thought to be around 1 nm[125], hence this value was chosen for $d_{traj}$. Choosing a parameter for the density of trajectory overlap atoms is more difficult, this was set to 20 atoms nm$^{-3}$ (around 1/4 of the density of atoms in pure Fe). Changing this value from 15 - 25 atoms nm$^{-3}$ was found to change the Fe content by at most 10 %, without changing the trend of a plot of Fe content with size.

This model for trajectory overlap removal is based on the assumption that the overlapped atoms come wholly from the surrounding matrix and form a spherical shell of fixed width, regardless of precipitate radius. The assumption of a shell of overlap atoms seems reasonable given the simulations of Vurpillot[125], which suggest the core is free of overlap atoms. Fixing the extent of the overlap distance as 1 nm regardless of size is perhaps the most limiting assumption. In reality this probably increases with particle size, but how the extent of trajectory overlaps varies with size is not well documented. Hence, for now at least, it seems most sensible to fix this as a set distance for all sizes. The assumption of a spherical shell also seems reasonable. In the reconstruction Cu precipitates appear elongated in $z$ (actually this is a compression in $x$ and $y$) but in the original material it is expected they are spherical or near spherical.

Assuming all the overlap atoms originate from the matrix is likely to be somewhat of a simplification to the real evaporation process, due to the presence of the interface. This interface is rich in Ni, Mn and Si (see Section 5.2.1.5), which have elemental evaporation fields of 35 V nm$^{-1}$, 30 V nm$^{-1}$ and 33 V nm$^{-1}$ respectively so predicting

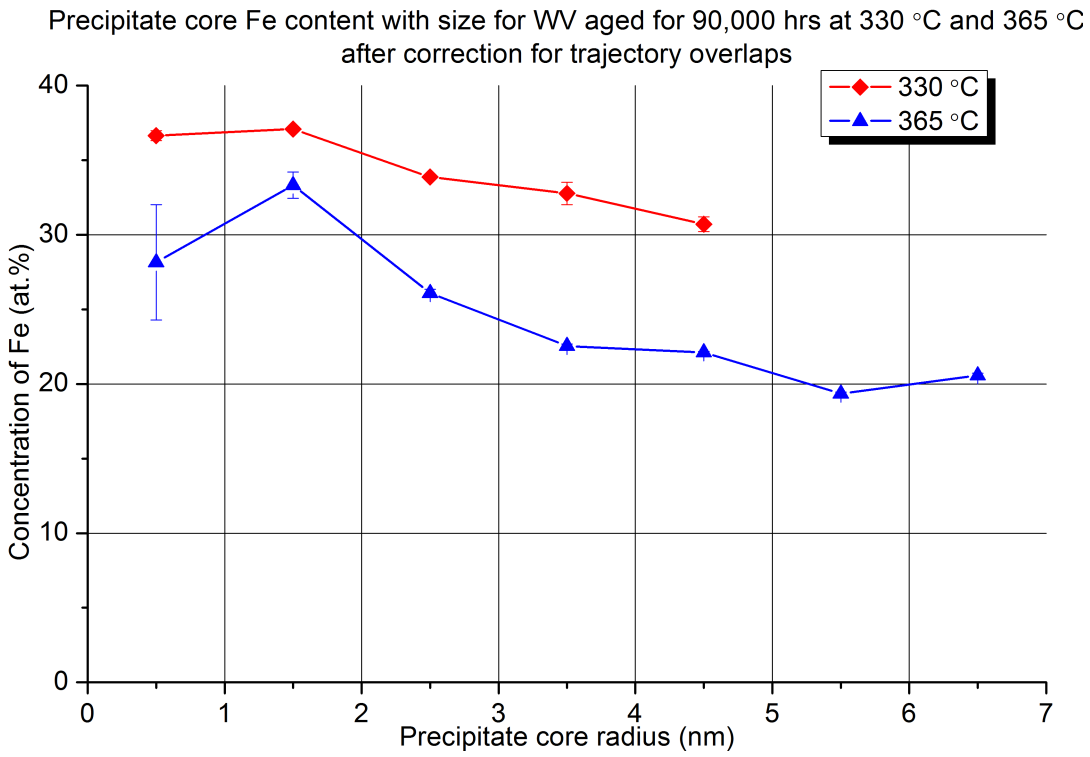


*Figure 5.10:* Change in precipitate Fe content with size after correction for trajectory overlap effects in the WV material after ageing at 330 °C and 365 °C for 90,000 hrs.

their contribution to trajectory aberrations is difficult[1]. However, given that the elemental evaporation fields of Ni, Mn and Si are similar to that of pure Fe (33 V $nm^{-1}$) it seems likely the interface region has an evaporation field close to, or slightly higher, than that of the matrix. It could therefore be argued that the interface is simply an extension of the matrix, as far as the evaporation process is concerned, so its only effect would come in when choosing the number of atoms of each type which make up $N_{traj}^{core}$ and $N_{traj}^{int}$. For now at least, it seems sensible to consider the approximation where the atoms contributing from trajectory overlaps come wholly from the matrix, which should provide some insight into the Fe content of these precipitates but still remain reasonably straightforward to apply.

Applying this correction to the precipitate composition reduces the Fe content of the core as shown in Figure 5.10. This correction has preserved the observation from Figure 5.9 of higher Fe content at lower ageing temperature. Applying the correction

[1] The quoted values are evaporation fields calculated for pure metals. In an alloy system different binding energies and work functions will result in slightly different evaporation fields.

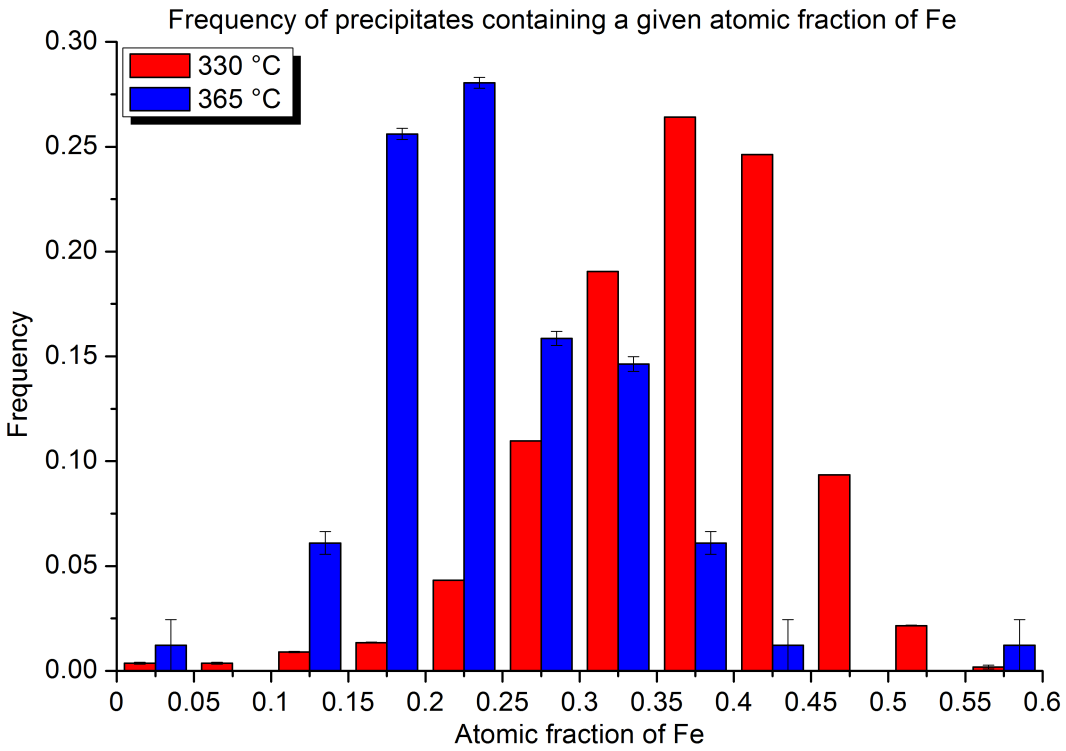


*Figure 5.11:* Frequency of clusters containing a given atomic fraction of Fe after correction for the influence of trajectory overlaps in the WV material aged at 330 °C and 365 °C for 90,000 hrs.

has decreased the overall Fe content of the precipitates and reduced the difference in Fe content with size. At the larger sizes, particularly at 365 °C, the correction has little effect. This is for two reasons, one, at this size the precipitates have interface widths around half the overlap distance so a large proportion of the overlap atoms end up in this region. Secondly, the relative proportion of atoms from overlaps is much smaller even without the presence of an interface.

As with the solute atoms in Section 5.2.1.3 it possible to plot the number of Fe atoms against the total number of atoms in the precipitate. This plot has considerable scatter, particularly from the 365 °C data. Instead, it is more useful to plot a histogram showing the frequency of precipitates containing a given fraction of Fe as is shown in Figure 5.11. This plot clearly illustrates the differing Fe contents with ageing temperature, at the lower temperature the distribution is shifted towards higher Fe contents. The 365 °C data shows a potentially interesting trend. Compared to the 330 °C distribution it is more asymmetric, with more precipitates with lower Fe

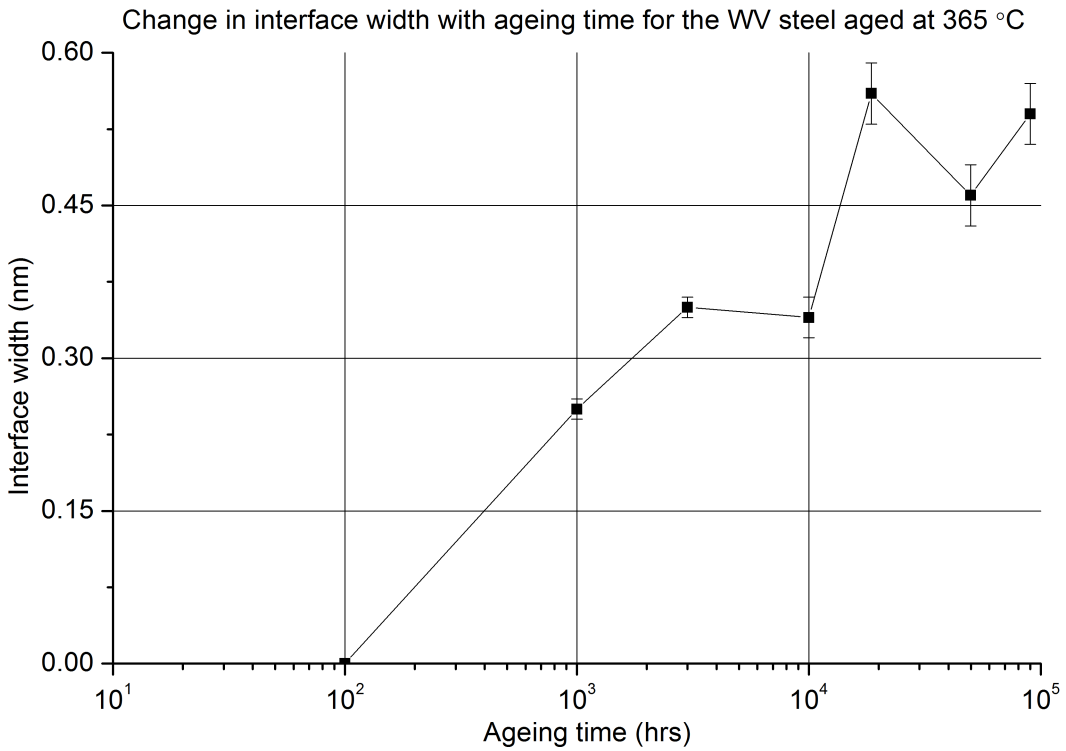


*Figure 5.12:* Variation in the width of the precipitate-matrix interface for the WV material aged for times up to 90,000 hrs at 365 °C.

contents than might be expected. This could indicate that there are two populations of precipitates; one population which remain coherent with the matrix and have bcc structure and one with lower Fe contents which have an semi-coherent 9R type structure. Further investigation will be required to confirm this hypothesis.

#### 5.2.1.5 Precipitate/Matrix Interface

The precipitate matrix interface was characterised using the method outlined in Section 4.2.1.5. The width of the interface was found to vary with ageing time at an ageing temperature of 365 °C as shown in Figure 5.12.

This clearly shows that the interface grows with ageing time even after ageing for 90,000 hrs, suggesting that the equilibrium level of segregation has not been obtained. For the WV material aged for 90,000 hrs at 330 °C the mean interface width, calculated as detailed in Section 4.2.1.5, was found to be 0.56 nm which is consistent with the observed mean interface width of 0.54 nm after ageing at 365 °C. This suggests there

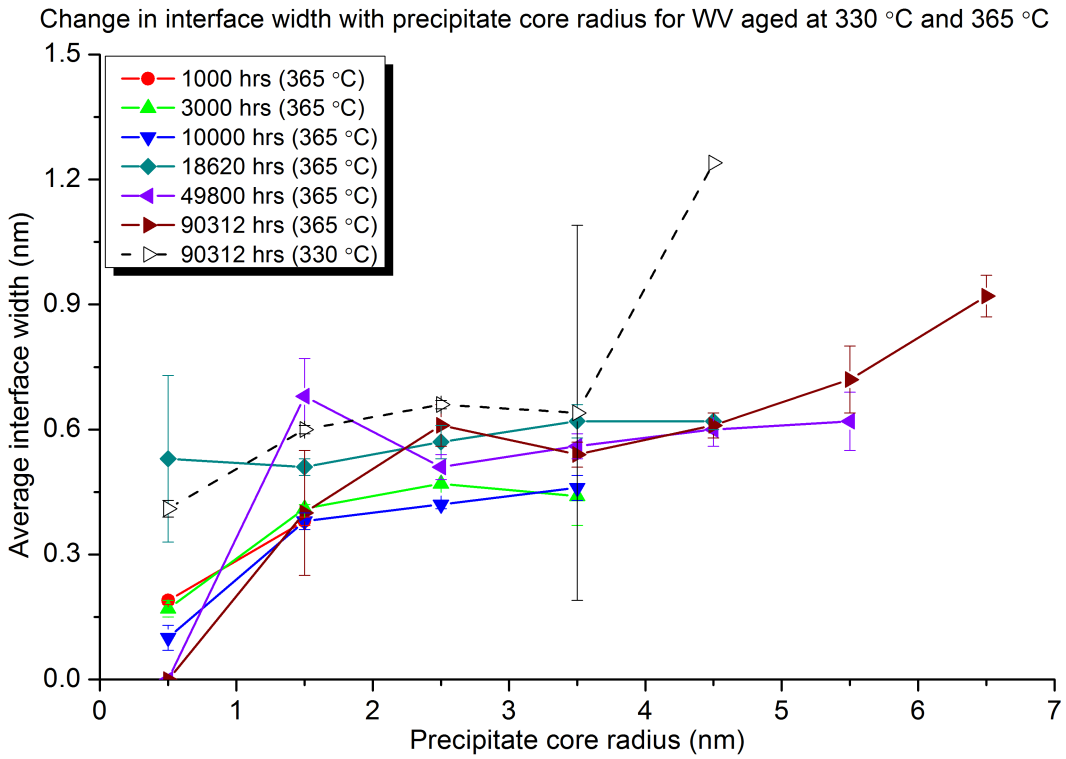


*Figure 5.13:* Change in interface size with precipitate core radius for the WV material aged for times up to 90,000 hrs at 365 °C and for 90,000 hrs at 330 °C.

is little change in segregation behaviour with ageing temperature. Whilst the mean interface width shows trends with ageing time, the precipitate core radii are different and hence this can mask more subtle differences in segregation behaviour. The change in interface width with core radius for each of the ageing times is shown in Figure 5.13.

This shows that at all the ageing times, larger precipitates have a wider interface. It also re-affirms the results from Figure 5.12 which, in most cases, gives a wider interface with longer ageing time. It also suggests that ageing at a lower temperature promotes a wider interface. This is not evident from looking at the mean interface width. Comparing the interface width between the 330 °C and 365 °C data after 90,000 hrs of ageing show that equivalently sized precipitates have a slightly wider interface when ageing at 330 °C. Above 3 - 4 nm in radius the 330 °C data has a large scatter as there are relatively few precipitates above this size.

The composition of the interface is also important as this will impact on the magnitude of the reduction in interfacial energy, the main driving force for the segregation[23, 56].

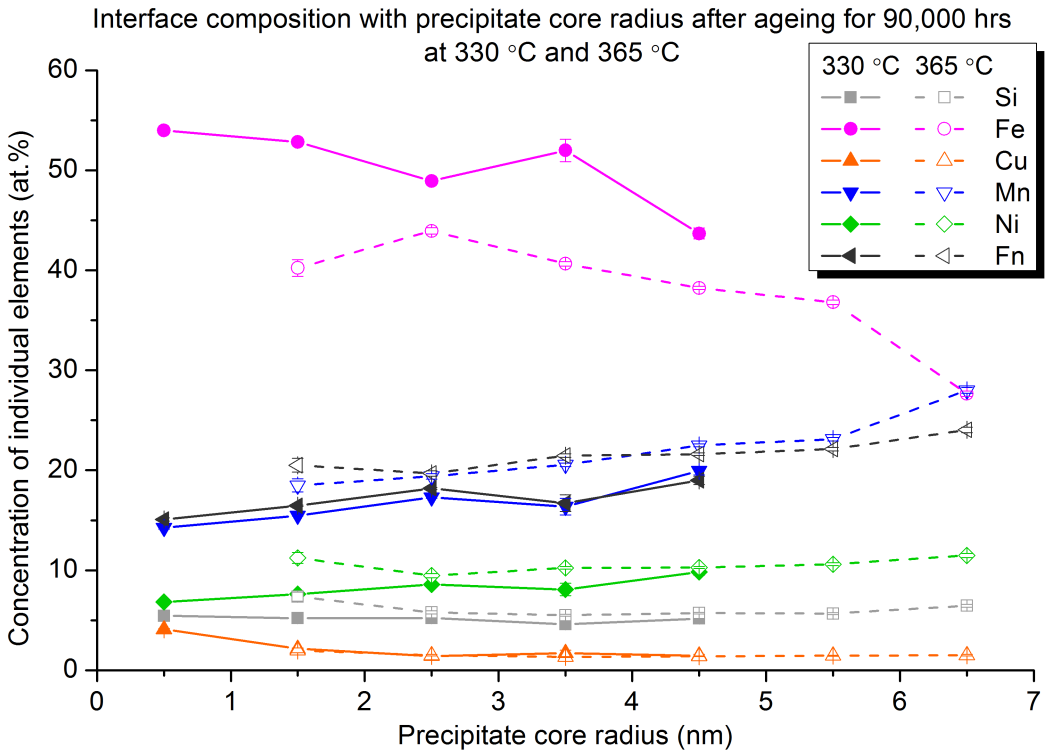


*Figure 5.14:* Interface composition with precipitate core radius for the WV weld after ageing for 90,000 hrs at 330 °C and 365 °C.

Like the precipitate core composition the interface composition will also be affected by trajectory overlaps. The number of atoms in the interface region from trajectory overlaps can be estimated using Equation 5.2. As for the core composition, the free parameters, $d_{traj}$ and $\Omega_{traj}$, the overlap distance and density respectively will be kept at 1 nm and 20 atoms nm$^{-3}$. This gives the composition of the interface after 90,000 hrs of ageing at 330 °C and 365 °C, as a function of precipitate core radius, as shown in Figure 5.14.

From Figure 5.14 there is still a significant proportion of Fe in the interface. As with the precipitate core (Figure 5.10), ageing at higher temperature results in less Fe in the interface. The Cu content of the interface is very low which is consistent with what would be expected. The Cu in the interface probably results from Cu diffusing into the core from the matrix. The trends seen with size are similar after ageing at 330 °C and 365 °C. The Ni (plus Fn), Mn and Si concentrations all increase with size, although this is probably due to the reducing Fe content. There is a slightly higher Ni, Mn and Si content in the interface of the material aged at 365 °C.

As mentioned above, the segregation of Ni, Mn and Si is thought to reduce the interfacial energy. The reduction in interfacial energy, $\Delta\sigma$, has been estimated using the same method as used previously by Morley[19]. That is using

$$\Delta\sigma = -kT\sum_i \Gamma_i^{relative} \tag{5.3}$$

Where $k$ is Boltzman's constant, $T$ is the ageing temperature and $\Gamma_i^{relative}$ is the relative Gibbsian interfacial excess of species $i$. Ignoring cross-terms, to a first order approximation $\Gamma_i^{relative}$ is given by

$$\Gamma_i^{relative} = \Gamma_i - \Gamma_{Cu}\frac{c_i^\alpha c_{Fe}^\beta - c_i^\beta c_{Fe}^\alpha}{c_{Cu}^\alpha c_{Fe}^\beta - c_{Cu}^\beta c_{Fe}^\alpha} - \Gamma_{Fe}\frac{c_{Cu}^\alpha c_i^\beta - c_{Cu}^\beta c_i^\alpha}{c_{Cu}^\alpha c_{Fe}^\beta - c_{Cu}^\beta c_{Fe}^\alpha} \tag{5.4}$$

with $c_i^{(\alpha,\beta)}$ the atomic fraction of element $i$ in the matrix ($\alpha$) or precipitate core ($\beta$) and $\Gamma_i$ is calculated from

$$\Gamma_i = \rho\Delta x(c_i^{int} - c_i^\beta) \tag{5.5}$$

with $\rho$ the atomic density, $\Delta x$ the width of the interface and $c_i^{int}$ the concentration of $i$ in the interface region, full details can be found in Morley[2][19].

Using Equations 5.3 - 5.5 the reduction in interfacial energy can be calculated for each precipitate. The reduction in interfacial energy for the precipitates after ageing at 330 °C and 365 °C for 90,000 hrs is shown in Figure 5.15.

Figure 5.15 shows that within the scatter of the data there appears to be no obvious change in the reduction in interfacial energy with ageing temperature. This is particularly the case in the range 1 - 3 nm where the statistics are best for both ageing temperatures. If the interfacial segregation was purely due to a minimisation of unfavourable Fe-Cu bonds it might be expected that there would be a greater reduction in energy at an ageing temperature of 365 °C. Since these precipitates

[2] This is a slight modification from Morley's calculations from ladder diagrams. In his case $\Delta x$ is the bin width of the profile and $(c_i^{int} - c_i^\beta)$ is replaced with a sum over all $p$ bins in the profile $\sum_{m=1}^{p}(c_i^m - c_i^{\alpha,\beta})$ where $\alpha$ or $\beta$ is chosen depending on whether the bin $m$ is deemed to be on the matrix or precipitate side of the interface.

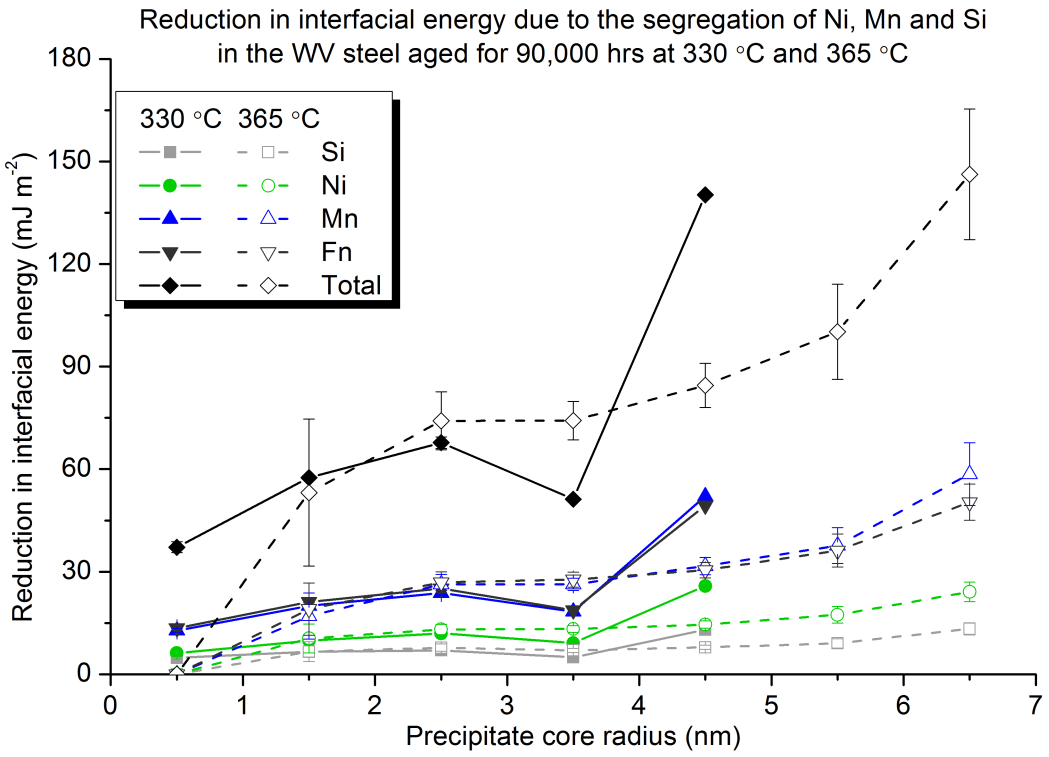


*Figure 5.15:* Reduction in interfacial energy with precipitate core radius due to the segregation of Ni, Mn and Si to the precipitates after ageing for 90,000 hrs at 330 °C and 365 °C.

contain less Fe, the difference in composition between matrix and precipitate is highest. However, with the greater undercooling at 330 °C it is possible that some precipitates may have transformed to a 9R structure. These precipitates may contain more Fe because of the slower diffusion rate. Hence, the smaller difference in precipitate and matrix composition may be offset by having a semi-coherent structure leading to similar levels of segregation between the two temperatures. Precipitate transformations may also be the reason the interfacial energy reduction increases with size above 4 nm. The are relatively few precipitates in the 0 - 1 nm range at 365 °C and these show no interfacial segregation, likewise there is only one precipitate in the ranges 3 - 4 nm and 4 - 5 nm in the 330 °C data.

Figure 5.15 also highlights that, for both the ageing temperatures and for all sizes, Ni (when including Fn) is most effective at reducing the interfacial energy, followed by Mn with only a small reduction in energy from the presence of Si. In addition, the reduction in interfacial energy due to Ni, Fn, Mn and Si also increases with size.

| Radius (nm) | Ageing time 1000 hrs | 3000 hrs | 10,000 hrs | 18,500 hrs | 50,000 hrs | 90,000 hrs |
|---|---|---|---|---|---|---|
| 0 - 1 | 19 ± 1 | 18 ± 2 | 14 ± 5 | 80 ± 29 | 0 ± 0 | 0 ± 0 |
| 1 - 2 | 35 ± 1 | 39 ± 1 | 37 ± 2 | 56 ± 5 | 81 ± 13 | 53 ± 22 |
| 2 - 3 | - | 46 ± 1 | 43 ± 2 | 74 ± 7 | 50 ± 3 | 74 ± 8 |
| 3 - 4 | - | 60 ± 16 | 48 ± 5 | 80 ± 8 | 63 ± 3 | 74 ± 6 |
| 4 - 5 | - | - | - | 73 ± 3 | 79 ± 8 | 85 ± 6 |
| 5 - 6 | - | - | - | - | 83 ± 7 | 100 ± 14 |
| 6 - 7 | - | - | - | - | - | 146 ± 19 |

*Table 5.1:* Total reduction interfacial energy, in mJ $m^{-2}$, due to segregation of Ni, Mn and Si at the precipitate/matrix interface in the WV steel aged at 365 °C.

Whilst the increased reduction with size due to Si is small, the fractional increase is similar to that for Ni and Mn. This probably reflects the fact that there is less Si in the interface than Ni and Mn. The similarity between the reduction in interfacial energy due Fn and Mn reflects the similar bulk concentrations of the two (1.4 at.% and 1.38 at.% for Fn and Mn respectively).

Figure 5.12 showed that the interface width was increasing with ageing time. It is therefore interesting to see if there is any change in the reduction in interfacial energy with ageing time. Table 5.1 details the average total reduction in interfacial energy due to the segregation of Ni, Mn and Si with ageing time for a given precipitate size range after ageing at 365 °C.

This shows that, as for the 90,000 hr data shown in Figure 5.15, there is a trend for an increasing reduction in interfacial energy with precipitate size for all the ageing times. With the scatter in the data it is difficult to say decisively whether there is any trend with ageing time. However, just considering the 0 - 4 nm radius particles in the data from ageing up to 10,000 hrs, where there is least scatter in the data, there is no significant change in the reduction in interfacial energy with ageing time.

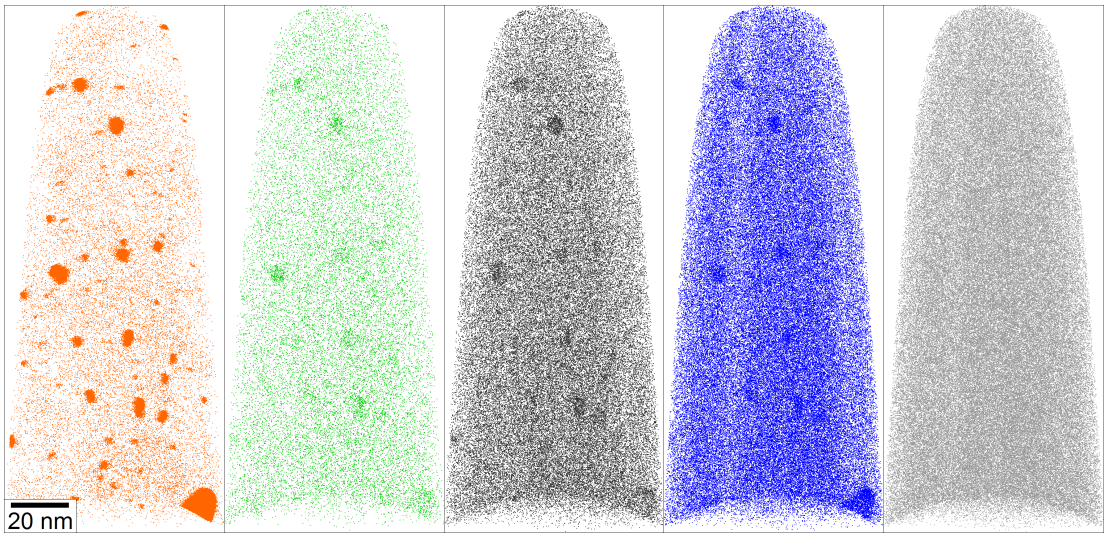


*(a)* Cu atoms. *(b)* Ni atoms. *(c)* Fn atoms. *(d)* Mn atoms. *(e)* Si atoms.

*Figure 5.16:* Atom maps showing the typical distribution of (a) Cu, (b) Ni, (c) Fn, (d) Mn and (e) Si atoms in the SG weld aged for 100,000 hrs at 330 °C.

### 5.2.2 SG Material

In order to understand the effect of Ni on the formation and evolution of Cu precipitates a low Ni weld with similar Cu, Mn and Si content has also been characterised with APT. From Section 5.1 the low Ni, SG weld aged under the same conditions as the high Ni, WV weld shows a much smaller hardness gain. This section will investigate some of the reasons for this. Atom maps from an SG weld aged at 330 °C and 365 °C for 100,000 hrs are shown in Figures 5.16 and 5.17.

In these atom maps and in much of the other data obtained from the SG material the larger precipitates in the 330 °C data, and virtually all the precipitates in the 365 °C data are adjacent to regions enriched C and Mo. This suggests that these have formed on dislocations or small carbides, indicating that homogeneous nucleation is much more difficult in these steels, particularly at lower supersaturations (higher temperature).

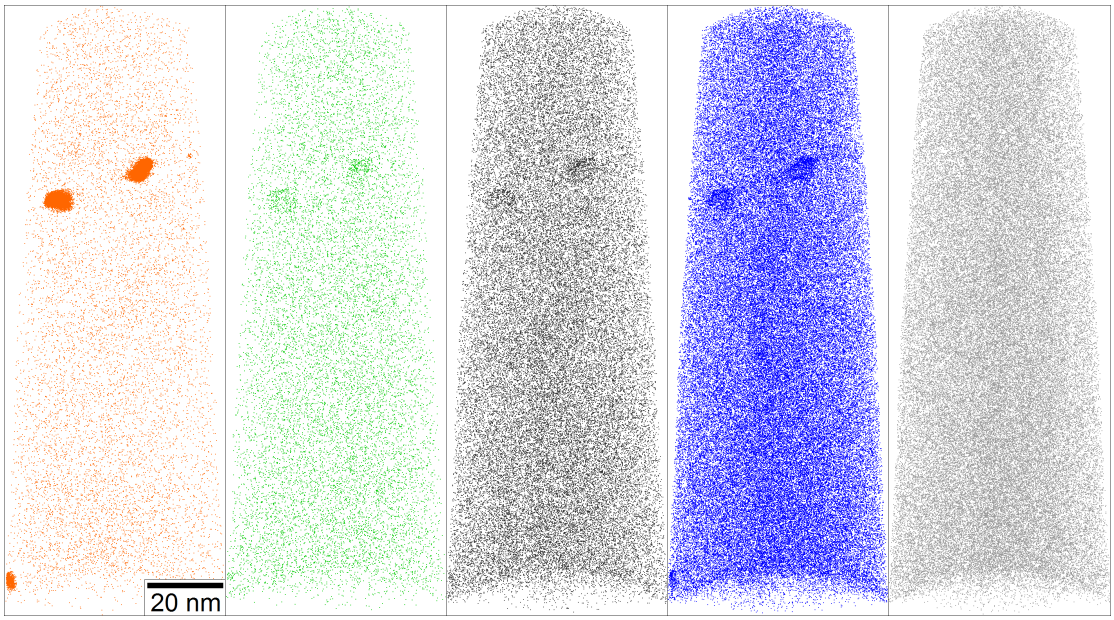


*(a)* Cu atoms. *(b)* Ni atoms. *(c)* Fn atoms. *(d)* Mn atoms. *(e)* Si atoms.

*Figure 5.17:* Atom maps showing the typical distribution of (a) Cu, (b) Ni, (c) Fn, (d) Mn and (e) Si atoms in the SG weld aged for 100,000 hrs at 365 °C. For clarity only 50 % of the Mn atoms are shown.

#### 5.2.2.1 Precipitate Size, Number Density and Volume Fraction

To compare the SG material with the WV material, it is useful only to select features from within the matrix and not those on dislocations. Precipitation on dislocations will be discussed in more detail in Section 5.4.3. Precipitate size, number density and volume fraction for the precipitates in the matrix of the SG steels aged for times up to 100,000 hrs are shown in Figure 5.18. As detailed in Section 4.2.1.2 Fn is included as a solute atom when cluster searching the SG steels despite the large proportion of Fe in the peak.

Comparing Figure 5.18 with Figure 5.4 it is clear that the precipitates in the SG material are much smaller, less numerous and have a lower volume fraction. In the SG material aged at 365 °C, the number density of precipitates after 100,000 hrs of ageing (0.04 x $10^{23}$ $m^{-3}$) is consistent with very few homogeneously nucleated precipitates in the matrix. This is around an order of magnitude less than in the WV steel after 90,000 hrs ageing at 365 °C and is consistent with the fact that Ni, in the presence of Mn, influences the formation of Cu precipitates. This will be discussed

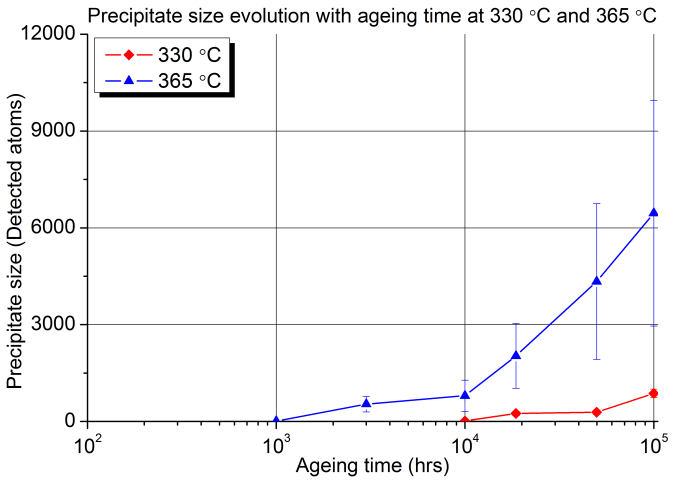


*(a)* Cluster size.

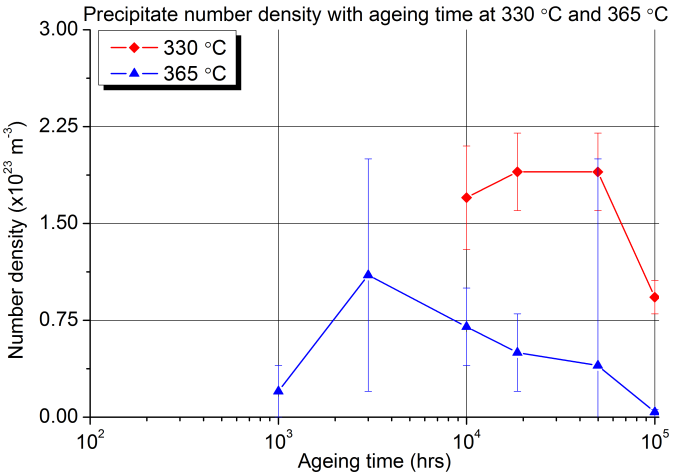


*(b)* Number density.

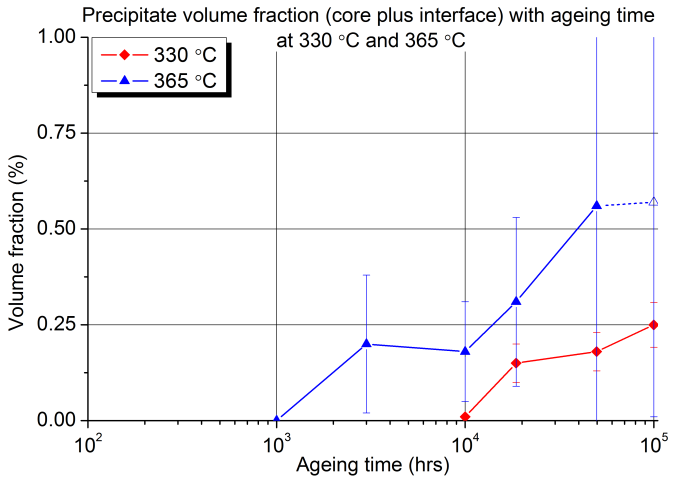


*(c)* Volume fraction.

*Figure 5.18:* (a) Cluster size, (b) Number density and (c) Volume fraction of the Cu-enriched precipitates in the SG specimens aged at 330 °C and 365 °C. Dashed line and unfilled point corresponding to 100,000 hrs of ageing at 365 °C is the estimated volume fraction from the precipitates in the matrix and at dislocations. 330 °C and 365 °C data for times up to 50,000 hrs from ECOPoSAP.

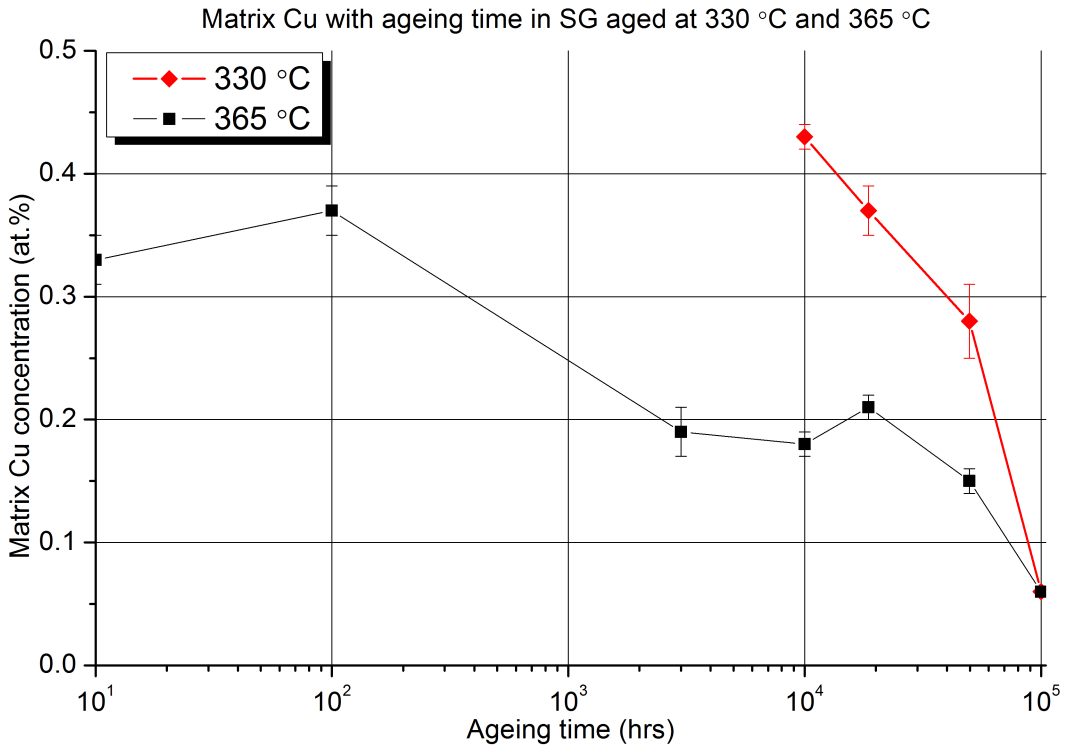


*Figure 5.19:* Measured matrix Cu content in the SG steels aged for times up to 100,000 hrs at 330 °C and 365 °C. 330 °C and 365 °C data for times up to 50,000 hrs from ECOPoSAP.

later in Section 7.3. It suggests that removing the Ni has reduced the driving force for precipitation, or at least made nucleation more difficult and is enough to give quite different microstructures.

#### 5.2.2.2 Matrix Composition

Understanding the influence of Ni, in the presence of Mn, on the solubility of Cu or the kinetics of its precipitation in Fe is important. This could also influence the parameters of KMC models which are used to predict the evolution of the mechanical properties of the RPV with time. The evolution of the matrix Cu level in the SG steel aged at 330 °C and 365 °C after ageing for times up to 100,000 hrs is shown in Figure 5.19.

Unlike the WV steel aged at 365 °C which appears to have approached the equilibrium Cu level after around 20,000 hrs of ageing, it is not possible to say whether either of the SG steels are reaching equilibrium. However, the matrix Cu levels in SG and WV

after the longest ageing times at 365 °C have reached approximately the same level (0.07 at.% in WV and 0.06 at.% in SG). For the SG steel aged at 330 °C, as with the WV steel, this has yet to reach equilibrium. After 90,000 hrs of ageing at 330 °C the matrix Cu level is 0.08 at.%, whereas after 100,000 hrs of ageing in the SG steel it is 0.06 at.%. What is evident is that after the same ageing time, the matrix Cu is less in the WV steel than the SG steel. The smaller interparticle distance in the WV steels mean diffusion distances are less and thus Cu depletes from the matrix more quickly. It is not possible to say whether Ni influences the solubility of Cu since the SG steels may not have reached equilibrium and hence the solubilities cannot be determined.

#### 5.2.2.3 Precipitate Composition

The composition of the precipitates in the SG steel was also investigated. As before, only homogeneously nucleated precipitates in the matrix will be considered here. However, the SG material aged at 365 °C for 100,000 hrs contained only 7 precipitates within the matrix and hence this data is provided for information only. It is unwise to draw firm conclusions from the limited number of precipitates and because very few precipitates were homogeneously nucleated. What is also evident in the mass spectra of the SG materials are peaks corresponding to Sn. Sn is present as an impurity in both the WV and SG steels with a nominal concentration of 0.007 at.%, but was not observed in the WV materials. Matrix, precipitate and interface concentrations of Sn are analysed in detail in Section 5.2.2.5. This section focusses on the main solute and Fe concentrations of precipitates in the SG steels. The concentration of the solutes Cu, Ni, Fn, Mn and Si in the precipitates in the SG steel after ageing for 100,000 hrs are shown in Figure 5.20.

After ageing at 330 °C the core compositions between SG and WV are slightly different. The SG material contains more Cu, which offsets their lower Mn and Ni content, which is not unexpected given the lower bulk Ni concentration. The Si content in the precipitates in SG is lower than in the equivalent WV precipitates

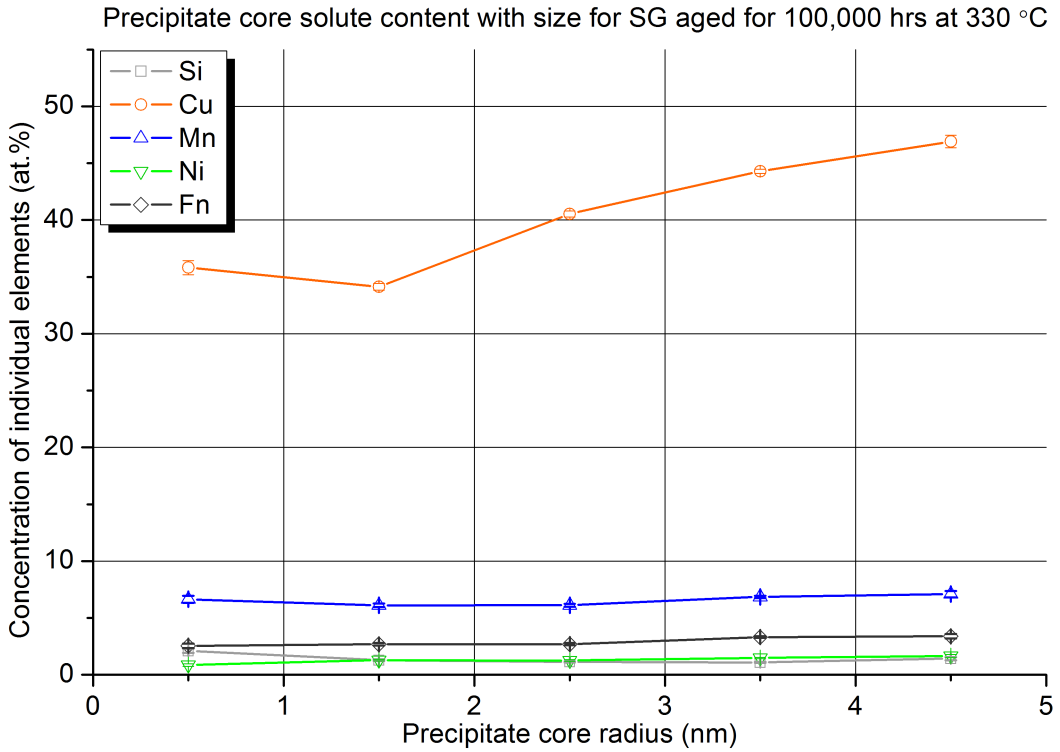


*(a)* Precipitate compositions with core radius after ageing for 100,000 hrs at 330 °C.

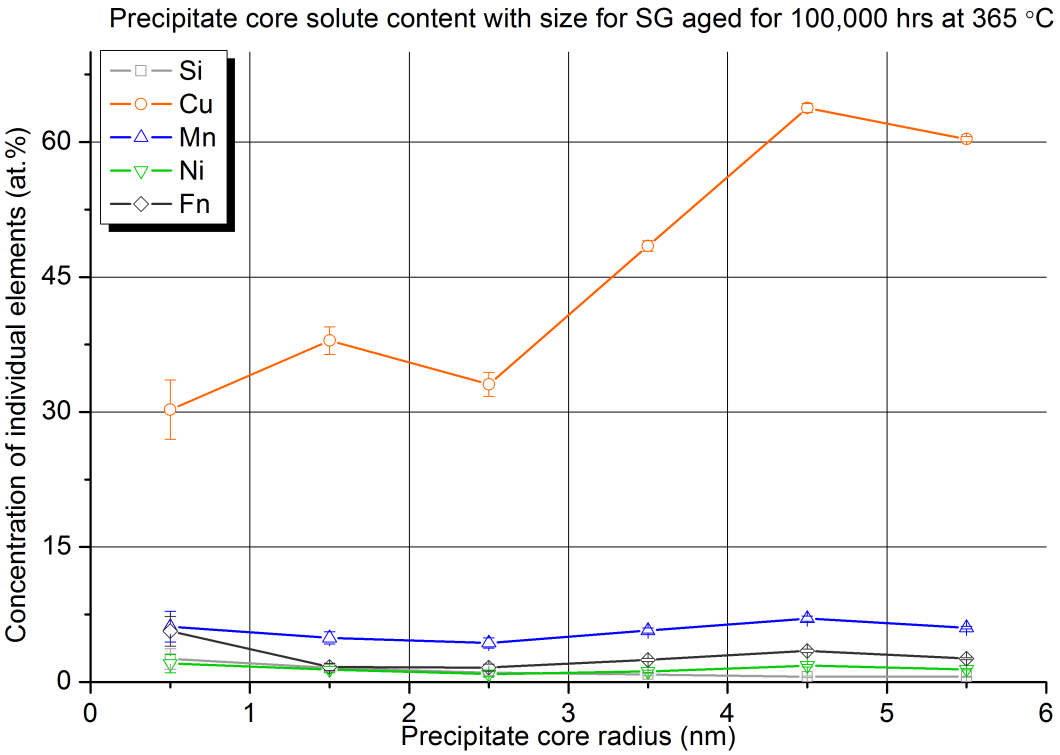


*(b)* Precipitate compositions with core radius after ageing for 100,000 hrs at 365 °C.

*Figure 5.20:* Mean precipitate core solute concentration observed in the SG steel aged at (a) 330 °C and (b) 365 °C for 100,000 hrs.

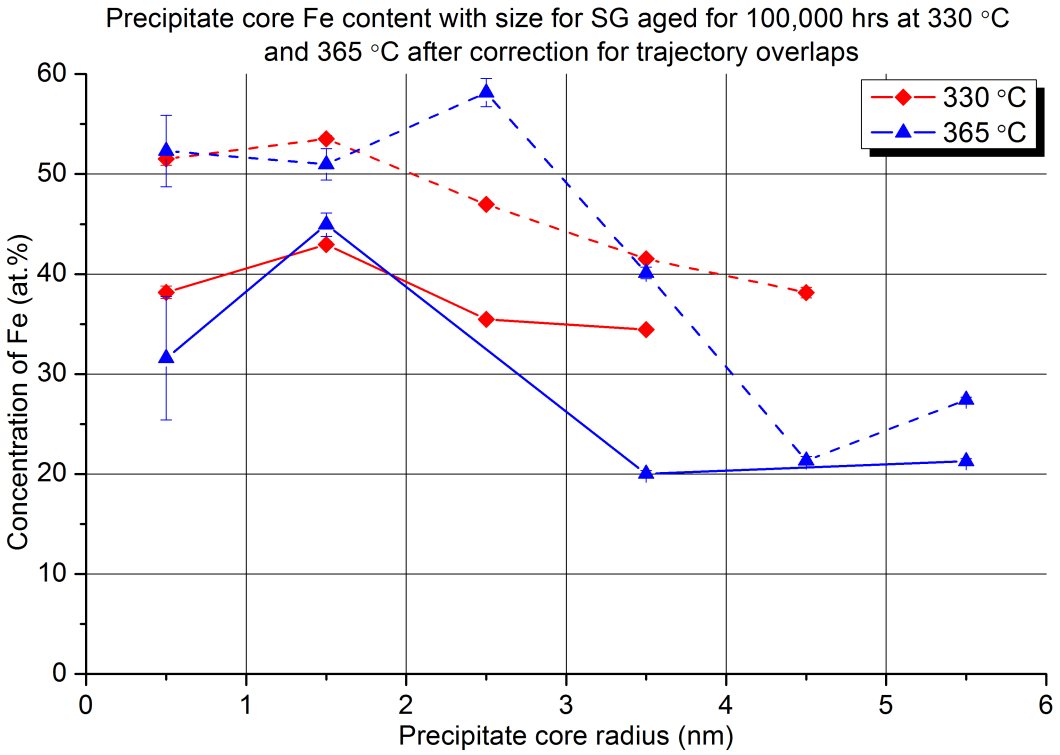


*Figure 5.21:* Variation of precipitate Fe content with core radius for the SG material aged for 100,000 hrs at 330 °C and 365 °C. Dashed lines show data before correction for trajectory overlaps.

and shows no significant change with size. Likewise, there is only a small variation in the Ni, Fn and Mn content with size, with the exception of the 0 - 1 nm precipitates which contain slightly more Si. It is much harder to draw significant comparisons with the 365 °C material given the small number of precipitates observed in the matrix. It appears that there is also no significant change in the mean Ni, Mn and Si content with size, which is consistent with all the other observations of WV and SG. The data do show a significant increase in Cu content with size, which must be offset by lower Fe contents. Within the scatter of the data from the low number of precipitates there does not seem to be any real difference in Ni, Mn and Si content of the precipitates with ageing temperature in the SG materials. The precipitates in the SG material aged at 365 °C contain less Mn, Ni and Fn than in the WV material. This could be due to a smaller influence of trajectory overlaps from the precipitate/matrix interface, which is consistent with the fact that there is much less interface segregation in the SG material.

The Fe content of the precipitates in the SG steel is shown in Figure 5.21. Again it is difficult to read too much into the data for 365 °C due to the limited number of precipitates[3]. The trend seen in the WV materials for higher Fe content with ageing temperature is not evident in the SG materials, but this could just be because of poor statistics. After applying the same correction for trajectory overlaps as for the WV data, it appears that the SG precipitates contain very similar levels of Fe, at least for the 330 °C data, where the statistics are best. The much larger drop in Fe content at the larger precipitate sizes after correction for trajectory overlaps compared to the WV material is most likely related to the small precipitate/matrix interface. This results in more Fe atoms being removed from the precipitate core than in the WV material which has a much larger interface.

#### 5.2.2.4 Matrix/Precipitate Interface

The extent of the interfacial segregation seen in the SG materials is much less than that observed in the WV material. The average interface widths for the WV and SG steels after 90,000 hrs and 100,000 hrs of ageing respectively are shown in Table 5.2.

| Material | Ageing time (hrs) | Interface width (nm) |
|---|---|---|
| WV 330 °C | 90,000 | 0.56 |
| WV 365 °C | 90,000 | 0.54 |
| SG 330 °C | 100,000 | 0.13 |
| SG 365 °C | 100,000 | 0.11 |

*Table 5.2:* Mean width of the precipitate/matrix interface for the WV and SG steels aged at 330 °C and 365 °C for 90,000 - 100,000 hrs.

As with the WV data, there is no change in the mean interface width with ageing temperature for the SG data. The smaller interface width is most likely related to the fact that there is less Ni in the bulk. This is reflected in the composition of the interface which shows less Ni in the SG material than the WV material, as shown in Figure 5.22.

[3] This is also the reason why there are no precipitates in the range 2 - 3 nm after correction. After removal of the Fe the radius of the cluster changes and in this case decreases enough to shift the

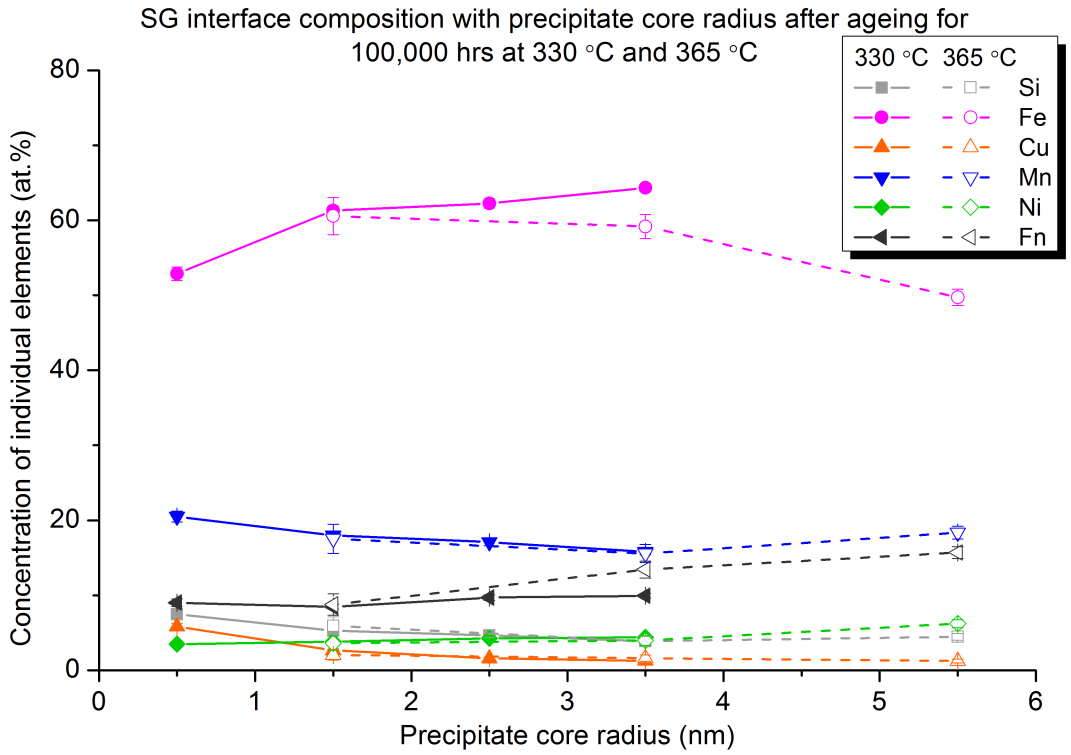


*Figure 5.22:* Interface composition of the SG material aged for 100,000 hrs at 330 °C and 365 °C.

The first point to note here is that there is around 10 % more Fe in the interface in the SG material aged at 330 °C, and 20 % more in the material aged at 365 °C, than in the WV materials at the same ageing temperatures. This is in contrast to the precipitate cores which contain similar levels of Fe. There is more Mn in the interface, ∼20 % in the SG material at 330 °C compared to ∼15 % in the WV material. The Fn content is slightly lower in the SG interface than in WV (∼10 % versus 13 - 14 % respectively for the 330 °C data). Likewise, for the Ni, this is 3 - 4 % versus 6 - 7 % respectively. There appears to be no change in interface composition with ageing temperature in the SG welds after ageing for 100,000 hrs.

The reduction in interfacial energy was also calculated for the precipitates in the SG steel. Tables 5.3 and 5.4 detail the reduction in interfacial energy due to the segregation of Ni, Fn, Mn and Si in the SG and WV steels aged at 330 °C for 100,000 hrs and 90,000 hrs respectively.

point from the 3 - 4 nm range to the 2 - 3 nm range.

| Size (nm) | Reduction in interfacial energy (mJ $m^{-2}$) | | | | |
|---|---|---|---|---|---|
| | Si | Ni | Mn | Fn | Total |
| 0 - 1 | 1.9 ± 0.2 | 0.8 ± 0.2 | 5.1 ± 0.5 | 2.2 ± 0.3 | 10.1 ± 1.1 |
| 1 - 2 | 2.2 ± 0.1 | 1.1 ± 0.1 | 6.1 ± 0.4 | 2.7 ± 0.2 | 12.1 ± 0.9 |
| 2 - 3 | 1.6 ± 0.3 | 1.4 ± 0.3 | 5.1 ± 0.7 | 2.8 ± 0.5 | 10.9 ± 1.8 |
| 3 - 4 | 2.1 ± 0.1 | 3.0 ± 0.1 | 8.1 ± 0.4 | 3.7 ± 0.3 | 16.7 ± 0.8 |

*Table 5.3:* Reduction in interfacial energy of the precipitates in the SG steel aged for 100,000 hrs at 330 °C.

| Size (nm) | Reduction in interfacial energy (mJ $m^{-2}$) | | | | |
|---|---|---|---|---|---|
| | Si | Ni | Mn | Fn | Total |
| 0 - 1 | 4.8 ± 0.2 | 6.2 ± 0.3 | 12.8 ± 0.6 | 13.5 ± 0.6 | 37.2 ± 1.6 |
| 1 - 2 | 6.6 ± 0.1 | 9.8 ± 0.1 | 20 ± 0.2 | 21.1 ± 0.2 | 57.5 ± 0.6 |
| 2 - 3 | 7.0 ± 0.2 | 11.9 ± 0.3 | 23.8 ± 0.7 | 25.1 ± 0.5 | 67.7 ± 1.7 |
| 3 - 4 | 5.0 ± 0.0 | 9.1 ± 0.0 | 18.4 ± 0.0 | 18.8 ± 0.0 | 51.2 ± 0.0 |
| 4 - 5 | 13.0 ± 0.0 | 25.8 ± 0.0 | 52.1 ± 0.0 | 49.3 ± 0.0 | 140.2 ± 0.0 |

*Table 5.4:* Reduction in interfacial energy of the precipitates in the WV steel aged for 90,000 hrs at 330 °C.

As might be expected given the smaller interface around the precipitates in SG, the reduction in interfacial energy is smaller than for the WV steel. The reduction in interfacial energy is around a third to a fifth in the SG steel compared to that in the WV steel. Unlike in the WV steel, there is limited effect of size on the reduction in interface energy in SG in the range 0 - 3 nm. There are signs of an increased reduction in energy as clusters grow larger than 3 nm. As reflected in the composition of the interface, where there was less Ni, the reduction in interface energy due to Ni is smaller than that of Mn.

#### 5.2.2.5 Presence of Sn

The presence of Sn in the SG material was noted by Sha et al.[64] and Morley[19]. This result is also observed here. Sn was not detected in the mass spectra of the WV steels. However, clear Sn peaks are observed in the SG mass spectra as shown in Figure 5.23. The strongest segregation of Sn to Cu-enriched precipitates is seen at precipitates on dislocations. Segregation of Sn to CRPs is also observed to precipitates

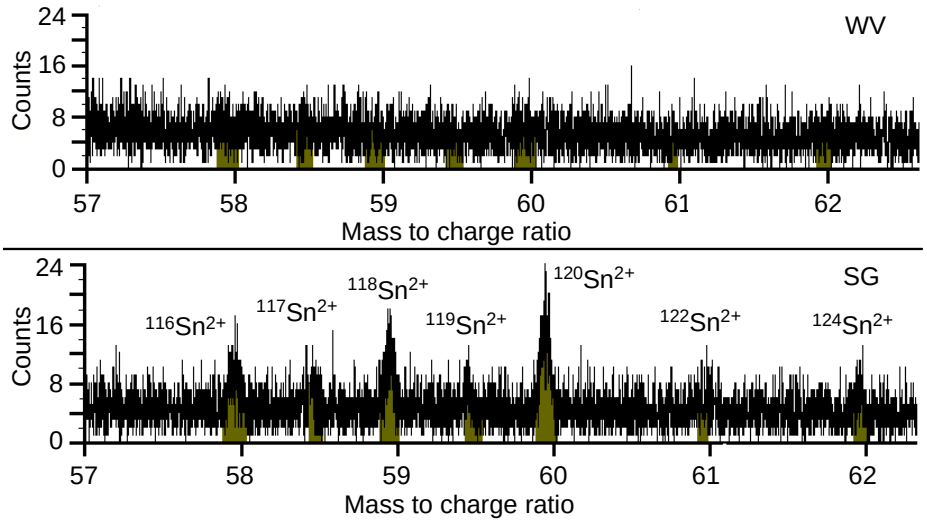


*Figure 5.23:* Sections of typical WV (top) and SG (bottom) mass spectra obtained after 90,000 hrs and 100,000 hrs of ageing at 330 °C.

in the matrix as shown in Figure 5.24.

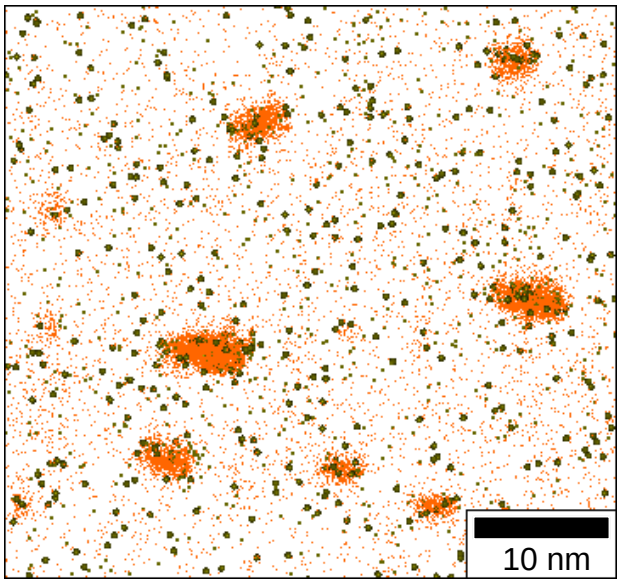


*Figure 5.24:* Section of an atom map of an SG steel aged for 100,000 hrs at 330 °C. Orange - Cu atoms, dark yellow spheres - Sn atoms.

The matrix Sn concentration is subject to significant noise due to the low number of counts in the Sn peaks and possibly some influence from the overlapping mass peaks of Ni and Fn with those of Sn at 58, 60, 61 and 62. The latter seems unlikely given that no Ni atoms are observed at 64, although a small Fe peak at 56 is observed so some of the 58 peak (corresponding to $^{116}Sn^{2+}$) may be Fe atoms. After correction for background noise (see Appendix C) the calculated isotope ratios closely match

those expected for Sn, indicating peak overlaps do not have a significant influence on the Sn concentration[4]. Noise corrected matrix concentrations of Sn were found to be 0.0024 ± 0.0001 at.%. The concentration of Sn in the core and interface of the matrix precipitates is shown in Table 5.5[5].

| Core radius | Sn concentration (%) | | |
|---|---|---|---|
| | Core | Interface | Whole |
| 0 - 1 nm | 0.3 ± 0.1 | 0.3 ± 0.1 | 0.2 ± 0.1 |
| 1 - 2 nm | 0.6 ± 0.1 | 0.3 ± 0.1 | 0.5 ± 0.1 |
| 2 - 3 nm | 1.0 ± 0.1 | 0.6 ± 0.1 | 0.8 ± 0.1 |
| 3 - 4 nm | 1.1 ± 0.1 | 0.6 ± 0.1 | 1.0 ± 0.1 |

*Table 5.5:* Sn concentration in the precipitates in SG aged for 100,000 hrs at 330 °C.

The concentration of Sn in the precipitates in SG aged at 330 °C increases with precipitate size. The percentage of the total number of Sn atoms which are in precipitates after ageing for 100,000 hrs at 330 °C is 61 %. This is in line with the value obtained by Morley[19] from the material aged at 365 °C for 50,000 hrs. It is difficult to draw firm conclusions for 365 °C due to the small number of precipitates but there does not appear to be any trend in Sn content with size. At 365 °C the percentage of the total number of Sn atoms which are in Cu-enriched precipitates was estimated to be 77 %. This is a substantial increase on the 20 - 60 % Morley estimated after 50,000 hrs of ageing.

## 5.3 Microstructural Evolution in the Low Cu Materials

As discussed in Section 5.1 some of the low Cu materials have shown apparent softening after ageing at different temperatures. One such steel was the low Cu high Ni, WF steel. This appears to have softened after 100,000 hrs of ageing at 330 °C but shown no significant change in hardness at 365 °C or 405 °C. The difference in

[4] See Appendix C for details of the calculated isotope ratios of the Sn peaks.
[5] The Sn concentration in the precipitates was not background corrected.

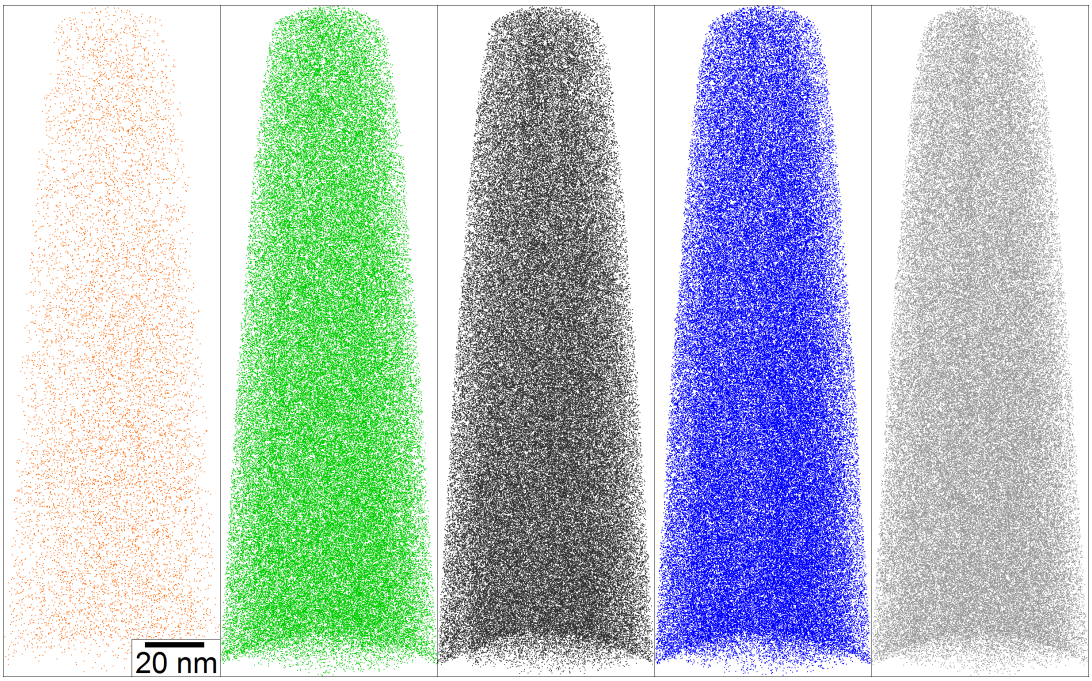


*(a)* Cu atoms. *(b)* Ni atoms. *(c)* Fn atoms. *(d)* Mn atoms. *(e)* Si atoms.

*Figure 5.25:* Atom maps showing the typical distribution of (a) Cu, (b) Ni, (c) Fn, (d) Mn and (e) Si atoms in the WF weld aged for 100,000 hrs at 330 °C. For clarity only 50 % of the Fn, Mn and Si atoms are shown.

hardness has been investigated by comparing the WF material aged for 100,000 hrs at 330 °C with that aged for 90,000 hrs at 405 °C. This steel is also the most likely low Cu candidate material for precipitating Ni-Mn-Si phases.

### 5.3.1 WF Materials

The material aged at 405 °C showed no significant change in hardness from the unaged condition. In contrast, the material aged at 330 °C has shown some significant softening. APT analysis has been carried out on the material aged at 330 °C for 100,000 hrs and after 90,000 hrs of ageing at 405 °C. Typical atom maps are shown in Figures 5.25 and 5.26.

There is no visible precipitation of any species within the matrix of these materials at either ageing temperature studied. This is to be expected given that there is no increase in hardness of these materials and the formation of any precipitates would

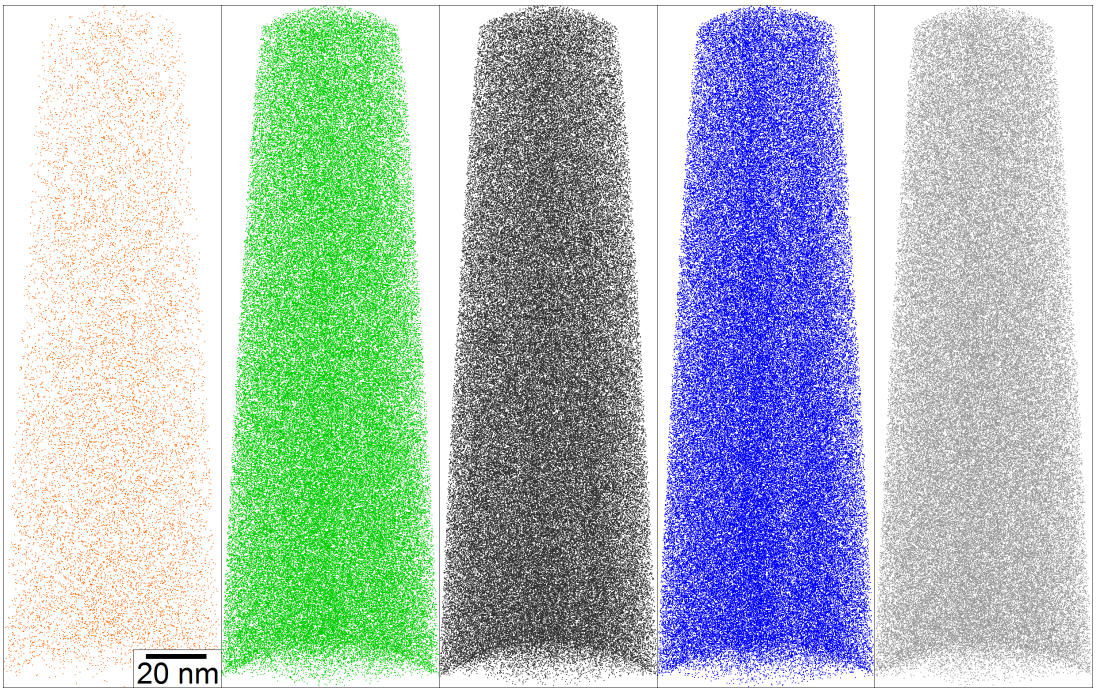


*(a)* Cu atoms. *(b)* Ni atoms. *(c)* Fn atoms. *(d)* Mn atoms. *(e)* Si atoms.

*Figure 5.26:* Atom maps showing the typical distribution of (a) Cu, (b) Ni, (c) Fn, (d) Mn and (e) Si atoms in the WF weld aged for 90,000 hrs at 405 °C. For clarity only 50 % of the Fn, Mn and Si atoms are shown.

most likely increase the hardness. Performing a cluster search (with solutes Cu, Ni, Mn, Si and Fn) on the data indicates there are a small number of fine scale precipitates present in both ageing conditions but in neither case are these above the number expected from a random distribution. In any case these precipitates do not contain significant proportions of the total solute in the system.

There are three possible explanations which could cause softening of a material; grain growth, coarsening of existing hardening features (precipitates or carbides) or a loss of Solid Solution Strength (SSS). These were discussed by Morley[19] when investigating softening of SP. The effect seen here in the WF steel is a temperature effect, with softening occurring at the lowest temperature. Thus the only feasible explanation seems to be the loss of SSS. This could occur through precipitation on grain boundaries and/or from segregation of elements to them. Examining differences in the matrix composition of the two steels may highlight whether this is occurring here. Table 5.6 details the noise corrected matrix composition of the WF steels aged for 100,000 hrs

| Element | Expected | 330 °C | 405 °C |
|---|---|---|---|
| Cu | 0.02 | 0.02 | 0.03 |
| Ni | 0.52 | 0.48 | 0.51 |
| Fn | 1.38 | 1.30 | 1.36 |
| Mn | 1.43 | 1.28 | 1.27 |
| Si | 1.05 | 1.02 | 0.99 |
| C | 0.18 | 0.01 | 0.004 |
| Mo | 0.20 | 0.17 | 0.16 |
| P | 0.016 | 0.02 | 0.01 |
| Cr | 0.10 | 0.09 | 0.08 |
| Fe | 94.95 | 95.61 | 95.59 |

*Table 5.6:* Noise corrected matrix composition of the WF steel aged for 100,000 hrs at 330 °C and 90,000 hrs at 405 °C. (Errors are less than 0.001 % for all elements.)

at 330 °C and 90,000 hrs at 405 °C. Noise correction was performed using the same method as for Sn detailed in Appendix C.

If the origin of the differences in hardening are due to the loss of SSS then it is differences between the two aged materials which is of importance, rather than differences from the initial bulk composition, which is included for reference in Table 5.6. A number of solutes display reductions from their expected bulk values after both ageing conditions. However, there are very few solute species which show any change in concentration between the two aged materials outside of a few hundredths of a percent. Fn shows the largest discrepancy between the two ageing conditions. This is still a difference of only 0.06 at.% but this is statistically significant.

It is unlikely that the small differences in the matrix composition would account for the observed difference in hardness. However, in the material aged at 330 °C a low-angle grain boundary has been observed, and this will be detailed in Section 5.4.2. Further analysis using TEM and optical microscopy is required to investigate larger areas of material to identify the reason for the observed softening.

## 5.4 Precipitation and Segregation to Grain Boundaries and Dislocations

So far this chapter has dealt with Cu-enriched precipitates which were homogeneously nucleated in the matrix which is the primary source of hardening in these steels. Precipitation on dislocations will also impact on dislocation motion as this will lead to some dislocation pinning. Precipitation at grain boundaries and dislocations more closely represents the conditions found in irradiated materials where there are many heterogeneous nucleation sites. Precipitates will nucleate more easily here and potentially provide an insight into what may occur in the matrix after even longer ageing times than have been studied in this project.

The results presented in this section are from grain boundaries and dislocations which have been found randomly during the course of this project and do not necessarily give the complete picture of what is occurring with ageing. Nonetheless, the results present some interesting phenomena which have not previously been observed in these materials. They also provide a starting point for a more detailed and systematic investigation of grain boundary evolution in the future.

### 5.4.1 High-Angle Grain Boundaries

Several specimens of the WV material have contained sections of high-angle grain boundaries, these have shown precipitation, segregation or a combination of the two. Three samples contained grain boundaries, two after ageing for 50,000 hrs at 365 °C and one after ageing for 90,000 hrs at 405 °C. These boundaries have been found randomly over the course of analysing many samples and, as such, the mis-orientation of the boundaries and their orientation within the sample could not be controlled. Hence, the results presented in this section may come from boundaries of differing mis-orientation which could account for some of the differences observed. Despite repeated efforts with the preparation of specimens by FIB, it has not been possible to

| Element | Monolayer excess (%) | |
|---|---|---|
| | 365 °C 50,000 hrs | 405 °C 90,000 hrs |
| C | 18.60 ± 0.56 | 11.38 ± 0.54 |
| Mn | 27.71 ± 0.80 | 25.68 ± 1.18 |
| Cr | 1.33 ± 0.05 | 0.46 ± 0.06 |
| Mo | 7.40 ± 0.21 | 7.86 ± 0.36 |
| P | 4.73 ± 0.13 | 8.63 ± 0.42 |
| Ni | 5.36 ± 0.27 | 4.32 ± 0.25 |
| Fn | 10.15 ± 0.52 | 8.13 ± 0.54 |
| Si | 3.36 ± 0.32 | 1.79 ± 0.18 |
| Cu | - | 0.31 ± 0.04 |

*Table 5.7:* Calculated Gibbsian interfacial excesses of atoms at the observed grain boundaries in the WV material aged for 50,000 hrs at 365 °C and 90,000 hrs at 405 °C in terms of percentage monolayer coverage of the close packed (110) planes in bcc Fe.

obtain a grain boundary in the unaged WV sample to provide a reference calibration.

#### 5.4.1.1 Solute Segregation

Solute segregation was observed at all the boundaries but in two there was an absence of precipitation. These were in the WV materials aged for 50,000 hrs at 365 °C and 90,000 hrs at 405 °C. The grain boundary observed in the 405 °C specimen is shown in Figures 5.27a to 5.27i.

From these atom maps it is clear that several species, notably C, Mn, Mo, Ni, Fn, P are heavily segregated to the boundary. For some species, namely Si, Cr and Cu the segregation is more difficult to see visually. Similar atom maps are obtained from the grain boundary in the WV material aged at 365 °C for 50,000 hrs. It is possible to quantify the level of segregation at the boundary by calculating the Gibbsian excess of each element at the boundary. These were calculated according to the method of Miller and Smith[101], taking the number of atoms in one monolayer of the close packed (110) plane in bcc Fe as 1.72 x $10^{19}$ atoms $m^{-2}$. The calculated excesses in terms of monolayer coverage are tabulated in Table 5.7.

By calculating the Gibbsian excess it is possible to detect segregation which is not as obvious from the atom maps in Figure 5.27. This shows that there is a small excess

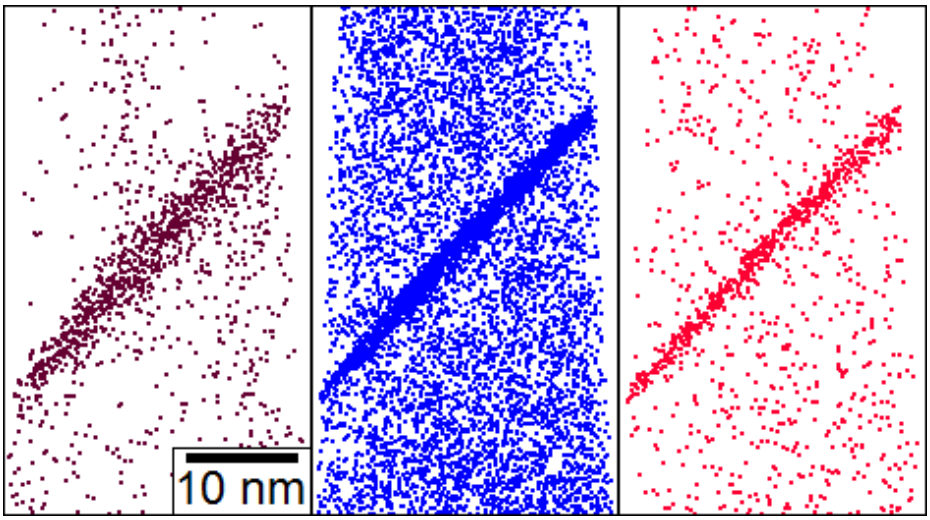


*(a)* C atoms. *(b)* Mn atoms. *(c)* Mo atoms.

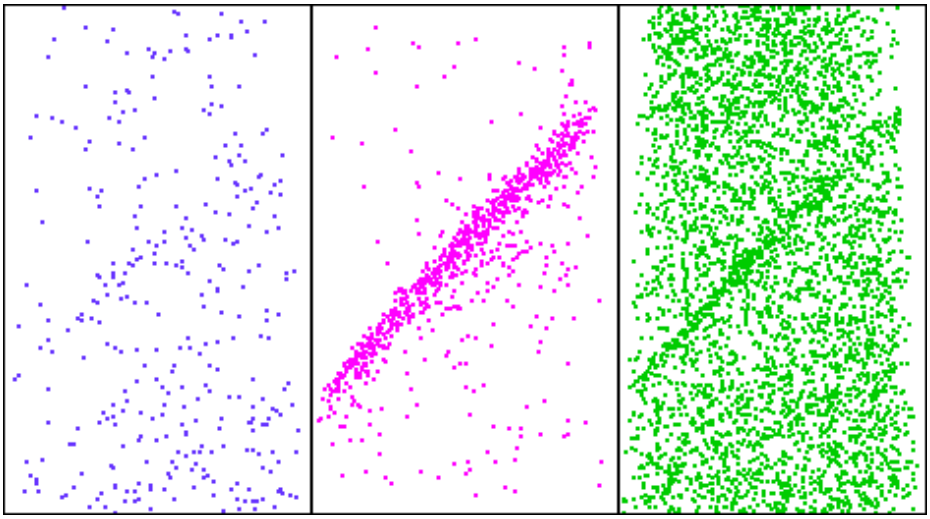

*(d)* Cr atoms. *(e)* P atoms. *(f)* Ni atoms.

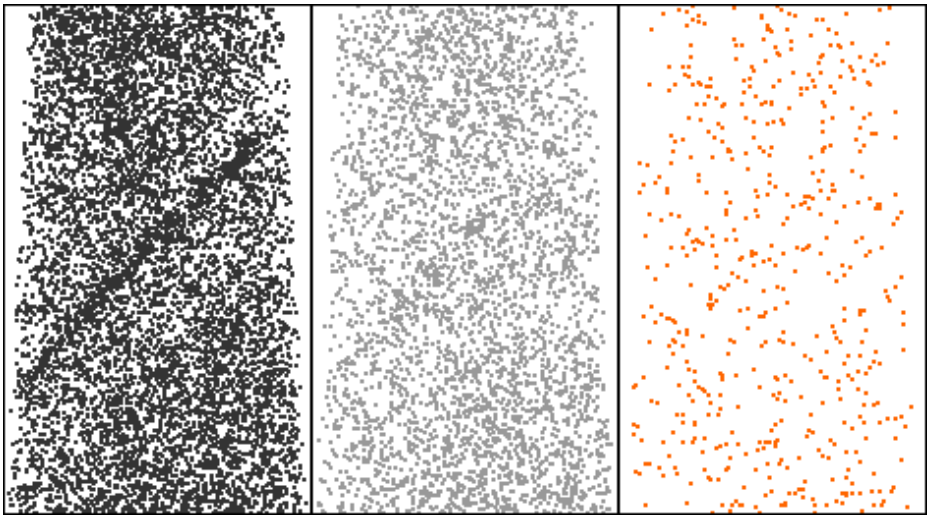

*(g)* Fn atoms. *(h)* Si atoms. *(i)* Cu atoms.

*Figure 5.27:* Grain boundary showing solute segregation of (a) C, (b) Mn, (c) Mo, (d) Cr, (e) P, (f) Ni, (g) Fn, (e) Si and (f) Cu from the WV material aged at 405 °C for 90,000 hrs.

of Cu atoms at the boundary at 405 °C, whereas a depletion of Cu was found in the boundary at 365 °C. Additionally, smaller excesses of Cr and Si were observed at 405 °C. In nearly all cases there is a reduction in the level of segregation at 405 °C compared to that at 365 °C, despite ageing for longer at higher temperature. The exception here is P, which nearly doubles, and Cu which was depleted at 365 °C. Although Mo shows a small increase, this is not statistically significant. The increase in P content in the 405 °C sample is consistent with the lower C content due to site competition and a repulsive interaction between C and P[104, 158].

It is thought that the segregation of a variety of elements to the boundaries at both temperatures is due to a co-segregation process similar to that of temper embrittlement as described in the pioneering work of Guttmann[104, 159]. Most likely this is initiated by C, which segregates to the boundaries during the post-weld heat treatments and improves the cohesion of the grain boundaries. This segregation of C drives Mo, Cr and Mn to the boundaries as all have strong positive interactions with C. These elements can then drive more C to the boundary, whilst the level of P at the boundary is enhanced by its strong attraction with Mo[6]. P can in turn cause segregation of Ni, along with more Mn and Cr. Ni along with Mn can attract Si as they also have positive interactions with one another. The presence of Si is interesting since it has a repulsive interaction with C[160]. It is thought the presence of Ni and Mn is the reason why Si is present and that its low concentration is due to the high levels of C at the boundary.

#### 5.4.1.2 Precipitation

One grain boundary observed after 50,000 hrs of ageing at 365 °C in the WV material shows Cu and non-Cu precipitation. Similar solute segregation to that described in the previous section is also seen. Figure 5.28 shows the atom map of the dataset containing the boundary of interest along with three precipitates which exhibit non-

[6] P is a strong interface segregant and would segregate to the boundary in the absence of any other elements.

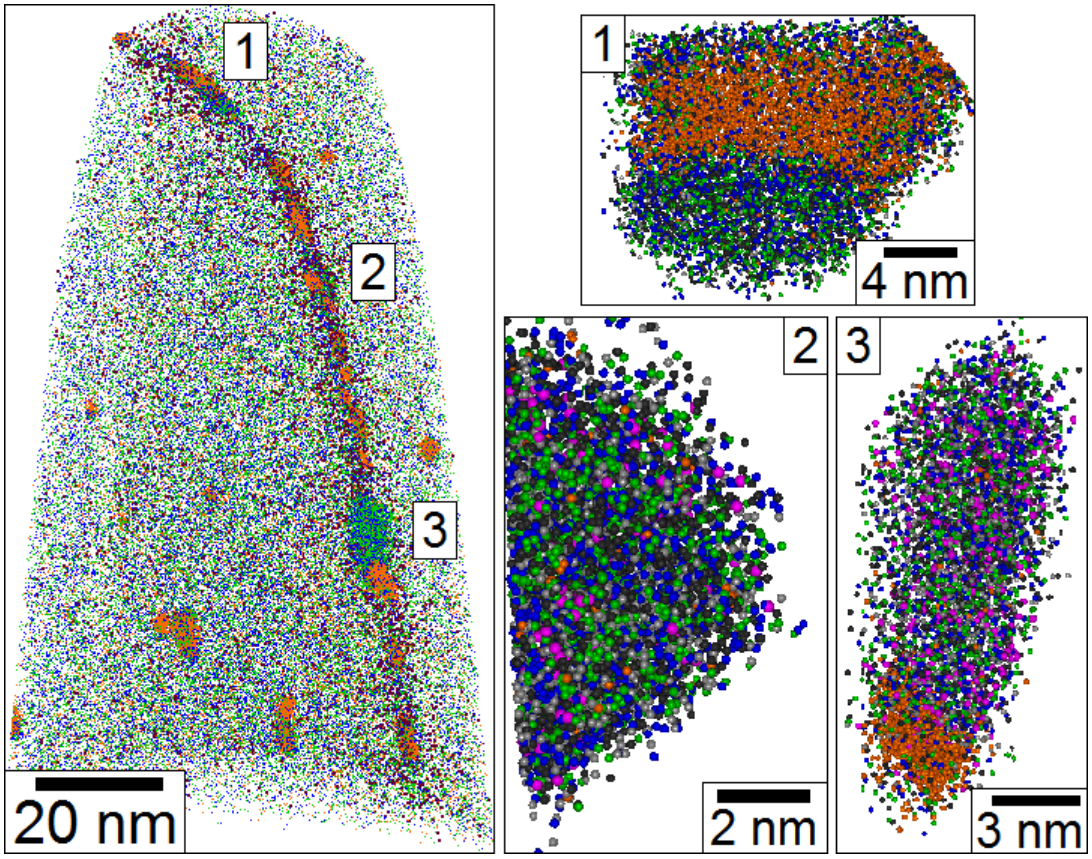


*Figure 5.28:* Atom map of WV aged for 50,000 hrs at 365 °C showing a grain boundary containing Cu and non-Cu precipitation. Dataset oriented such that the boundary is side on (into plane of paper). Images 1 - 3 show three precipitates from the boundary in more detail. Colours: C - brown, Cu - orange, Ni - green, Mn - blue, Fn - dark grey, Si - light grey, P - magenta.

Cu precipitation.

The first thing to note here is that with the exception of precipitate 1 in Figure 5.28, the precipitates of interest were at the edge of the analysis volume and are therefore not whole. Two of the Ni-Mn-Si features in Figure 5.28 are associated with Cu-enriched precipitates. This is also thought to be the case with precipitate 2, with the associated Cu-enriched precipitate lying outside the analysed volume. It is not possible to definitively say whether the Cu-enriched precipitate or Ni-Mn-Si feature nucleated first. It is also worth noting that precipitate 1 is very flat compared to 2 and 3, indicating it is likely to be constrained by the boundary.

The composition of the three precipitates from Figure 5.28 is shown in Table 5.8. The associated Cu rich regions have been excluded from the analysis to get the composition

| Precipitate | Si | Fe | Cu | Ni | Mn | P | Fn | Other |
|---|---|---|---|---|---|---|---|---|
| 1 | 3.1 ± 0.1 | 46.7 ± 0.4 | 1.4 ± 0.1 | 8.2 ± 0.2 | 22.4 ± 0.3 | 0.1 ± 0.02 | 17.7 ± 0.3 | 0.4 ± 0.1 |
| 2 | 11.0 ± 0.3 | 44.7 ± 0.4 | 0.5 ± 0.1 | 9.7 ± 0.3 | 11.9 ± 0.3 | 1.5 ± 0.1 | 19.7 ± 0.4 | 1.0 ± 0.1 |
| 3 | 12.4 ± 0.2 | 36.1 ± 0.3 | 0.5 ± 0.1 | 10.7 ± 0.2 | 15.4 ± 0.2 | 1.3 ± 0.1 | 22.5 ± 0.2 | 1.2 ± 0.1 |

*Table 5.8:* Composition of the Ni-Mn-Si features observed at the grain boundary in Figure 5.28.

of the Ni-Mn-Si precipitates.

The composition of the features in Table 5.8 show some scatter between them. However, they all contain significant quantities of Ni and Mn and in precipitates 2 and 3 significant Si too. All precipitates contain very small amounts of Cu. Precipitates 2 and 3 also contain high levels of P, which in the matrix is nominally present at only 0.018 at.%. As discussed in Section 5.4.1.1 P has a strong interaction with Ni, which may explain its enhanced presence in these particles. Despite it being a strong interface segregant, it is distributed fairly uniformly throughout the Ni-Mn-Si features rather than at the interface. As with the Cu-enriched precipitates there are significant quantities of Fe in these precipitates. The Fe content of these precipitates is at least partly expected to be influenced by Fe from trajectory overlaps, as is the case for Cu particles.

### 5.4.2 Low-Angle Grain Boundaries

In the WF material aged for 100,000 hrs at 330 °C a dislocation network thought to form part of a low angle grain boundary was observed. Implicitly, dislocations are not detectable in APT datasets since the small changes in the crystal lattice are not observable. Nonetheless, the presence of dislocations can be inferred from lines enriched in C and Mo, which segregate to the dislocation cores. Atom maps showing the distribution of Cu, Ni, Fn, Mn, Si, C and Mo are shown in Figure 5.29. An atom map showing a portion of this dataset containing a dislocation and two Ni-Mn-Si

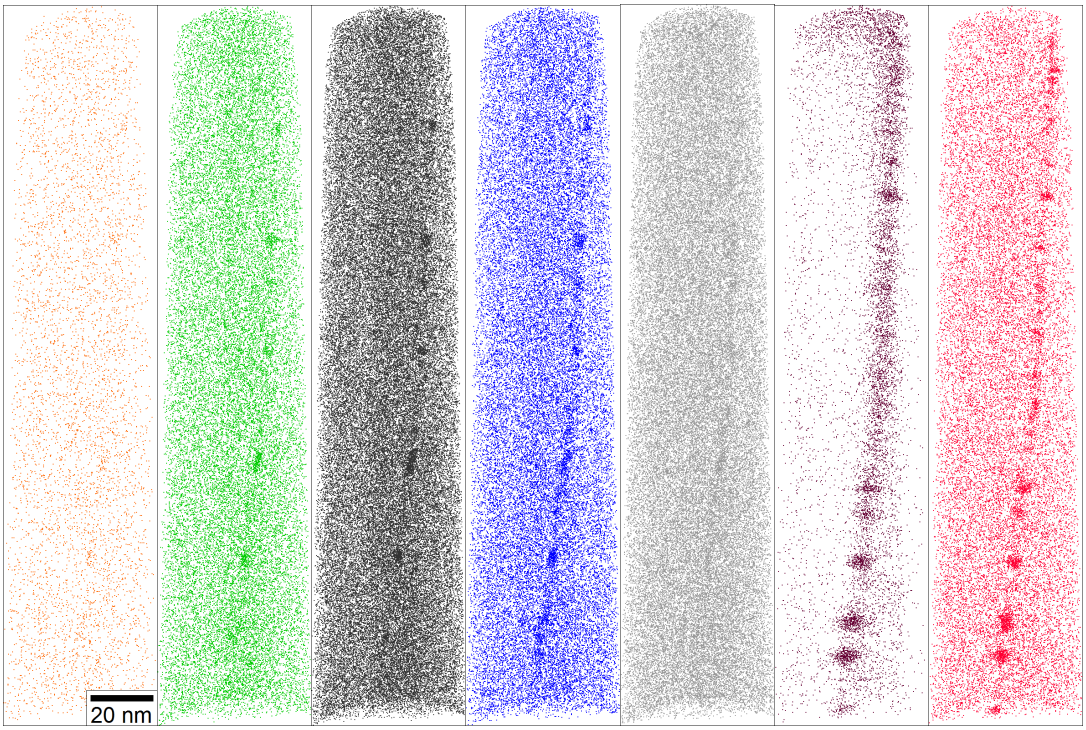


*(a)* Cu. *(b)* Ni. *(c)* Fn. *(d)* Mn. *(e)* Si. *(f)* C. *(g)* Mo.

*Figure 5.29:* Atom maps showing the distribution of (a) Cu, (b) Ni, (c) Fn, (d) Mn (e) Si, (f) C and (g) Mo atoms in a WF weld specimen aged for 100,000 hrs at 330 °C containing a low angle grain boundary. Dataset oriented such that the boundary is side on (into plane of paper). For clarity only 50 % of the Ni, Fn and Si atoms and 25 % of the Mn atoms are shown.

precipitates is shown in Figure 5.30.

The mean size and composition of these features are detailed in Table 5.9. These features are much smaller than those observed at the high angle boundary shown in Section 5.4.1, which perhaps reflects the fact that dislocations are less favourable nucleation sites than high-angle grain boundaries or that there is some influence of Cu precipitates or a combination of the two. These precipitates contain significant quantities of Fe as was found in those at high-angle grain boundaries. These contain similar Mn levels, less Si and more Ni and Fn, but the low number of precipitates makes comparison difficult. Additionally, these precipitates do not contain any P, which was observed at levels around 1.5 at.% in two of the precipitates at the high-angle boundary.

The presence of Ni-Mn-Si precipitates at grain boundaries in low Cu steels has

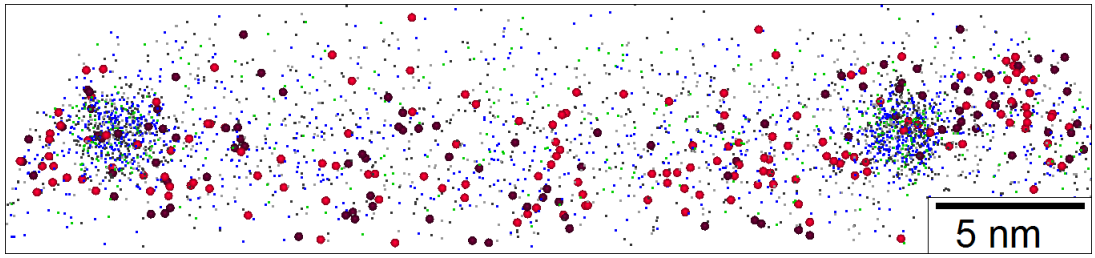


*Figure 5.30:* Section of the dataset shown in Figure 5.29 showing a dislocation with two associated Ni-Mn-Si precipitates. Colour legend, Cu - orange, Ni - green, Mn - blue, Fn - dark grey, Si - light grey, C - brown, Mo - red.

| Size (atoms) | Si | Fe | Cu | Ni | Mn | P | Fn |
|---|---|---|---|---|---|---|---|
| 1600 | 4.7 | 58.1 | 0.7 | 6.4 | 15.7 | - | 14.1 |
| ± 250 | ± 0.2 | ± 0.4 | ± 0.1 | ± 0.2 | ± 0.3 | - | ± 0.3 |

*Table 5.9:* Mean size and composition of the Ni-Mn-Si precipitates observed at a dislocation forming part of a low-angle grain boundary in the WF material aged for 100,000 hrs at 330 °C.

interesting consequences, in terms of understanding whether LBPs form in thermally aged steels. This will be discussed further in Chapter 7.

### 5.4.3 Dislocations

Several specimens in both the SG and WV material contained dislocations. The specimens containing dislocations were; WV aged for 3000 hrs and 90,000 hrs at 365 °C and SG aged for 100,000 hrs aged at 330 °C and 365 °C. This should give some insight into the evolution of precipitates on dislocations with ageing time in the WV material and with ageing temperature in the SG steel.

#### 5.4.3.1 WV Material

Figure 5.31 shows precipitates on a dislocation in the material aged for 3,000 hrs at 365 °C. This clearly shows the segregation of both C and Mo to the core of the dislocation, most likely in the tensile region below the extra half plane, with the Cu precipitates forming in the compressive region above the dislocation core.

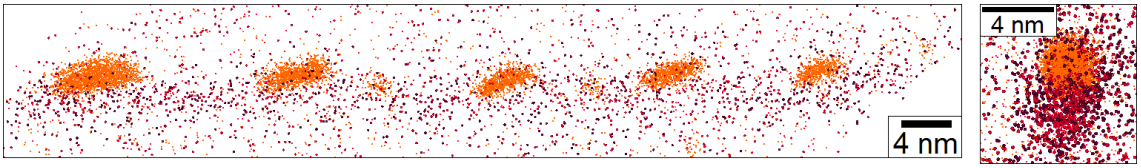


*(a)* Atom map of a dislocation showing Cu, C and Mo atoms, side on and end on views.

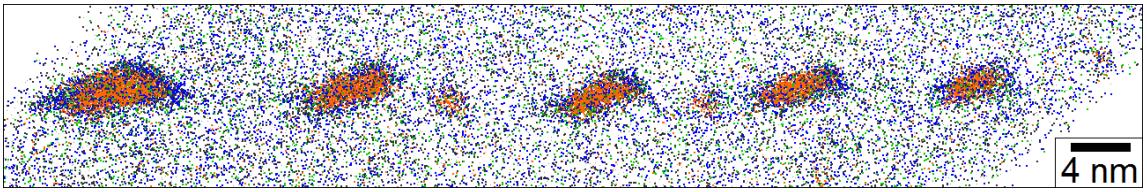


*(b)* Atom map of the same dislocation showing Cu, Ni, Fn, Mn and Si atoms.

*Figure 5.31:* Atom maps showing a dislocation observed in a dataset after 3000 hrs of ageing at 365 °C. (a) showing Cu, Mo and C atoms along the dislocation and end on, (b) showing Cu, Ni, Fn, Mn and Si atoms in the region around the dislocation. Colour legend, Cu - orange, Ni - green, Mn - blue, Fn - dark grey, Si - light grey, C - brown, Mo - red.

| Ageing time | | Average size (Det. atoms) | Core size (Det. atoms) | Interface width (nm) |
|---|---|---|---|---|
| 3000 hrs | Matrix | 1170 ± 49 | 625 ± 29 | 0.35 ± 0.01 |
| | Dislocation | 3115 ± 670 | 1744 ± 403 | 0.53 ± 0.03 |
| 90,000 hrs | Matrix | 11854 ± 1223 | 7868 ± 849 | 0.54 ± 0.03 |
| | Dislocation | 11115 ± 3068 | 6922 ± 2011 | 0.66 ± 0.09 |

*Table 5.10:* Average precipitate size and interface widths for the precipitates observed in the matrix and on dislocations in the WV steels aged for 3000 hrs and 90,000 hrs at 365 °C.

A comparison between precipitates observed on dislocations with those in the matrix is shown in Tables 5.10 and 5.11 for the WV steel aged at 365 °C for times of 3000 hrs and 90,000 hrs.

After 3000 hrs the precipitates on dislocations contain, on average, more than twice the number of atoms than those in the matrix (equating to a radius approximately 0.8 nm larger) and have a wider interface. After 90,000 hrs both the precipitate size and the interface width are within the margins of error.

Comparison of the precipitate core compositions between precipitates on dislocations and the matrix, after 3000 hrs indicates that precipitates on dislocations contain more Cu, Ni, Fn and Mn. Si content shows no change between the two and the Fe content is lower in the particles on dislocations. At 90,000 hrs, a slightly different trend is

| Ageing time | | Si | Fe | Cu | Ni | Mn | Fn | P |
|---|---|---|---|---|---|---|---|---|
| 3000 hrs | M | 2.0 ± 0.02 | 48.2 ± 0.1 | 32.9 ± 0.1 | 2.9 ± 0.03 | 7.6 ± 0.04 | 6.2 ± 0.04 | 0.04 ± 0.003 |
| | D | 1.9 ± 0.1 | 39.4 ± 0.3 | 37.7 ± 0.3 | 3.5 ± 0.1 | 9.9 ± 0.2 | 6.9 ± 0.2 | 0.03 ± 0.01 |
| 90,000 hrs | M | 2.9 ± 0.02 | 25.4 ± 0.1 | 40.9 ± 0.1 | 5.2 ± 0.03 | 14.4 ± 0.04 | 10.9 ± 0.04 | 0.04 ± 0.003 |
| | D | 2.1 ± 0.1 | 22.7 ± 0.2 | 47.3 ± 0.2 | 4.6 ± 0.1 | 13.3 ± 0.1 | 9.4 ± 0.1 | 0.07 ± 0.01 |

*Table 5.11:* Average precipitate core composition for the precipitates observed in the matrix and on dislocations in the WV steels aged for 3000 hrs and 90,000 hrs at 365 °C. (M = Matrix, D = Dislocation).

seen. Whilst the precipitates on dislocations contain more Cu and less Fe, as seen at 3000 hrs, they contain less Ni, Fn, Mn and Si. It is worth remembering here, that there are relatively few precipitates on dislocations in both datasets so the statistics are relatively poor. Nonetheless, there appears to be subtle differences in size and composition between precipitates in the matrix and at dislocations, particularly at shorter ageing times. Additionally, one precipitate from the 90,000 hr dataset which was observed on a dislocation is shown in Figure 5.32. Again the dislocation is evident from the segregation of C and Mo to its core.

The precipitate on the left in Figure 5.32 is a Cu precipitate with an associated Ni-Mn-Si rich region. It is most likely a duplex particle with one nucleating the other. As with the high-angle grain boundary it is not possible to determine which of these features nucleated first, or if at one stage they were two distinct precipitates which have amalgamated into the particle seen. The composition of this feature (in at.%) is 30 % Cu, 15 % Mn, 6 % Ni, 13 % Fn, 4 % Si, 32 % Fe. Excluding the Cu part of this feature gives the composition of the Ni-Mn-Si feature as 1 % Cu, 19 % Mn, 9 % Ni, 19 % Fn, 6 % Si, 44 % Fe.

As in the WF material shown in Section 5.4.2 and the high-angle grain boundary in Section 5.4.1 there is evidence for the formation of Ni-Mn-Si precipitates, both in materials containing Cu and in materials which are virtually Cu free.

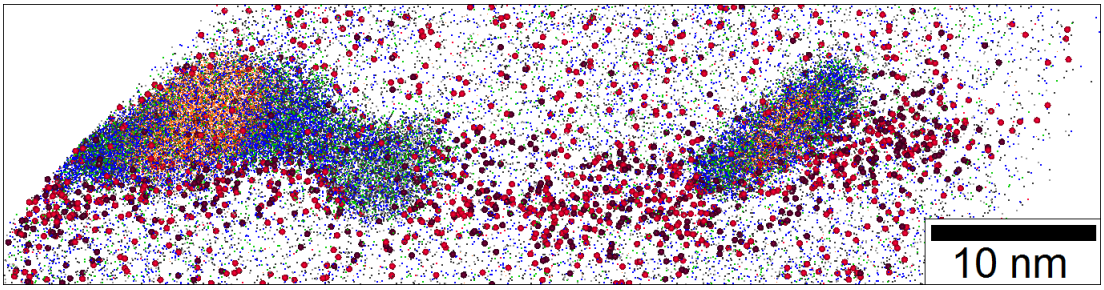


*Figure 5.32:* Ni-Mn-Si precipitate (left hand precipitate) observed along a dislocation in the WV material aged for 90,000 hrs at 365 °C. Colour legend, Cu - orange, Ni - green, Mn - blue, Fn - dark grey, Si - light grey, C - brown, Mo - red.

| Ageing temperature | | Average size (Det. atoms) | Core size (Det. atoms) | Interface width (nm) |
|---|---|---|---|---|
| 330 °C | Matrix | 870 ± 131 | 696 ± 111 | 0.13 ± 0.01 |
| | Dislocation | 4920 ± 1228 | 4210 ± 1162 | 0.21 ± 0.01 |
| 365 °C | Matrix | 6454 ± 3497 | 5886 ± 3198 | 0.11 ± 0.02 |
| | Dislocation | 30613 ± 14110 | 28838 ± 13746 | 0.15 ± 0.02 |

*Table 5.12:* Average precipitate size and interface widths for the precipitates observed in the matrix and on dislocations in the SG steels aged for 100,000 hrs at 330 °C and 365 °C.

#### 5.4.3.2 SG Material

In the SG material after 100,000 hrs, nearly all the precipitates observed in the material aged at 365 °C were observed on dislocations. In the 330 °C material there were a number of precipitates which were observed at dislocations.

Unlike in the WV material where, after ageing for 90,000 hrs the precipitates on dislocations were the same size, Table 5.12 shows that in the SG material there is significant difference between the two at both ageing temperatures. Precipitates on dislocations are much larger, containing between three and four times the number of atoms (approximately one and a half to two times the radius). The difference in the interface width is within errors at 365 °C. Whereas it is larger for the precipitates on dislocations at 330 °C.

In the material aged at 330 °C for 100,000 hrs the compositions of the features on dislocations are quite similar to those in the matrix. As seen from Table 5.13 there are small increases in Cu and Sn and small reductions in Si, Fe, Ni, Mn and Fn seen in

| Ageing temp | | Si | Fe | Cu | Ni | Mn | Fn | Sn |
|---|---|---|---|---|---|---|---|---|
| 330 °C | M | 1.2 ± 0.03 | 45.1 ± 0.13 | 41.4 ± 0.13 | 1.4 ± 0.03 | 6.6 ± 0.07 | 3.0 ± 0.05 | 0.9 ± 0.03 |
| | D | 0.8 ± 0.02 | 42.5 ± 0.11 | 46.2 ± 0.11 | 1.0 ± 0.02 | 5.7 ± 0.05 | 2.1 ± 0.03 | 1.1 ± 0.02 |
| 365 °C | M | 0.7 ± 0.04 | 29.6 ± 0.21 | 57.9 ± 0.23 | 1.4 ± 0.05 | 6.1 ± 0.11 | 2.7 ± 0.07 | 1.3 ± 0.05 |
| | D | 0.4 ± 0.01 | 23.7 ± 0.08 | 64.7 ± 0.09 | 1.0 ± 0.02 | 6.5 ± 0.05 | 1.8 ± 0.03 | 1.4 ± 0.02 |

*Table 5.13:* Average precipitate core composition for the precipitates observed in the matrix and on dislocations in the SG steels aged for 100,000 hrs at 330 °C and 365 °C. (M = Matrix, D = Dislocation).

the precipitates on dislocations. After ageing at 365 °C the same trend is seen, with the exception of Mn which shows a small increase and Sn which remains constant.

### 5.4.4 Comparison of Ni-Mn-Si Precipitation at Grain Boundaries and Dislocations

There are many similarities between the Ni-Mn-Si precipitates observed at dislocations and grain boundaries. A brief comparison of the features observed in the WV material at dislocations and grain boundaries and those observed in the WF material from Section 5.4.2 is made here. The average composition of the twelve largest precipitates (all between 1 nm and 3 nm in radius) in the grain boundary in the WF material, along with the composition of the precipitates observed on dislocations and grain boundaries in the WV material are shown in Table 5.14.

At first glance these precipitates don't appear to show any obvious trends, but it is clear they all have very low Cu contents (<1.5 %). However, precipitates 2 and 3 from the grain boundary (starred in Table 5.14) are not whole features. Looking at the trends present without these indicates that there is increasing Ni content with size, along with decreasing Fe content. There appears to be no trend with size for Mn or Si, Mn initially increases before decreasing whilst the opposite is observed

| Material | Location | Size | Si | Fe | Cu | Ni | Mn | P | Fn |
|---|---|---|---|---|---|---|---|---|---|
| WF 330 °C 100,000 hrs | Dislocations (Low-angle GB) | 1600 ± 250 | 4.7 ± 0.2 | 58.1 ± 0.4 | 0.7 ± 0.1 | 6.4 ± 0.2 | 15.7 ± 0.3 | - - | 14.1 ± 0.3 |
| WV 365 °C 50,000 hrs | GB - precipitate 1 | 15,400 | 3.1 ± 0.1 | 46.7 ± 0.4 | 1.4 ± 0.1 | 8.2 ± 0.2 | 22.4 ± 0.3 | 0.1 ± 0.02 | 17.7 ± 0.3 |
| WV 365 °C 50,000 hrs | GB - precipitate 2 | 12,300* | 11 ± 0.3 | 44.7 ± 0.4 | 0.5 ± 0.1 | 9.7 ± 0.3 | 11.9 ± 0.3 | 1.5 ± 0.1 | 19.7 ± 0.4 |
| WV 365 °C 50,000 hrs | GB - precipitate 3 | 31,800* | 12.4 ± 0.2 | 36.1 ± 0.3 | 0.5 ± 0.1 | 10.7 ± 0.2 | 15.4 ± 0.2 | 1.3 ± 0.1 | 22.5 ± 0.2 |
| WV 365 °C 90,000 hrs | Dislocation | 22,200 | 6.2 ± 0.2 | 43.9 ± 0.3 | 1.2 ± 0.1 | 9.1 ± 0.2 | 18.9 ± 0.3 | 0.4 ± 0.04 | 19.4 ± 0.3 |

*Table 5.14:* Composition of the Ni-Mn-Si precipitates observed at grain boundaries and dislocations in the WF and WV steels. *Indicates whole feature not detected, therefore the size is underestimated.

for Si. Interestingly, the two partial precipitates have similar ratios of Ni:Mn:Si of approximately 3:1:1.

## 5.5 Summary

This chapter has reported the experimental results of the thermal ageing of a number of RPV steels. Hardness data showed that the high Cu, high Ni welds have significantly increased in hardness, by as much 50 % in the case of the WV steel aged for 100,000 hrs at 330 °C. This is much more than in the low Ni counterparts.

The WV and SG steels were also characterised with APT after 90,000 hrs and 100,000 hrs of ageing at 330 °C and 365 °C. In the SG material the majority of precipitates were observed at dislocations, particularly in the material aged for 100,000 hrs at 365 °C in contrast to the WV materials where there was significant precipitation in the matrix. The precipitate size, number density and volume fraction were consistent with a coarsening population of precipitates. Matrix Cu levels in the WV and SG steels after 90,000 - 100,000 hrs of ageing were found to be around 0.06 - 0.08 at.%. The matrix Cu levels fell fastest in the high Ni welds indicating some influence of Ni on the kinetics of Cu precipitation. The influence of Ni on the Cu solubility could not be determined as it is not known if the low Ni steels have reached the equilibrium matrix Cu concentration.

Precipitate composition, the precipitate/matrix interfaces and precipitate Fe content were characterised with respect to the precipitate radius. In general, there was little change in the solute composition with precipitate radius. Sn was detected in the precipitates in the SG steels but not in the WV steels. Ideas to correct the Fe content of the precipitates due to the atoms from trajectory overlaps were also presented. This reduces the Fe content of the precipitates by around 10 % depending on the precipitate size. There was a temperature dependence on the Fe content of the precipitates: ageing at lower temperature resulted in a higher Fe content. Smaller

precipitates also have higher concentrations of Fe. Segregation of Ni, Mn and Si to the precipitate-matrix interface appears to result in a slightly wider interface with lower ageing temperature for equivalently sized precipitates. Wider interfaces were also observed in the materials with higher bulk Ni. Interface compositions were found to contain significant quantities of Fe, with little change in Ni, Mn and Si concentration with precipitate size. Lower Ni contents in the interface were observed in the low Ni steel. The reduction in interfacial energy due to the segregation of Ni, Mn and Si was also investigated. In the WV material, there was a trend for increasing reduction with precipitate size, but not with ageing time or temperature. These trends were not observed in the SG material, where reductions in interfacial energy were much less than in the WV material.

Several of the high Ni specimens, namely WV and WF, contained grain boundaries and/or dislocations. The level of solute segregation to grain boundaries in the WV steels was studied and indicated a co-segregation process was likely to be occurring from the large number of solute species at the grain boundaries.

Several Ni-Mn-Si precipitates were observed in the high and low Cu materials at both high and low-angle grain boundaries and at dislocations. In the high Cu materials the Ni-Mn-Si features were associated with Cu-enriched precipitates, whilst in the low-angle boundary in WF there was very little Cu association with these phases. No evidence of these features nucleating homogeneously in the matrix was observed. This is the first evidence of these features observed in thermally aged materials.

Furthermore, some steels have shown statistically significant softening, such as the WF steel aged at 330 °C. APT was performed on the specimens aged for 100,000 hrs at 330 °C and 90,000 hrs at 405 °C to investigate potential evidence for softening. The only feasible explanation appears to be loss of SSS although no significant differences in matrix compositions were observed.

# 6. Lattice Kinetic Monte Carlo Simulations of RPV Steels

APT is a useful technique for studying the long time evolution of Cu-enriched precipitates. It is less suited to studying the early stages of Cu precipitation, that is before the onset of visible precipitates, due to the fact that not all the evaporated ions are detected. This limits the ability to study the very small clusters, which would be detected as a group of only a few atoms. A Lattice-Kinetic-Monte-Carlo (LKMC) model, developed by Hirosawa and Sha[56] was used to investigate the early stages of solute clustering and, in particular, the role of Ni, Mn and Si fluctuations in the formation of Cu-enriched precipitates.

## 6.1 Introduction and Overview of Previous Work

The original code was written and developed at Oxford by Hirosawa and Sha[56]. Full details of the model are given in Morley[19]. The LKMC model is based upon the 5 element Fe-Cu-Ni-Mn-Si system, which is a simplified version of the weld and plate materials studied in the previous chapter by APT. The model simulates microstructural evolution using one vacancy in a 128x128x128 atom bcc Fe lattice. Simulations were started from a random configuration of solute atoms. To obtain computational efficiency the model is based upon the first order residence time algorithm[161] which ensures a transition between an atom and the vacancy occurs on every Monte-Carlo (MC) step. The real time is computed based upon a sum

of the mean residence time of each configuration, rescaled to take into account the much higher vacancy concentration of the simulation. In the simulation the vacancy concentration is 5 x $10^{-7}$, whist the thermal vacancy concentration at 365 °C is approximately 2 x $10^{-13}$. Interaction potentials are based upon first nearest-neighbour pair-wise interactions, which have been derived using literature data from binary alloy phase diagrams, *ab initio* simulations and binary alloy systems. Table 6.1 details the interaction parameters used in these simulations, which were originally calculated by Gang Sha[162]. These values have been derived from values of the cohesive energy, the nearest neighbour distance, vacancy formation energy, vacancy binding energy, diffusion co-efficient, the activation energy for substitutional diffusion along with the solubilities of various elements in one another. The values used to calculate the potentials in Table 6.1 can be found, with appropriate references, in Appendix D.

Morley[19] investigated the robustness of the model by looking at the influence of considering only first nearest neighbour interactions, one of the main simplifications used. He also looked at the effect of using different random starting configurations and what effect changing the solute-vacancy interactions had on the results of the simulation. The effect of starting from different random solute configurations and only considering first neighbour interactions were not found to drastically alter the simulated results. Morley also noted that although the solute-vacancy interaction potentials are approximations, they are reasonable. Large changes to the mobility of Ni and Mn did not greatly affect the kinetics of phase decomposition.

As with any computational model there are some limitations which have to be introduced for reasons of efficiency. In this model there are a couple of simplifications which potentially limit the usefulness of the model for studying the very long time evolution of Cu precipitation. Consequently, the model does not take into account lattice strain caused by the presence of Cu precipitates in the Fe matrix. In addition, the simulation uses a fixed bcc lattice so the transformation of Cu precipitates from bcc to 9R and eventually to fcc cannot be included. Finally, the limited number of atoms means that even if all the Cu atoms were in a single precipitate, the size would

| Parameter | Value |
|---|---|
| $\epsilon_{FeCu}$ | -87380 |
| $\epsilon_{FeNi}$ | -102650 |
| $\epsilon_{FeMn}$ | -90790 |
| $\epsilon_{FeSi}$ | -101550 |
| $\epsilon_{FeV}$ | -32330 |
| $\epsilon_{CuNi}$ | -93830 |
| $\epsilon_{CuMn}$ | -82090 |
| $\epsilon_{CuSi}$ | -92810 |
| $\epsilon_{CuV}$ | -18280 |
| $\epsilon_{NiMn}$ | -93550 |
| $\epsilon_{NiSi}$ | -104290 |
| $\epsilon_{NiV}$ | -32040 |
| $\epsilon_{MnSi}$ | -91470 |
| $\epsilon_{MnV}$ | -14450 |
| $\epsilon_{SiV}$ | -7120 |
| $\epsilon_{VV}$ | -13510 |
| $\epsilon_{FeFe}$ | -103250 |
| $\epsilon_{CuCu}$ | -82460 |
| $\epsilon_{NiNi}$ | -106970 |
| $\epsilon_{MnMn}$ | -83490 |
| $\epsilon_{SiSi}$ | -107310 |
| | |
| $\nu_{Fe}$ | $3.35\text{x}10^{15}$ |
| $\nu_{Cu}$ | $6.92\text{x } 10^{14}$ |
| $\nu_{Ni}$ | $1.70\text{x}10^{15}$ |
| $\nu_{Mn}$ | $1.81\text{x}10^{15}$ |
| $\nu_{Si}$ | $7.53\text{x}10^{14}$ |
| | |
| $e_{0,Fe}$ | 96200 |
| $e_{0,Cu}$ | 96200 |
| $e_{0,Ni}$ | 85600 |
| $e_{0,Mn}$ | 82100 |
| $e_{0,Si}$ | 96200 |

*Table 6.1:* Interaction parameters, in J $\text{mol}^{-1}$, and atomic vibration frequencies, in $\text{s}^{-1}$ used in the LKMC simulation. Negative potentials indicate that the interaction is energetically favourable. Values calculated by G. Sha[162].

still be smaller than the size of some of the largest precipitates seen in the thermally aged materials. Whilst these simplifications restrict the ability to study the long term evolution of particles, they are not of major concern in this work since the focus is on the early stages of Cu precipitate formation where these effects have a very small influence.

### 6.1.1 New Features and Aims of This Study

In the current work, the core code of the model which determines the solute-vacancy jump, and the interaction potentials upon which the model is based have been left unchanged. A number of revisions have been made to the original code to reduce the complexity and to increase the computational efficiency. Several new features have been added to enhance the analysis of the data from the simulation. A copy of the revised code for the Monte-Carlo model is given in Appendix E.1. The major changes and additions to the code have been highlighted. A summary of the revisions and new features is given below.

1. Revisions

    - Changes to the calculation of the periodic boundary conditions which provide a speed gain when using a 128x128x128 lattice size (or any cell with size $2^n$ atoms). This more than doubles the number of atoms in the cell from that used previously (a 100x100x100 atom cell).

    - Scripting to allow multiple simulations to run at once without the need for user input.

    - The pseudo-random number generator has been updated to the Marsenne Twister algorithm from the drand48 function. Marsenne Twister is considered to be a better random number generator since it is both faster and has a longer period (time before the sequence is repeated).

    - Each solute atom is now referred to by a unique ID which can be used to

track different atoms, as opposed to a generic 1 identifying all Cu atoms, 2 for all Ni atoms etc which was previously used. Fe atoms are not tracked and thus keep their original ID of 0, whilst vacancies are now referred to as -1 (previously 5).

- General code optimisations.

2. New features

- Information on the number of times the vacancy has been at a given lattice site after a given number of steps.
- A file recording the position of all clusters containing 4 or more solute atoms and the IDs of all the solutes contained within it is output each time the cluster search is performed.
- The file of clustered solute atoms can be used to look at the environment around the final position of Cu precipitates at earlier times in the simulation i.e before a cluster nucleated at that site. This has been used to produce a video showing the cluster evolution in these regions as the simulation progresses. Additional programs were written to perform this analysis (see Appendix E.2.1).
- The ID and new position of a solute atom is recorded each time it exchanges with a vacancy.
- The files detailing the solute vacancy swaps were used to produce a video focussed on a specific region where a given cluster has formed. Two ancillary programs have been written for this purpose (see Appendix E.2.2). This provides further insight into the detailed mechanisms of cluster formation.
- Information is also recorded about the number of times particular solute species have exchanged with the vacancy and the average distance they have migrated from their original lattice site.

The LKMC simulations in this study focussed on simplified versions of the WV and SG welds studied with APT, that is the two highest Cu steels with high and low Ni content. The composition of the two simulated steels is shown in Table 6.2.

| Material | Cu | Ni | Mn | Si |
|---|---|---|---|---|
| SG | 0.43 | 0.29 | 1.52 | 0.81 |
| WV | 0.44 | 1.66 | 1.38 | 0.75 |

*Table 6.2:* Composition of the simulated steels in at.%, bal. Fe.

Simulations were run at the same three ageing temperatures as the experimental work, for 5 x $10^{11}$ MC steps at 330 °C and $10^{12}$ MC steps at 365 °C and 405 °C. This equates to simulated times of approximately 12 x $10^6$ hrs, 1.6 x $10^6$ hrs and 100,000 hrs for the three temperatures respectively. One simulation was run in full for each of the material and temperature combinations giving six simulations in total. Four additional simulations of each material and temperature combination were run for $10^{10}$ MC steps (just beyond the onset of visible clustering). This improved the statistics for the work on the early stages of clustering and for calculation of the energy barrier to nucleation in Section 6.2.2. As shown by Morley[19] errors in the number density can be approximated by those of the Poisson-type error, $\sqrt{Number}/Volume$. This has been used in this work where only one simulation has been run. In the cases where more than one simulation was run, errors were calculated using the standard error in the mean (Equation 4.1).

The work in this chapter is primarily focussed on the very early stages of nucleation to investigate the origins of the differing behaviour of the SG and WV steels. This involved using the simulations to investigate any differences in the activation energy for the formation of critical nucleus. These results were compared to the values calculated by Morley[19] for the APT work. The simulations were then used to investigate the environment around Cu atoms and Cu-enriched precipitates using some of the new features of the simulation.

## 6.2 Microstructural Evolution

From the experimental work in the previous chapter it is clear there is a significant difference in microstructural evolution between the high and low Ni steels. The simulation has been used to investigate if there is any difference in nucleation and growth or coarsening of clusters in the simulation. The simulated datasets can be treated as APT data and can be analysed using all the same techniques, the only exception being the values used for the cluster selection parameters. These have to be reduced to account for the fact that there are no losses due to detection efficiency, hence all the atoms are present in the simulation. For consistency with the previous simulation results the parameters were kept the same, hence solutes Cu, Ni, Mn and Si were used with a $d_{max} = 0.3$ nm, $L = e = 0.25$ nm, $N_{min} = 20$. For comparison the parameters used for the experimental work were $d_{max} = 0.5$ nm, $L = e = 0.4$ nm, $N_{min} = 16$.

### 6.2.1 Precipitate Size and Number Density

The size and number density of precipitates observed in the simulated SG and WV steels at the three ageing temperatures is shown in Figure 6.1.

Figure 6.1a shows that the mean sizes of the precipitates in the simulated WV and SG steels are almost identical, with the exception of those at 405 °C where the SG precipitates are larger. This is consistent with what is observed experimentally in the SG steels aged at higher temperature. Comparison of the matrix Cu levels in both cases indicates similar amounts of Cu have been incorporated into precipitates. In the SG steel aged at high temperature (corresponding to a low supersaturation) Cu precipitates are hard to nucleate and hence they form heterogeneously on dislocations and at grain boundaries. It is not possible to include this in the simulations and thus very few nuclei become super-critical. Those that do are relatively far apart and consequently have large diffusion fields. The driving force for coarsening is small and

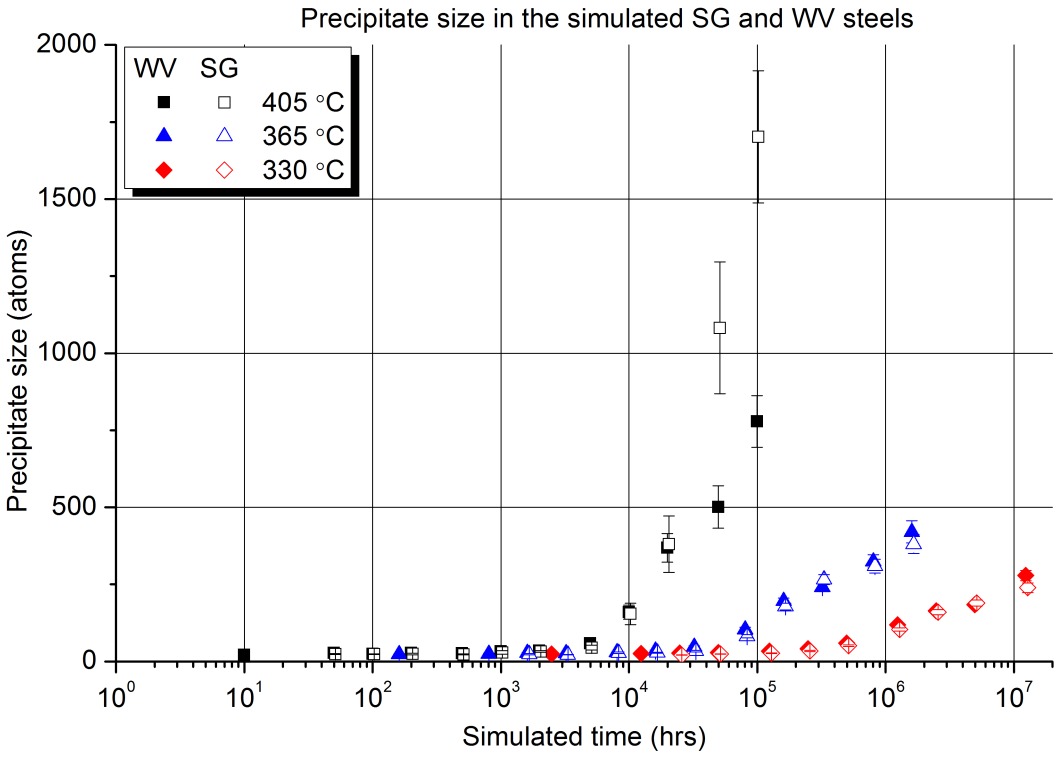


*(a)* Mean precipitate size.

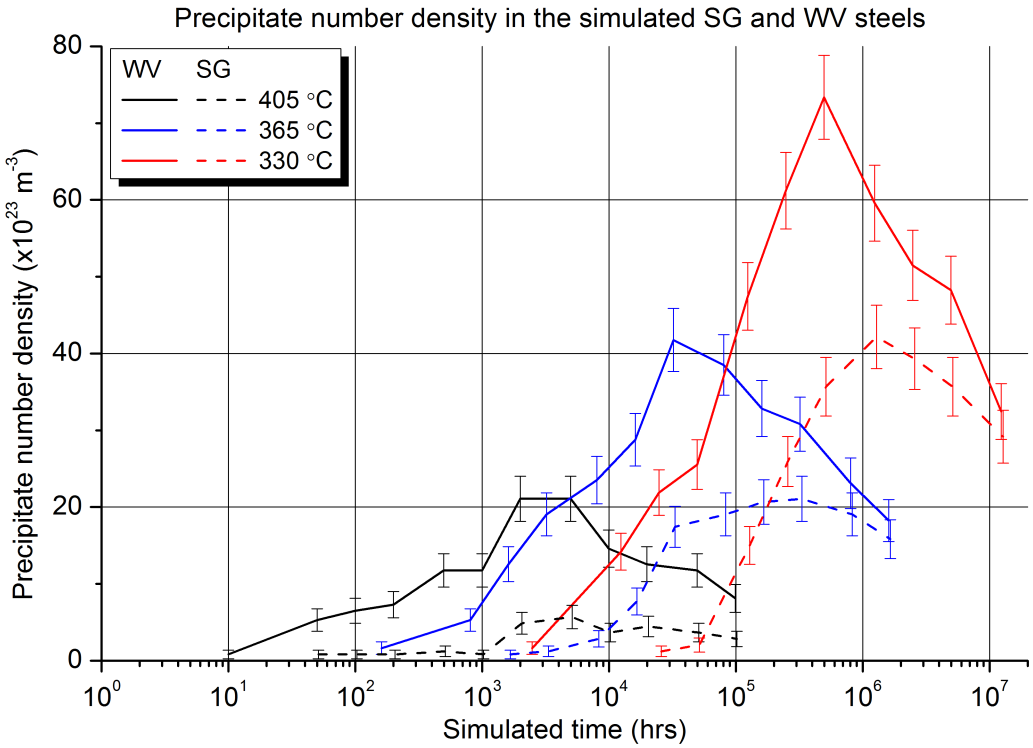


*(b)* Mean precipitate number density.

*Figure 6.1:* (a) Mean precipitate size and (b) precipitate number density in the simulated SG and WV steels with simulated ageing time.

these precipitates reach their large sizes by growth. The presence of Ni (or a higher supersaturation) decreases the barrier to nucleation and thus more super-critical nuclei form. Here, coarsening is more favourable since precipitates are naturally closer together. This is a slower process and as such the low Ni steel aged at 405 °C has a larger mean size at the end of the simulation.

The number density of features follows expectations with a higher density observed at a lower ageing temperature and with higher bulk Ni content. This is consistent with what is observed in the experimental work, albeit with number densities in the simulations being much higher than those observed experimentally.

The increases in number density compared to the experimental data could, in part, be attributed to a number of factors. The effective 100 % detection efficiency of the simulation will mean clusters which would not be detected in the APT work are detectable in the simulations. To reproduce the effect of imperfect detection, 63 % of the atoms in the simulated data were randomly removed. The datasets were cluster searched using the same parameters as for the experimental work. The number densities before and after efficiency degradation for the WV simulation at an ageing temperature of 365 °C are shown in Figure 6.2.

This shows that a lower detection efficiency can result in a significant reduction in the number of detected clusters. This can, in part, account for some of the increase in the number density of features in the simulation, particularly at the shorter ageing times. Here features are smaller and the lower detection efficiency has a greater impact. At the longer times, reduced detector efficiency cannot account for the higher number density of features. This may be accounted for by the limited simulated volume and the fact that some clusters could be double counted due to the periodic boundary conditions.

The important result here is that the simulation correctly reproduces the trends observed in the experimental data, as the focus of the KMC modelling is on the early stages of Cu precipitation.

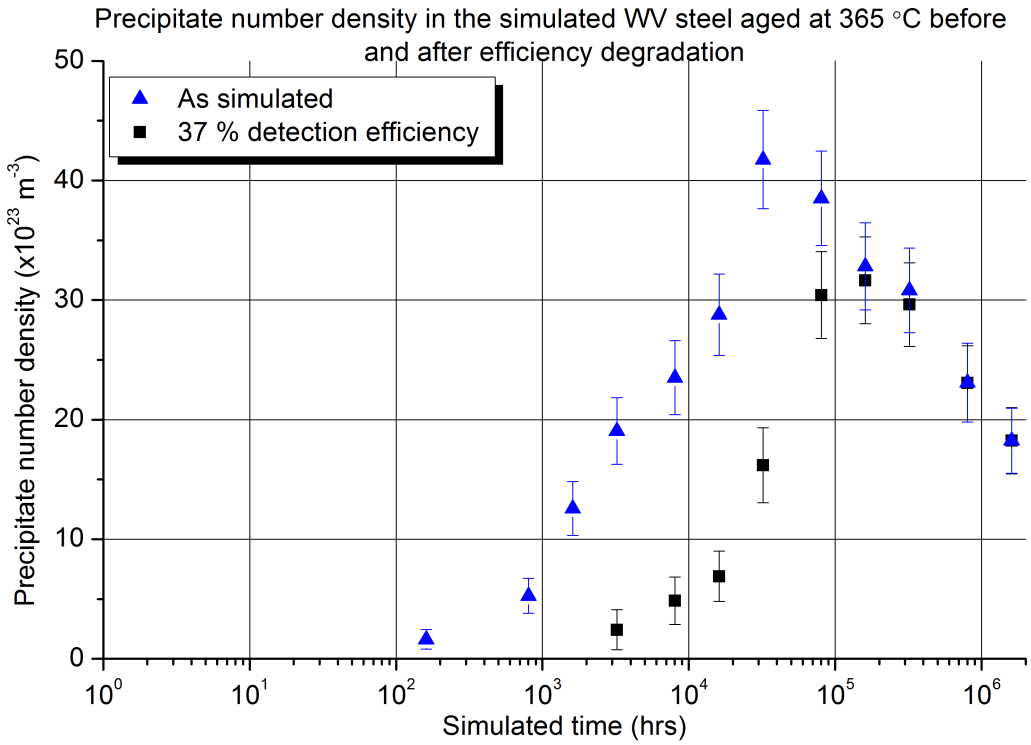


*Figure 6.2:* Effect of detection efficiency on the number density of precipitates detected in the WV weld after simulated ageing at 365 °C.

### 6.2.2 Nucleation and Growth

To understand the influence of Ni on the nucleation of features in the simulation it is useful to estimate the activation energy for nucleation, $\Delta G$. The homogeneous nucleation rate, $N_{hom}$, is given by

$$N_{hom} = A_0 \exp\left(-\frac{\Delta G_m}{kT}\right) \exp\left(-\frac{\Delta G^*}{kT}\right) \tag{6.1}$$

where $\Delta G_m$ is the activation energy for atomic migration and $\Delta G^*$ the energy barrier for the formation of a critical nucleus. $A_0$ is a factor which accounts for the vibration frequency of the atoms, the area of the critical nucleus and the number of atom sites per unit volume. The first exponential, $\exp\left(-\frac{\Delta G_m}{kT}\right)$, gives the rate at which atoms can be added to the critical nucleus and the second exponential, $\exp\left(-\frac{\Delta G^*}{kT}\right)$, gives the concentration of critical nuclei in the material, $k$ is Boltzmann's constant and $T$ is the temperature. From Equation 6.1 a plot of $\ln N_{hom}$ versus $1/T$ will give a straight line (assuming a constant $A_0$) with gradient equal to $\Delta G/R$, where $\Delta G = \Delta G_m + \Delta G^*$.

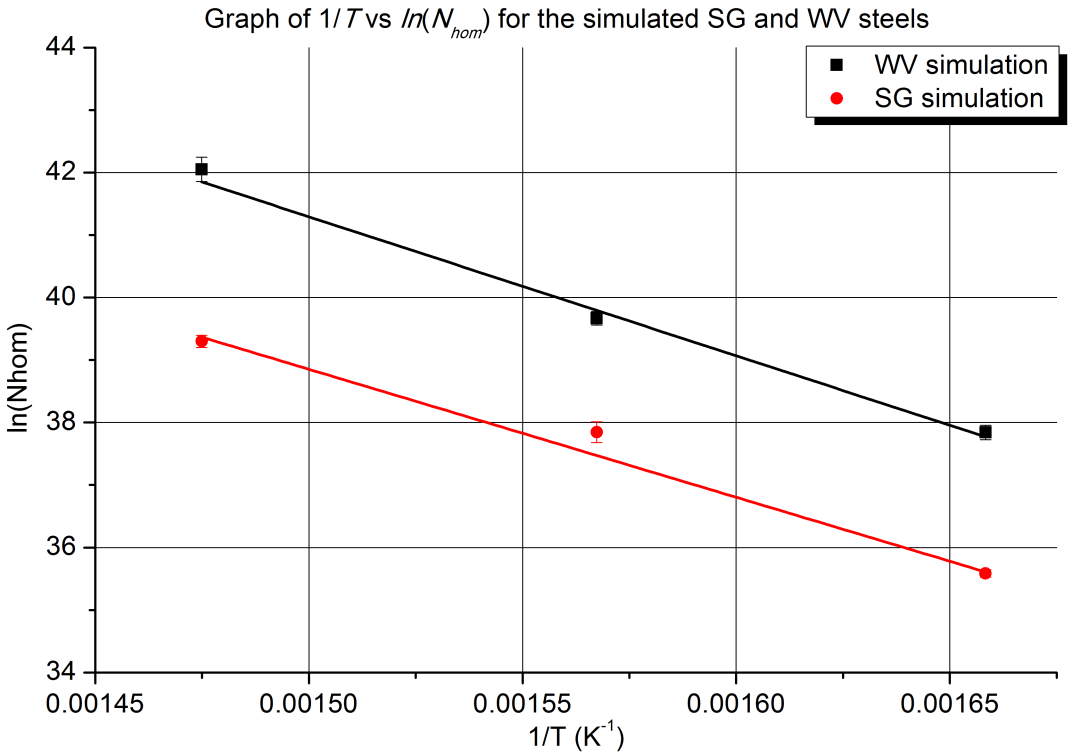


*Figure 6.3:* Arrhenius plot of $\ln N_{hom}$ versus $1/T$ for the simulated SG and WV steels.

Morley[19] used this to estimate $\Delta G$ for the experimental work. This plot is shown for the simulated data in Figure 6.3.

The homogeneous nucleation rate was approximated as the gradient of the steepest part of a plot of the number density versus time, in seconds, on a linear scale. Values of $N_{hom}$ for the simulations are calculated from the mean number density of clusters observed in four simulations of each material. Table 6.3 details the estimated activation energies for the simulations along with those calculated by Morley[19] from the experimental data.

| Material | $\Delta G$ (kJ mol$^{-1}$) | |
|---|---|---|
| | Experiment | Simulation |
| SG | 237 | 170 ± 12 |
| WV | 248 ± 28 | 185 ± 16 |

*Table 6.3:* Estimated activation energies for homogeneous nucleation in the SG and WV steels from experiment and simulation. Experimental values calculated by Morley[19].

The estimated activation energies for both the simulated SG and WV steels are less than those from the experimental data. However, both the activation energies from

the simulation are within calculated errors of one another as is seen experimentally. It was not possible to obtain an error estimate for SG from the experimental data as only two points were available for the Arrhenius plot. The activation energies are close to that of $\Delta G_m$ the activation energy for atomic migration of Cu in Fe (approximately 239 kJ mol$^{-1}$[163]). This indicates that the size of the critical nucleus is likely to be very small. The simulation appears to replicate the nucleation of Cu precipitates reasonably well and this should provide useful data when this is investigated in Section 6.3. Given that only three points are available for the Arrhenius plot, small fluctuations in these values can have significant impact on the results, particularly in the points at 330 °C and 405 °C which are the two extremes of the plot.

## 6.3 Influence of Solute Elements on Precipitate Formation

Investigating the nucleation behaviour of the model provides a benchmark against the experimental data. Although the activation energies calculated from the simulated data are lower than calculated experimentally, the trends seen are in line with one another. In the SG data a slower nucleation rate is observed, along with a lower peak number density of features. The emergence of detectable clusters also occurs later than in the WV simulations. The model should therefore provide some insight into the early stages of nucleation of Cu precipitates, particularly the influence of Ni and the local chemical environment around very fine scale clusters and groups of a few Cu atoms. A number of techniques have been used to investigate the early stages of nucleation. These include investigating the environment around Cu atoms, the number of atoms of each element which are isolated (entirely surrounded by Fe atoms) and the environment around where Cu-enriched precipitates have subsequently nucleated. Finally, two videos have been produced to study the nucleation and evolution of clusters in the simulation. Most of the figures and data reported here

are from the SG and WV simulations at 365 °C but many of the trends seen are also observed at the other two temperatures.

### 6.3.1 Isolated Solute Atoms

Having 100 % of the atoms in the simulated datasets mean it is possible to perform analyses which are not feasible with the experimental data. One such analysis is to study the number of isolated solute atoms in the dataset, that is solute atoms which are entirely surrounded by Fe atoms in their eight first nearest neighbour sites. This should highlight the first elements that start to cluster together. For this analysis a cluster is defined as a group of two or more solute atoms in nearest neighbour sites. It is possible to investigate both the number of solutes which are isolated and the respective fraction of each element which are isolated. The fraction of isolated solutes has been studied here as this removes the effects of the differing number of each atomic species.

Figure 6.4 shows the fraction of each solute species which are wholly surrounded by Fe atoms in the WV and SG simulations with ageing time for simulated ageing at 365 °C. Similar results are seen for the simulated SG and WV steels at 330 °C and 405 °C.

As seen in Figure 6.4a a greater fraction of solute atoms are isolated in the SG steel, which reflects the fact that there are fewer solute atoms in this simulation. What is evident from both the SG and WV simulations is that the fraction of isolated Si atoms decreases much more slowly and much later than Cu, Ni and Mn. This may indicate that Si is not influencing the early stages of cluster formation and could also be related to its lower mobility the other elements in the simulations. Cu, Ni and Mn begin to cluster together after less than a hour of ageing. In the WV steel Cu is first to show an appreciable difference in the fraction of atoms which are isolated, closely followed by Ni and then Mn, with the rate at which atoms are clustering also greatest for Cu. In the SG steel, again Cu is first to show an appreciable reduction in the number of

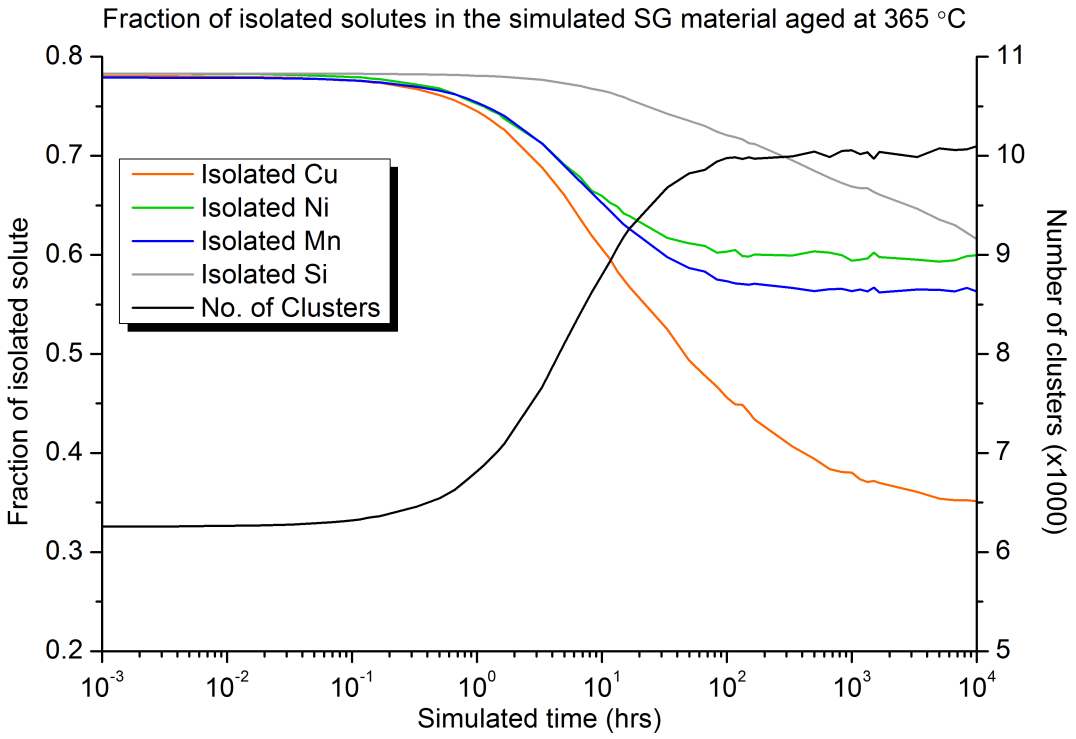


*(a)* Fraction of isolated solutes in the simulated SG steel.

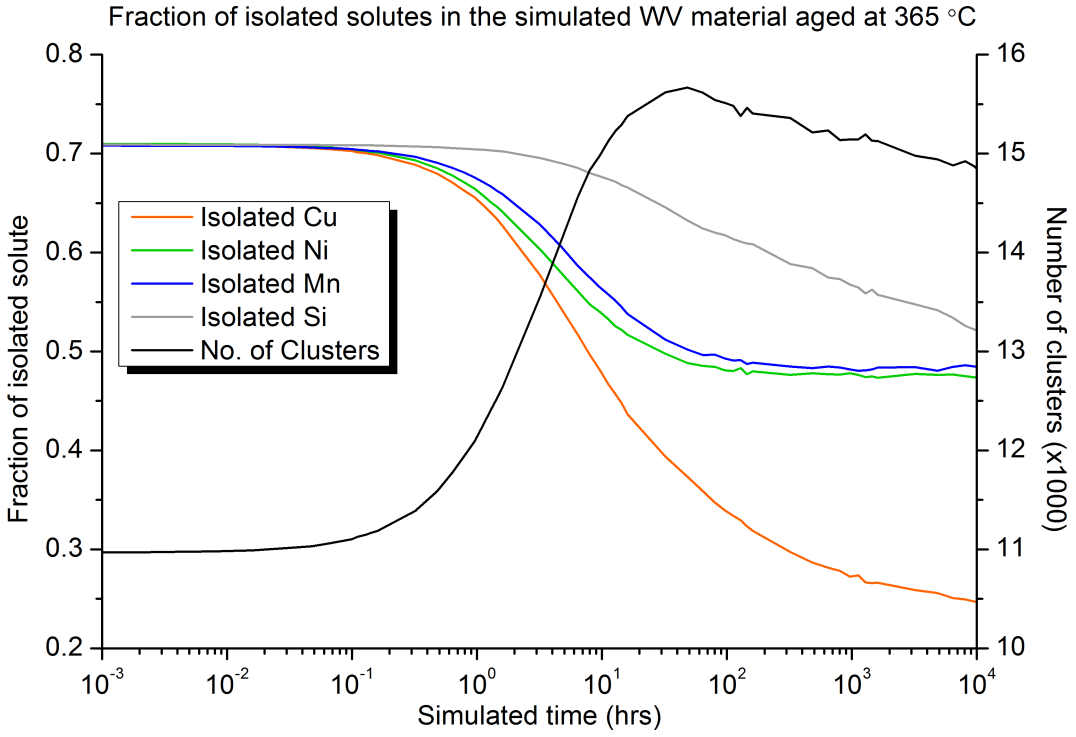


*(b)* Fraction of isolated solutes in the simulated WV steel.

*Figure 6.4:* Fraction of each isolated solute species in the (a) SG and (b) WV steels after simulated ageing at 365 °C.

isolated solute atoms. Ni and Mn show signs of clustering at near identical times. Also, in the SG steel a greater fraction of Mn than Ni becomes clustered, whereas in the WV steel a slightly higher fraction of Ni atoms are clustered. In the WV steels the reduction in the fraction of Ni and Mn which are isolated show a similar decrease after 10,000 hrs, around 22 - 23 %. For Si this is 20 % and Cu 46 %. This is a slight increase over the SG steels where reductions in isolated solutes of each element are 18 %, 21 %, 18 % and 43 % for Ni, Mn, Si and Cu respectively.

These results suggest that both Ni and Mn are involved in the early stages of phase decomposition, possibly by reducing the interfacial energy of early stage Cu-enriched precipitates. Aside from the fraction of solute which is isolated and the later clustering of Ni, the progression of clustering appears similar between the SG and WV steels. These small differences in the number of clusters and the slightly earlier clustering of Ni, could be responsible for the increased number of Cu-enriched precipitates in the WV steels over the SG ones. Alternatively, this could just reflect the higher solute content of the WV alloy as solutes are initially closer together.

### 6.3.2 Environment Around Cu Atoms

It is also possible to look at the environment around Cu atoms and Cu atom pairs. Morley[19] investigated this for the WV steel at the three ageing temperatures, but only after 5 x $10^8$ MC steps, which was the point in the simulations at which Cu started to become non-randomly distributed. This analysis has been extended in this work to look at both the WV and SG steels over several time-steps covering the whole range of MC steps.

Figures 6.5a and 6.5b show the concentration of Ni, Mn and Si in the nearest neighbour sites around single Cu atoms and nearest neighbour Cu atom pairs (referred to as dimers) for the SG and WV simulations at 365 °C.

At the beginning of the simulation the environment around Cu atoms and Cu dimers

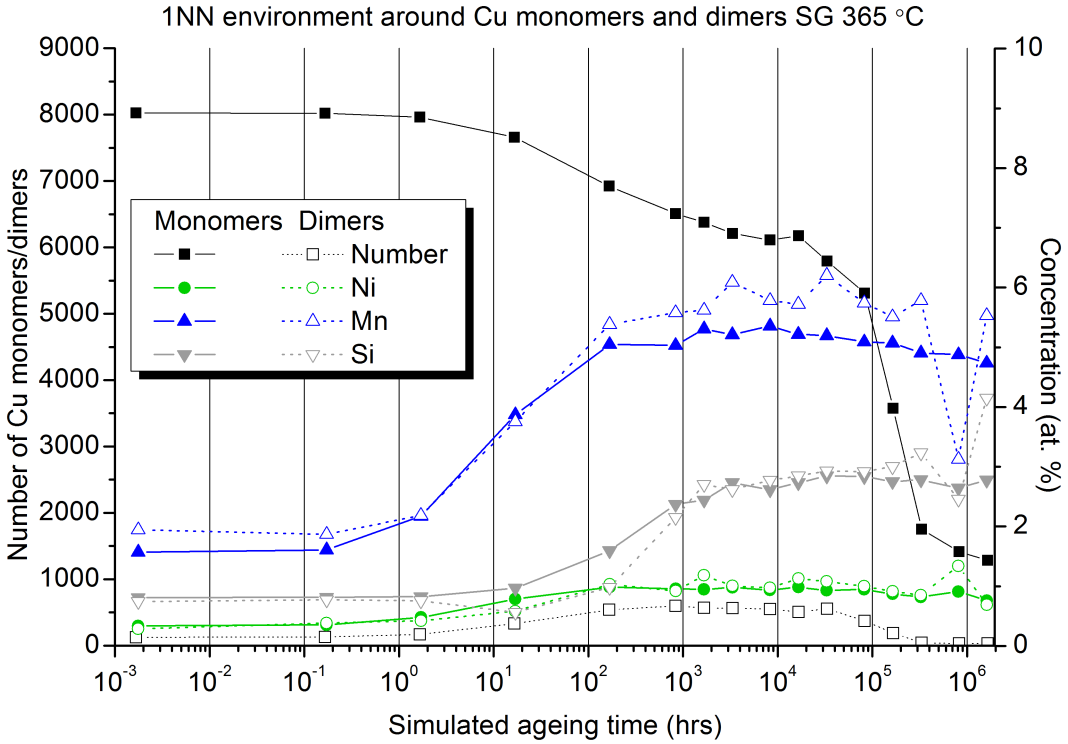


*(a)* Simulated SG steel aged at 365 °C.

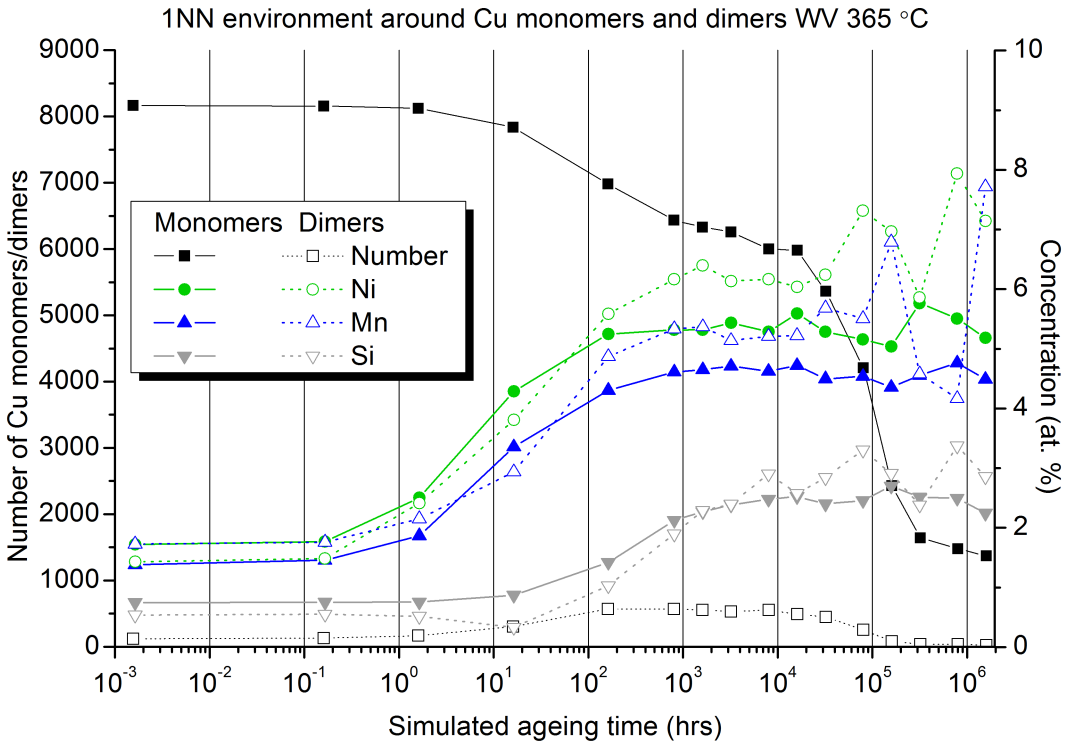


*(b)* Simulated WV steel aged at 365 °C.

*Figure 6.5:* Nearest neighbour environment around single Cu atoms (monomers) and Cu atom pairs (dimers) after simulated ageing at 365 °C in the (a) SG and (b) WV steels.

is typical of that of the matrix, which is to be expected given the random starting configuration. As the simulation progresses, the nearest neighbour sites of Cu atoms become enriched in Ni and Mn atoms in the WV steels. In the SG steels, only a small enrichment of Ni is seen which is not unexpected given the lower bulk Ni content, but perhaps surprisingly this is not offset by a significant increase in Mn. Si appears to become associated with Cu atoms a couple of orders of magnitude later in time than Ni and Mn. This is consistent with the later clustering of Si shown in Figure 6.4. After significant clusters start to become visible, (after around 100 - 1000 hrs in the 365 °C simulations in Figure 6.5) the enrichment of Ni, Mn and Si plateaus. The environment around the Cu dimers is very similar to that of the single atoms, except that enrichment reaches a higher plateau value. However, this could just be a feature of the fact that a Cu dimer has proportionally fewer nearest neighbour sites per atom (7) than a single atom (8).

The results presented in Figure 6.5 were for the SG and WV simulations at 365 °C. Very similar results are observed for the simulations at 330 °C and 405 °C with the exception of the time at which enrichment occurs. At 405 °C enrichment occurs earlier than at 365 °C and at 330 °C enrichment occurs at a slightly later time.

These results indicate that in the very early stages of phase decomposition, even before visible clustering is detected that Ni and Mn atoms are associated with Cu atoms and Cu dimers. This is evident from the fact that enrichment is occurring at the nearest neighbour sites despite the number of single Cu atoms and dimers remaining fairly constant. This indicates that both Ni and Mn appear to have some involvement in the early stages of Cu precipitation.

### 6.3.3 Environment Around the Nucleation Sites of Precipitates

The previous sections have shown that the environment around Cu atoms in the simulation becomes enriched in Ni and Mn, and that these species cluster together,

at least on the scale of a few atoms if not into large precipitates. Logically, the next step is to investigate the chemical environment around the sites at which precipitates have subsequently formed in the simulation. The simulation records the position of all clusters containing 4 or more solute atoms and the identities of all solute atoms within it at various time-steps. The positions of clusters at the end of the simulation are also known. Thus it is possible to investigate the clusters which have formed in the immediate vicinity of these positions before a precipitate subsequently nucleated there. For this analysis the final positions of all precipitates containing 10 or more solute atoms were used. In the majority of cases these clusters contain upwards of 25 % Cu.

As a useful qualitative analysis tool, videos were produced showing the location, composition and size of clusters above 4 atoms in size and their evolution as the simulation progressed. These videos can be found on the attached DVD (see the folder entitled "Environment around Cu precipitates"). A series of screen shots from the videos of the WV and SG steel undergoing simulated ageing at 365 °C are shown in Figures 6.6 and 6.7. In the videos, spheres are coloured orange, green, blue or grey depending on whether the most common element present is Cu, Ni, Mn or Si respectively. The sizes of the spheres are related to the sizes of the cluster, the larger the sphere the larger the cluster. The transparent light grey spheres show the final position and size of precipitates larger than 10 atoms at the end of the simulation. It is the environment around these sites which will be investigated in more detail later in this section.

The videos show the presence of a high density of Ni-Mn clusters. These are also evident from Figures 6.6 and 6.7. These clusters are constantly appearing and dissolving during the simulation. In the high Ni, WV steel, there are considerably more of these clusters and many more clusters containing mostly Ni, which is consistent with the higher bulk Ni content of this alloy.

The environment around the sites at which Cu-enriched precipitates subsequently form

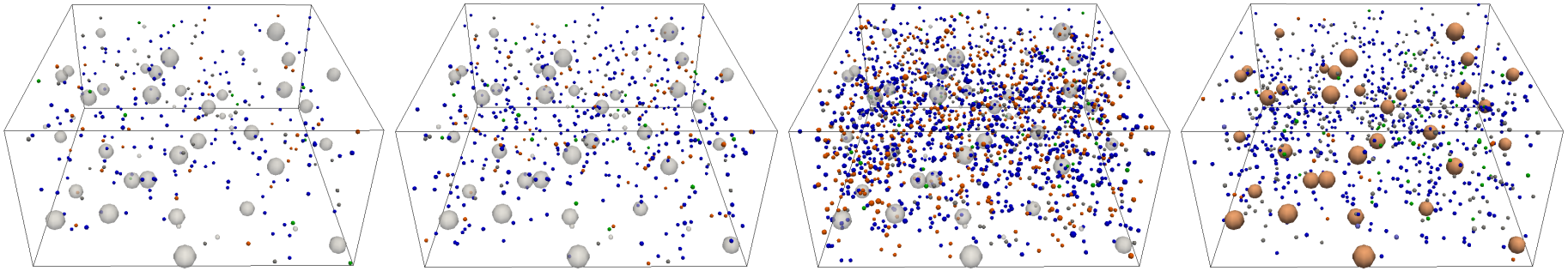

*(a)* Initial distribution of clusters.

*(b)* Distribution of clusters after 6 hrs.

*(c)* Distribution of clusters after 5000 hrs.

*(d)* Distribution of clusters after 1.6 x $10^6$ hrs.

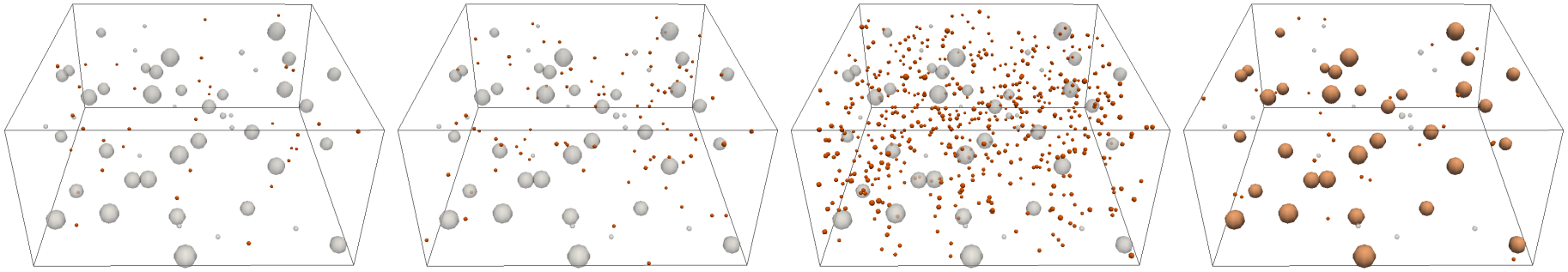

*(e)* Initial distribution of Cu clusters.

*(f)* Distribution of Cu clusters after 6 hrs.

*(g)* Distribution of Cu clusters after 5000 hrs.

*(h)* Distribution of Cu clusters after 1.6 x $10^6$ hrs

*Figure 6.6:* Frames from the video showing evolution of clusters larger than 4 atoms during the simulated ageing of the SG steel at 365 °C. Coloured spheres indicate the most common element in the cluster as follows: Orange spheres - Cu, green spheres - Ni, blue spheres - Mn, dark grey spheres - Si. The transparent light grey spheres show the final position and size of precipitates larger than 10 atoms at the end of the simulation.

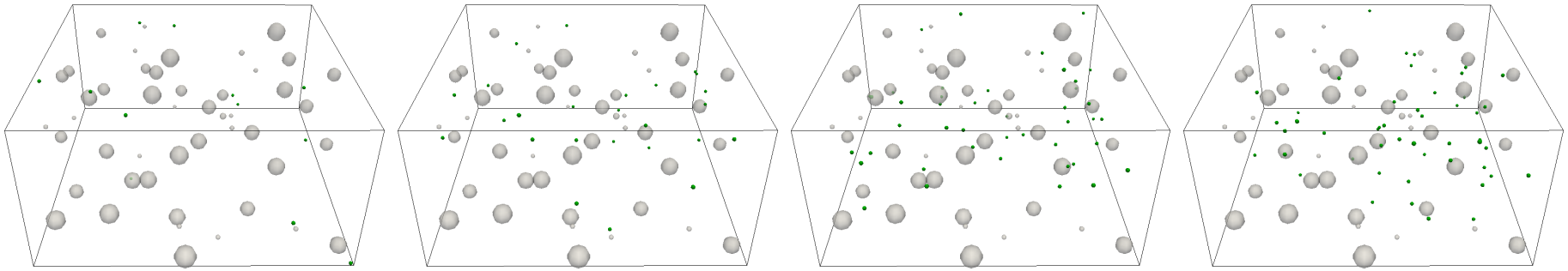

*(i)* Initial distribution of Ni clusters.

*(j)* Distribution of Ni clusters after 6 hrs.

*(k)* Distribution of Ni clusters after 5000 hrs.

*(l)* Distribution of Ni clusters after 1.6 x $10^6$ hrs.

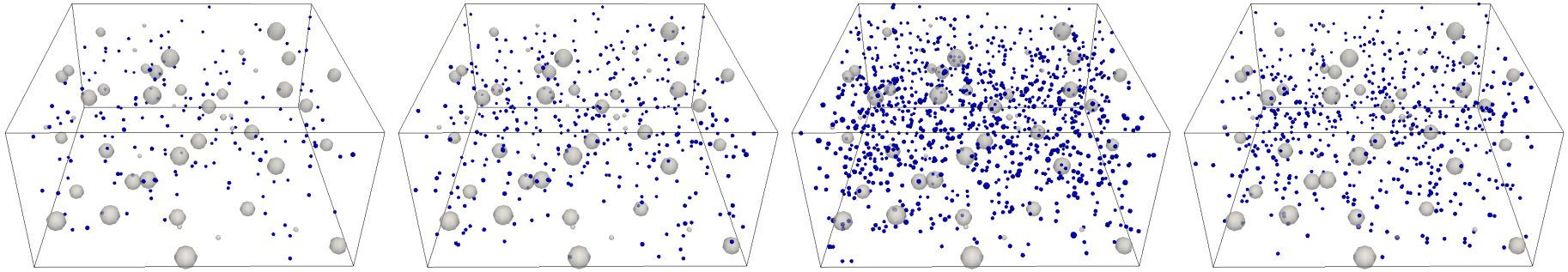

*(m)* Initial distribution of Mn clusters.

*(n)* Distribution of Mn clusters after 6 hrs.

*(o)* Distribution of Mn clusters after 5000 hrs.

*(p)* Distribution of Mn clusters after 1.6 x $10^6$ hrs.

*Figure 6.6:* Frames from the video showing evolution of clusters larger than 4 atoms during the simulated ageing of the SG steel at 365 °C. Coloured spheres indicate the most common element in the cluster as follows: Orange spheres - Cu, green spheres - Ni, blue spheres - Mn, dark grey spheres - Si. The transparent light grey spheres show the final position and size of precipitates larger than 10 atoms at the end of the simulation.

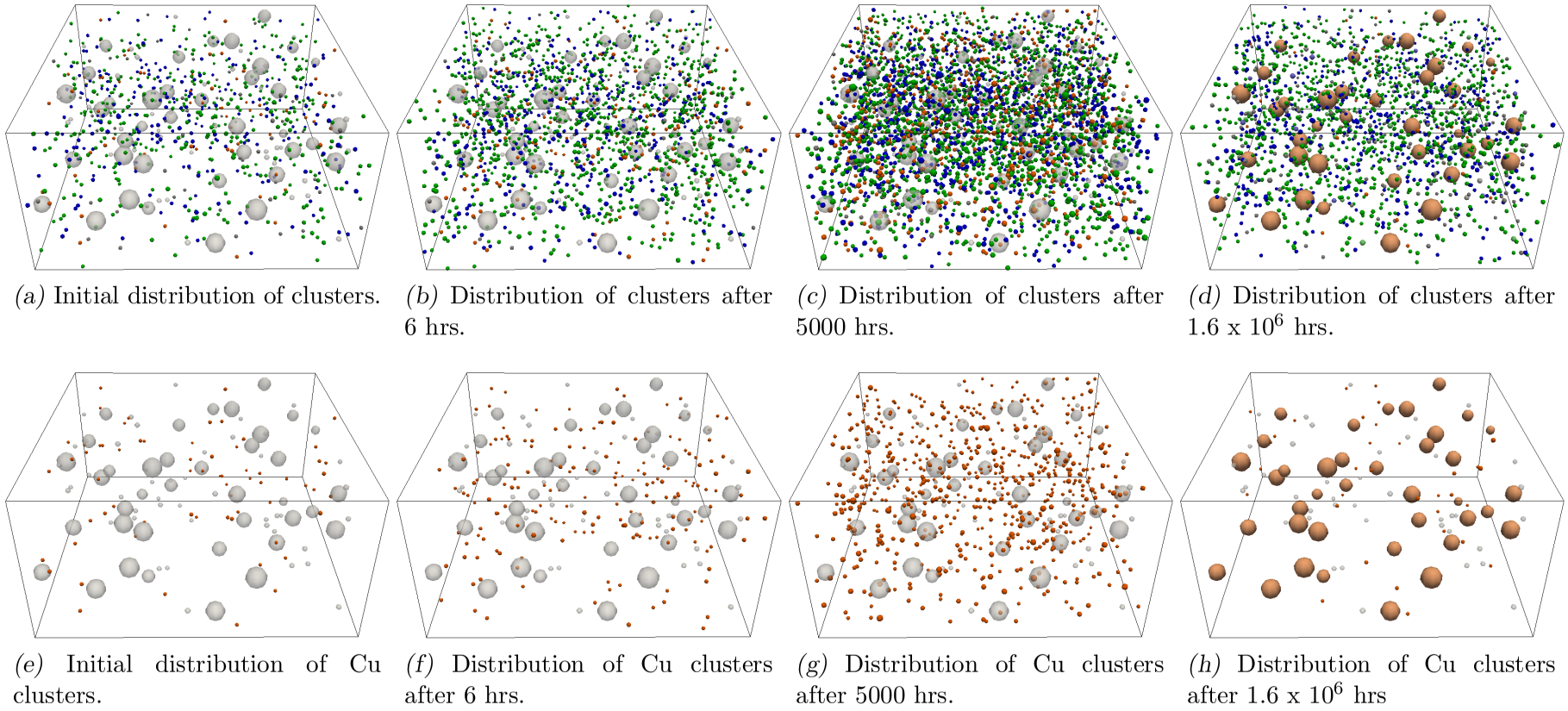

*(a)* Initial distribution of clusters.

*(b)* Distribution of clusters after 6 hrs.

*(c)* Distribution of clusters after 5000 hrs.

*(d)* Distribution of clusters after 1.6 x $10^6$ hrs.

*(e)* Initial distribution of Cu clusters.

*(f)* Distribution of Cu clusters after 6 hrs.

*(g)* Distribution of Cu clusters after 5000 hrs.

*(h)* Distribution of Cu clusters after 1.6 x $10^6$ hrs

*Figure 6.7:* Frames from the video showing evolution of clusters larger than 4 atoms during the simulated ageing of the WV steel at 365 °C. Coloured spheres indicate the most common element in the cluster as follows: Orange spheres - Cu, green spheres - Ni, blue spheres - Mn, dark grey spheres - Si. The transparent light grey spheres show the final position and size of precipitates larger than 10 atoms at the end of the simulation.

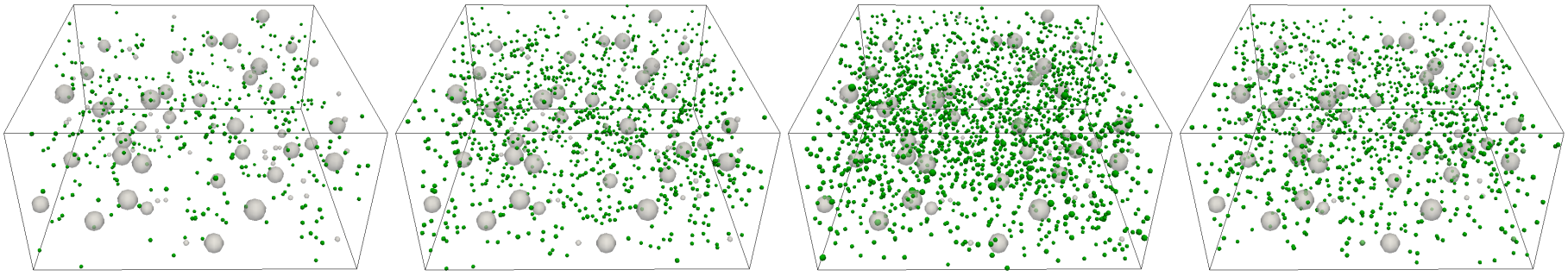

*(i)* Initial distribution of Ni clusters.

*(j)* Distribution of Ni clusters after 6 hrs.

*(k)* Distribution of Ni clusters after 5000 hrs.

*(l)* Distribution of Ni clusters after 1.6 x $10^6$ hrs.

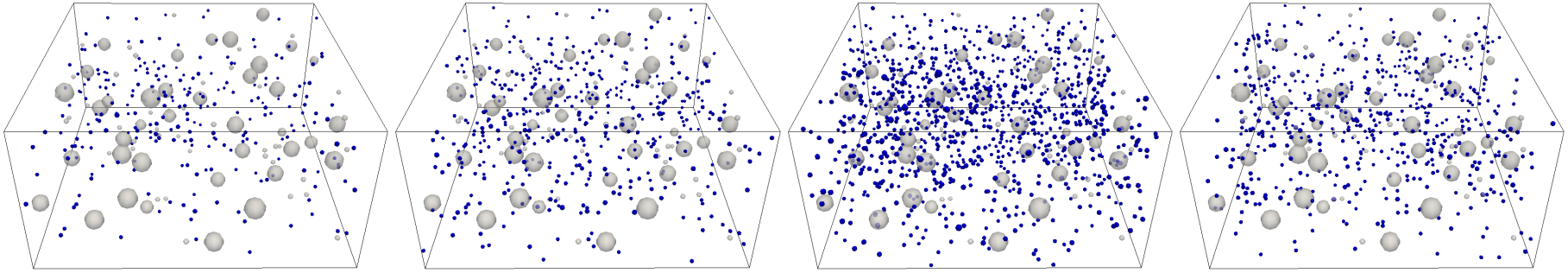

*(m)* Initial distribution of Mn clusters.

*(n)* Distribution of Mn clusters after 6 hrs.

*(o)* Distribution of Mn clusters after 5000 hrs.

*(p)* Distribution of Mn clusters after 1.6 x $10^6$ hrs.

*Figure 6.7:* Frames from the video showing evolution of clusters larger than 4 atoms during the simulated ageing of the WV steel at 365 °C. Coloured spheres indicate the most common element in the cluster as follows: Orange spheres - Cu, green spheres - Ni, blue spheres - Mn, dark grey spheres - Si. The transparent light grey spheres show the final position and size of precipitates larger than 10 atoms at the end of the simulation.

has been investigated by looking at the number density of clusters in the regions within 2 nm of the centre of where a precipitate was located at the end of the simulation (light grey spheres in Figures 6.6 and 6.7). The composition of the clusters detected in these regions was then investigated. As the simulation progresses clusters coarsen and migrate slightly from their initial nucleation site (this can be seen in the videos). Hence, looking at the very end of the simulation does not give the whole picture about the environment around the sites where the precipitates nucleated. To investigate the environment at the position of nucleation it is necessary to investigate the environment around the positions of Cu-enriched precipitates at, or just after the onset of growth. In this case the majority of precipitates will still be at, or very close to, their original nucleation site and should be large enough to be easily detectable. In all the WV simulations the onset of growth starts at about $10^9$ MC steps and at around 5 x $10^9$ MC steps in the SG simulations. The same four simulations of each condition as those used in Section 6.2.2 were used to investigate the number density and composition of clusters at the sites at which Cu-enriched precipitates had formed after $10^{10}$ MC steps.

Figures 6.8 and 6.9 show the distribution of Cu atoms in each simulation after $10^{10}$ MC steps corresponding to simulated ageing times of ∼250,000 hrs, ∼16,000 hrs, ∼1000 hrs at ageing temperatures of 330 °C, 365 °C and 405 °C respectively.

If nucleation of Cu precipitates is happening uniformly in the matrix then no correlation between the number density of Ni and Mn clusters and the subsequent nucleation sites of Cu-enriched precipitates should be observed, i.e the number density of Ni-Mn clusters should be homogeneous throughout the simulated volume. Conversely, if nucleation involves the interaction of Cu with sub-critical Ni-Mn(Si) clusters, then it would be expected that the regions where these clusters were locally higher in number density would be more favourable sites for Cu precipitation. Table 6.4 shows, for a given number of MC steps, if there was a statistically significant increase in the number density of clusters in the regions within ±2 nm in $x$, $y$ and $z$ of the centre of where Cu-enriched precipitates were located after $10^{10}$ MC

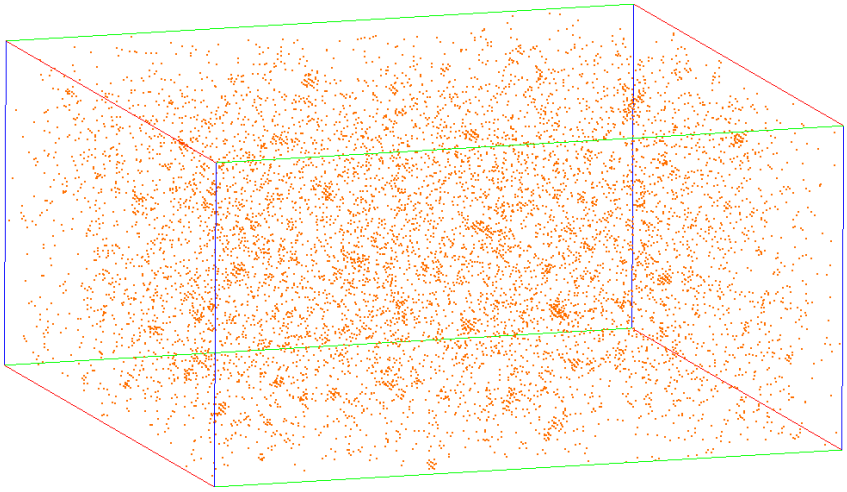

*(a)* Simulated SG atom map after $10^{10}$ MC steps at 330 °C.

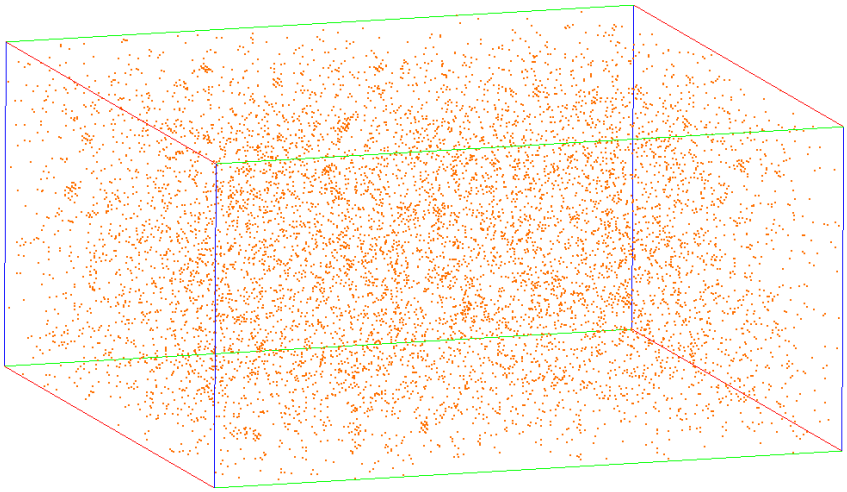

*(b)* Simulated SG atom map after $10^{10}$ MC steps at 365 °C.

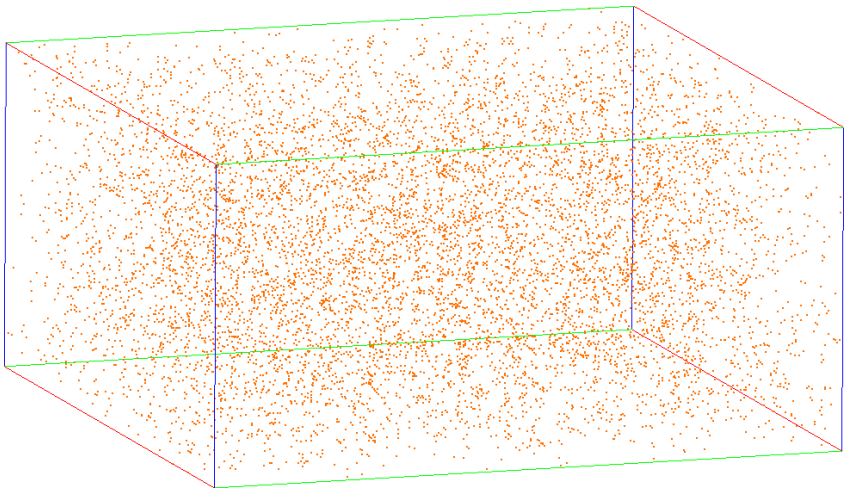

*(c)* Simulated SG atom map after $10^{10}$ MC steps at 405 °C.

*Figure 6.8:* Simulated atom maps of the SG steels after $10^{10}$ MC steps (a) 330 °C, (b) 365 °C and (c) 405 °C.

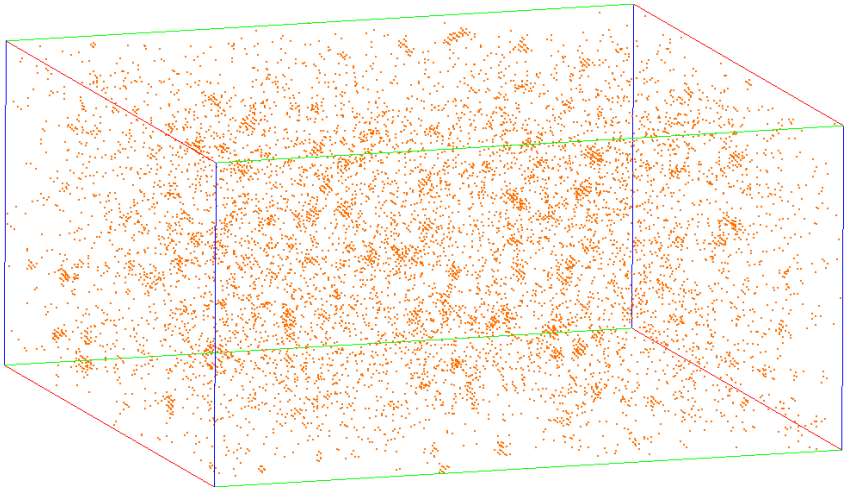

*(a)* Simulated WV atom map after $10^{10}$ MC steps at 330 °C.

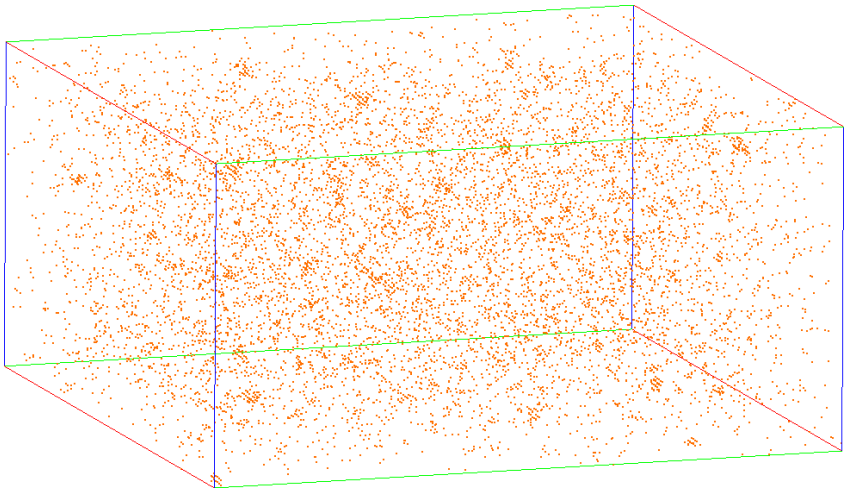

*(b)* Simulated WV atom map after $10^{10}$ MC steps at 365 °C.

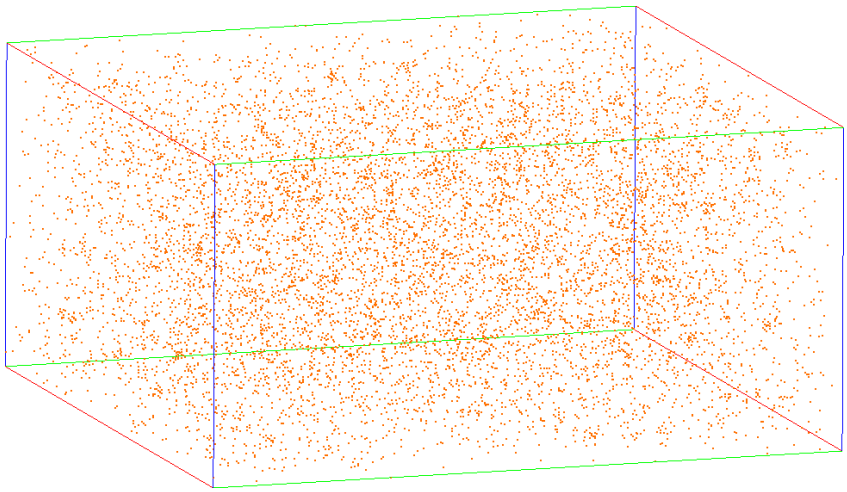

*(c)* Simulated WV atom map after $10^{10}$ MC steps at 405 °C.

*Figure 6.9:* Simulated atom maps of the WV steels after $10^{10}$ MC steps (a) 330 °C, (b) 365 °C and (c) 405 °C.

steps compared to the remaining volume[1]. Statistical significance was defined as the difference in the number densities being larger than the error in the difference, i.e $N_d^{(L)} - N_d^{(U)} > \sqrt{(\Delta N_d^{(L)})^2 + (\Delta N_d^{(U)})^2}$. Where $N_d^{(L/U)}$ and $\Delta N_d^{(L/U)}$ are the number density and error in the number density of clusters, with $L$ and $U$ indicating the regions within/outside of the subsequent nucleation sites of Cu-enriched precipitates. In Table 6.4, 'Y' indicates that there was a statistically significant increase, 'N' indicates there is no significant increase.

Table 6.4 indicates that around the time at which Cu-enriched precipitates are nucleating (approximately $10^8$ - $10^9$ MC steps for WV and 5 x $10^8$ - 5 x $10^9$ MC steps for SG) there appears to be more Ni-Mn clusters in the regions where Cu-enriched precipitates are nucleating than those where they are not. In Figure 6.4 a * indicates the approximate point at which visible clustering becomes detectable. This is particularly the case for the WV steels where there is a significantly higher number of clusters well before the precipitation of Cu becomes detectable. This is less so for the SG steels, except after simulated ageing at 405 °C. It is possible that at the higher temperature, with a lower supersaturation, that the nucleation of Cu-enriched precipitates requires the presence of Ni and Mn to lower the interfacial energy and hence the barrier to nucleation. This is consistent with the observed APT results for SG at the higher temperatures where the majority of the precipitates are observed at dislocations. This suggests that these clusters may well be involved in the nucleation of Cu-enriched precipitates.

The evolution of the composition of the clusters at the sites of Cu-enriched precipitates and those in the remaining volume, is shown in Figure 6.10. This shows the evolution of the composition of all the clusters larger than 4 atoms in size. Solid lines indicate the composition of the clusters which were within 2 nm of where a precipitate was subsequently located after $10^{10}$ MC steps. The dashed lines are those in the volume not associated with the final position of a Cu-enriched precipitate.

[1] That is in those regions outside the 4 nm cubes surrounding the subsequent nucleation sites of Cu-enriched precipitates.

| Number of MC steps | WV 405 °C | SG 405 °C | WV 365 °C | SG 365 °C | WV 330 °C | SG 330 °C |
|---|---|---|---|---|---|---|
| 1 E+00 | Y | N | N | N | N | N |
| 1 E+05 | Y | N | N | N | N | N |
| 5 E+05 | Y | N | N | N | N | N |
| 1 E+06 | Y | N | N | N | Y | N |
| 2 E+06 | Y | Y | N | N | Y | N |
| 3 E+06 | N | Y | N | N | Y | N |
| 4 E+06 | N | Y | Y | N | Y | N |
| 5 E+06 | Y | Y | N | N | Y | N |
| 6 E+06 | Y | Y | N | N | Y | N |
| 7 E+06 | Y | Y | N | N | Y | N |
| 8 E+06 | Y | Y | Y | N | Y | N |
| 9 E+06 | Y | Y | Y | N | Y | N |
| 1 E+07 | Y | Y | Y | N | Y | N |
| 2 E+07 | Y | Y | Y | N | N | N |
| 3 E+07 | Y | Y | Y | N | Y | N |
| 4 E+07 | Y | Y | N | N | Y | N |
| 5 E+07 | Y | Y | N | N | N | N |
| 6 E+07 | Y | Y | Y | N | Y | N |
| 7 E+07 | Y | Y | Y | N | N | N |
| 8 E+07 | Y | Y | Y | N | Y | N |
| 9 E+07 | Y | Y | Y | N | Y | N |
| 1 E+08 | Y* | Y | Y* | Y | N* | Y |
| 2 E+08 | Y | Y | Y | N | Y | N |
| 3 E+08 | Y | Y | Y | N | Y | N |
| 4 E+08 | Y | Y | Y | Y | Y | N |
| 5 E+08 | Y | Y* | Y | Y | Y | N |
| 6 E+08 | Y | Y | Y | N | Y | N |
| 7 E+08 | Y | Y | Y | Y | Y | Y |
| 8 E+08 | N | Y | Y | Y | Y | Y |
| 9 E+08 | Y | Y | Y | Y | N | N |
| 1 E+09 | Y | Y | Y | N* | Y | N* |
| 2 E+09 | Y | Y | Y | Y | Y | N |
| 3 E+09 | Y | Y | Y | N | Y | Y |
| 4 E+09 | Y | Y | Y | Y | Y | Y |
| 5 E+09 | Y | Y | Y | Y | Y | N |
| 6 E+09 | Y | Y | Y | Y | Y | Y |
| 7 E+09 | Y | Y | Y | Y | Y | Y |
| 8 E+09 | Y | Y | Y | Y | Y | Y |
| 9 E+09 | Y | Y | Y | Y | Y | Y |

*Table 6.4:* For a given number of MC steps a 'Y' indicates there was a statistically significant (as defined in the main text) increase in cluster number density in the regions where Cu-enriched precipitates were present after $10^{10}$ MC steps, whilst 'N' indicates there was no increase. *Indicates the approximate point at which visible clustering becomes detectable.

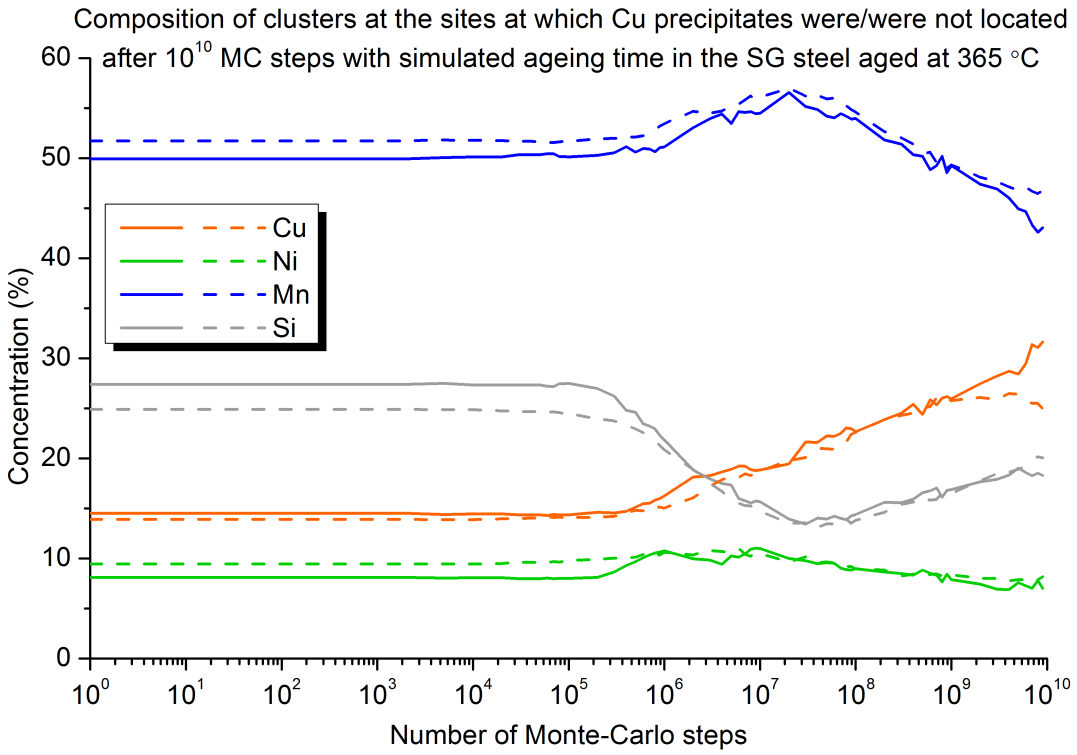


*(a)* SG simulation aged at 365 °C.

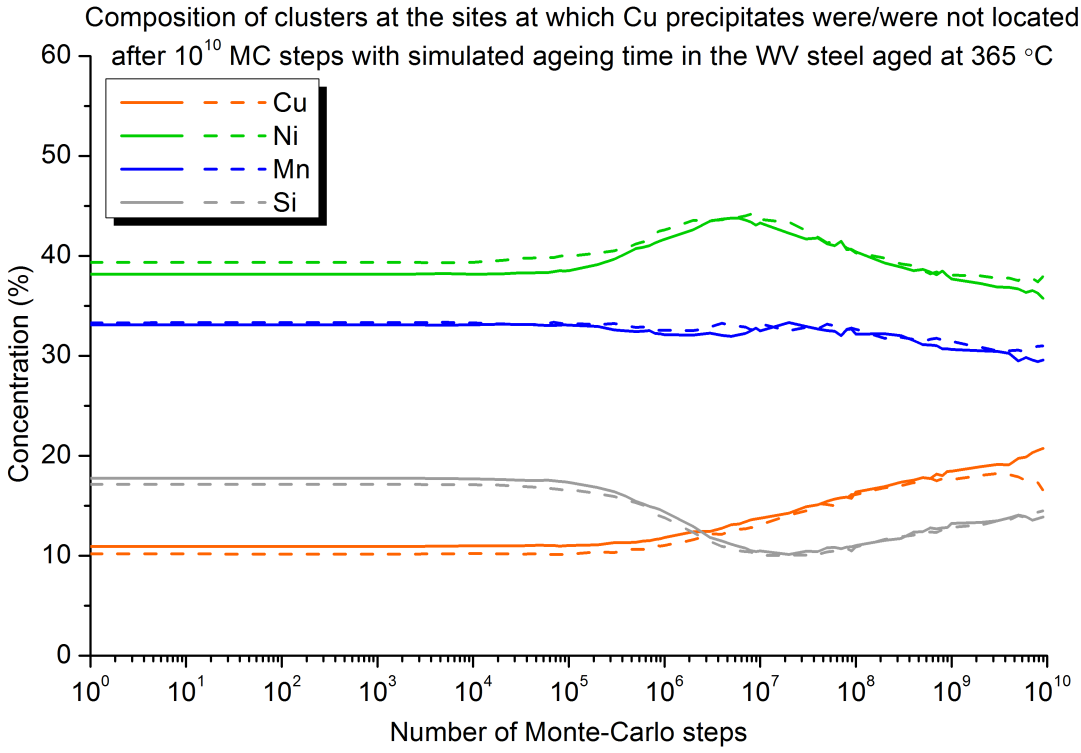


*(b)* WV simulation aged at 365 °C.

*Figure 6.10:* Composition of the clusters around the sites of Cu precipitates (solid lines) and those not associated with these sites (dashed lines) for the (a) SG and (b) WV simulations aged at 365 °C.

Whilst Figure 6.10 is for the 365 °C simulation, the results take the same form after the same number of MC steps in the simulations at 330 °C and 405 °C. It is clear that there is no significant difference in the average composition of features, regardless of their location relative to the final position of Cu-enriched precipitates. In the early stages of the simulations the clusters are predominantly Ni-Mn-Si rich, and contain relatively little Cu. In the WV simulations, Ni is the most common constituent of the clusters whilst in the SG simulations the concentration of Ni is much lower which reflects the lower bulk Ni content of this steel. After around $10^6$ - $10^7$ MC steps the Mn concentration of the clusters in the SG steel peaks as does the Ni content in the WV steel. This probably reflects the observations from Section 6.3.2 that Ni and Mn enrich around the sites of Cu atoms and pairs of Cu atoms. The differences in Mn and Si enrichment between the two is probably related to the fact that Figure 6.10 considers clusters greater than 4 atoms rather than only single or pairs of Cu atoms. As the simulation progresses the clusters enrich in Cu at the expense of Ni, Mn and Si. The reduction and subsequent increase in Si arises from the fact that the number of Ni and Mn atoms in these clusters initially increases more quickly than Si before slowing, whilst the number of Si atoms increases more linearly over the same range.

After $10^{10}$ MC steps the Cu concentration in small clusters not associated with Cu-enriched precipitates starts to decrease. This reflects the fact that the Cu that was in those clusters is progressively being incorporated into larger Cu clusters located elsewhere in the simulation. Hence, over time the local matrix Cu in these regions will become depleted.

### 6.3.4 The Evolution of Ni-Mn Clusters

The previous sections in this chapter have shown strong indications that Ni-Mn clusters are involved in the early stages of Cu precipitation. The evolution of the population of Ni-Mn clusters and their association with Cu atoms is studied in more detail in this section.

| No. of Cu atoms | Number of MC steps | | | | | | | |
|---|---|---|---|---|---|---|---|---|
| | 1 | 1E+04 | 1E+05 | 1E+06 | 1E+07 | 1E+08 | 2E+08 | 3E+08 |
| 0 | 1564 | 1569 | 1587 | 1680 | 1992 | 1851 | 1814 | 1816 |
| 1 | 244 | 244 | 246 | 292 | 511 | 559 | 529 | 523 |
| 2 | 29 | 30 | 30 | 33 | 74 | 129 | 136 | 135 |
| 3 | 3 | 4 | 4 | 4 | 11 | 21 | 25 | 28 |
| 4 | 0 | 0 | 0 | 0 | 2 | 3 | 6 | 6 |
| 5 | 0 | 0 | 0 | 0 | 0 | 0 | 1 | 2 |

*Table 6.5:* Number of clusters containing a given number of Cu atoms and 3 Ni or Mn atoms in the WV simulation at an ageing temperature of 365 °C.

The maximum separation method was used to identify all instances where 2, or more, solute atoms were within the $d_{max}$ distance of 0.3 nm. This information was then used to investigate the number of Cu atoms associated with a cluster containing a given number of Ni or Mn atoms and how this evolved in the simulation. As an example, Table 6.5 shows the number of instances where a cluster containing a total of 3 Ni or Mn atoms was associated with a given number of Cu atoms. In this case between 0 and 5 Cu atoms, after a given number of MC steps in the WV simulation at an ageing temperature of 365 °C. For example, row 2 shows the number of clusters containing 1 Cu atom and 3 Ni or Mn atoms after a given number of MC steps.

Figure 6.11 shows the number of clusters containing 4 Ni or Mn atoms and between 0 and 4 Cu atoms at different points in the WV simulation at an ageing temperature of 365 °C. The results for different materials, ageing temperatures and a different number of Ni or Mn atoms all show the same trends. This shows that in all cases, whether for a cluster containing 4 Ni or Mn atoms and no Cu atoms or one containing 4 Ni or Mn atoms and 4 Cu atoms, that initially the number of these clusters increases. After around $10^7$ MC steps the population of each of these clusters plateaus. This indicates that a dynamic equilibrium was reached. Hence, the rate of new clusters of each type is balanced by the number which are growing or shrinking to join the population containing 1 extra/1 less Ni or Mn atom or 1 extra/1 less Cu atom. This holds for at least $10^{10}$ MC steps in the example given in Figure 6.11.

In addition to looking at how the population of clusters containing $X$ Ni or Mn atoms

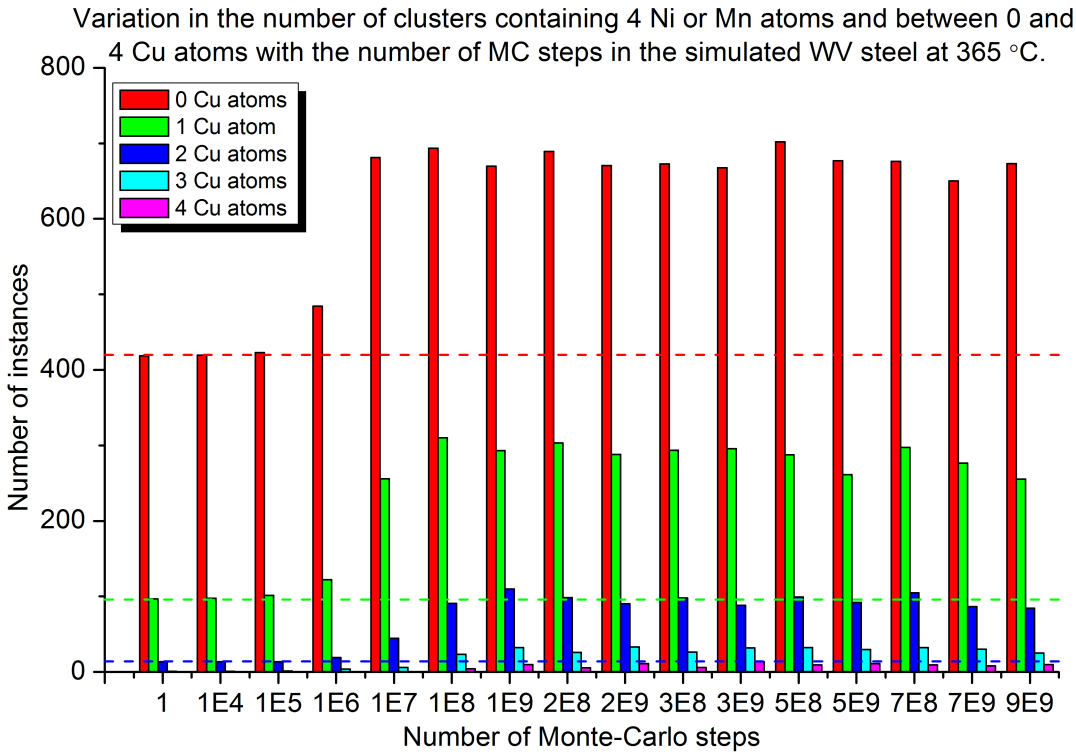


*Figure 6.11:* Number of clusters in the WV simulation at 365 °C containing 4 Ni or Mn atoms and between 0 and 4 Cu atoms after a given number of MC steps. Dashed lines indicate the number of instances in the initial random solid solution.

and a constant number of Cu atoms changes with ageing time (as in Figure 6.11), it is possible to investigate the distribution of clusters containing $X$ Ni or Mn atoms and $Y$ Cu atoms at different ageing times, as in Figure 6.12. This is the same as changing the $x$ axis from being time based (or the number of MC steps) to being different numbers of Cu atoms associated with a cluster containing a given number of Ni or Mn atoms. Figure 6.12 shows the number of instances where a given number of Cu atoms (between 0 - 7) were in a cluster containing between three and five Ni or Mn atoms in the WV and SG simulations at 365 °C. Very similar trends are seen in all the high Ni simulations and the low Ni simulations, so only the results from the WV and SG simulations at 365 °C are presented here.

In all cases in Figure 6.12, the SG simulations contain fewer instances of a cluster containing a given number of Ni, Mn and Cu atoms. This reflects the lower number of these clusters that will be present in this steel as a result of the lower bulk Ni content. As the simulation progresses, the number of instances of a larger number of

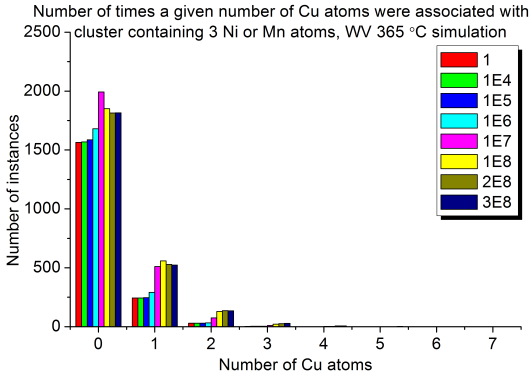


*(a)* Number of instances of a cluster containing 3 Ni or Mn atoms and a given number of Cu atoms, WV simulation at 365 °C.

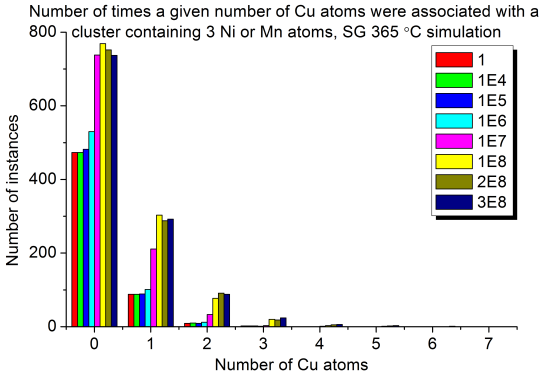


*(b)* Number of instances of a cluster containing 3 Ni or Mn atoms and a given number of Cu atoms, SG simulation at 365 °C.

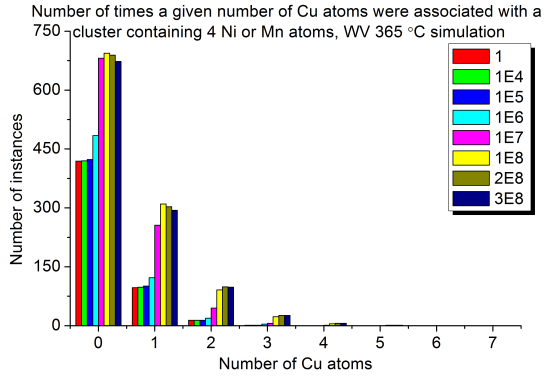


*(c)* Number of instances of a cluster containing 4 Ni or Mn atoms and a given number of Cu atoms, WV simulation at 365 °C.

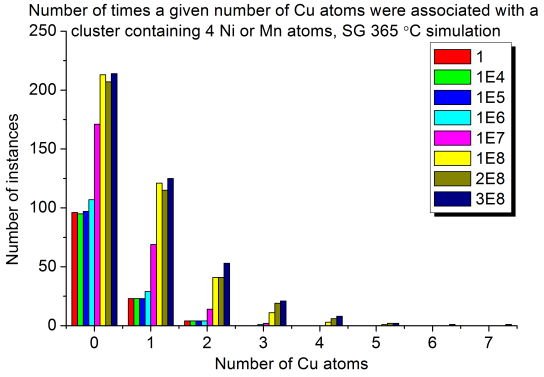


*(d)* Number of instances of a cluster containing 4 Ni or Mn atoms and a given number of Cu atoms, SG simulation at 365 °C.

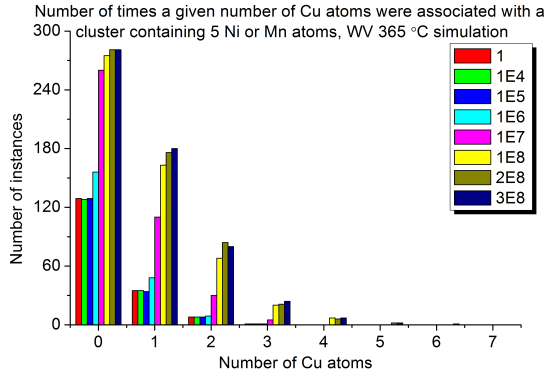


*(e)* Number of instances of a cluster containing 5 Ni or Mn atoms and a given number of Cu atoms, WV simulation at 365 °C.

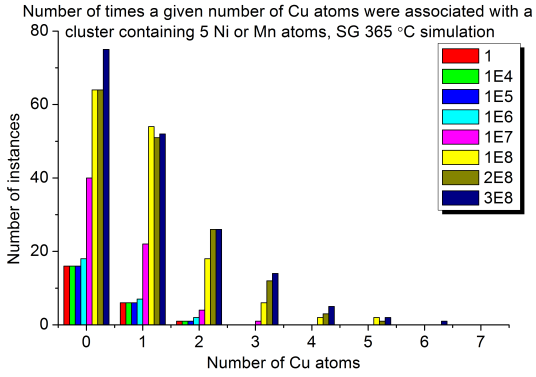


*(f)* Number of instances of a cluster containing 5 Ni or Mn atoms and a given number of Cu atoms, SG simulation at 365 °C.

*Figure 6.12:* Number of instances of a cluster containing between 3 and 5 Ni or Mn atoms and having a given number of Cu atoms associated with it in the SG and WV simulations at 365 °C.

Cu atoms associated with a cluster containing the same number of Ni or Mn atoms increases. For example, for a cluster containing 4 Ni or Mn atoms the number of clusters also containing 3 Cu atoms increases from 1 after 1 x $10^8$ MC steps to 26 after 3 x $10^8$ MC steps. In the corresponding SG simulation there are 21 after 3 x $10^8$ MC steps. This trend is repeated for all instances of clusters containing between 1 and 8 Ni or Mn atoms for both the SG and WV simulations. The only difference is that in the SG simulations the number of instances of a given combination is less.

It is important to remember that these only give a snapshot of the simulation after a given number of MC steps and in reality things are constantly evolving. Nonetheless, it again suggests that sub-critical Ni and Mn clusters are involved in the precipitation of Cu. Furthermore, the discrepancies between high and low Ni steels could be related to the fact that there are simply fewer of these clusters in the low Ni materials. This will be discussed in more detail in Section 7.3.

### 6.3.5 Cu-enriched Precipitate Nucleation Mechanisms

The results presented so far in this chapter have shown that sub-critical Ni-Mn clusters are involved at the very early stages of the precipitation of Cu. Currently little has been said about the mechanism by which Cu-enriched precipitates nucleate. This could be one of three ways:

- Heterogeneous nucleation on sub-critical Ni-Mn clusters. In this case a sudden jump in the size of the cluster and its Cu concentration would be expected at the point of nucleation.
- Impingement of two (or more) sub-critical clusters which form one super-critical nucleus. In this case there would be sudden jump in the cluster size, but the composition would remain roughly constant.
- Evolution from sub-critical Ni-Mn clusters. In this case the size would increase gradually and the composition would slowly increase in Cu and decrease in Ni

and Mn.

To investigate which nucleation mechanism may be occurring in these steels the composition and size evolution with time has been investigated for four clusters. Two are from the WV simulation at a temperature of 365 °C and two from the SG simulation also at 365 °C. The two clusters from the WV simulation reach similar final sizes of 950 atoms whilst in the SG steel the largest two clusters have sizes of around 900 and 700 atoms. The evolution of the size of these four clusters with the number of MC steps is shown in Figure 6.13a. To see the relative change in composition of these features the ratio of Cu:Ni+Mn+Si is plotted against the number of MC steps and is shown in Figure 6.13b. A ratio below 1 indicates clusters are Ni, Mn and Si rich conversely, a ratio above 1 means clusters are Cu rich.

Figure 6.13a does not show any sudden jump in the size of any of the four features at the early times which might be indicative of an impingement or heterogeneous nucleation mechanism. The composition of two of the features (those with dashed lines in Figure 6.13b) show sharp increases in the Cu content of the clusters at the point at which they become visible. This could indicate that for these two clusters a heterogeneous nucleation process is occurring, whilst an evolutionary mechanism seems likely for the other two clusters based on their composition. Although, for the cluster represented by solid black line it is possible this may show some variation in composition prior to it being detected in the simulation i.e prior to 1 x $10^9$ MC steps. The exact mechanism is tricky to pinpoint, as in the case of these four clusters, nucleation occurs between MC steps at which data is available. Atom maps of 4 nm x 4 nm x 4 nm regions centred around the nucleation site of largest SG and WV precipitates studied (corresponding to the red and black solid lines in Figure 6.13) are shown in Figures 6.14 and 6.15.

These atom maps show that these two clusters become visible after 1 x $10^{10}$ MC steps in the SG steel and 1 x $10^9$ MC steps in the WV steel. Prior to that the clusters are not evident in these small volumes and are also not detectable with a cluster

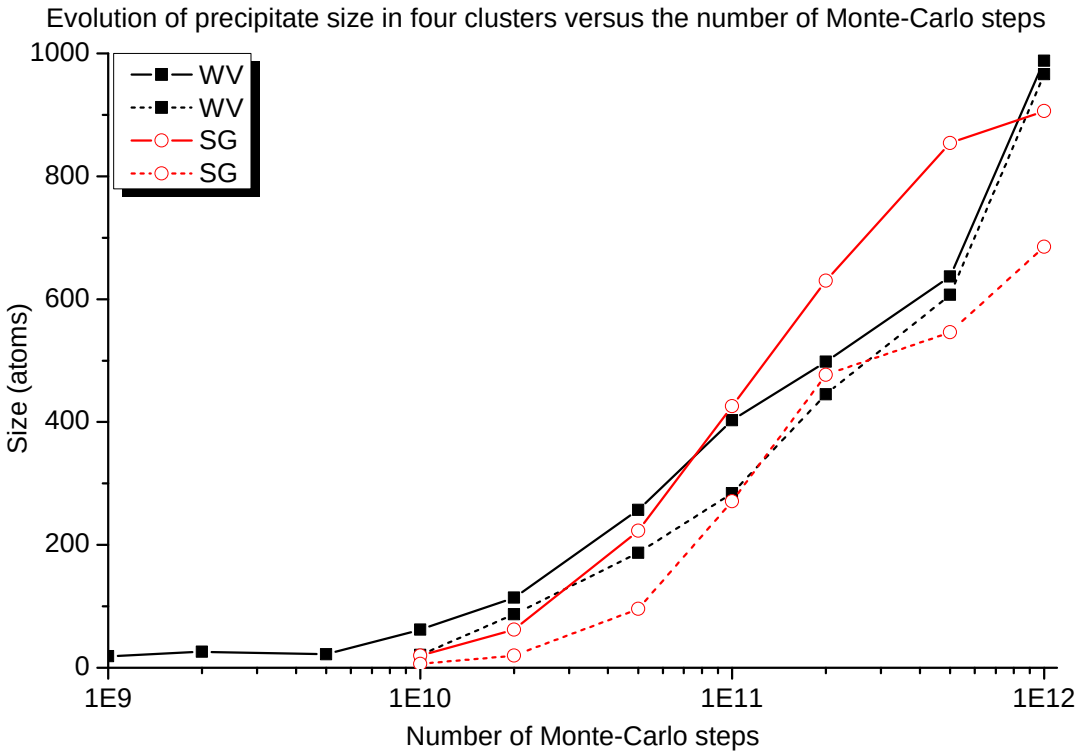


*(a)* Cluster size evolution.

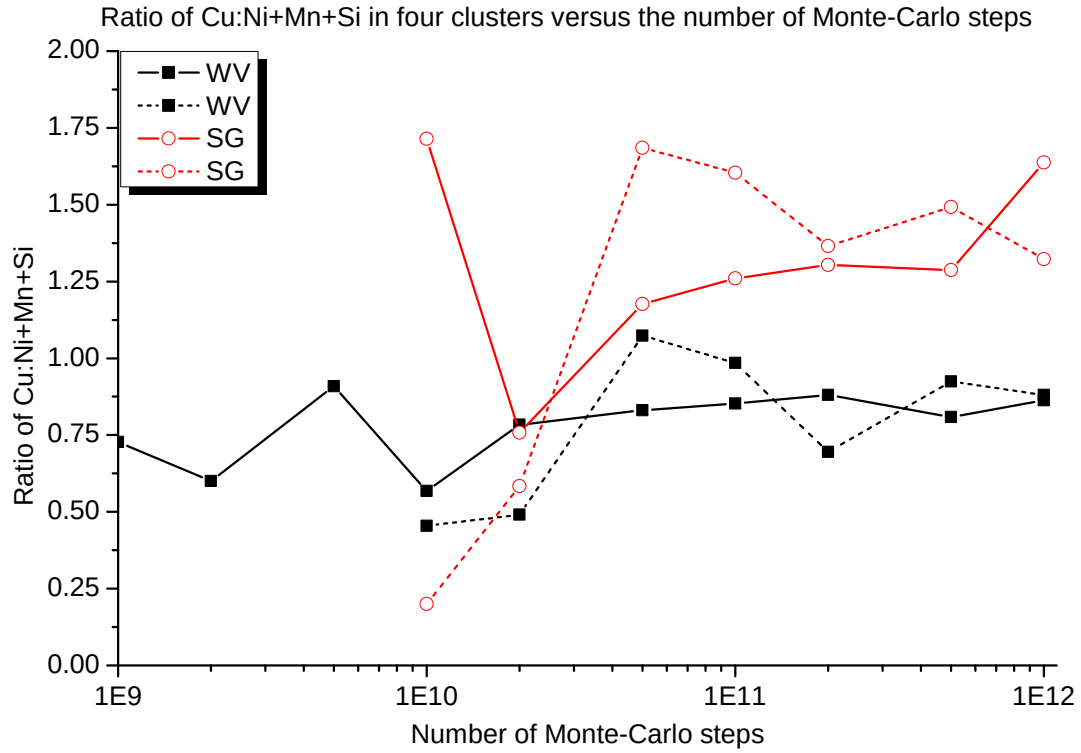


*(b)* Composition evolution.

*Figure 6.13:* (a) Cluster size evolution versus number of MC steps and (b) ratio of Cu:Ni+Mn+Si in the clusters with number of MC steps for four clusters from the WV and SG simulations at 365 °C. Dashed/solid lines and filled/unfilled shapes correspond to the same cluster in (a) and (b).

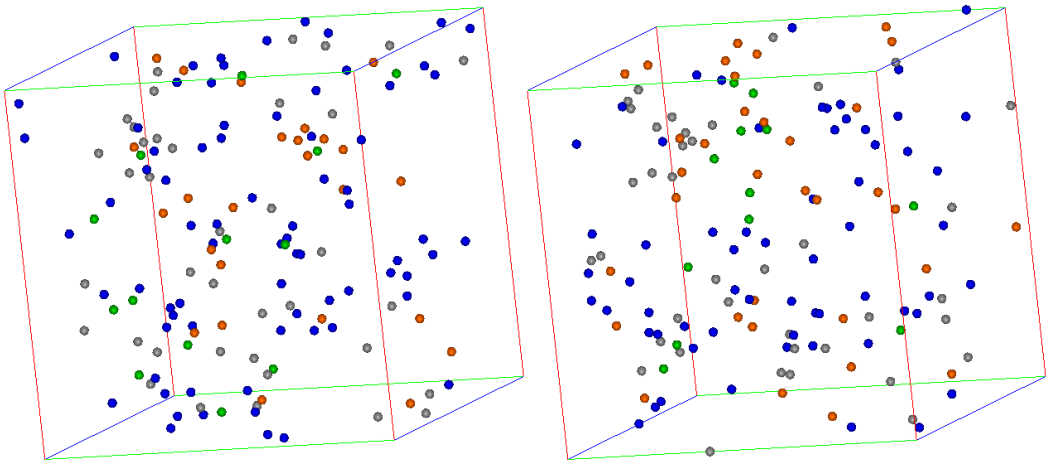

*(a)* 1 x $10^9$ MC steps.



*(b)* 5 x $10^9$ MC steps.

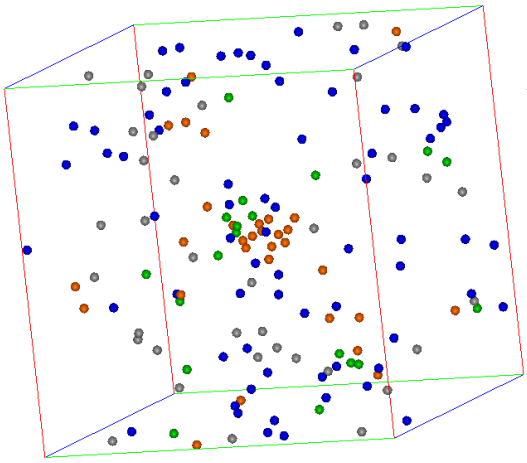

*(c)* 1 x $10^{10}$ MC steps.

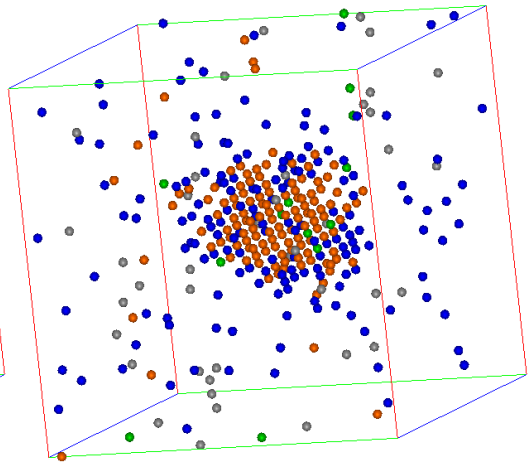

*(d)* 5 x $10^{10}$ MC steps.

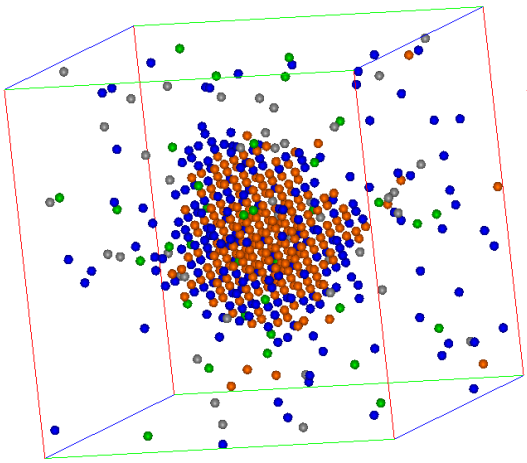

*(e)* 1 x $10^{11}$ MC steps.

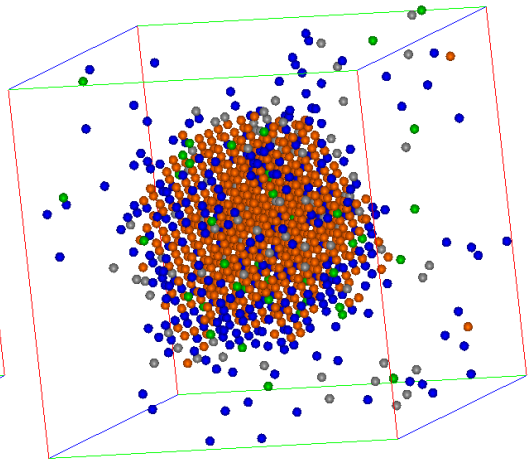

*(f)* 1 x $10^{12}$ MC steps.

*Figure 6.14:* Atom maps showing a 4 nm cubic region around the site at which a Cu-enriched precipitate formed in the SG 365 °C simulation after (a) 1 x $10^9$ MC steps, (b) 5 x $10^9$ MC steps, (c) 1 x $10^{10}$ MC steps, (d) 5 x $10^{10}$ MC steps, (e) 1 x $10^{11}$ MC steps, (f) 1 x $10^{12}$ MC steps. Spheres coloured as follows: orange - Cu atoms, green - Ni atoms, blue - Mn atoms and grey - Si atoms, Fe atoms not shown for clarity.

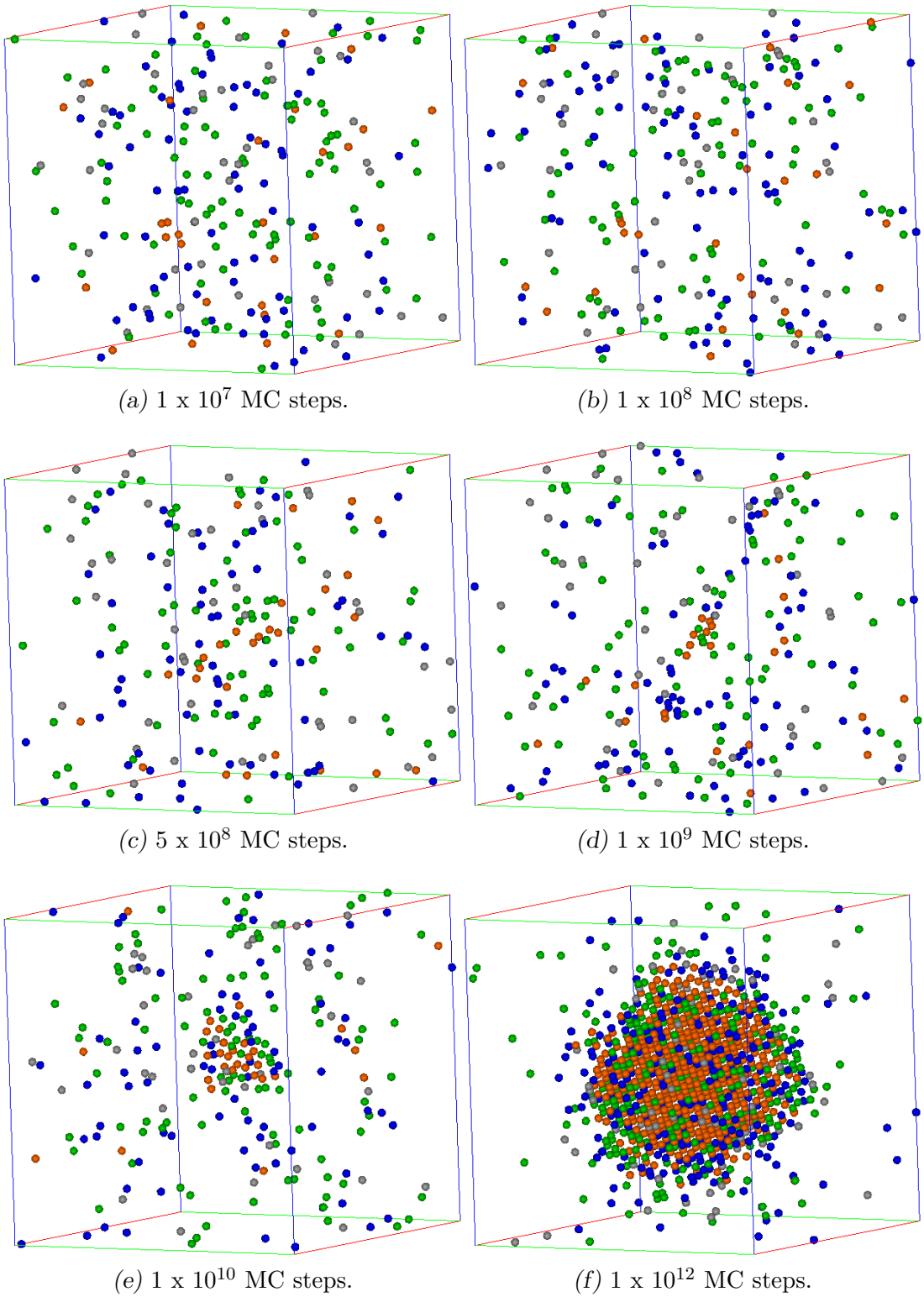

*(a)* 1 x $10^7$ MC steps. *(b)* 1 x $10^8$ MC steps.

*(c)* 5 x $10^8$ MC steps. *(d)* 1 x $10^9$ MC steps.

*(e)* 1 x $10^{10}$ MC steps. *(f)* 1 x $10^{12}$ MC steps.

*Figure 6.15:* Atom maps showing a 4 nm cubic region around the site at which a Cu-enriched precipitate formed in the WV 365 °C simulation after (a) 1 x $10^7$ MC steps, (b) 1 x $10^8$ MC steps, (c) 5 x $10^8$ MC steps, (d) 1 x $10^9$ MC steps, (e) 1 x $10^{10}$ MC steps, (f) 1 x $10^{12}$ MC steps. Spheres coloured as follows: orange - Cu atoms, green - Ni atoms, blue - Mn atoms and grey - Si atoms, Fe atoms not shown for clarity.

search. In Figure 6.14c it appears the early stage cluster is a hybrid of a Ni-Mn rich and Cu rich region. This is also evident in the WV steel in Figure 6.15d. For at least two of the clusters studied, an evolutionary mechanism whereby Cu-enriched clusters grow from an initial Ni-Mn(Si) rich cluster seems most likely. It is also possible that all three mechanisms may occur. Further, investigation with smaller timesteps between the output of atom maps is required to conclusively determine which nucleation mechanism(s) is/are occurring. Videos like those produced in the Section 6.3.6 may also provide insight into the specific nucleation mechanisms at play.

### 6.3.6 Visualisation of Cluster Formation

The final topic in this chapter again concerns the early stages of cluster formation and provides more of an illustrative perspective to some the previous quantitative analysis. One of the aims of the Monte-Carlo modelling in this project was to produce a video which showed the formation of clusters in the simulation. The ability to track individual solute atoms, combined with the fact that the final position of the clusters is known, makes it is possible to produce a video centred at the position of a cluster at the end of the simulation and study the movement of atoms at this point throughout the simulation. Given the large number of solute jumps involved it is not possible to show every solute jump made in the formation of a cluster. Instead the positions of solute atoms are shown after every 50,000 solute jumps for the first 20 million solute-vacancy transitions and then after every 2 million solute transitions. This ensures that more detailed information is retained about the early stages of nucleation. With the current set up it is not possible to determine the time-scale of these videos.

The attached DVD contains videos showing the formation of individual clusters in the WV and SG simulations at an ageing temperature of 365 °C. These can be found in the folder “Visualisation of Cluster Formation”. Frames from the videos showing the approximate point of nucleation of a cluster in the SG and WV simulations are shown in Figure 6.16.

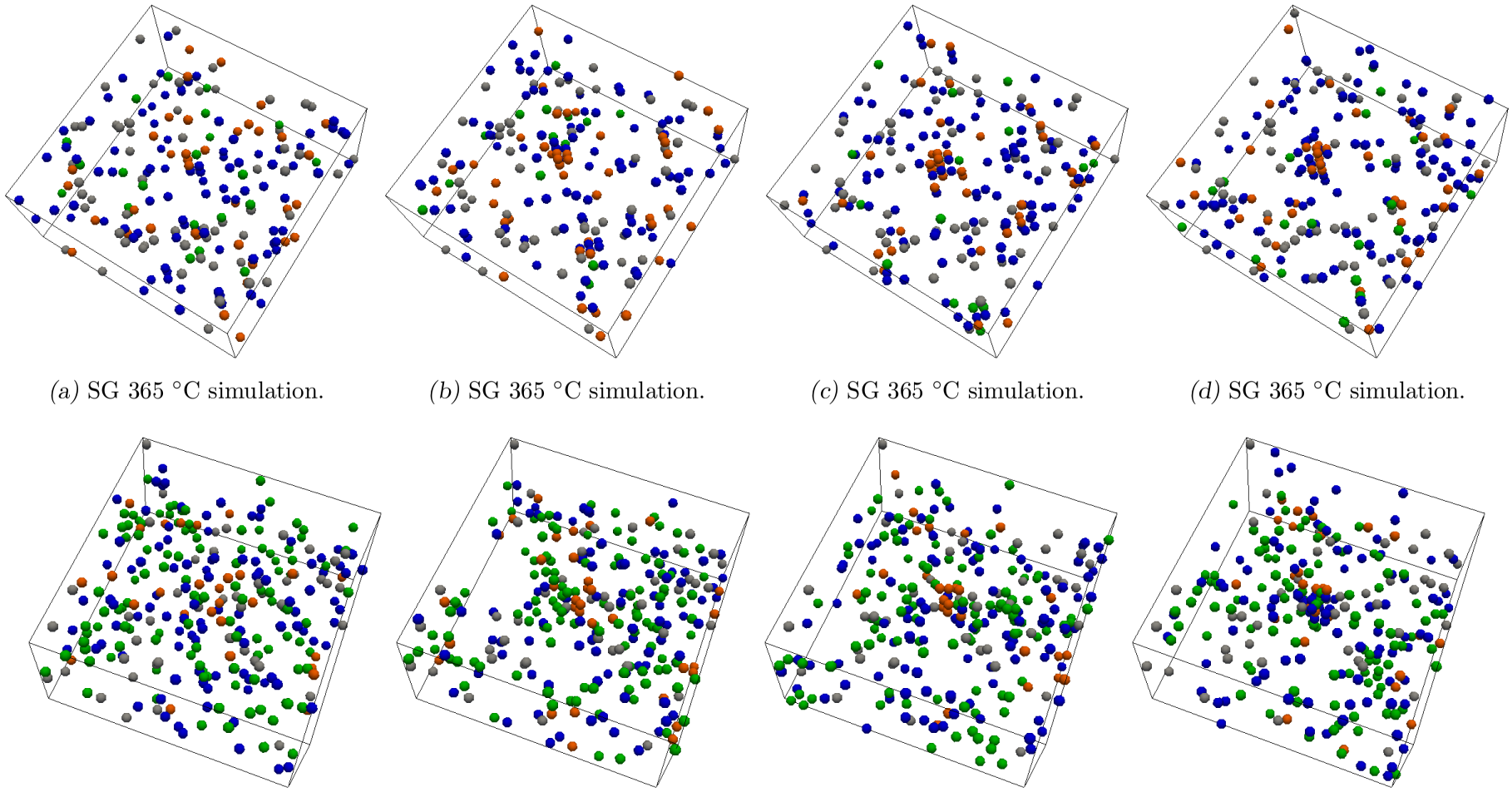

*(a)* SG 365 °C simulation. *(b)* SG 365 °C simulation. *(c)* SG 365 °C simulation. *(d)* SG 365 °C simulation.

*(e)* WV 365 °C simulation. *(f)* WV 365 °C simulation. *(g)* WV 365 °C simulation. *(h)* WV 365 °C simulation.

*Figure 6.16:* Frames from the video showing the formation of clusters during simulated ageing of the SG ((a) - (d)) and WV ((e) - (h)) steels at 365 °C. Orange spheres - Cu atoms, green spheres - Ni atoms, blue spheres - Mn atoms, grey spheres - Si atoms. Fe atoms not shown for clarity.

Figure 6.16 demonstrates that there are differences between the two simulations at the point which a visible cluster first becomes evident. As would be expected, in the higher Ni steel, WV, there is more Ni associated with the cluster than in the SG simulation. In most frames in Figures 6.16e to 6.16h there are roughly equal proportions of Mn and Ni. In the SG simulations, there are only one or two Ni atoms associated with the Cu cluster, primarily it is associated with Mn. In both the SG and WV simulations there are fewer Si atoms than Ni or Mn atoms associated with the Cu cluster. This is consistent with the previous work in this chapter, in that Si is not active in the early stages of nucleation. As the simulations progress, the Cu cluster grows and evolves to have a nearly pure Cu core with Ni, Mn and Si atoms moving around at the interface between the Cu precipitate and the Fe matrix. The Fe matrix is not shown in the videos or Figure 6.16 for clarity.

In both cases shown in Figure 6.16 Cu-enriched precipitates appear to be associated with Ni and/or Mn atoms at the onset of their formation.

## 6.4 Summary

The Monte-Carlo simulations have been extended to obtain more detailed information on the formation and evolution of Cu-enriched precipitates under thermal ageing conditions. Various techniques have been used which all indicate that there is a strong synergy between the early stages of Cu-precipitation and the presence of Ni and Mn.

It was observed that the first species to show non-randomness was Cu, closely followed by Ni and Mn. Si clustering occurred much later indicating it is unlikely to be active in the very early stages of Cu precipitation. Ni and Mn were also found to enrich in the nearest neighbour sites of Cu atoms and Cu atom pairs before visible clustering became evident. This segregation to the interface will lower the interfacial energy of small clusters making nucleation more favourable.

The simulations also reveal the presence of a high number density of sub-critical Ni-Mn rich clusters which constantly form and dissolve as the simulation progresses. These sub-critical clusters were found to be more numerous in the regions where a Cu-enriched precipitate subsequently formed. In the WV steel these sub-critical clusters were more numerous and more Ni-rich, reflecting the higher bulk Ni content of the this alloy.

The evolution of the sub-critical clusters and their association with Cu with time was also studied by looking at the population of clusters containing a given number of Ni, Mn and Cu atoms. It was found that as the simulation progressed, more Cu atoms became associated with a cluster containing a given number of Ni and Mn atoms. There were more instances of this association in the higher Ni steel than in the low Ni one. Again this reflected the fact that there are more sub-critical Ni-Mn clusters in the high Ni steel.

Investigation of the precise role of Ni and Mn in the nucleation/formation of a Cu-enriched precipitate was performed and was found to be variable. It appears that Cu-enriched precipitates can evolve with time from a cluster initially rich in Ni and Mn. However, an impingement mechanism (two or more sub-critical clusters combining to make one stable cluster) or heterogeneous nucleation on sub-critical Ni-Mn clusters cannot be discounted. Neither can it be ruled out that a combination of these three mechanisms is occurring.

# 7. Discussion

Section 2.5 presented an overview of some of the main unresolved issues from the literature on the formation and evolution of Cu-enriched precipitates in RPV steels and model alloys. There were five main issues that were identified:

- The need to understand the long term trends in mechanical properties as a function of alloy composition.
- There is relatively little data on the long-term evolution of Cu-enriched precipitates under thermal ageing.
- The Fe content of precipitates is relatively poorly understood.
- The formation of Ni-Mn-Si precipitates in thermally aged materials has been postulated but not directly observed.
- The effects of different solute atoms on the formation of Cu-enriched precipitates are not well understood.

These issues will be addressed and discussed in the context of the APT and Monte-Carlo modelling work presented in Chapters 5 and 6.

## 7.1 Relation of Microstructural Data to Hardness Changes

Before discussing the reasons for observed differences in hardening between the high Cu SG and WV steels and the low Cu WF steels, it is important to discuss some of the

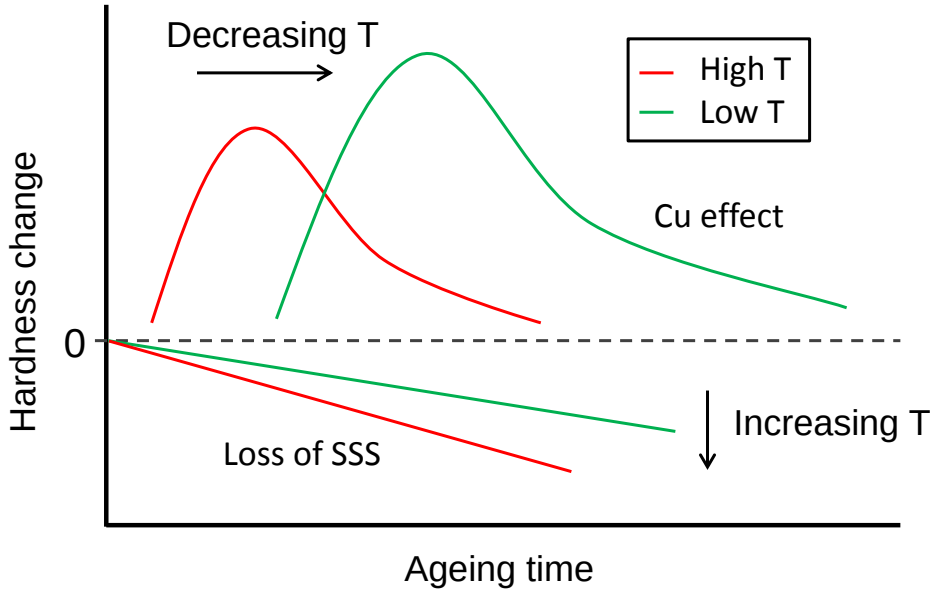


*Figure 7.1:* Schematic diagram showing the possible contributions to the changes in hardness from Cu precipitation and loss of SSS with ageing temperature.

effects that are at play in these steels and their contribution to the hardness. There are two effects which cause hardness changes in these materials: the precipitation of Cu, which increases the hardness, and the loss of solid solution strength (SSS) due to precipitation, and the segregation of elements at grain boundaries, these will reduce the hardness[1]. The contribution of these effects and their approximate relation with ageing temperature are shown schematically in Figure 7.1.

At higher temperatures, the maximum hardening increase due to Cu is smaller and occurs more quickly than at lower temperatures. The loss of SSS is also temperature dependent and will be accelerated at higher temperature due to the increased mobility of solutes. Eventually this effect will be lost altogether as the solubility limit increases at higher temperature. For the high Cu steels, Cu precipitation will be the dominant contributor to the hardness changes.

[1] For small grained materials segregation to grain boundaries can increase the hardness due to increases in the Hall-Petch co-efficient. The steels in this work are relatively coarse grained and hence this effect will be small.

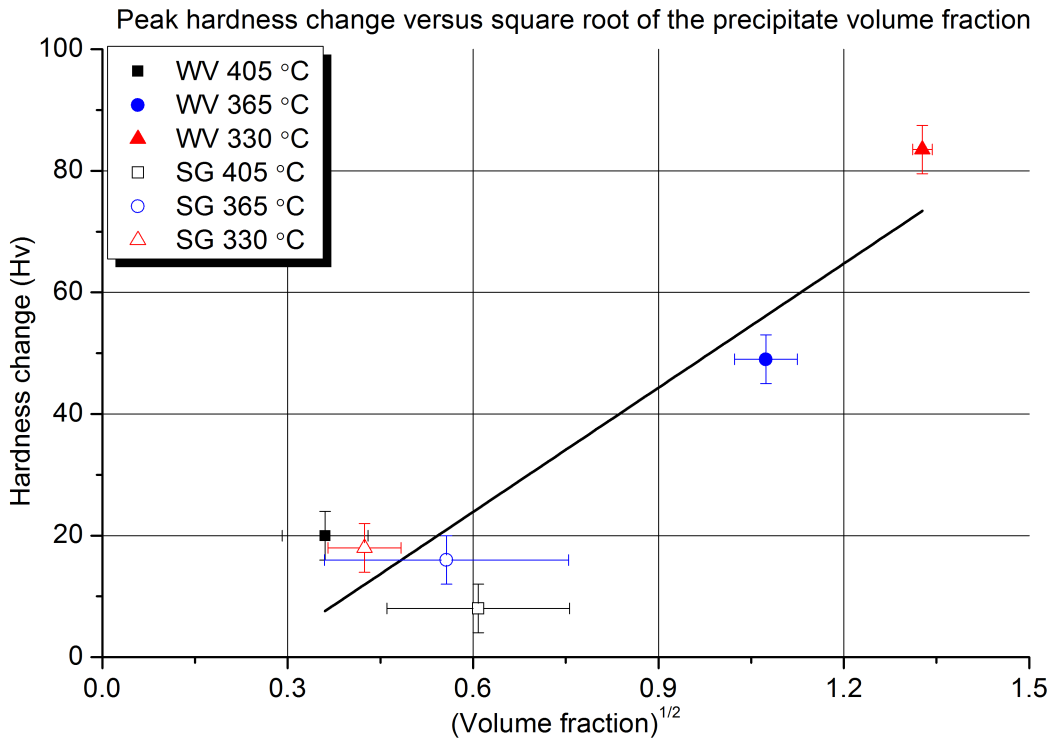


*Figure 7.2:* Plot of the square root of the precipitate volume fraction versus the peak hardness change for the WV and SG steels. All data except for the WV steels aged at 330 °C and 365 °C from the ECOPoSAP data of Morley.

### 7.1.1 High Cu Materials, WV and SG

According to the Russell-Brown model[164] the maximum change in strength should be proportional to the square root of the volume fraction of precipitates, provided precipitates are of equal, or near equal size. A plot of the peak hardness value versus the square root of the corresponding volume fraction is shown in Figure 7.2 for the WV and SG steels for all temperatures studied.

There is some scatter, particularly for the SG steels aged at the two highest temperatures but a reasonable overall fit to the data is observed. This indicates that the increases in hardness of these alloys are mainly due to the presence of Cu precipitates. The Russell-Brown model also predicts that the change in strength due to the precipitates should be inversely proportional to the distance between them for materials in the overaged state. The inter-particle spacing can easily be calculated from the number density. Figure 7.3 shows the inverse of the inter-particle distance

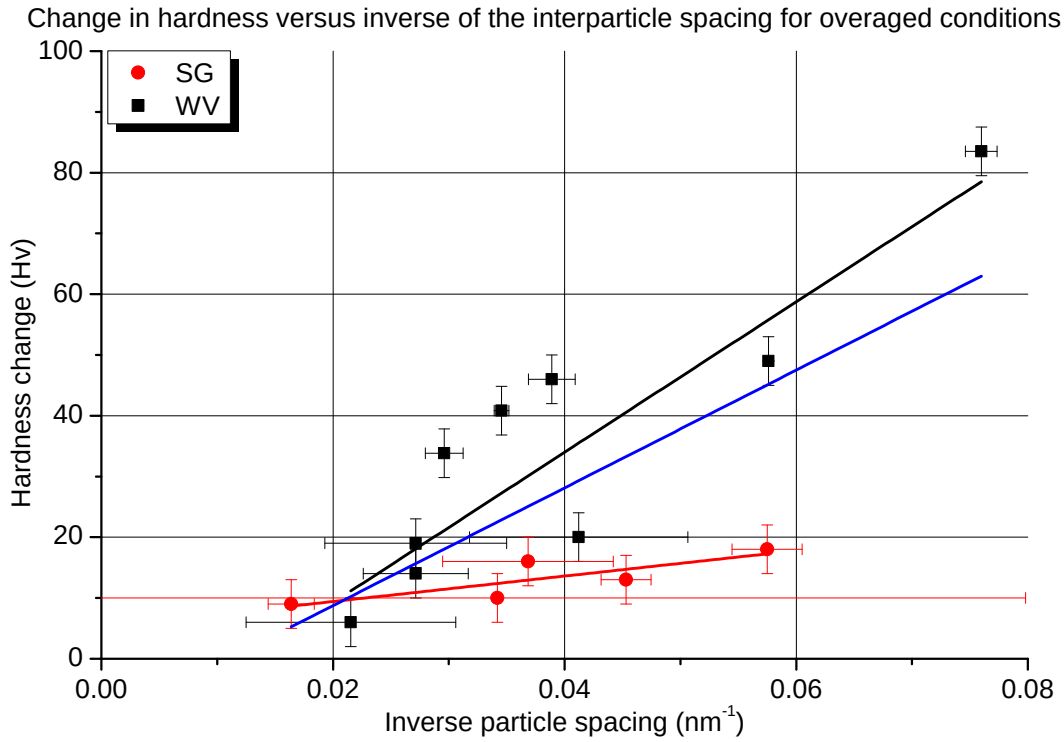


*Figure 7.3:* Plot of the inverse of the inter-particle spacing versus the change in hardness for the WV and SG steels which have been overaged. Black fitted line is the fit for the WV data only, red fitted line for the SG data only and blue fitted line the fit for all the data. Data points are a combination of those from this study and those from the ECOPoSAP data of Morley.

versus the change in hardness for materials which have been overaged.

The linear fits to the data in Figure 7.3 indicate a relatively poor fit if the data from both the SG and WV steels are combined (blue line). However, if plotted individually for the WV (black line), and SG steels (red line), better fits are obtained. The gradient of these fits is related to how effective an obstacle the particles are to dislocation motion. The steeper the gradient the more effective obstacles the precipitates are. Figure 7.3 indicates that the features in the WV steel are better obstacles to dislocations than the precipitates in the SG steel.

It is important to remember that there is an associated distribution of precipitate sizes, so some features may be better obstacles than others, particularly semi-coherent 9R or incoherent fcc precipitates. Notwithstanding this, the increased hardening capability of the WV precipitates could be due to a number of reasons. The majority of the features in the SG steels were observed on dislocations and were very large, probably

with a semi-coherent 9R, or fcc like structure. This is particularly the case at 365 °C and most likely in the material aged at 405 °C too. At the lower ageing temperature of 330 °C some smaller precipitates were also observed which were not associated with dislocations. Whilst these large features will be significant obstacles to dislocations, due to their size and structure, they are relatively far apart and so do not have such a large contribution to the hardening. The WV steels will contain a mixture of both transformed and untransformed precipitates. However, in this case the precipitates are much closer together than in the SG steels so dislocations will encounter more precipitates and hence there is a larger increase in hardening. It is also possible that the Ni-Mn-Si-rich interface stabilises smaller precipitates. Hence this will reduce the coarsening of these precipitates maintaining a shorter inter-particle distance and thus also increasing the hardening in the WV steels compared to the SG ones. If this is the case then the SG steels are likely to overage more quickly, and softening effects may become significant. This could be the reason for the lower than expected hardening of the SG material aged at 405 °C as seen in Figure 7.2.

It is also worth noting here the work of Liu[165] who thermally aged similar Fe-Cu alloys with different additions of Ni, Mn and Si. She observed a poor fit to the Russell-Brown model, but this was improved when the square root of the volume fraction was multiplied by the measured precipitate Cu concentration. No correction for the influence of trajectory overlap effects was made to the composition of the precipitates. She concluded that the different Cu contents resulted in precipitates with different shear moduli. A relationship between Cu content and hardness change was not observed in the data from this project.

### 7.1.2 Softening of WF During Thermal Ageing

A number of steels with low Cu contents appear to have softened. Section 5.3.1 investigated the difference in hardening in the WF steels aged at 330 °C and 365 °C. At the lower ageing temperature softening was seen, whilst no appreciable changes

in hardness were observed after ageing at 365 °C and 405 °C. It seems that the only plausible explanation of this difference would be due to a loss of SSS.

After ageing for 90,000 hrs and 100,000 hrs at 330 °C and 405 °C respectively no significant change in the matrix composition was observed. However, precipitation of Ni, Mn and Si was observed at a low angle boundary in the material aged at 330 °C. Without further investigation it is not possible to determine whether this is a feature of ageing (as opposed to from the post weld heat treatment) and is not also occurring at the higher temperatures. If this is only occurring at the lower temperature then it may explain some of the difference in hardness observed. The formation of Ni-Mn-Si precipitates will be discussed in detail in Section 7.5. It is also possible there are other effects occurring which APT is not able to detect, particularly if this involves N, which overlaps in the mass spectra with Si and is thus not identifiable with APT. Titchmarsh observed the formation of nitrides in other steels within this project and it is also a possible source of softening.

## 7.2 Effects of Long Term Thermal Ageing on RPV Microstructure

APT characterisation of the RPV microstructures was carried out in Chapter 5. A number of the results need discussing in more detail and in the context of the work of others.

### 7.2.1 Effect of Alloy Ni Content in the Presence of Mn

The different bulk Ni content of the two alloys SG and WV has produced quite differing microstructures after thermal ageing for 90,000 - 100,000 hrs. This is particularly evident when comparing Figures 5.2 and 5.3 with Figures 5.16 and 5.17. There is a much lower density of smaller precipitates in the SG steels compared to the WV

steels. In the SG steel aged for 100,000 hrs at 365 °C the majority of the precipitates observed were associated with dislocations[2]. The larger precipitates in the SG steel aged at 330 °C for 100,000 hrs were also associated with dislocations. Whereas in the WV steels, only a small number of precipitates were associated with dislocations.

This indicates that it is much harder to nucleate Cu-enriched precipitates in the SG steels than the WV steels. At the higher temperatures, where there is a slightly smaller driving force, precipitation occurs primarily heterogeneously at dislocations and grain boundaries in the SG steels. Reducing the temperature increases the driving force, but reduces the kinetics and thus results in some small precipitates in the matrix along with larger ones on dislocations. In the WV steels, the large number of precipitates in the matrix indicates that the additional bulk Ni content makes it easier to nucleate Cu-enriched precipitates. This, in turn, suggests that Ni must be active in the precipitation of Cu, as will be discussed later.

### 7.2.2 Matrix Cu Concentration

The slow diffusion of Cu in Fe[24] means it takes considerable time to approach the equilibrium matrix Cu level and hence obtain the solubility limit. For this reason the low temperature solubility of Cu in Fe at is not particularly well documented. The long ageing times in this project provide some additional information. Additionally, it is also possible to see any effects of Ni on the solubility or kinetics of Cu in Fe.

Selected values of the matrix Cu concentration after thermal ageing are shown in Table 7.1. This indicates that there is some influence of Ni on the kinetics of precipitation in these steels. After 18,500 hrs of ageing, at both temperatures the matrix Cu content is considerably lower in the WV steels than the SG steels. Lower matrix Cu content in the WV steels is also seen at other ageing times. The higher number density of precipitates caused by the presence of Ni results in reduced diffusion

[2] It is not possible to directly observe dislocations in APT datasets. However, it is possible to infer their presence from elements segregated to them. In this case they can be identified from lines enriched in C and Mo.

| | | 18,500 hrs | 90,000 hrs | 100,000 hrs |
|---|---|---|---|---|
| SG | 330 °C | 0.37 ± 0.02* | - | 0.06 ± 0.0003 |
| SG | 365 °C | 0.21 ± 0.01* | - | 0.06 ± 0.0003 |
| WV | 330 °C | 0.27 ± 0.02* | 0.08 ± 0.0003 | - |
| WV | 365 °C | 0.07 ± 0.0005 | 0.07 ± 0.0003 | - |

*Table 7.1:* Matrix Cu concentration (in at.%) of the SG and WV steels after thermal ageing at 330 °C and 365 °C for 18,500 hrs, 90,000 hrs and 100,000 hrs. *ECOPoSAP data of Morley.

distances and thus faster depletion of Cu from the matrix. This is consistent with the evidence from the Monte-Carlo modelling in Chapter 6. The influence of Ni on the nucleation of Cu-enriched precipitates is discussed in Section 7.3.

The only steel to have approached equilibrium is the WV steel aged at 365 °C. The solubility limit was measured to be 0.07 at.%. This is consistent with the generally accepted value of 0.05 - 0.07 at.%[4, 166]. It is not possible to comment on whether Ni affects the solubility since the low Ni steels may not have yet reached equilibrium.

### 7.2.3 Matrix-Precipitate Interfaces

In agreement with the work of others[60, 63], segregation of Ni, Mn and Si was observed at the interfaces of CRPs in this work. This segregation was found to lower the interfacial energy between the Cu-enriched precipitate and the surrounding matrix. Predominantly the reduction in interfacial energy comes from the segregation of Ni, with smaller contributions from Mn and Si. The method for analysis of interfaces presented in Section 4.2.1.5 provides new information about the width of the interface of which there is little information in the literature. The precipitate-matrix interface will be discussed with reference to precipitate size, ageing temperature, composition and bulk Ni content.

#### 7.2.3.1 Effect of Precipitate Size

In all cases observed in both the WV and SG steels, precipitates with a larger core radius (Cu rich region) have a wider Ni-Mn-Si rich interface. This is in part consistent with the conclusions of Morley[19] that the interfacial segregation reduces the interfacial energy by reducing the number of unfavourable Fe-Cu bonds. This does not fully explain the increased interfacial segregation with precipitate size. If this was wholly the underlying driving force for segregation then the interface width would likely remain constant with size. This is not observed in this case. The increased interface width with larger precipitate size indicates that segregation must also occur to minimise the increase in interfacial energy due to lattice strain. This would increase with precipitate size, and be dependent on whether the precipitates were bcc or 9R.

#### 7.2.3.2 Effect of Ageing Temperature

There is some effect of ageing temperature on the amount of interfacial segregation observed. In the WV material, ageing at a lower temperature promoted a slightly wider interface than ageing at higher temperature for equivalently sized precipitates. This is particularly the case for the smaller particles up to 2 - 3 nm in radius. Above this size there are very few precipitates in the WV material aged at 330 °C for 90,000 hrs. The observed differences in precipitate core composition cannot explain this difference since particles contain slightly lower Cu at the lower ageing temperature. A possible explanation is that some of the precipitates at the lower ageing temperature have transformed to 9R at a slightly smaller radius than at the higher temperature. Transformed precipitates would cause greater lattice strain and thus may cause increased interfacial segregation. Due to the small number of particles in the SG material aged at 365 °C for 100,000 hrs, it is not possible to draw any firm conclusions on the effect of ageing temperature in the low Ni case.

#### 7.2.3.3 Interface Composition

The composition of the interface region is very low in Cu for all ageing times and temperatures, in both the SG and WV materials. The small levels of Cu observed in the interface region are likely to come from Cu which is diffusing through the interface to the Cu rich core.

There is an apparent trend in the WV steels for a more Ni-Mn-Si rich interface at higher ageing temperature. The ratio of Ni:Mn:Si at the two ageing temperatures for equivalent sized precipitates is roughly constant, but does increase with size. For precipitates 0 - 1 nm in radius, this ratio is approximately 4:3:1 increasing to 6:4:1 for the very largest precipitates but in neither case does this appear to tend towards any known silicide compound[167]. It is possible that the segregation of these elements to the interface may assist the nucleation, or be a precursor to, the formation of more distinct Ni-Mn-Si particles at the precipitate-matrix interface.

## 7.3 Non-Equilibrium Clustering Effects on Cu-enriched Precipitate Formation

The experimental evidence shows that the increased bulk Ni content of the WV weld over the SG weld produces a larger number of Cu-enriched precipitates which correlates to a larger increase in hardness. Complimentary MC simulations have been used to investigate the early stages of formation of Cu-enriched precipitates in the WV and SG steels.

Simulations by Seko et al.[53] and Al Motasem et al.[54] have suggested that Ni lowers the activation energy for the formation of critical nuclei by segregating to the interface. In both the experimental and simulation work the estimated energy barrier ($\Delta G = \Delta G_m + \Delta G^*$) for homogeneous nucleation in the WV and SG steels were comparable to one another. This suggests that some other effects may be at play.

Simulations by Cerezo et al.[55, 135] proposed that Cu-enriched precipitates nucleate via a cluster assisted nucleation mechanism on transient sub-critical Ni-Mn clusters.

The MC simulations in this work have demonstrated that both Ni and Mn are enriched in the first nearest neighbour sites of Cu atoms and Cu atom pairs before the onset of visible clustering. In the SG steels there is less Ni enrichment, but this reflects the lower bulk Ni content of the alloy. In addition, in the SG steel the point at which Ni starts to cluster is later than in the WV steel. Both the level of enrichment of Mn around Cu atoms/Cu atom pairs and the point at which Mn atoms start to cluster does not appear to be related to the bulk Ni content.

The simulations indicate that small sub-critical clusters of Ni and Mn are constantly forming and dissolving. The low driving force and high barrier to nucleation mean large precipitates do not form but it is consistent with the observation of transient sub-critical clusters seen in the simulations. In the simulations, these sub-critical clusters of Ni and Mn were observed to play an important role in the formation of Cu-enriched precipitates. The sites at which Cu-enriched precipitates formed in the simulation were found to be regions which contained locally more of these Ni-Mn clusters. This was particularly the case in the WV simulations but was also observed in the SG steels. Additionally, there was evidence of these clusters being associated with an increasing number of Cu atoms as the simulation progressed. The videos showing the formation of Cu-enriched precipitates also show that in the early stages of nucleation Cu atoms appear to be associated with small Ni and Mn clusters.

There are three possible formation mechanisms by which Cu-enriched precipitates may form. This could be heterogeneous nucleation on a sub-critical Ni-Mn cluster, impingement of two or more sub-critical nuclei creating one super-critical nucleus and finally, Cu-enriched precipitates could evolve from clusters initially rich in Ni and Mn. Analysis of the formation and evolution of four Cu-enriched precipitates suggests that they can evolve from a Ni-Mn rich cluster to a Cu-rich one. It is possible that all three mechanisms or some combination of them occur. Further analysis of a larger number

of particles with more frequent output of atom maps from the simulation and/or more detailed analysis of the videos presented in Section 6.3.6 is required to conclusively determine the precise mechanism by which Cu-enriched precipitates form.

In the SG steels the sub-critical clusters are richer in Mn, which again reflects the fact that the bulk Ni content of the alloy is lower. It is thought that the more numerous population of Cu-enriched precipitates and thus greater hardening in the higher Ni, WV weld is because of the much higher number density of these clusters. This means there are a greater number of favourable nucleation sites. In addition, the Ni content of these clusters could also have an influence since the Cu-Mn and Mn-Fe interactions are slightly less favourable than Cu-Ni and Ni-Fe interactions. Thus a more Mn rich cluster would be a slightly less effective nucleation site than a more Ni rich one.

The evidence from the simulations suggests that there is very little effect of Si on the formation of Cu-enriched precipitates. Si is incorporated into clusters much later than Cu, Ni or Mn since the number of isolated Si atoms decreases more slowly. This is perhaps a feature of its low mobility combined with its more unfavourable interaction with vacancies than Cu, Ni and Mn. It is also observed to have a much lower enrichment around the sites of Cu atoms and Cu atom pairs in the WV steel. The precipitate nucleation videos also show that there are relatively few Si atoms compared to Ni and Mn atoms at the early stages of Cu precipitation.

## 7.4 Fe Content of Precipitates

### 7.4.1 SANS vs APT

The Fe content of Cu-enriched precipitates has been a topic of discussion for many years. This centres around conflicting results from APT and SANS, with APT suggesting precipitates contain significant quantities of Fe and SANS data interpreted to give virtually Fe free precipitates. The origins of this discrepancy are discussed

here.

Both APT and SANS have limitations which must account for the observed disparities between the results. SANS offers no direct measurement of precipitate composition, this has to be inferred from the scattering ratio $A = (N + M)/N$ where $M$ and $N$ are the magnetic and nuclear scattering components respectively. To estimate the composition from this ratio assumptions have to be made regarding the magnetic state of the precipitates. Also a number of compositions can be consistent with a given $A$ ratio. Typically the assumption used is that precipitates are non-magnetic as this simplifies the scattering ratio allowing the absolute volume fraction to be determined independently of the composition of the features. The assumption of non-magnetic precipitates was put into question by Fine[26] and more recently by Schober et al.[27, 28]. This potentially questions the results of near Fe-free CRPs from SANS since for precipitates to be magnetic they would require reasonable levels of Fe. Thus it seems reasonable that the interpretation of SANS data underestimates the true Fe content of Cu-enriched precipitates. Conversely, APT suffers from artefacts which artificially inflate the measured Fe content. Trajectory overlap effects caused by differences in local magnification can lead to significant proportions of Fe being incorrectly positioned with the precipitates. The Fe resulting from trajectory overlaps is impossible to distinguish from the Fe which was incorporated into the particle prior to APT analysis, although attempts have been made in this study and by Morley[10] to correct the composition for these trajectory overlap ions.

### 7.4.2 Could Fe be in Precipitates?

The results from Section 5.2.1.4 are consistent with the earlier work of Morley[10, 19] that ageing at a lower temperature produces precipitates which contain more Fe. This indicates that precipitates must contain some Fe as this result comes from precipitates which are of comparable size and thus cannot be related to APT artefacts. The largest precipitates ($> 5$ nm in radius) contained around 20 % Fe in the WV material aged at

365 °C for 90,000 hrs, whilst at 330 °C the Fe content is around 5 - 10 % larger. The correction method used by Morley is likely to mask variations in Fe content with size. It is possible that there could be significant variation in Fe content with size, since the precipitate structure is known to change e.g from bcc to 9R[37, 41]. A correction to account for the Fe from trajectory overlaps has been applied in this work which aimed to retain any size dependence of the Fe content. The resulting corrected Fe contents showed a falling Fe content with increasing precipitate size.

The Fe contents measured in this work indicate that even the largest precipitates contain significant quantities of Fe. Refinements to the free parameters, $\Omega_{traj}$ and $d_{traj}$, used to calculate the number of overlap ions may decrease the Fe content further. The numbers chosen are likely to be conservative estimates. The Cu rich end of the Fe-Cu phase diagram indicates that Fe is virtually insoluble in Cu, much like Cu is in Fe. This suggests that the Cu-rich particles seen in these steels should be virtually free of Fe. The caveat here is that Cu has an fcc structure whilst the smallest precipitates observed in these steels have bcc structure, and even the largest transformed precipitates may still not be fully fcc. Additionally, these precipitates could be far from equilibrium and the Fe content, given sufficient time, may reduce to much lower levels.

It is thought that at least for the smaller sizes, bcc Cu-rich precipitates are stabilised by the presence of Fe[19]. After precipitates transform from bcc to a 9R type structure the Fe content would be expected to decrease, since this is a less favourable environment for Fe. It is thought that precipitates undergo this transformation at around 2 - 3 nm[41, 43], but being a martensitic process this is highly temperature dependent. This coincides with the largest drop in Fe content at both ageing temperatures, indicating that there could be some dependence of precipitate structure on Fe content. It was not possible to observe the structure of the precipitates in the APT data and then relate this to the Fe content to confirm or deny a dependence of crystal structure on the precipitate Fe content.

## 7.5 Ni-Mn-Si Precipitates

The precipitation of Ni, Mn and Si has been observed in irradiated steels with low Cu contents[73, 88]. So far there has been no evidence for the formation of these phases in thermally aged RPV materials reported in the literature. Several Ni-Mn-Si precipitates have been observed in the thermally aged materials in both high and low Cu containing steels. A summary of these findings is given here.

### 7.5.1 Observations of Ni-Mn-Si Precipitates

#### 7.5.1.1 Matrix

In all the steels studied there has been no evidence for any non-Cu precipitation within the matrix. This is consistent with a high barrier for nucleation and a low driving force for precipitation of Ni, Mn and Si within the matrix. The simulations indicate that transient sub-critical Ni-Mn clusters form, but these do not grow into large scale precipitates.

#### 7.5.1.2 Grain Boundaries and Dislocations

Evidence of large Ni-Mn-Si precipitates has been observed at dislocations and grain boundaries. It is thought that these phases correspond to the predicted "Late Blooming Phases" of Odette[14]. In the high-Cu steels, the precipitates observed were, in all cases, associated with a Cu precipitate. The one possible exception here is a precipitate at the edge of the analysis volume. In this instance it is thought an associated Cu-enriched precipitate may have been located outside the analysis volume.

In the low Cu WF material, a low angle grain boundary was observed to contain a population of small Ni-Mn-Si precipitates along the dislocations making up the boundary. In contrast to the high Cu materials, these precipitates were not associated with any Cu, which is not unexpected given the very low Cu content of this alloy. In

addition, these precipitates were much smaller than those observed in the high Cu materials.

The composition of the precipitates detected does not appear to follow any trends or consistent stoichiometry of Ni:Mn:Si, although precipitates 2 and 3 from the grain boundary (see Figure 5.28) are close to a G-Phase type $A_{16}B_6Si_7$ stoichiometry. Without further characterisation from TEM to obtain the structure it is not possible to confirm these as G-Phase type precipitates[168]. Interestingly, the precipitates in the low Cu WF material have Ni:Mn:Si ratios close to that of the precipitate-matrix interface. The limited number of precipitates here make it difficult to draw firm conclusions on their type and to make comparisons between them. However, it is possible to postulate some ideas on the mechanism by which these phases may have formed.

Furthermore, the observation of these phases at grain boundaries and dislocations has implications for the whole vessel and not just the more heavily irradiated regions. Given sufficient time and favourable nucleation sites, these phases form under thermal ageing conditions and could lead to grain boundary embrittlement in regions not previously thought to be of concern.

### 7.5.2 Kinetics of Formation of Ni-Mn-Si Precipitates

The absence of any large Ni-Mn-Si precipitates in the matrix, even after 100,000 hrs of ageing, is consistent with the initial predictions of Odette[14] that the kinetics of formation would be very slow under thermal ageing. The presence of these precipitates at dislocations and grain boundaries indicate that these phases can form under thermal ageing. Nucleating these features via heterogeneous nucleation at dislocations and grain boundaries will be more favourable, and would be facilitated by faster diffusion of solute species. Thus it may be possible to nucleate these features on existing Cu-enriched precipitates in the matrix after very long ageing times in high Cu steels. This mechanism of LBP formation on existing Cu-enriched precipitates has been observed

in low-flux, long time, neutron irradiated materials by Odette and Nanstad[169] and Miller et al.[170]. The observed association of Ni-Mn-Si precipitates with Cu particles indicates this may be a viable nucleation method, although, in this work it has not been possible to verify whether the Cu-enriched or Ni-Mn-Si rich particle was present first. The similarities between the ratio of Ni:Mn:Si in the matrix-precipitate interface and the small particles in WF may be an indication that the interfacial segregation may promote, or be a precursor to, the early stages of formation of a Ni-Mn-Si rich phase.

# 8. Conclusions

The work in this thesis presents the results and subsequent discussion of a study into the long term thermal ageing of a number of RPV steel welds. APT and complimentary LKMC simulations were performed on a number of welds containing systematic variations in Ni and Cu. The aim of this study was to further develop the understanding of the influence of alloying additions, primarily Ni and Mn on the formation and evolution of Cu-enriched precipitates under thermal ageing. Additionally, this work has facilitated a study of precipitation and solute segregation at grain boundaries and dislocations. The main conclusions are summarised briefly below.

1. **The effects of bulk Ni content on the thermally aged microstructure of steels containing Mn.**

   Ni was found to have a strong influence on the observed microstructure after long term thermal ageing. In the low Ni, SG weld the majority of observed precipitation occurred at dislocations at the highest ageing temperature. Potentially, this has implications for studies of CRP formation using accelerated ageing at higher temperatures particularly in low Ni steels, since a small temperature reduction has produced quite differing microstructures in the SG steel. Conversely, in the high Ni steel, the majority of precipitates were observed in the matrix and were much larger and more numerous at both ageing temperatures.

2. **Low temperature solubility of Cu in Fe.**

   The solubility limit for the WV steel at an ageing temperature of 365 °C was

found to be 0.07 ± 0.001 at.%. For the WV steel aged at 330 °C, the equilibrium matrix Cu level may not have been obtained. This was also the case for the SG steels at both 330 °C and 365 °C. Ni appears to affect the kinetics of precipitation since the matrix Cu was found to be lower in the WV welds than the SG welds after the same ageing time. It was not possible to comment on any effect of Ni on the solubility limit.

3. **The influence of long term thermal ageing on the precipitate-matrix interface.**

   After ageing for 90,000 - 100,000 hrs, larger precipitates were found to have a wider Ni, Mn, Si interface. This is thought to be due to a combination of lattice strain, precipitate transformation and a minimisation of unfavourable Fe-Cu bonds. Ageing at a lower temperature produced a slightly wider interface. A narrower interface was found in the SG materials. A larger reduction in interfacial energy due to the segregation of Ni, Mn and Si was found for larger precipitates and with higher bulk Ni content. There was no change in interfacial energy reduction with ageing time or temperature.

4. **The influence of dislocations on Cu precipitation.**

   In the SG steels the presence of the majority of precipitates at dislocations after ageing at higher temperatures indicates that homogeneous nucleation is difficult in these steels. At lower supersaturations heterogeneous nucleation at dislocations is more favourable. In the WV steel aged for 3000 hrs at 365 °C precipitates formed at dislocations were found to be larger, slightly more Cu rich and have a wider interface than those in the matrix. After 90,000 hrs of ageing precipitates at dislocations had a higher Cu content. Their sizes and interface widths were comparable to those in the matrix. C and Mo were found to be segregated to dislocations in these materials.

5. **The Fe content of Cu-enriched precipitates.**

   The Fe content of precipitates was investigated and a method to correct

the composition for the effect of trajectory overlap ions presented. The previous analysis of Morley[19] has been extended to compare equivalently sized precipitates formed at different ageing temperatures. The Fe content was found to be higher at lower ageing temperatures and with smaller precipitate sizes. It was not possible to determine the precipitate structure and hence if this was correlated with any change in Fe content. However, the largest drop in Fe content occurred at around 2 - 3 nm, which coincides with the approximate radius at which the bcc to 9R transformation is thought to occur. The largest precipitates were found to contain around 20 % Fe, which is still more Fe than expected from the Fe-Cu phase diagram.

6. **The effects of Ni and Mn on the formation of Cu-enriched precipitates.**
   Simulations of the thermal ageing of the WV and SG steels were used to investigate the early stages of Cu precipitation. Ni and Mn were found to be enriched in the first nearest neighbour sites of Cu atoms and Cu atom pairs. Sub-critical Ni-Mn clusters were found to be constantly forming and dissolving and be more numerous in the sites at which Cu-enriched precipitates had formed. There was evidence for an increasing number of Cu atoms being associated with small Ni-Mn clusters as ageing progressed. The precise method of Cu-enriched precipitate formation appears to be variable as a number of diverse nucleation pathways are possible in this multi-component system. In the clusters observed it appears Cu-enriched precipitates can evolve from an initial cluster rich in Ni and Mn. Si does not appear to be active in the formation of Cu-enriched precipitates. The differences between the SG and WV steels appear to be related to the fact that there are many more potential nucleation sites in the WV material, due to the greater number of Ni-Mn clusters.

7. **Solute segregation to grain boundaries.**
   Without the levels of solute segregation in the as received material, it is difficult to draw firm conclusions on the influence of thermal ageing on the levels of solute segregation at grain boundaries. However, it is thought that the presence

of a large number of elements at the boundary is the result of a co-segregation process similar to that proposed by Guttmann[159, 171, 172]. Higher P levels were observed when the C content at the boundary was lower. This is consistent with site competition or a repulsive interaction between the two[104] and the work of many others.

8. **Ni-Mn-Si precipitation.**

   Ni-Mn-Si precipitates have been observed in thermally aged RPV materials for the first time. These precipitates were observed in the high Ni WV and WF materials at dislocations and grain boundaries. In the high Cu materials these were associated with Cu-enriched precipitates. It was not possible to determine whether the Ni-Mn-Si or Cu precipitate acted as a nucleation site for the other. The ratio of Ni:Mn:Si of some of the precipitates is close to that of G-Phase. This indicates that the Ni-Mn-Si precipitates observed in irradiated steels are thermodynamically favourable and suggests that the formation of these features is enhanced by irradiation rather than induced by irradiation.

# 9. Future Work

The work presented in this thesis has attempted to answer some of the outstanding questions concerning the alloy element effects on Cu precipitation. However, in the course of the project some new avenues for investigation have arisen which could not be fully completed within the time-frame of this project. Likewise, there are still some outstanding issues in the existing work which could warrant further analysis.

### Studies of Grain Boundaries

This work has uncovered interesting phenomena occurring at grain boundaries. It has not been possible to carry out an in depth investigation in this area but it raises some important questions about grain boundary embrittlement.

The as-received material needs to be investigated to obtain the base line levels of solute segregation so changes with ageing temperature can be determined. Furthermore, a more systematic investigation of the formation of Ni-Mn-Si precipitates at grain boundaries should be carried out to give insights into the nucleation and growth of these features with ageing time and temperature and their association with Cu-enriched precipitates. These precipitates could lead to embrittlement of the boundary and thus make these materials susceptible to intergranular fracture. Hence, the mechanical properties of such interfaces require investigation. The small amount of remaining long term aged materials mean micro-cantilever testing is likely to be the best method for mechanical testing of grain boundary specimens.

### Changes in Precipitate Composition with their Structure

Another question which remains unresolved is the Fe content of Cu-enriched clusters. This is a long standing issue and is unlikely to be resolved in the near future. However, it may be possible to improve the understanding by investigating changes in composition between the coherent, semi-coherent and incoherent Cu-enriched precipitates. This is potentially possible using a combination of APT and FIM. FIM could be used to identify an untransformed or transformed precipitate and APT used to determine its chemical composition.

### KMC Modelling

So far the work on the modelling has demonstrated that the assumptions used are reasonable[19]. This project has added to this by implementing some new analysis techniques and providing more information on the evolution of Cu-enriched precipitates as the simulation progressed. Further investigation of the precise formation mechanism is possible with more frequent output of atom maps and from the analysis of a greater number of precipitates. The parameterisation of the simulation is still the same as that when the model was first developed. In this time newer, and potentially more accurate data may now be available which could be used to refine the pairwise potentials currently used. Additionally, quantum mechanical calculations of potentials in principle, facilitate the study of more complex systems and allow concentration dependent terms to be introduced into the potentials. This may help resolve some of the known issues with the model, most notably the time scaling.

### Investigation of Other Materials

Some other materials, notably SF and PE, have similar chemical composition but show different hardness changes with long term thermal ageing. As with the WF materials studied in this project it would be interesting to perform APT analysis of some of these

materials to relate these differences to any change in microstructure. Additionally, the materials in this project only allow the effect of bulk Ni to be investigated. To investigate how changes in bulk Mn and Si content affect the precipitation of Cu, a wider range of alloys needs to be studied. Newer reactors typically have very low Cu contents and so thermal ageing studies of a broader range of low Cu materials are also important.

# References

[1] World Nuclear Association, World Nuclear Power Reactors and Uranium Requirements.

[2] World Nuclear Association, Nuclear Power Reactors (2012).
URL `http://www.world-nuclear.org/info/inf32.html`

[3] C A English, J M Hyde, Radiation Damage of Reactor Pressure Vessel Steels, In: R M Konings (Editor), *Comprehensive Nuclear Materials*, Elsevier Ltd, 2012, Chapter 4.05, pgs. 151–180.

[4] M K Miller, P Pareige, M G Burke, Understanding Pressure Vessel Steels: An Atom Probe Perspective, *Materials Characterization*, **44** (2000), pgs. 235–254.

[5] D N Seidman, R S Averback, K Benedek, Displacement Cascades. Dynamics and Atomic Structure, *Physica Status Solidi B*, **144** (1987), pgs. 85–104.

[6] G R Odette, G E Lucas, Recent Progress in Understanding Reactor Pressure Vessel Steel Embrittlement, *Radiation Effects and Defects in Solids*, **144** (1998), pgs. 189–231.

[7] G R Odette, G E Lucas, Embrittlement of Nuclear Reactor Pressure Vessels, *Journal of Materials*, **53** (2001), pgs. 18–22.

[8] T R Allen, J T Busby, Radiation Damage Concerns for Extended Light Water Reactor Service, *Journal of Materials*, **61** (2009), pgs. 29–34.

[9] M Akamatsu, J C Van Duysen, P Pareige, P Auger, Experimental Evidence of Several Contributions to the Radiation Damage in Ferritic Alloys, *Journal of Nuclear Materials*, **225** (1995), pgs. 192–195.

[10] A Morley, G Sha, S Hirosawa, A Cerezo, G D W Smith, Determining the Composition of Small Features in Atom Probe: bcc Cu-Rich Precipitates in an Fe-Rich Matrix, *Ultramicroscopy*, **109** (2009), pgs. 535–540.

[11] M Lambrecht, L Malerba, A Almazouzi, Influence of Different Chemical Elements on Irradiation-Induced Hardening Embrittlement of RPV Steels, *Journal of Nuclear Materials*, **378** (2008), pgs. 282–290.

[12] J T Buswell, W J Phythian, R J McElroy, S Dumbill, P H N Ray, J Mace, R N Sinclair, Irradiation-Induced Microstructural Changes, and Hardening Mechanisms, in Model PWR Reactor Pressure Vessel Steels, *Journal of Nuclear Materials*, **225** (1995), pgs. 196–214.

[13] R Chaouadi, R Gerard, Copper Precipitate Hardening of Irradiated RPV Materials and Implications on the Superposition Law and Re-Irradiation Kinetics, *Journal of Nuclear Materials*, **345** (2005), pgs. 65–74.

[14] G R Odette, Radiation Induced Microstructural Evolution in Reactor Pressure Vessel Steels, In: I M Robertson, L E Rehn, S J Zinkle, W J Phythian (Editors), *Materials Research Society Symposium Proceedings*, Volume 373, Materials Research Society, Boston, MA, 1995, pgs. 137–148.

[15] G R Odette, R K Nanstad, Predictive Reactor Pressure Vessel Steel Irradiation Embrittlement Models: Issues and Opportunities, *Journal of Materials*, **61** (2009), pgs. 17–23.

[16] P Auger, P Pareige, M Akamatsu, D Blavette, APFIM Investigation of Clustering in Neutron-Irradiated Fe-Cu Alloys and Pressure Vessel Steels, *Journal of Nuclear Materials*, **225** (1995), pgs. 225–230.

[17] F Bergner, M Lambrecht, A Ulbricht, A Almazouzi, Comparative Small-Angle Neutron Scattering Study of Neutron-Irradiated Fe, Fe-Based Alloys and a Pressure Vessel Steel, *Journal of Nuclear Materials*, **399** (2010), pgs. 129–136.

[18] R G Carter, N Soneda, K Dohi, J M Hyde, C A English, W L Server, Microstructural Characterization of Irradiation-Induced Cu-Enriched Clusters in Reactor Pressure Vessel Steels, *Journal of Nuclear Materials*, **298** (2001), pgs. 211–224.

[19] A Morley, Thermal Ageing of Low Alloy Steels, DPhil Thesis, University of Oxford (2008).

[20] P Pareige, M K Miller, Characterization of Neutron-Induced Copper-Enriched Clusters in Pressure Vessel Steel Weld: An APFIM Study, *Applied Surface Science*, **94-95** (1996), pgs. 370–377.

[21] P Pareige, K F Russell, M K Miller, APFIM Studies of the Phase Transformations in Thermally Aged Ferritic FeCuNi Alloys: Comparison With Aging Under Neutron Irradiation, *Applied Surface Science*, **94-95** (1996), pgs. 362–369.

[22] D Isheim, M Gagliano, M E Fine, D N Seidman, Interfacial Segregation at Cu-Rich Precipitates in a High-Strength Low-Carbon Steel Studied on a Sub-Nanometer Scale, *Acta Materialia*, **54** (2006), pgs. 841–849.

[23] R Prakash Kolli, D N Seidman, The Temporal Evolution of the Decomposition of a Concentrated Multicomponent FeCu-Based Steel, *Acta Materialia*, **56** (2008), pgs. 2073–2088.

[24] G Salje, M Feller-Kniepmeier, The Diffusion and Solubility of Copper in Iron, *Journal of Applied Physics*, **48** (1977), pgs. 1833–1839.

[25] B D Wirth, P Asoka-Kumar, R H Howell, G R Odette, P A Sterne, Positron Annihilation Spectroscopy and Small Angle Neutron Scattering Characterization of Nanostructural Features in Irradiated Fe-Cu-Mn Alloys, In:

G E Lucas, M A Snead, M A Kirk Jnr, R G Elliman (Editors), *Materials Research Society Symposium Proceedings*, Volume 650, Materials Research Society, Boston, MA, 2001, pgs. R6.5.1–6.

[26] M E Fine, J Liu, M Asta, An Unsolved Mystery: The Composition of bcc Cu Alloy Precipitates in bcc Fe and Steels, *Materials Science and Engineering: A*, **463** (2007), pgs. 271–274.

[27] M Schober, E Eidenberger, H Leitner, P Staron, D Reith, R Podloucky, A Critical Consideration of Magnetism and Composition of (bcc) Cu Precipitates in (bcc) Fe, *Applied Physics A: Materials Science and Processing*, **99** (2010), pgs. 697–704.

[28] M Schober, E Eidenberger, P Staron, H Leitner, Critical Consideration of Precipitate Analysis of Fe-1at.% Cu Using Atom Probe and Small-Angle Neutron Scattering, *Microscopy and Microanalysis*, **17** (2011), pgs. 26–33.

[29] P Asoka-Kumar, B D Wirth, P A Sterne, R H Howell, G R Odette, Composition and Magnetic Character of Nanometre-Size Cu Precipitates on Reactor Pressure Vessel Steels: Implications for Nuclear Power Plant Lifetime Extension, *Philosophical Magazine Letters*, **82** (2002), pgs. 609–615.

[30] S R Goodman, S S Brenner, J R Low Jnr, An FIM-Atom Probe Study of the Precipitation of Copper From Iron-1.4at. Pct Copper. Part 1: Field Ion Microscopy, *Metallurgical Transactions*, **4** (1973), pgs. 2363–2369.

[31] S R Goodman, S S Brenner, J R Low Jnr, An FIM-Atom Probe Study of the Precipitation of Copper From Iron-1.4at. Pct Copper. Part 2: Atom Probe Analysis, *Metallurgical Transactions*, **4** (1973), pgs. 2371–2378.

[32] P Auger, P Pareige, M Akamatsu, J C Van Duysen, Microstructural Characterization of Atom Clusters in Irradiated Pressure Vessel Steels and Model Alloys, *Journal of Nuclear Materials*, **211** (1994), pgs. 194–201.

[33] A Cerezo, T J Godfrey, C R M Grovenor, M G Hetherington, R M Hoyle, J P Jakubovics, J A Liddle, G D W Smith, G M Worrall, Materials Analysis With a Position-Sensitive Atom Probe, *Journal of Microscopy*, **154** (1989), pgs. 215–225.

[34] F Soisson, G Martin, A Barbu, Copper Precipitation in Dilute Iron-Copper Alloys: A Monte Carlo Simulation, *Annales De Phsyique Colloque*, **20** (C3) (1995), pgs. 13–20.

[35] F Soisson, A Barbu, G Martin, Monte Carlo Simulations of Copper Precipitation in Dilute Iron-Copper Alloys During Thermal Ageing and Under Electron Irradiation, *Acta Materialia*, **44** (1996), pgs. 3789–3800.

[36] S Lozano-Perez, J M Titchmarsh, M L Jenkins, Determination of the Fe Content of Embedded Cu-Rich Particles in Ferritic Alloys Using Energy-Filtered TEM, *Ultramicroscopy*, **106** (2006), pgs. 75–91.

[37] P J Othen, M L Jenkins, G D W Smith, W J Phythian, Transmission Electron Microscope Investigations of the Structure of Copper Precipitates in Thermally-Aged Fe-Cu and Fe-Cu-Ni, *Philosophical Magazine Letters*, **64** (1991), pgs. 383–391.

[38] R Monzen, M Iguchi, M L Jenkins, Structural Changes of 9R Copper Precipitates in an Aged Fe-Cu Alloy, *Philosophical Magazine Letters*, **80** (2000), pgs. 137–148.

[39] E Kozeschnik, Thermodynamic Prediction of the Equilibrium Chemical Composition of Critical Nuclei: bcc Cu Precipitation an $\alpha$-Fe, *Scripta Materialia*, **59** (2008), pgs. 1018–1021.

[40] M Perez, F Perrard, V Massardier, X Kleber, A Deschamps, H de Monestrol, P Pareige, G Covarel, Low-Temperature Solubility of Copper in Iron: Experimental Study Using Thermoelectric Power, Small Angle X-Ray Scattering and Tomographic Atom Probe, *Philosophical Magazine*, **85** (2005), pgs. 2197–2210.

[41] P J Othen, M L Jenkins, G D W Smith, High-Resolution Electron Microscopy Studies of the Structure of Cu Precipitates in $\alpha$-Fe, *Philosophical Magazine A*, **70** (1994), pgs. 1–24.

[42] R Monzen, M L Jenkins, A P Sutton, The bcc-to-9R Martensitic Transformation of Cu Precipitates and the Relaxation Process of Elastic Strains in an Fe-Cu Alloy, *Philosophical Magazine A*, **80** (2000), pgs. 711–723.

[43] L P Vandenbossche, M J Konstantinović, A Almazouzi, L R Dupré, Magnetic Evaluation of the Hardening and Softening of Thermally Aged Iron-Copper Alloys, *Journal of Physics D: Applied Physics*, **40** (2007), pgs. 4114–4119.

[44] T Harry, D J Bacon, Computer Simulation of the Core Structure of the 111 Screw Dislocation in $\alpha$-Iron Containing Copper Precipitates : I. Structure in the Matrix and a Precipitate, *Acta Materialia*, **50** (2002), pgs. 195–208.

[45] D J Bacon, Y N Osetsky, Hardening Due to Copper Precipitates in $\alpha$-Iron Studied by Atomic-Scale Modelling, *Journal of Nuclear Materials*, **329-333** (2004), pgs. 1233–1237.

[46] D J Bacon, Y N Osetsky, Modelling Dislocation-Obstacle Interactions in Metals Exposed to an Irradiation Environment, *Materials Science and Engineering: A*, **400-401** (2005), pgs. 353–361.

[47] S Lozano-Perez, M L Jenkins, J M Titchmarsh, Evidence for Deformation-Induced Transformations of Cu-Rich Precipitates in an Aged FeCu Alloy, *Philosophical Magazine Letters*, **86** (2006), pgs. 367–374.

[48] K E Easterling, H M Miekk-Oja, The Martensite Transformation of Iron Precipitates in a Copper Matrix, *Acta Metallurgica*, **15** (1967), pgs. 1133–1141.

[49] K E Easterling, G C Weatherly, On the Nucleation of Martensite in Iron Precipitates, *Acta Metallurgica*, **17** (1969), pgs. 845–852.

[50] K E Easterling, P R Swann, Nucleation of Martensite in Small Particles, *Acta Metallurgica*, **19** (1971), pgs. 117–121.

[51] W Wang, B Zhou, G Xu, D Chu, J Peng, High-Resolution Electron Microscopy Characterization of 2H and 9R Variant in the Ferritic Steels Containing Copper, *Materials Characterization*, **62** (2011), pgs. 438–441.

[52] Q L Wang, J Z Zhao, A Model Describing the Microstructure Evolution in Fe-Cu Alloys During Thermal Aging, *Materials Science and Engineering: A*, **528** (2010), pgs. 268–272.

[53] A Seko, N Odagaki, S R Nishitani, I Tanaka, H Adachi, Free-Energy Calculation of Precipitate Nucleation in an Fe-Cu-Ni Alloy, *Materials Transactions JIM*, **45** (2004), pgs. 1978–1981.

[54] A T Al-Motasem, M Posselt, F Bergner, Nanoclusters in bcc-Fe Containing Vacancies, Copper and Nickel: Structure and Energetics, *Journal of Nuclear Materials*, **418** (2011), pgs. 215–222.

[55] A Cerezo, S Hirosawa, I Rozdilsky, G D W Smith, Combined Atomic-Scale Modelling and Experimental Studies of Nucleation in the Solid State, *Philosophical Transactions of the Royal Society of London. Series A*, **361** (2003), pgs. 463–477.

[56] A Cerezo, S Hirosawa, G Sha, G D W Smith, 3-D Atomic-Scale Experimental and Modelling Studies of the Early Stages of Precipitation, In: J M Howe, D E Laughlin, J K Lee, U Dahmen, W A Soffa (Editors), *Solid-to-Solid Phase Transformations in Inorganic Materials 2005: Volume 1 - Diffusional Transformations*, TMS, 2005, pgs. 251–262.

[57] T Koyama, H Onodera, Computer Simulation of Phase Decomposition in Fe-Cu-Mn-Ni Quaternary Alloy Based on the Phase-Field Method, *Materials Transactions JIM*, **46** (2005), pgs. 1187–1192.

[58] T Koyama, K Hashimoto, H Onodera, Phase-Field Simulation of Phase Transformation in Fe-Cu-Ni-Mn Quaternary Alloy, *Materials Transactions JIM*, **47** (2006), pgs. 2765–2772.

[59] J T Buswell, C A English, M G Hetherington, W J Phythian, G D W Smith, G M Worrall, An Analysis of Small Clusters Formed in Thermally Aged and Irradiated Fe-Cu and Fe-Cu-Ni Model Alloys, In: N H Packan, R E Stoller, A S Kumar (Editors), *Effects of Radiation on Materials: 14th International Symposium (Vol 2) ASTM STP 1046*, American Society for Testing and Materials, Philadephia, 1990, pgs. 127–153.

[60] D Isheim, R Prakash Kolli, M E Fine, D N Seidman, An Atom-Probe Tomographic Study of the Temporal Evolution of the Nanostructure of Fe-Cu Based High-Strength Low-Carbon Steels, *Scripta Materialia*, **55** (2006), pgs. 35–40.

[61] A Seko, S R Nishitani, I Tanaka, H Adachi, E Fujita, First-Principles Calculation on Free Energy of Precipitate Nucleation, *Computer Couplings of Phase Diagrams and Thermochemistry*, **28** (2004), pgs. 173–176.

[62] R Monzen, K Takada, C Watanabe, Coarsening of Spherical Cu Particles in an $\alpha$-Fe Matrix, *ISIJ International*, **44** (2004), pgs. 442–444.

[63] K Osamura, H Okuda, K Asano, M Furusaka, K Kishida, F Kurosawa, R Uemori, Sans Study Of Phase-Decomposition In Fe-Cu Alloy With Ni And Mn Addition, *ISIJ International*, **34** (1994), pgs. 346–354.

[64] G Sha, A Morley, A Cerezo, G D W Smith, Partitioning and Segregation of Trace Element Sn in a Low-Alloy Steel, *Philosophical Magazine Letters*, **87** (2007), pgs. 327–339.

[65] M K Miller, M A Sokolov, K F Russell, R K Nanstad, Atom Probe Tomography of Radiation-Sensitive KS-01 Weld, *Philosophical Magazine*, **85** (2005), pgs. 401–408.

[66] G R Odette, On the Dominant Mechanism of Irradiation Embrittlement of Reactor Pressure Vessel Steels, *Scripta Metallurgica*, **17** (1983), pgs. 1183–1188.

[67] R Prakash Kolli, R M Wojes, S Zaucha, D N Seidman, A Subnanoscale Study of the Nucleation, Growth, and Coarsening Kinetics of Cu-Rich Precipitates in a Multicomponent FeCu Based Steel, *International Journal of Materials Research*, **99** (2008), pgs. 513–527.

[68] D A Porter, K E Easterling, *Phase Transformations in Metals and Alloys*, 2nd Edition, Chapman & Hall, 1992.

[69] E Meslin, B Radiguet, P Pareige, A Barbu, Kinetic of Solute Clustering in Neutron Irradiated Ferritic Model Alloys and a French Pressure Vessel Steel Investigated by Atom Probe Tomography, *Journal of Nuclear Materials*, **399** (2010), pgs. 137–145.

[70] M M Ghoneim, F H Hammad, Pressure Vessel Steels: Influence of Chemical Composition on Irradiation Sensitivity, *International Journal of Pressure Vessels and Piping*, **74** (1997), pgs. 189–198.

[71] M G Burke, R J Stofanak, J M Hyde, C A English, W L Server, Microstructural Aspects of Irradiation Damage in A508 Gr 4N Forging Steel: Composition and Flux Effects, In: M L Grossbeck, T R Allen, R G Lott, A S Kumar (Editors), *Effects of Radiation on Materials: 21st International Symposium ASTM STP 1447*, ASM International, 2002, pgs. 194–207.

[72] M K Miller, P Pareige, Atomic Level Characterization of Neutron Irradiated Pressure Vessel Steels, In: G E Lucas, L L Snead, M A Kirk, R G Eliman (Editors), *Materials Research Society Symposium Proceedings*, Volume 650, Materials Research Society, Boston, MA, 2001, pgs. R6.1.1–12.

[73] J M Hyde, G Sha, E A Marquis, A Morley, K B Wilford, T J Williams, A Comparison of the Structure of Solute Clusters Formed During Thermal Ageing and Irradiation, *Ultramicroscopy*, **111** (2011), pgs. 664–71.

[74] M Hasegawa, Y Nagai, T Toyama, Y Nishiyama, M Suzuki, A Alamazouzi, E Van Walle, R Gerard, Evolution of Irradiation-Induced Cu Precipitation and Defects in Surveillence Test Specimens of Pressure Vessel Steels of Nuclear Power Reactors: Positron Annihilation and 3 Dimensional Atom Probe Study, In: *Proceedings of the International Symposium on Research for Ageing Management of Light Water Reactors*, Fukui City, Japan, 2007, pgs. 327–344.

[75] P Pareige, J C Van Duysen, P Auger, An APFIM Study of the Microstructure of a Ferrite Alloy After High Fluence Neutron Irradiation, *Applied Surface Science*, **67** (1993), pgs. 342–347.

[76] B Radiguet, P Pareige, A Barbu, Irradiation Induced Clustering in Low Copper or Copper Free Ferritic Model Alloys, *Nuclear Instruments and Methods in Physics Research Section B: Beam Interactions with Materials and Atoms*, **267** (2009), pgs. 1496–1499.

[77] K Fujii, K Fukuya, Characterization of Defect Clusters in Ion-Irradiated A533B Steel, *Journal of Nuclear Materials*, **336** (2005), pgs. 323–330.

[78] A Hardouin Duparc, C Moingeon, N Smetniansky-de Grande, A Barbu, Microstructure Modelling of Ferritic Alloys Under High Flux 1 Mev Electron Irradiations, *Journal of Nuclear Materials*, **302** (2002), pgs. 143–155.

[79] B Radiguet, A Barbu, P Pareige, Understanding of Copper Precipitation Under Electron or Ion Irradiations in FeCu0.1 wt % Ferritic Alloy by Combination of Experiments and Modelling, *Journal of Nuclear Materials*, **360** (2007), pgs. 104–117.

[80] S C Glade, B D Wirth, G R Odette, P Asoka-Kumar, P A Sterne, R H Howell, Positron Annihilation Spectroscopy and Small-Angle Neutron Scattering Characterization of the Effect of Mn on the Nanostructural Features Formed in Irradiated Fe-Cu-Mn Alloys, *Philosophical Magazine*, **85** (2005), pgs. 629–639.

[81] M K Miller, B D Wirth, G R Odette, Precipitation in Neutron-Irradiated FeCu and FeCuMn Model Alloys: A Comparison of APT and SANS Data, *Materials Science and Engineering: A*, **353** (2003), pgs. 133–139.

[82] J M Hyde, C A English, An Analysis of the Structure of Irradiation Induced Cu-Enriched Clusters in Low and High Nickel Welds, In: G E Lucas, L L Snead, M A Kirk, R G Elliman (Editors), *Materials Research Society Symposium Proceedings*, Volume 650, Materials Research Society, Boston, MA, 2001, pgs. R6.6.1–12.

[83] K Fukuya, K Ohno, H Nakata, S Dumbill, J M Hyde, Microstructural Evolution in Medium Copper Low Alloy Steels Irradiated in a Pressurized Water Reactor and a Material Test Reactor, *Journal of Nuclear Materials*, **312** (2003), pgs. 163–173.

[84] F Bergner, A Ulbricht, H Hein, M Kammel, Flux Dependence of Cluster Formation in Neutron-Irradiated Weld Material, *Journal of Physics: Condensed Matter*, **20** (2008), pg. 104262.

[85] M K Miller, D T Hoelzer, F Ebrahimi, J R Hawthorne, M G Burke, Microstructural Characterization of Irradiated Fe-Cu-Ni-P Model Steels, In: G J Theus, J R Weeks (Editors), *Environmental Degradation of Materials in Nuclear Power Systems - Water Reactors*, The Metallurgical Society, 1988, pgs. 133–139.

[86] M K Miller, M A Sokolov, R K Nanstad, K F Russell, APT Characterization of High Nickel RPV Steels, *Journal of Nuclear Materials*, **351** (2006), pgs. 187–196.

[87] M K Miller, K F Russell, J Kocik, E Keilova, Embrittlement of Low Copper VVER 440 Surveillance Samples Neutron-Irradiated to High Fluences, *Journal of Nuclear Materials*, **282** (2000), pgs. 83–88.

[88] M K Miller, K F Russell, J Kocik, E Keilova, Atom Probe Tomography of 15Kh2MFA Cr-Mo-V Steel Surveillance Specimens, *Micron*, **32** (2001), pgs. 749–755.

[89] M K Miller, K F Russell, Embrittlement of RPV Steels: An Atom Probe Tomography Perspective, *Journal of Nuclear Materials*, **371** (2007), pgs. 145–160.

[90] M K Miller, A A Chernobaeva, Y I Shtrombakh, K F Russell, R K Nanstad, D Y Erak, O O Zabusov, Evolution of The Nanostructure of VVER-1000 RPV Materials Under Neutron Irradiation and Post Irradiation Annealing, *Journal of Nuclear Materials*, **385** (2009), pgs. 615–622.

[91] T Takeuchi, A Kuramoto, J Kameda, T Toyama, Y Nagai, M Hasegawa, T Ohkubo, T Yoshiie, Y Nishiyama, K Onizawa, Effects of Chemical Composition and Dose on Microstructure Evolution and Hardening of Neutron Irradiated Reactor Pressure Vessel Steels, *Journal of Nuclear Materials*, **402** (2010), pgs. 93–101.

[92] M K Miller, *Atom Probe Tomography Analysis at the Atomic Level*, Kluwer Academic/ Plenum Publishers, New York, 2000.

[93] E Meslin, B Radiguet, P Pareige, C Toffolon, A Barbu, Irradiation-Induced Solute Clustering in a Low Nickel FeMnNi Ferritic Alloy, *Experimental Mechanics*, **51** (2011), pgs. 1453–1458.

[94] R Ngayam-Happy, C S Becquart, C Domain, L Malerba, Formation and Evolution of MnNi Clusters in Neutron Irradiated Dilute Fe Alloys Modelled by a First Principle-Based AKMC Method, *Journal of Nuclear Materials*, **426** (2012), pgs. 198–207.

[95] M K Miller, M G Burke, An Atom Probe Field Ion Microscopy Study of Neutron-Irradiated Pressure Vessel Steels, *Journal of Nuclear Materials*, **195** (1992), pgs. 68–82.

[96] M G Burke, M Watanabe, D B Williams, J M Hyde, Quantitative Characterization of Nanoprecipitates in Irradiated Low-Alloy Steels: Advances in the Application of FEG-STEM Quantitative Microanalysis to Real Materials, *Journal of Materials Science*, **41** (2006), pgs. 4512–4522.

[97] P Pareige, K F Russell, R E Stoller, M K Miller, Influence of Long-Term Thermal Aging on the Microstructural Evolution of Nuclear Reactor Pressure Vessel Materials: An Atom Probe Study, *Journal of Nuclear Materials*, **250** (1997), pgs. 176–183.

[98] M K Miller, K F Russell, APFIM Characterization of a High Phosphorus Russian RPV Weld, *Applied Surface Science*, **94-95** (1996), pgs. 378–383.

[99] M Charleux, F Livet, F Bley, F Louchet, Y Bréchet, Thermal Ageing of an Fe-Cu Alloy: Microstructural Evolution and Precipitation Hardening, *Philosophical Magazine A*, **73** (1996), pgs. 883–897.

[100] S Vaynman, D Isheim, R Prakash Kolli, S P Bhat, D N Seidman, M E Fine, High-Strength Low-Carbon Ferritic Steel Containing Cu-Fe-Ni-Al-Mn Precipitates, *Metallurgical and Materials Transactions A*, **39** (2008), pgs. 363–373.

[101] M K Miller, G D W Smith, Atom Probe Analysis of Interfacial Segregation, *Applied Surface Science*, **87-88** (1995), pgs. 243–250.

[102] M K Miller, R Jayaram, K F Russell, Characterization of Phosphorus Segregation in Neutron-Irradiated Russian Pressure Vessel Steel Weld, *Journal of Nuclear Materials*, **225** (1995), pgs. 215–224.

[103] R G Faulkner, R B Jones, Zheng Lu, P E J Flewitt, Grain Boundary Impurity Segregation and Neutron Irradiation Effects in Ferritic Alloys, *Philosophical Magazine*, **85** (2005), pgs. 2065–2099.

[104] M Guttmann, Ph Dumoulin, M Wayman, The Thermodynamics of Interactive Co-Segregation of Phosphorus and Alloying Elements in Iron and Temper-Brittle Steels, *Metallurgical Transactions A*, **13** (1982), pgs. 1693–1711.

[105] K Ebihara, M Yamaguchi, Y Nishiyama, K Onizawa, H Matsuzawa, Effect of Carbon on Irradiation-Induced Grain-Boundary Phosphorus Segregation in Reactor Pressure Vessel Steels Using First-Principles-Based Rate Theory Model, *Journal of Nuclear Materials*, **414** (2011), pgs. 328–335.

[106] M K Miller, M G Hetherington, M G Burke, Atom Probe Field-Ion Microscopy: A Technique for Microstructural Characterization of Irradiated Materials on the Atomic Scale, *Metallurgical Transactions A*, **20A** (1989), pgs. 2651–2661.

[107] T Toyama, Y Nagai, A Almazouzi, M Hatakeyama, M Hasegawa, T Ohkubo, E Van Walle, R Gerard, Intergranular Segregation at a Small Angle Grain Boundary in Pressure Vessel Steel of a Commercial Nuclear Reactor Studied by Laser-Assisted 3D Atom Probe, *Unpublished Research.*

[108] A D Romig, J I Goldstein, Determination of the Fe-Ni and Fe-Ni-P Phase Diagrams at Low Temperatures (700 to 300 C), *Metallurgical Transactions A*, **11** (1980), pgs. 1151–1159.

[109] T B Massalski, H Okamoto, P R Subramanian, L Kacprzak, *Binary Alloy Phase Diagrams*, 2nd Edition, ASM International, Ohio, 1990.

[110] M K Miller, A Cerezo, M G Hetherington, G D W Smith, *Atom Probe Field Ion Microscopy*, Oxford Science Publications, Oxford, 1996.

[111] D J Larson, D T Foord, A K Petford-Long, H Liew, M G Blamire, A Cerezo, G D W Smith, Field-Ion Specimen Preparation Using Focused Ion-Beam Milling, *Ultramicroscopy*, **79** (1999), pgs. 287–293.

[112] K Thompson, D Lawrence, D J Larson, J D Olson, T F Kelly, B Gorman, In Situ Site-Specific Specimen Preparation for Atom Probe Tomography, *Ultramicroscopy*, **107** (2007), pgs. 131–139.

[113] L Yao, K A Powers, M K Miller, Structural and Compositional Characterization of Grain Boundary in Radiation-Tolerant Nanostructured Alloys, In: *52nd IFES*, 2012.

[114] A Cerezo, T J Godfrey, G D W Smith, Application of a Position-Sensitive Detector to Atom Probe Microanalysis, *Review of Scientific Instruments*, **59** (1988), pgs. 862–866.

[115] M K Miller, R G Forbes, Atom Probe Tomography, *Materials Characterization*, **60** (2009), pgs. 461–469.

[116] T T Tsong, Field Ion Image Formation, *Surface Science*, **70** (1978), pgs. 211–233.

[117] T F Kelly, P P Camus, D J Larson, L M Holzman, S S Bajikar, On the Many Advantages of Local-Electrode Atom Probes, *Ultramicroscopy*, **62** (1996), pgs. 29–42.

[118] B Gault, M P Moody, F De Geuser, A La Fontaine, L T Stephenson, D J Haley, S P Ringer, Spatial Resolution in Atom Probe Tomography, *Microscopy and Microanalysis*, **16** (2010), pgs. 99–110.

[119] G Da Costa, F Vurpillot, A Bostel, M Bouet, B Deconihout, Design of a Delay-Line Position-Sensitive Detector with Improved Performance, *Review of Scientific Instruments*, **76** (2005), pg. 013304.

[120] B Gault, F de Geuser, L T Stephenson, M P Moody, B C Muddle, S P Ringer, Estimation of the Reconstruction Parameters for Atom Probe Tomography, *Microscopy and Microanalysis*, **14** (2008), pgs. 296–305.

[121] D J Haley, T Petersen, G Barton, S P Ringer, Influence of Field Evaporation on Radial Distribution Functions in Atom Probe Tomography, *Philosophical Magazine*, **89** (2009), pgs. 925–943.

[122] B Gault, M P Moody, J M Cairney, S P Ringer, *Atom Probe Microscopy*, 1st Edition, Springer, New York, 2012.

[123] M K Miller, M G Hetherington, Local Magnification Effects in the Atom Probe, *Surface Science*, **246** (1991), pgs. 442–449.

[124] F De Geuser, W Lefebvre, F Danoix, F Vurpillot, B Forbord, D Blavette, An Improved Reconstruction Procedure for the Correction of Local Magnification Effects in Three-Dimensional Atom-Probe, *Surface and Interface Analysis*, **39** (2007), pgs. 268–272.

[125] F Vurpillot, A Bostel, D Blavette, Trajectory Overlaps and Local Magnification in Three-Dimensional Atom Probe, *Applied Physics Letters*, **76** (2000), pgs. 3127–3129.

[126] P Camus, D J Larson, T F Kelly, A Method for Reconstructing and Locating Atoms on The Crystal Lattice in Three-Dimensional Atom Probe Data, *Applied Surface Science*, **87-88** (1995), pgs. 305–310.

[127] F Vurpillot, L Renaud, D Blavette, A New Step Towards the Lattice Reconstruction in 3DAP, *Ultramicroscopy*, **95** (2003), pgs. 223–229.

[128] K M Delargy, The Microstructure and Design of High Chromium Nickel-Base Superalloys, DPhil Thesis, University of Oxford (1981).

[129] E A Marquis, J M Hyde, Applications of Atom-Probe Tomography to the Characterisation of Solute Behaviours, *Materials Science and Engineering: R: Reports*, **69** (2010), pgs. 37–62.

[130] A Cerezo, M G Hetherington, Visualisation and Analysis of 3-Dimensional Atom Probe Data, *Colloque de Physique*, **50** (1989), pgs. 523–528.

[131] J M Hyde, T J Williams, A Cerezo, Statistical Analysis of Atom Probe Data: Detecting the Early Stages of Solute Clustering and/or Co-Segregation, *Ultramicroscopy*, **109** (2009), pgs. 502–509.

[132] R Prakash Kolli, D N Seidman, Comparison of Compositional and Morphological Atom-Probe Tomography Analyses for a Multicomponent Fe-Cu Steel, *Microscopy and Microanalysis*, **13** (2007), pgs. 272–284.

[133] A Heinrich, T Al-Kassab, R Kirchheim, Investigation of the Early Stages of Decomposition of Cu0.7at.% Fe with the Tomographic Atom Probe, *Materials Science and Engineering: A*, **353** (2003), pgs. 92–98.

[134] D Vaumousse, A Cerezo, P J Warren, A Procedure for Quantification of Precipitate Microstructures from Three-Dimensional Atom Probe Data, *Ultramicroscopy*, **95** (2003), pgs. 215–221.

[135] A Cerezo, L Davin, Aspects of the Observation of Clusters in the 3-Dimensional Atom Probe, *Surface and Interface Analysis*, **39** (2007), pgs. 184–188.

[136] D Vaumousse, An Atom Probe Study of Fine Scale Structure in AlMgSi(Cu) Alloys, DPhil Thesis, University of Oxford (2003).

[137] W Lefebvre, F Danoix, G Da Costa, F De Geuser, H Hallem, A Deschamps, M Dumont, 3DAP Measurements of Al Content in Different Types of Precipitates in Aluminium Alloys, *Surface and Interface Analysis*, **39** (2007), pgs. 206–212.

[138] L T Stephenson, M P Moody, P V Liddicoat, S P Ringer, New Techniques for the Analysis of Fine-Scaled Clustering Phenomena Within Atom Probe Tomography (APT) Data, *Microscopy and Microanalysis*, **13** (2007), pgs. 448–463.

[139] M Ester, H Kriegel, J Sander, X Xu, A Density-Based Algorithm for Discovering Clusters in Large Spatial Databases with Noise, In: E Simoudis, J Han, U Fayyad (Editors), *Second International Conference on Knowledge, Discovery and Data Mining*, AAAI Press, Menlo Park, CA, 1996, pgs. 10–15.

[140] W Lefebvre, T Philippe, F Vurpillot, Application of Delaunay Tessellation for the Characterization of Solute-Rich Clusters in Atom Probe Tomography, *Ultramicroscopy*, **111** (2011), pgs. 200–206.

[141] T Philippe, O Cojocaru-Miredin, F De Geuser, S Duguay, W Lefebvre, G Da Costa, D Blavette, Clustering and Nearest Neighbour Distances in Atom-Probe Tomography, *Ultramicroscopy*, **109** (2009), pgs. 1304–1309.

[142] A V Ceguerra, M P Moody, L T Stephenson, R K W Marceau, S P Ringer, A Three-Dimensional Markov Field Approach for the Analysis of Atomic Clustering in Atom Probe Data, *Philosophical Magazine*, **90** (2010), pgs. 1657–1683.

[143] W E Lorensen, H E Cline, Marching Cubes: A High Resolution 3D Surface Construction Algorithm, *ACM SIGGRAPH Computer Graphics*, **21** (1987), pgs. 163–169.

[144] O C Hellman, J A Vandenbroucke, J Rusing, D Isheim, D N Seidman, Analysis of Three-dimensional Atom-Probe Data by the Proximity Histogram, *Microscopy and Microanalysis*, **6** (2000), pgs. 437–444.

[145] J Rusing, J T Sebastian, O C Hellman, D N Seidman, Three-Dimensional Investigation of Ceramic/Metal Heterophase Interfaces by Atom-Probe Microscopy, *Microscopy and Microanalysis*, **6** (2000), pgs. 445–451.

[146] J M Hyde, M G Burke, B Gault, D W Saxey, P D Styman, K B Wilford, T J Williams, Atom Probe Tomography of Reactor Pressure Vessel Steels: An Analysis of Data Integrity, *Ultramicroscopy*, **111** (2011), pgs. 676–682.

[147] M K Miller, G D W Smith, An Atom Probe Study of the Anomalous Field Evaporation of Alloys Containing Silicon, *Journal of Vacuum Science and Technology*, **19** (1981), pgs. 57–61.

[148] B Gault, F Danoix, K Hoummada, D Mangelinck, H Leitner, Impact of Directional Walk on Atom Probe Microanalysis, *Ultramicroscopy*, **113** (2012), pgs. 182–191.

[149] D Kingham, The Post-Ionization of Field Evaporated Ions: A Theoretical Explanation of Multiple Charge States, *Surface Science*, **116** (1982), pgs. 273–301.

[150] Y Zhou, C Booth-Morrison, D N Seidman, On the Field Evaporation Behavior of a Model Ni-Al-Cr Superalloy Studied by Picosecond Pulsed-Laser Atom-Probe Tomography, *Microscopy and Microanalysis*, **14** (2008), pgs. 571–580.

[151] E W Müller, T T Tsong, *Field Ion Microscopy Principles and Applications*, 1st Edition, American Elsevier Publishing Company, New York, 1969.

[152] L T Stephenson, M P Moody, B Gault, S P Ringer, Estimating the Physical Cluster-Size Distribution Within Materials Using Atom-Probe, *Microscopy Research and Technique*, **74** (2011), pgs. 799–803.

[153] J M Hyde, E A Marquis, K B Wilford, T J Williams, A Sensitivity Analysis of the Maximum Separation Method for the Characterisation of Solute Clusters, *Ultramicroscopy*, **111** (2011), pgs. 440–447.

[154] L T Stephenson, M P Moody, S P Ringer, Theory of Solute Clustering in Materials for Atom Probe, *Philosophical Magazine*, **91** (2011), pgs. 2200–2215.

[155] J M Hyde, R M Boothby, C A English, P D Styman, H Thompson, G D W Smith, K B Wilford, T J Williams, Microstructural Characterisation of Nanometre Scale Irradiation Damage in High-Ni Weld, In: *Supplementary Proceedings Volume 2: Materials Properties, Characterisation and Modelling*, TMS, Orlando, Florida, 2012, pgs. 489–502.

[156] R K W Marceau, G Sha, R Ferragut, A Dupasquier, S P Ringer, Solute Clustering in Al-Cu-Mg Alloys During the Early Stages of Elevated Temperature Ageing, *Acta Materialia*, **58** (2010), pgs. 4923–4939.

[157] J A Liddle, G D W Smith, G B Olson, Alloy Carbide Precipitation in a High Cobalt-Nickel Secondary Hardening Steel, *Journal de Physique Colloque*, **47** (C7) (1986), pgs. 223–231.

[158] M Guttmann, Thermochemical Interactions Versus Site Competition in Grain Boundary Segregation and Embrittlement in Multicomponent Systems, *Journal de Physique IV Colloques*, **05** (C7) (1995), pgs. 85–96.

[159] M Guttmann, Grain Boundary Segregation, Two Dimensional Compound Formation, and Precipitation, *Metallurgical Transactions A*, **8** (1977), pgs. 1383–1401.

[160] M Guttmann, Temper Embrittlement and Ternary Equilibrium Segregation, *Materials Science and Engineering*, **42** (1980), pgs. 227–232.

[161] W M Young, E W Elcock, Monte Carlo Studies of Vacancy Migration in Binary Ordered Alloys: I, *Proceedings of the Physical Society*, **89** (1966), pgs. 735–746.

[162] G Sha, A Cerezo, G D W Smith, Thermal Decomposition of Pressure Vessel Steels, Technical report, University of Oxford (2005).

[163] M S Anand, Diffusion of Copper in Iron, *Journal of Applied Physics*, **37** (1966), pgs. 4248–4251.

[164] K C Russell, L M Brown, A Dispersion Strengthening Model Based on Differing Elastic Moduli Applied to the Iron-Copper System, *Acta Metallurgica*, **20** (1972), pgs. 969–974.

[165] L Liu, Effects of Solute Elements on Hardening and Microstructural Changes of Thermally Aged RPV Model Alloys Using Three-dimensional Atom Probe, Masters Thesis, University of Tokyo (2011).

[166] M K Miller, K F Russell, P Pareige, M J Starink, R C Thomson, Low Temperature Copper Solubilities in Fe-Cu-Ni, *Materials Science and Engineering: A*, **250** (1998), pgs. 49–54.

[167] M E Schlesinger, Thermodynamics of Solid Transition-Metal Silicides, *Chemical Reviews*, **90** (1990), pgs. 607–628.

[168] Discussions with J M Titchmarsh.

[169] G R Odette, R K Nanstad, A Brief History and Current Status of Insight on Late Blooming Ni-Mn-Si Phases in Irradiated RPV Steels, Presentation at the Perform 60 Meeting, Seville (2012).

[170] M K Miller, K A Powers, R K Nanstad, P Efsing, Atom Probe Tomography Characterizations of High Nickel, Low Copper Surveillance RPV Welds Irradiated to High Fluences, *Journal of Nuclear Materials*, **437** (2013), pgs. 107–115.

[171] M Guttmann, The Link Between Equilibrium Segregation and Precipitation in Ternary Solutions Exhibiting Temper Embrittlement, *Metal Science*, **10** (1976), pgs. 337–341.

[172] M Guttmann, Equilibrium Segregation in a Ternary Solution: A Model for Temper Embrittlement, *Surface Science*, **53** (1975), pgs. 213–227.

[173] T J Wilkes, J M Titchmarsh, G D W Smith, D A Smith, R F Morris, S Johnston, T J Godfrey, P Birdseye, The Fracture of Field-Ion Microscope Specimens, *Journal of Physics D: Applied Physics*, **5** (1972), pgs. 2226–2230.

[174] P H T Philipsen, E J Baerends, Cohesive Energy of 3d Transition Metals: Density Functional Theory Stomic and Bulk Calculations, *Physical Review B*, **54** (1996), pgs. 5326–5333.

[175] B Farid, R Godby, Cohesive Energies of Crystals, *Physical Review B*, **43** (1991), pgs. 14248–14250.

[176] W Martienssen, H Warlimont (Editors), *Springer Handbook of Condensed Matter and Materials Data*, 1st Edition, Springer, 2005.

[177] C Kittel, *Introduction to Solid State Physics*, 8th Edition, Wiley, 2004.

[178] P Ehrhart, *Atomic Defects in Metals*, Landolt-Börnstein: Numerical Data and Functional Relationships in Science and Technology - New Series, Vol. 25, Springer, 1991.

[179] J Vanhellemont, M Suezawa, I Yonenaga, On the Impact of Germanium Doping on the Vacancy Formation Energy in Czochralski-Grown Silicon, *Journal of Applied Physics*, **108** (2010), pg. 016105.

[180] Y Iijima, K Kimura, K Hirano, Self-Diffusion and Isotope Effect in $\alpha$-Iron, *Acta Metallurgica*, **36** (1988), pgs. 2811–2820.

[181] K Hirano, M Cohen, B L Averbach, Diffusion of Nickel into Iron, *Acta Metallurgica*, **9** (1961), pgs. 440–445.

[182] K Nohara, K Hirano, Diffusion of Mn(54) in Iron and Iron-Manganese Alloys, In: *Proceedings of International Conference on the Science and Technology of Iron and Steel*, Tokyo, 1970, pgs. 1267–1273.

[183] V T Borisov, V M Golikov, B Y Ljubov, G V Scherbedinsky, Research with Radioisotopes, In: R C Extermann (Editor), *Proceedings of UNESCO International Conference on Radioisotopes*, Volume 1, Pergamon Press, 1958.

[184] A Moslang, E Albert, E Recknagel, A Weidinger, P Moser, Interaction of vacancies with impurities in Iron, *Hyperfine Interactions*, **15/16** (1983), pgs. 409–412.

[185] G Brauer, K Popp, Neutron Embrittlement of Reactor Pressure Vessel Steels: A Challenge to Positron Annihilation and Other Methods, *Physica Status Solidi A*, **102** (1987), pgs. 79–90.

# Appendix

# A. Selection of Appropriate Image Regions for APT Reconstruction

To ensure the best quality atom probe data it is important to select suitable regions in depth so as to exclude the initial stages of evaporation, which may contain oxides, and to select a region of uniform evaporation. Likewise an $x$-$y$ region needs to be selected so as to remove artefacts from debris on the local electrode deposited from previous specimen fractures.

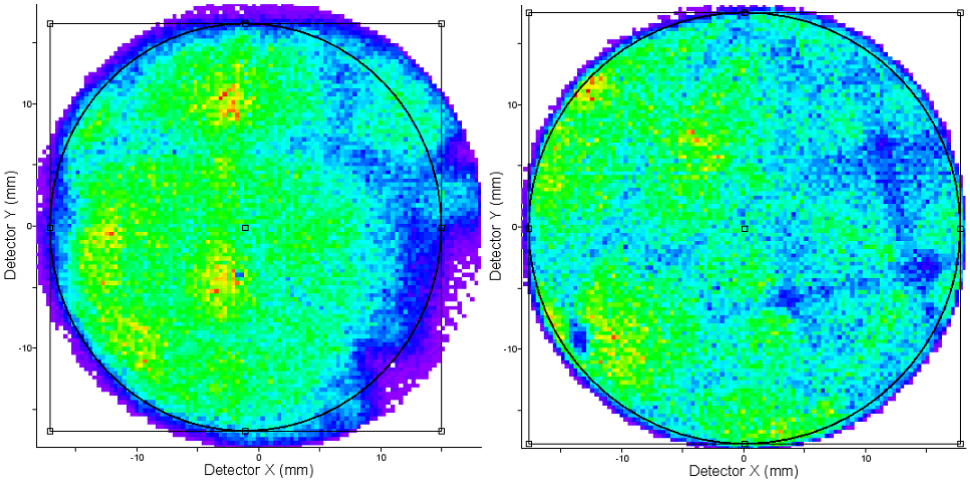


*(a)* Detector hitmap showing low density regions around the edge of the hitmap caused by debris on the local electrode.

*(b)* Detector hitmap showing a good quality hitmap free from any electrode effects.

*Figure A.1:* (a) Poor quality detector hitmap showing many regions of low density caused from debris on the local electrode and (b) good quality hitmap free from such effects which also shows the presence of an (020) pole in this specimen.

Debris deposited on the local electrode can block the path of ions evaporated from the tip from reaching the detector, this causes regions on the edge of the detector where

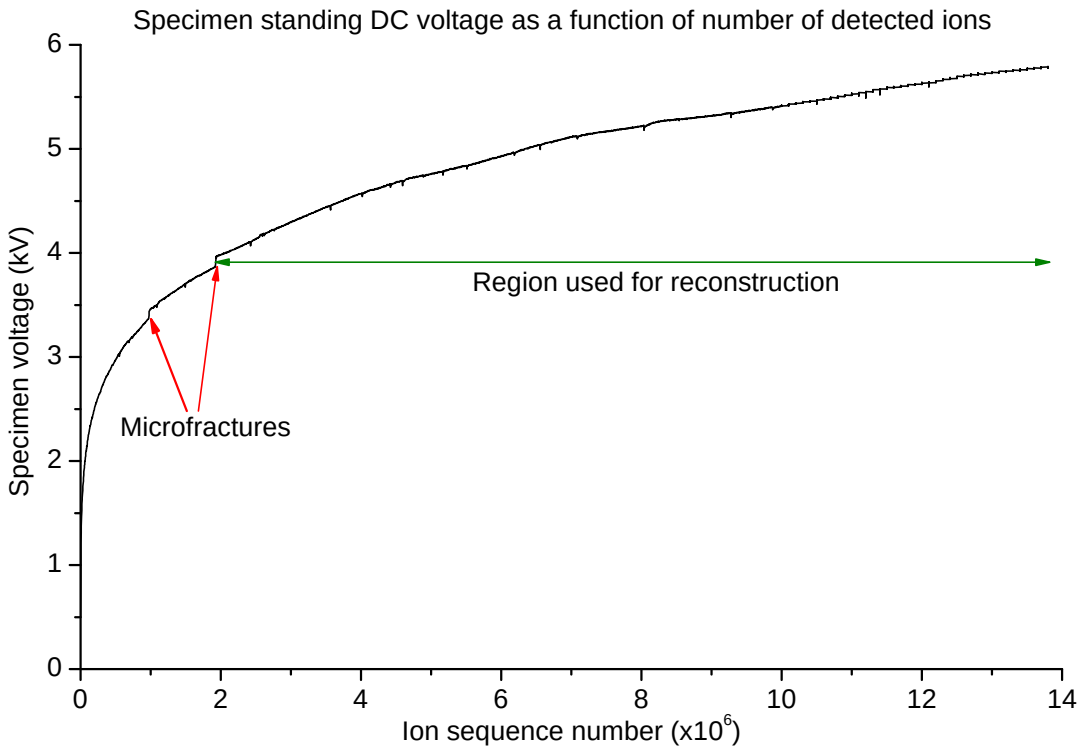


*Figure A.2:* Evolution of the voltage showing a region containing two small microfractures, and a region free of microfractures used for the reconstruction.

the are very few hits, as shown in Figure A.1a. Suitable $x$-$y$ regions should be selected so as to exclude these regions from the analysis. By comparison Figure A.1b shows a detector hitmap from an electrode free of debris, hence there are no low density regions around the edge of the detector.

In terms of selecting a suitable depth region, the initial period of evaporation will contain mainly ions from the specimen's surface oxide as noted above, hence the data will not be of interest. During the analysis the specimen is subject to high stress from the voltage pulses which can cause the tip to fracture. This can be a local melting of the tip, brittle fracture or shear[173], and results in a tip too blunt to continue with the analysis. In some cases this fracture is small and the resulting tip is still suitable for analysis[173]. It is also possible that this could result in some localised heating at the apex if the microfracture is associated with a small arc. This could, in principle, affect the microstructure at the apex. The resulting specimen will be slightly blunter and hence there will be an increase in the specimen voltage as highlighted in Figure A.2. These regions should not be used for analysis as they are

not from a continuous portion of the tip. In the example in Figure A.2 the indicated region should be used as this shows a region of uniform evaporation.

# B. Hardness Evolution of Each Alloy with Ageing Temperature

The following graphs show the hardness evolution of each of the materials with ageing temperature. Figure B.1 shows the evolution of the low Ni welds, Figure B.2, the high Ni welds and Figure B.3 the plate materials. The evolution of these materials with ageing time and temperature is discussed in detail in Section 5.1.

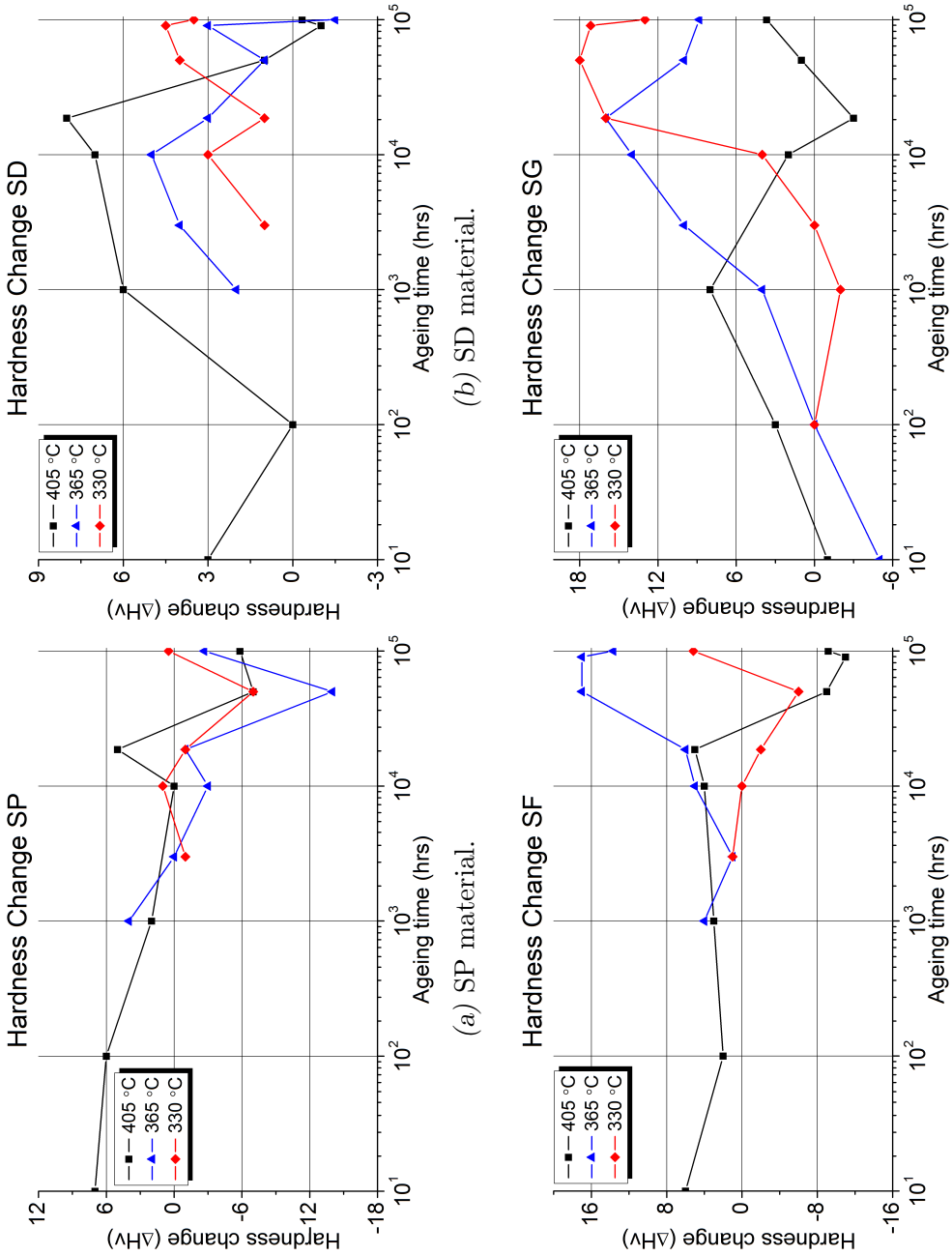


(a) SP material. (b) SD material. (c) SF material. (d) SG material.

*Figure B.1:* Hardness evolution with ageing time for the low Ni materials (a) SP, (b) SD, (c) SF and (d) SG. Errors are ±4 Hv and are not shown for clarity.

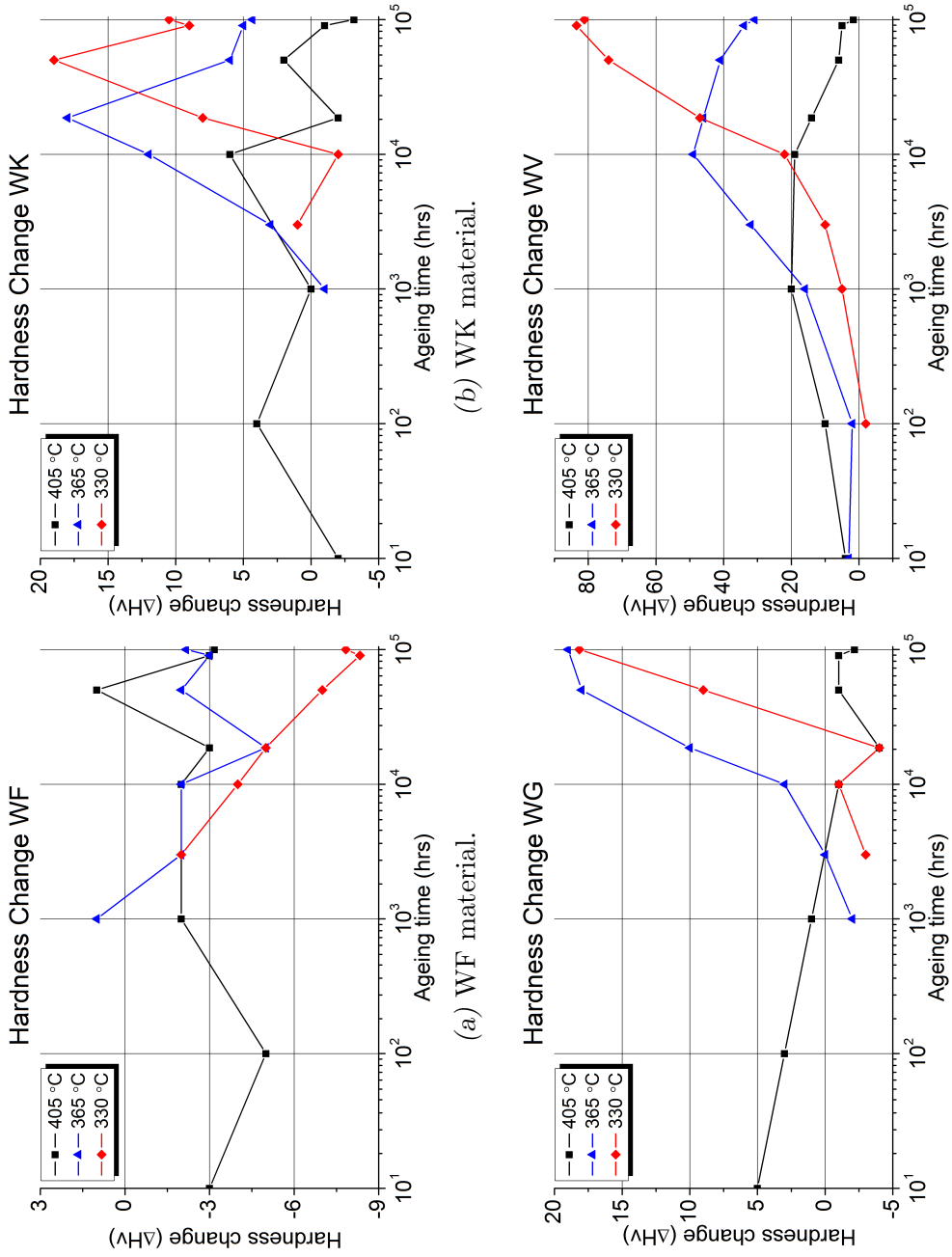


(a) WF material. (b) WK material. (c) WG material. (d) WV material.

*Figure B.2:* Hardness evolution with ageing time for the high Ni materials (a) WF, (b) WK, (c) WG and (d) WV. Errors are ±4 Hv and are not shown for clarity.

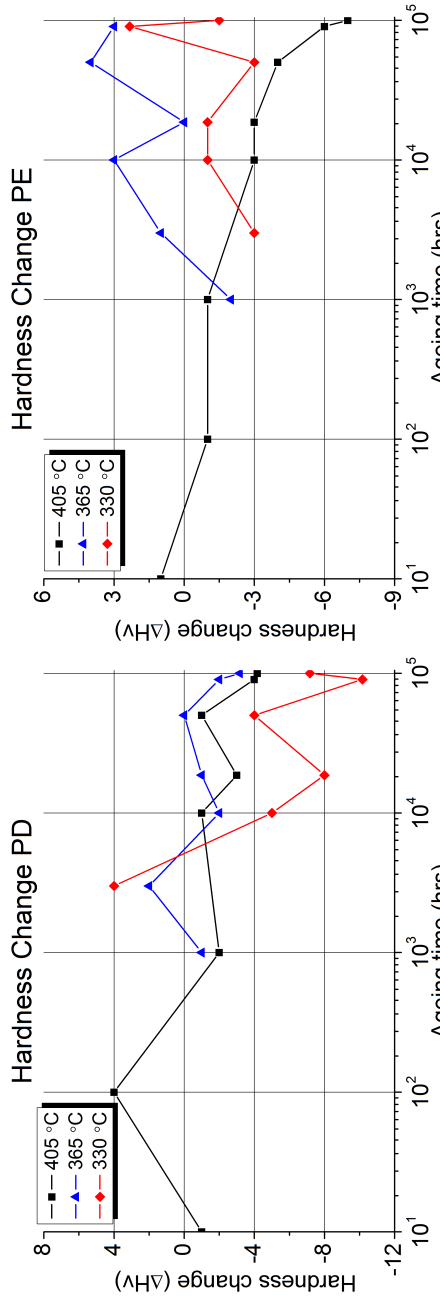


(*a*) PD material.

(*b*) PE material.

*Figure B.3:* Hardness evolution with ageing time for the plate materials (a) PD and (b) PE. Errors are ±4 Hv and are not shown for clarity.

# C. Noise Correction of Sn Peaks

Noise counts have a significant effect on the measured quantity of Sn observed in the SG steels. To obtain accurate quantification of the Sn in the SG steel it is necessary to correct the measured Sn counts for this noise. This is particularly the case for the matrix Sn level. Around the precipitates where Sn is concentrated nearly all the Sn counts would be expected to be from genuine Sn ions. For this reason, and for the sake of simplicity only the matrix Sn counts will be background corrected.

The raw counts of each isotope of Sn (116 - 122 amu) are shown in Table C.1. The Sn isotopes of 112, 114 and 115 are not evident in the mass spectrum are not ranged as Sn. These peaks represent less than 2 % of the total Sn in the system so will not have significant effect on the overall result.

| Sn isotope | Dataset 1 | Dataset 2 | Dataset 3 | Dataset 4 | Dataset 5 |
|---|---|---|---|---|---|
| 116 | 1069 | 481 | 428 | 264 | 1360 |
| 117 | 498 | 234 | 204 | 124 | 603 |
| 118 | 1084 | 448 | 438 | 235 | 1387 |
| 119 | 579 | 302 | 257 | 147 | 798 |
| 120 | 1386 | 508 | 497 | 294 | 1701 |
| 122 | 343 | 171 | 146 | 76 | 401 |
| 124 | 500 | 256 | 233 | 131 | 647 |

*Table C.1:* Number of ions of each Sn isotope in the SG material aged for 100,000 hrs at 330 °C.

The fractional abundance of each of these species should agree with the expected isotopic abundances. This should indicate if there is any influence of overlapping peaks, for instance from Ni and Fe. The fractional abundance of each peak is detailed in Table C.2. For comparison the expected fraction and the isotopic abundance of

| Sn isotope | Isotope abundance (%) | Expected fraction | Calculated fraction 1 | 2 | 3 | 4 | 5 |
|---|---|---|---|---|---|---|---|
| 116 | 14.54 | 0.15 | 0.20 | 0.20 | 0.19 | 0.21 | 0.20 |
| 117 | 7.68 | 0.08 | 0.09 | 0.10 | 0.09 | 0.10 | 0.09 |
| 118 | 24.22 | 0.25 | 0.20 | 0.19 | 0.20 | 0.18 | 0.20 |
| 119 | 8.59 | 0.09 | 0.11 | 0.13 | 0.12 | 0.12 | 0.12 |
| 120 | 32.58 | 0.33 | 0.25 | 0.21 | 0.23 | 0.23 | 0.25 |
| 122 | 4.63 | 0.05 | 0.06 | 0.07 | 0.07 | 0.06 | 0.06 |
| 124 | 5.79 | 0.06 | 0.09 | 0.11 | 0.11 | 0.10 | 0.09 |

*Table C.2:* Measured fraction of each isotope of Sn, uncorrected for background noise, for the data in Table C.1 for datasets 1 to 5.

each Sn isotope is also shown.

This indicates that for the two main isotopes 118 and 120 the Sn level is below the expected level, whereas for the $^{116}Sn^{2+}$ peak there is too much Sn, probably from overlap with the $^{58}Fe^{+}$ peak. The more minor isotopes generally show good agreement with the expected fraction. The influence of peak overlaps seems to be limited to the $^{116}Sn^{2+}$ isotope.

Background noise correction of the Sn peaks was performed by ranging the mass spectrum as shown in Figure C.1.

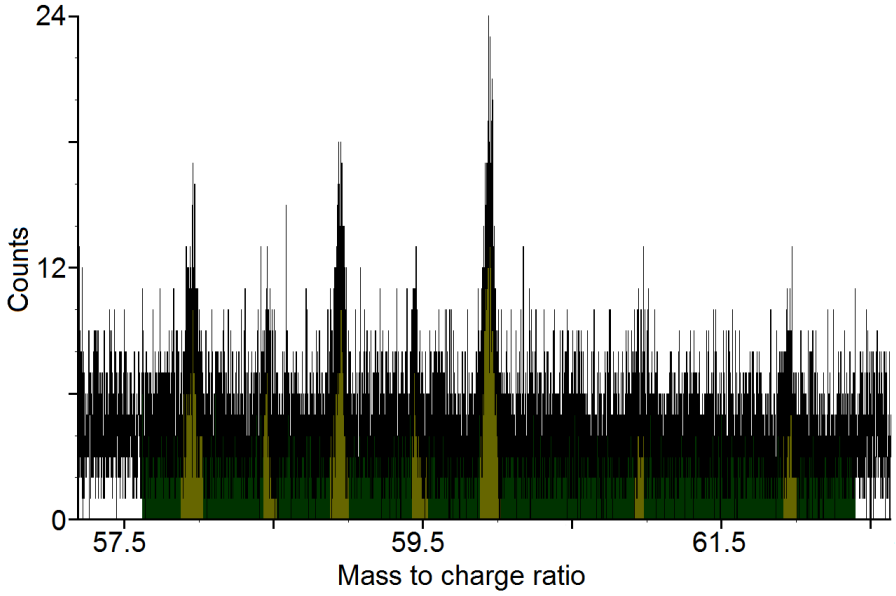


*Figure C.1:* SG mass spectrum showing noise ranges (dark green regions) used for the Sn background noise correction.

These noise ranges were used to calculate the average number of noise ions in each bin in the mass spectrum. The corresponding number of ions of noise in each of the Sn peaks can thus be calculated by multiplying the average number of noise counts in each bin by the number of mass bins in each range. Subtracting this from the raw number of counts of each Sn isotope gives the noise corrected Sn counts. The noise corrected ratios of the Sn isotopes are shown in Table C.3.

| Sn isotope | Isotope abundance (%) | Expected fraction | Calculated fraction | | | | |
|---|---|---|---|---|---|---|---|
| | | | 1 | 2 | 3 | 4 | 5 |
| 116 | 14.54 | 0.15 | 0.20 | 0.22 | 0.19 | 0.24 | 0.20 |
| 117 | 7.68 | 0.08 | 0.06 | 0.04 | 0.05 | 0.06 | 0.05 |
| 118 | 24.22 | 0.25 | 0.25 | 0.28 | 0.28 | 0.24 | 0.26 |
| 119 | 8.59 | 0.09 | 0.05 | 0.06 | 0.06 | 0.05 | 0.08 |
| 120 | 32.58 | 0.33 | 0.36 | 0.33 | 0.33 | 0.36 | 0.35 |
| 122 | 4.63 | 0.05 | 0.03 | 0.03 | 0.03 | 0.00 | 0.02 |
| 124 | 5.79 | 0.06 | 0.04 | 0.03 | 0.06 | 0.05 | 0.05 |

*Table C.3:* Measured isotopic fractions of each Sn isotope after background noise correction for datasets 1 to 5.

After noise correction, these fractions are much closer to the expected values as calculated from the isotopic abundances. There are, of course, some deviations but these are to be expected given the small sizes of the peaks.

# D. Values Used for Monte-Carlo Modelling Parameters

The tables below detail the values of the cohesive energy, nearest neighbour distance, vacancy formation energy, diffusion coefficient, vacancy binding energy, substitutional diffusion activation energy and solid solubilities used to calculate the parameters used in the Monte-Carlo modelling as detailed in Table 6.1 in Chapter 6.

| Element | Cohesive energy kJ $mol^{-1}$ | Ref No. |
|---|---|---|
| Fe | -413 | [174] |
| Cu | -336 | [174] |
| Ni | -428 | [174] |
| Mn | -282 | [174] |
| Si | -446 | [175] |

*Table D.1:* Values used for the cohesive energy between a Fe atom and another element in the simulation.

| Element | Nearest neighbour Distance (nm) | Ref No. |
|---|---|---|
| Fe | 0.248 | [176] |
| Cu | 0.256 | [176] |
| Ni | 0.249 | [176] |
| Mn | 0.224 | [177] |
| Si | 0.235 | [176] |

*Table D.2:* Values used for the nearest neighbour distance in the pure metal of each element in the simulation.

| Element | Vacancy formation energy (kJ mol$^{-1}$) | Ref No. |
|---|---|---|
| Fe | 154 | [35] |
| Cu | 124 | [35] |
| Ni | 173 | [178] |
| Mn | 154 | |
| Si | 386 | [179] |

*Table D.3:* Values used for the vacancy formation energy in the pure metal of each element in the simulation.

| Element | Diffusion coefficient (x10$^{-4}$ m$^2$ s$^{-1}$) | Temperature (K) | Ref No. |
|---|---|---|---|
| Fe | 2.8 | 766 - 1148 | [180] |
| Cu | 0.57 | 1073 - 1173 | [163] |
| Ni | 1.4 | 873 - 953 | [181] |
| Mn | 1.5 | 973 - 1033 | [182] |
| Si | 0.62 | | [183] |

*Table D.4:* Values used for the diffusion co-efficient of Cu, Ni, Mn and Si in Fe.

| Element | Vacancy binding energy (kJ mol$^{-1}$) | Ref No. |
|---|---|---|
| Fe | | |
| Cu | 10.6 | [184] |
| Ni | 20.3 | [184] |
| Mn | 14.5 | [185] |
| Si | 20.3 | [184] |

*Table D.5:* Values used for the vacancy binding energy.

| Element | Activation energy (kJ mol$^{-1}$) | Ref No. |
|---|---|---|
| Fe | 251 | [180] |
| Cu | 239 | [163] |
| Ni | 246 | [181] |
| Mn | 222 | [182] |
| Si | 221 | [183] |

*Table D.6:* Values used for the activation energy for substitutional diffusion.

| Elements | | Solubility limit (at.%) | Temp (K) | Ref No. |
|---|---|---|---|---|
| Fe | Cu | 0.026 | 638 | |
| Fe | Ni | 5.53 | 773 | [109] |
| Fe | Mn | 3.05 | 673 | [109] |
| Fe | Si | 19.60 | 1548 | [109] |
| Cu | Ni | | | |
| Cu | Mn | | | |
| Cu | Si | 11.40 | 1126 | [109] |
| Ni | Mn | 9 | 859 | [109] |
| Ni | Si | 14.70 | 1308 | [109] |
| Mn | Si | 6 | 908 | [109] |

*Table D.7:* Solid solubilities of each combination of elements used in the simulation.

# E. Monte-Carlo Simulation and Analysis Code

## E.1 LKMC Code

Changes from the original code are highlighted as follows:

Underlined green text indicates new code

Crossed out red text indicates deleted code

Code which is not highlighted as above has not been changed.

```
#ifdef DEBUG
    #include <assert.h>
    #define ASSERT(f) {if(!(f)){ printf("Assertion failed: %s - %d
",__FILE__,__LINE__);getchar();}}
#else
    #define ASSERT(f) {}
#endif

#ifdef x64 // if 64 bit environment
#define FMT_LLU "I64u"
#define FMT_LLU_32 "I32u"
#else
#define FMT_LLU "llu"
#define FMT_LLU_32 "u"
#endif

#include <stdio.h>
#include <stdlib.h>
#include <string.h>
#include <sys/time.h>
#include <time.h>
#include <limits.h>
#include <math.h>
#include <float.h>
#include "GSsimulation_parameters.h"
#include "drand48SFMT.h"


void#include "zlib.h"
#include "zconf.h"
#include "memoryallocs.h"
#include "getatomtype.h"


int Atoms_Arrangement();(int ****vacancyprofile);
void Define_Lookup_Table();
void Periodic_Boundary_Conditions(int, int, int, int);
void Vacancy_Coordinates(int, int, int, int, int);
voidint Cluster_Analysis();(unsigned long long
monte_carlo_steps,double *real_time,int file_number, int*
the_value_of_e);
voidint Saving_Atoms_Arrangement(int file_number);
voidint Exchange_Positions();(int *p_ , int *q_ , int *r_ , int
*neighbours,



    /* Atom species among Fe(0), Cu(1), Ni(2), Mn(3), Si(4) and
vacancy(5) */
int atom[AXIAL_ATOMS_NUMBER + 4][AXIAL_ATOMS_NUMBER +
4][AXIAL_ATOMS_NUMBER + 4];
                          int neighbours_[6][8], float *w, float *a,
double *real_time,int ****vacancyprofile);

int savevacancypositions(int file_number, int**** vacancyprofile,
double *real_time, unsigned long long monte_carlo_steps);
int Atom_Tracker(int l, int m, int n);
int binary_search(int l, int m, int n);
int countmoves(int Atom_ID);
int print_positions(unsigned long long monte_carlo_steps);
int diffusion(int* the_value_of_e);
```

```
int int_cmp(const void *a, const void *b);
void floatSwapBytes(float *inFloat); // Converts pos file from litte
endian to big endian.

//added 13/6/11
//Reverse the byte order for a given float. Used to set output order
for "pos" file format which is big-endian
//Use a union to avoid strict-aliasing error
typedef union {
   float f;
   char c[4];
} FloatSwapUnion ;

//----------------Globally Available Arrays-------------------------
--//
int Coordinates_of_Vacancy[VACANCY_NUMBER][3];   /* 3 corresponds to
x, y and z coordinates */
int Coordinates_of_Vacancy[VACANCY_NUMBERNN_vector[2][8][3];     /*
Vectors to nearest neighbour positions [layer along z
direction][coordination number][x, y or z coordinate] */
int NN_vector[2][8][3];
float partial_transition_probability[6][6][17];    /* Jumping
probability in the form of exp (-delta E / RT) */
double partial_transition_probability[6][6][17];
    float pre_factor[6];  /* pre-factors of transition probabilities
*/
double pre_factor[6];

static double monte_carlo_steps;
static double real_time;


float interaction[6][6] = {
    {VFeFe, VFeCu, VFeNi, VFeMn, VFeSi, VFeV},
    {VFeCu, VCuCu, VCuNi, VCuMn, VCuSi, VCuV},
    {VFeNi, VCuNi, VNiNi, VNiMn, VNiSi, VNiV},
    {VFeMn, VCuMn, VNiMn, VMnMn, VMnSi, VMnV},
    {VFeSi, VCuSi, VNiSi, VMnSi, VSiSi, VSiV},
    {VFeV, VCuV, VNiV, VMnV, VSiV, VVV}
};
//----------------------------------------------------------------------
--//


//----------Globally Available items for Atom_Tracker----------------
--//
int amTracking;
int Number_of_atoms_to_track;
int *Atoms_to_track;

gzFile *Atom_track_filename;
char Atoms_filename[100];
//----------------------------------------------------------------------
-//


//--------------Pointers for dynamically allocated memory------------
--------//
int*** solute_number;   /* Three-dimensional array indicating a solute
number */
int* cluster_size;
```

```
int* number_of_clusters;
int** Coordinates_of_Atoms_for_Clusters;
int** Coordinates_of_Solute_Atoms;
int *pointer ;
int**** vacancyprofile; // stores the number of times a vacancy has
been at a given site
int* cluster_contents;  // stores the identities of solutes in
clusters indexed by cluster_size[e].
int ***atom;
unsigned long long* No_of_Moves;
//-------------------------------------------------------------------
--------//

/*********************************************************************/
/* Main function  */
/*********************************************************************/
int main~~()~~(int argc, const char *argv[])
{


    ~~int j, k;~~
    if(AXIAL_ATOMS_NUMBER % 2){
        printf("This is an error : Axial atoms number *must* be even.
Recompile.");
        return 1;
    }
    // RANDOM NUMBER GENERATOR CHANGED FROM DRAND48() TO MERSENNE
TWISTER ALGORITHM  PS 14/6/11

    int b=0, c=0; //Changed to  "b" and "c" from "j" and "k" as j and
k used below when static ints removed PS 14/6/11
    unsigned long long monte_carlo_steps=0;  //moved into main() and
static removed PS 11/6/11
    double real_time = 0;   //moved into main() and static removed PS
11/6/11
    const int Total_Analysis_Times = sizeof(time_for_analysis) /
sizeof(~~double~~unsigned long long);
    const int Total_Saving_Times = sizeof(time_for_saving) /
sizeof(~~double~~unsigned long long);
    int p_[8], q_[8], r_[8];  /* Coordinates of nearest neighbor atoms
around the vacancy */
    int neighbours[6];
    int neighbours_[6][8];   /* Numbers of nearest neighbor solute
atoms and vacancies around the two.
        [number of possible different atom or vacancy
types]([Coordination number]) */
    float w[8];    /* transition probability for the i-th nearest
neighbor atom */
    float a[8];    /* relative probabilities from 0 to 1 */
    char step_time[20];
    int the_value_of_e; // used to carry the value of e from cluster
analysis to diffusion analysis.

    //------dynamically allocates memory for large arrays.-----------
-------------//
        atom = allocatememory3d(AXIAL_ATOMS_NUMBER ,
AXIAL_ATOMS_NUMBER, AXIAL_ATOMS_NUMBER);
        if(!atom){
            printf("~~Never close this window!!\~~Failed to allocate
memory for atom on line %d.\n~~");~~",__LINE__);
    ~~srand48(0);~~                                        /*        exit(1);
```

```
        }
        vacancyprofile = allocatememory4d(VACANCY_NUMBER,
AXIAL_ATOMS_NUMBER , AXIAL_ATOMS_NUMBER, AXIAL_ATOMS_NUMBER);
        if(!vacancyprofile){
            printf("Failed to allocate memory for vacancyprofile on
line %d.\n",__LINE__);
            exit(1);
        }

        solute_number =
allocatememory3d(AXIAL_ATOMS_NUMBER,AXIAL_ATOMS_NUMBER,AXIAL_ATOMS_NUM
BER);
        if(!solute_number){
            printf("Failed to allocate memory for solute_number on
line %d.\n",__LINE__);
            exit(1);
        }
        pointer  = (int*)malloc((TOTAL_SOLUTE_ATOMS_NUMBER +
1)*sizeof(int));  /* Pointer for solute numbers */
        if(!pointer){
            printf("Failed to allocate memory for pointer on line
%d.\n",__LINE__);
            exit(1);
        }
        Coordinates_of_Atoms_for_Clusters =
allocatememory2d(TOTAL_SOLUTE_ATOMS_NUMBER + 1,3); //allocates memory
for Coordinates_of_Atoms_for_Clusters
        if(!Coordinates_of_Atoms_for_Clusters){
            printf("Failed to allocate memory for
Coordinates_of_Atoms_for_Clusters on line %d.\n",__LINE__);
            exit(1);
        }
        Coordinates_of_Solute_Atoms =
allocatememory2d(TOTAL_SOLUTE_ATOMS_NUMBER + 1,3);  //allocates memory
for Coordinates_of_Solute_Atoms
        if(!Coordinates_of_Solute_Atoms){
            printf("Failed to allocate memory for
Coordinates_of_Solute_Atoms on line %d.\n",__LINE__);
            exit(1);
        }
        cluster_size = (int*)malloc((TOTAL_SOLUTE_ATOMS_NUMBER +
1)*sizeof(int)); /* Number of clusters havind size[] */
        if(!cluster_size){
            printf("Failed to allocate memory for cluster_size on line
%d.\n",__LINE__);
            exit(1);
        }
        number_of_clusters = (int*)malloc((TOTAL_SOLUTE_ATOMS_NUMBER +
1)*sizeof(int));
        if(!number_of_clusters){
            printf("Failed to allocate memory for number_of_clusters
on line %d.\n",__LINE__);
            exit(1);
        }
        cluster_contents =
(int*)calloc(TOTAL_SOLUTE_ATOMS_NUMBER,sizeof(int)); // allocates
memory for cluster contents.
        if(!cluster_contents){
            printf("Failed to allocate memory for cluster_contents on
line %d.\n",__LINE__);
            exit(1);
```

```
        }
        No_of_Moves = (unsigned long long*)
calloc(TOTAL_SOLUTE_ATOMS_NUMBER+1,sizeof(unsigned long long));
        if(!No_of_Moves){
            printf("Failed to allocate memory for No_of_Moves on line
%d.\n",__LINE__);
            exit(1);
        }
        //NOTE THE FIRST ELEMENT IN THIS ARRAY WILL NOT GET USED SINCE
IT TAKES IN THE ATOM ID WHICH START AT 1
    //-----------------------------------------------------------------
-------------//


    //----Initialization of Random No. Generator---------------------
//
        uint32_t seed;      // seed for random No. generator.

        seed = (uint32_t)time(0);       // Sets seed to the time
changed by PS 13/6/11
        init_gen_rand(seed); // Initializes random No. generator
changed by PS 13/6/11
    //-----------------------------------------------------------------
-//


    //----This is the setup to find the date---//
        struct timeval tv,tvend;
        time_t rawtime;
        struct tm * timeinfo;
    //-----------------------------------------------------------------
//


    //------Set-up for Atom_Tracker-----------------------------//
        sprintf(Atoms_filename,"Tracked Atom Positions-%dK-%d",
(int)TEMP,VERSION_NO);

        Atom_track_filename = gzopen(Atoms_filename,"wb");
        if(Atom_track_filename == NULL) is set to 0*/){
            printf("gz open error\n");
            exit(1);
        }
    //-----------------------------------------------------------------
-------------//

    printf("Running Correctedmonte8-PS-%d. The seed was:
%"FMT_LLU_32".\n",VERSION_NO,seed);
    printf("Arranging Atoms\n");
    if(Atoms_Arrangement();(vacancyprofile)){
        printf("Atoms_Arrangement failed");
        exit(1);
    }
    printf("Atoms Arranged\n"); // Added PS 14/6/11

    Define_Lookup_Table();
    printf("Look-Up Table Defined\n"); // Added PS 14/6/11

    gettimeofday(&tv, NULL);

    if(print_positions(monte_carlo_steps)){
```

```
        printf("Initial positions not printed to file correctly");
        exit(1);
    }

    for (monte_carlo_steps=1;
monte_carlo_steps<=TOTAL_MONTE_CARLO_STEPS; monte_carlo_steps++){

        /* Exchange between a vacancy and an atom */
        if(Exchange_Positions();( p_ , q_ , r_ , neighbours,
neighbours_,
                    w, a,&real_time, vacancyprofile)){ //
Changed as Static int removed PS 14/6/11
            printf("Error in Exchange_Positions.\n");
            exit(1);
        }
        /* To the function of cluster analysis  */   //Changed to  "b"
from "j" PS 14/6/11
        for (jb=0; jb<Total_Analysis_Times; jb++){

            if(monte_carlo_steps == time_for_analysis[jb]){
                gettimeofday(&tvend, NULL);
                printf("It's taken %f seconds so
far.\n",(tvend.tv_sec-tv.tv_sec) + (float)(tvend.tv_usec-
tv.tv_usec)/1000000.0);
                time(&rawtime);
                timeinfo = localtime(&rawtime);
                strftime(step_time,20,"%d-%b  %H:%M",timeinfo);
                printf("Correctedmonte8-PS-%d. Current Step:
%"FMT_LLU". Time: %s\n",VERSION_NO,time_for_analysis[b],step_time);
                printf("Analysing Clusters\n");
                if(Cluster_Analysis();          (monte_carlo_steps,
&real_time,b, &the_value_of_e)){
                    printf("Error in cluster search.\n");
                    exit(1);
                }
                break;
            }
        }

        /* To the function of saving of atoms arrangements  */
//Changed to  "c" from "k" PS 14/6/11

        for (kc=0; kc<Total_Saving_Times; kc++){
            if(monte_carlo_steps == time_for_saving[kc]){
                printf("Saving Positons\n");
                if(Saving_Atoms_Arrangement(k);c)){
            }                   printf("Error in
Saving_Atoms_Arrangement.\n");
        }           exit(1);
                }
    }
if(savevacancypositions(c,vacancyprofile,&real_time,monte_carlo_steps)
){
                    printf("Error in savevacancypositions.\n");
                    exit(1);
                }
                break;
            }
        }
    }
```

```
    if(print_positions(monte_carlo_steps)){
        printf("Final positions not printed to file correctly.\n");
        exit(1);
    }

    //Closes file with tracked atom positions
    printf("Closing the file handle\n");
    if(gzclose(Atom_track_filename) != 0){
        printf("Error closing gzip file.\n");
        exit(1);
    }

    if(diffusion(&the_value_of_e)){
        printf("Error in diffusion.\n");
        exit(1);
    }

    gettimeofday(&tvend, NULL);

    //--------------------Frees the dynamically allocated memory.-----
-------------------------//
        freememory3d(AXIAL_ATOMS_NUMBER, AXIAL_ATOMS_NUMBER,
AXIAL_ATOMS_NUMBER, atom);
        free(pointer);

freememory3d(AXIAL_ATOMS_NUMBER,AXIAL_ATOMS_NUMBER,AXIAL_ATOMS_NUMBER,
solute_number);
        freememory2d((TOTAL_SOLUTE_ATOMS_NUMBER + 1),3,
Coordinates_of_Atoms_for_Clusters);
        freememory2d((TOTAL_SOLUTE_ATOMS_NUMBER + 1),3,
Coordinates_of_Solute_Atoms);
        free(cluster_size);
        free(number_of_clusters);
        free(cluster_contents);

freememory4d(VACANCY_NUMBER,AXIAL_ATOMS_NUMBER,AXIAL_ATOMS_NUMBER,AXIA
L_ATOMS_NUMBER,vacancyprofile);
        free(Atoms_to_track);
        free(No_of_Moves);
    //-----------------------------------------------------------------
----------------------//

    printf("Correctedmonte8-PS-%d Completed. It took %f
seconds.\n",VERSION_NO,(tvend.tv_sec-tv.tv_sec) +
(float)(tvend.tv_usec-tv.tv_usec)/1000000.0);

    return 0;
}


/*********************************************************************/
/* Initial arrangement of atoms and vacancies at all lattice sites   */
/*********************************************************************/
voidint Atoms_Arrangement()(int ****vacancyprofile)
{
    int l, m, n, i;


    // No longer required as initialized to zero when memory allocated
PS Jun 2011
```

```
    /*-- Arrangement of Fe atoms (Here is possible to be omitted) --*/
    for (l=0; l<AXIAL_ATOMS_NUMBER + 4; l++)
        for (m=0; m<AXIAL_ATOMS_NUMBER + 4; m++)
            for (n=0; n<AXIAL_ATOMS_NUMBER + 4; n++){
                atom[l][m][n]=0;
    }}--*/

    //Solute Atoms are now allocated a unique number between 1 and
TOTAL_SOLUTE_ATOMS_NUMBER based on their species.
    // WHEN INTERACTION PARAMETERS, TRANSITION PROBABILITIES ETC ARE
DEFINED AND ONLY SPECIES INFORMATION IS NEEDED THE
    //ORIGINAL DEFININITIONS ARE RETAINED I.E 0=FE, 1=CU, 2=NI, 3=MN,
4=SI, 5=V.


    /*-- Arrangement of Cu atoms --*/
    /* All coordinates have values between 2 and AXIAL_ATOMS_NUMBER +
1 */
    for (i=01; i<=CU_ATOMS_NUMBER; i++){
        l = (int)((drand48())(((float)gen_rand32()/4294967295.0f) *
AXIAL_ATOMS_NUMBER + 2);
        m = (int)((drand48())(((float)gen_rand32()/4294967295.0f) *
AXIAL_ATOMS_NUMBER + 2);
        n = (int)((drand48())(((float)gen_rand32()/4294967295.0f) *
AXIAL_ATOMS_NUMBER + 2);
            if(atom[l][m][n] != 0){
                i = i - 1;}
            else{
                Periodic_Boundary_Conditions(l, m, n, 1);}
    }

    /*-- Arrangement of Ni atoms --*/
    for (i=0; i<NI_ATOMS_NUMBER; i++){
        l = (int)(drand48() * AXIAL_ATOMS_NUMBER + 2);
        m = (int)(drand48() * AXIAL_ATOMS_NUMBER + 2);
        n = (int)(drand48() * AXIAL_ATOMS_NUMBER + 2);
            if(atom[l][m][n] != 0){
                i = i - 1;}
            else{
                Periodic_Boundary_Conditions(l, m, n, 2);}
    }

    /*-- Arrangement of Mn atoms --*/
    for (i=0; i<MN_ATOMS_NUMBER; i++){
        l = (int)(drand48() * AXIAL_ATOMS_NUMBER + 2);
        m = (int)(drand48() * AXIAL_ATOMS_NUMBER + 2);
        n = (int)(drand48() * AXIAL_ATOMS_NUMBER + 2);
            if(atom[l][m][n] != 0){
                i = i - 1;}
            else{
                Periodic_Boundary_Conditions(l, m, n, 3);}
    }

    /*-- Arrangement of Si atoms --*/
    for (i=0; i<SI_ATOMS_NUMBER; i++){
        l = (int)(drand48() * AXIAL_ATOMS_NUMBER + 2);
        m = (int)(drand48() * AXIAL_ATOMS_NUMBER + 2);
        n = (int)(drand48() * AXIAL_ATOMS_NUMBER + 2);
            if(atom[l][m][n] != 0){
                i = i - 1;};
            }
```

```
            else{
                Periodic_Boundary_Conditions(l, m, n, 4);}i);
                if(Atom_Tracker(l,m,n) != 0){
                    printf("Error outputting atoms for atom tracking
on line: %d\n",__LINE__);
                    return 1;
                }

            }
    }

    /*-- Arrangement of Ni atoms --*/
    for (i=CU_ATOMS_NUMBER+1; i<=(CU_ATOMS_NUMBER+NI_ATOMS_NUMBER);
i++){
        l = (int)(((float)gen_rand32()/4294967295.0f) *
AXIAL_ATOMS_NUMBER );
        m = (int)(((float)gen_rand32()/4294967295.0f) *
AXIAL_ATOMS_NUMBER );
        n = (int)(((float)gen_rand32()/4294967295.0f) *
AXIAL_ATOMS_NUMBER );
        if(atom[l][m][n] != 0){
            i = i - 1;}
        else{
            Periodic_Boundary_Conditions(l, m, n, i);
            if(Atom_Tracker(l,m,n) != 0){
                printf("Error outputting atoms for atom tracking on
line: %d\n",__LINE__);
                return 1;
            }
        }
    }

    /*-- Arrangement of vacancies --*/Mn atoms --*/
    for (i=0; i<VACANCY=(CU_ATOMS_NUMBER;+NI_ATOMS_NUMBER+1);
i<=(CU_ATOMS_NUMBER+NI_ATOMS_NUMBER+MN_ATOMS_NUMBER); i++){
        l = (int)((drand48())(((float)gen_rand32()/4294967295.0f) *
AXIAL_ATOMS_NUMBER + 2);
        m = (int)((drand48())(((float)gen_rand32()/4294967295.0f) *
AXIAL_ATOMS_NUMBER + 2);
        n = (int)((drand48())(((float)gen_rand32()/4294967295.0f) *
AXIAL_ATOMS_NUMBER + 2);
        if(atom[l][m][n] != 0){
            i = i - 1;}
        else{
            Periodic_Boundary_Conditions(l, m, n, 5i);
            if(Atom_Tracker(l,m,n) != 0){
                printf("Error outputting atoms for atom tracking on
line: %d\n",__LINE__);
                return 1;
            }
        }
    }

    /*-- Arrangement of Si atoms --*/
    for (i=(CU_ATOMS_NUMBER+NI_ATOMS_NUMBER+MN_ATOMS_NUMBER+1);
i<=TOTAL_SOLUTE_ATOMS_NUMBER; i++){
        l = (int)(((float)gen_rand32()/4294967295.0f) *
AXIAL_ATOMS_NUMBER );
        m = (int)(((float)gen_rand32()/4294967295.0f) *
AXIAL_ATOMS_NUMBER );
```

```
        n = (int)(((float)gen_rand32()/4294967295.0f) *
AXIAL_ATOMS_NUMBER );
        if(atom[l][m][n] != 0){
            i = i - 1;}
        else{
            Periodic_Boundary_Conditions(l, m, n, i);
            if(Atom_Tracker(l,m,n) != 0){
                printf("Error outputting atoms for atom tracking on
line: %d\n",__LINE__);
                return 1;
            }
        }
    }


    // N.B VACANCIES ARE NOW IDENTIFED BY -1 WHEN USED IN ATOM.
    /*-- Arrangement of vacancies --*/
    for (i=0; i<VACANCY_NUMBER; i++){
        l = (int)(((float)gen_rand32()/4294967295.0f) *
AXIAL_ATOMS_NUMBER );
        m = (int)(((float)gen_rand32()/4294967295.0f) *
AXIAL_ATOMS_NUMBER );
        n = (int)(((float)gen_rand32()/4294967295.0f) *
AXIAL_ATOMS_NUMBER );
        if(atom[l][m][n] != 0){
            i = i - 1;}
        else{
            Periodic_Boundary_Conditions(l, m, n, -1);
            Vacancy_Coordinates(l, m, n, 5, i);}
    }
            vacancyprofile[i][l][m][n] +=1;
        }
    }

return 0;
}


/*********************************************************************/
/* Definition of lookup tables */
/*********************************************************************/
void Define_Lookup_Table()
{
    int h, i, j, x_, y_, z_;

    doublefloat interaction[6][6] = {
        {VFeFe, VFeCu, VFeNi, VFeMn, VFeSi, VFeV},
        {VFeCu, VCuCu, VCuNi, VCuMn, VCuSi, VCuV},
        {VFeNi, VCuNi, VNiNi, VNiMn, VNiSi, VNiV},
        {VFeMn, VCuMn, VNiMn, VMnMn, VMnSi, VMnV},
        {VFeSi, VCuSi, VNiSi, VMnSi, VSiSi, VSiV},
        {VFeV, VCuV, VNiV, VMnV, VSiV, VVV}
    };

    doublefloat atomic_vibration_frequency[6] = {
        FFe, FCu, FNi, FMn, FSi, FV
    };

    doublefloat e0[6] = {
        e0Fe, e0Cu, e0Ni, e0Mn, e0Si, e0V
    };
```

```
    const doublefloat R = 8.31441;    /* gas constant */

    /*----------------------------------------*/
    /* Definition of nearest neighbour vectors */
    /*----------------------------------------*/
    for (i=0; i<2; i++)
        for (j=0; j<8; j++){
            switch(i){
                case 1:
                /* in the case of starting points of vectors from
                odd layers of the z direction */
                    switch(j){
                        case 0: x_ = 0; y_ = 0; z_ =  1; break;
                        case 1: x_ = 1; y_ = 0; z_ =  1; break;
                        case 2: x_ = 1; y_ = 1; z_ =  1; break;
                        case 3: x_ = 0; y_ = 1; z_ =  1; break;
                        case 4: x_ = 0; y_ = 0; z_ = -1; break;
                        case 5: x_ = 1; y_ = 0; z_ = -1; break;
                        case 6: x_ = 1; y_ = 1; z_ = -1; break;
                        case 7: x_ = 0; y_ = 1; z_ = -1; break;
                    }
                    NN_vector[i][j][0] = x_;
                    NN_vector[i][j][1] = y_;
                    NN_vector[i][j][2] = z_;
                break;

                case 0:
                /* in the case of starting points of vectors from
                even layers of the z direction */
                    switch(j){
                        case 0: x_ = -1; y_ = -1; z_ =  1; break;
                        case 1: x_ =  0; y_ = -1; z_ =  1; break;
                        case 2: x_ =  0; y_ =  0; z_ =  1; break;
                        case 3: x_ = -1; y_ =  0; z_ =  1; break;
                        case 4: x_ = -1; y_ = -1; z_ = -1; break;
                        case 5: x_ =  0; y_ = -1; z_ = -1; break;
                        case 6: x_ =  0; y_ =  0; z_ = -1; break;
                        case 7: x_ = -1; y_ =  0; z_ = -1; break;
                    }
                    NN_vector[i][j][0] = x_;
                    NN_vector[i][j][1] = y_;
                    NN_vector[i][j][2] = z_;
                break;
            }
        }

    /*-----------------------------------------------------------------
-*/
    /* Definition of partial transition probability and its pre-factor
*/
    /*-----------------------------------------------------------------
-*/
    for (h=0; h<6; h++)
        for (i=1; i<6; i++)
            for (j=-8; j<9; j++){
                partial_transition_probability[h][i][j+8] = expexpf
((-1.0)* ((j)*
                (interaction[h][i] - interaction[i][5] +
interaction[0][5] -
                interaction[0][h])) / (2.* R * TEMP));
```

```
                /*above calculation formula was modified by adding
with last three terms on 23Nov05*/
        pre_factor[h] = atomic_vibration_frequency[h] *
            expexpf((-1.0)* e0[h] /(R * TEMP));
    }

}


/*****************************************************************/
/*  Exchange between a vacancy and a nearest neighbor atom */
/*****************************************************************/
voidint Exchange_Positions()( int *p_ , int *q_ , int *r_ , int
*neighbours, int neighbours_[6][8],  float *w,
{
    static                                  float *a,   double
*real_time, int ****vacancyprofile)  // Changed as Static int removed
PS 14/6/11
{

    const float TwoTempR = 2.0*TEMP*8.31441;    /* gas constant */
    int h,i,j,;
    int l,m,n;
    static int p,q,r;  /* Coordinates of the selected vacancy */
    static int p_[8], q_[8], r_[8];  /* Coordinates of nearest
neighbor atoms around the vacancy */

    static int neighbours[6];
    static int neighbours_[6][8];
        /* Numbers of nearest neighbor solute atoms and vacancies
around the two.
        [number of possible differentg; // reduces atom or vacancy
types]([Coordination number]) */

    static double w[8];     /* transition probability for the i-th
nearest neighbor atom */
    static double a[8];     /* relative probabilities from 0[][][][] to 1
*/a single digit species identifier.

    static double    int d,e,f;

    int u = 0;
    int found; //Did we find a vacancy?
    float sum_of_probabilities;
    static double s;float s; // a buffer to hold the sum of the
partial transition probs before transfer to w[] PS
    static double
    float k;                    /*;/* Random number between 0 and 1 */
    double interaction[6][6] = {
        {VFeFe, VFeCu, VFeNi, VFeMn, VFeSi, VFeV},
        {VFeCu, VCuCu, VCuNi, VCuMn, VCuSi, VCuV},
        {VFeNi, VCuNi, VNiNi, VNiMn, VNiSi, VNiV},
        {VFeMn, VCuMn, VNiMn, VMnMn, VMnSi, VMnV},
        {VFeSi, VCuSi, VNiSi, VMnSi, VSiSi, VSiV},
        {VFeV, VCuV, VNiV, VMnV, VSiV, VVV}
    };
    const double R = 8.31441;    /* gas constant */
    static int label;                   /* Instead of "goto" */
    label = 0;

    /*----------------------------------------*/
```

```
    /* Random selection of a vacancy to migrate */
    /*-----------------------------------------*/
    h = (int)(drand48() *#if VACANCY_NUMBER); >1
    h = (int)(((float)gen_rand32()/4294967295.0) * VACANCY_NUMBER);
ASSERT(h<VACANCY_NUMBER);
#else
h=0;
#endif

    p = Coordinates_of_Vacancy[h][0];
    q = Coordinates_of_Vacancy[h][1];
    r = Coordinates_of_Vacancy[h][2];


    /*-----------------------------------------*/
    /* Nearest neighbor atoms around the vacancy */
    /*-----------------------------------------*/
    for (i=0; i<8; i++){
        p_[i] = ((p +
NN_vector[r%2&1][i][0];])+AXIAL_ATOMS_NUMBER)%AXIAL_ATOMS_NUMBER;
//+AXIAL_ATOMS_NUMBER is to remove negative modulus error
        q_[i] = ((q +
NN_vector[r%2&1][i][1];])+AXIAL_ATOMS_NUMBER)%AXIAL_ATOMS_NUMBER;
        r_[i] = ((r +
NN_vector[r%2&1][i][2];])+AXIAL_ATOMS_NUMBER)%AXIAL_ATOMS_NUMBER;


        for (j=0; j<6; j++){
            neighbours[j] = 0;
            neighbours_[j][i] = 0;
        }
    }

    /*-----------------------------------------------------------------
-----*/
    /* Counting the numbers of nearest neighbor solute atoms and
vacancies
       around the two */
    /*-----------------------------------------------------------------
-----*/

    for (i=0; i<8; i++){
        neighbours[(
        // this turns atom[l[m][n] from a solute ID into an atom type
0-5.
        switch(atom[p + NN_vector[r%2][_[i][0]][q +
NN_vector[r%2][_[i][]][r_[i]]){
            case -1]]: neighbours[5]++; break;    // case of Vacancy
            [case 0: neighbours[0]++; break;
            default:
                neighbours[getAtomType(atom[p_[i]][q_[i]][r +
NN_vector[_[i]])]++;
                break;
        }

        int odd;
        odd = (r%2][i][2]])] += +1)&1;
        for (j=0; j<8; j++){
            neighbours_[(atom[
        // this is used to simplify the switch statement below.
```

```
            d =((p_[i] + NN_vector[(r +
1)%2[odd][j][0]])+AXIAL_ATOMS_NUMBER)%AXIAL_ATOMS_NUMBER;
                [e =((q_[i] + NN_vector[(r +
1)%2[odd][j][1]])+AXIAL_ATOMS_NUMBER)%AXIAL_ATOMS_NUMBER;
                [f =((r_[i] + NN_vector[(r +
1)%2[odd][j][2])])[])+AXIAL_ATOMS_NUMBER)%AXIAL_ATOMS_NUMBER;

            // this turns atom[l[m][n] from a solute ID into an atom
type 0-5.
            switch(atom[d][e][f]){
                case -1: neighbours_[5][i] += ]+=1; break;  // case of
Vacancy
                case 0: neighbours_[0][i]+=1; break;    // case of Fe
                default:
                    neighbours_[getAtomType(atom[d][e][f])][i]+=1;
        }            break;
    }        }
        }
    }


    /*-----------------------------------------*/
    /* Judgement of the exchange between the two */
    /*-----------------------------------------*/
    sum_of_probabilities = 0.;
    for (i=0; i<8; i++){
        s = 1.0;

        // this turns atom[l[m][n] from a solute ID into an atom type
0-5.
        switch(atom[p_[i]][q_[i]][r_[i]]){
            case -1: g=5; break;    //case of vacancy
            case 0: g=0; break;     // case of Fe
            default:
                g=getAtomType(atom[p_[i]][q_[i]][r_[i]]);
                break;
        }

        for (j=1; j<6; j++){
            s = s *= *=
partial_transition_probability[(atom[p_[i]][q_[i]][r_[i]])][g]
                [j][neighbours[j] - neighbours_[j][i] + 8];
        }
        w[i] = pre_factor[(atom[p_[i]][q_[i]][r_[i]])][g] * s
            * exp expf
((interaction[5][5]+interaction[(atom[p_[i]][q_[i]][r_[i]])][(atom[p_[
i]][q_[i]][r_[i]])][g][g]
            -2.0 * interaction[5][(atom[p_[i]][q_[i]][r_[i]])])/ (2.*
R * TEMP));        /* modified on 6 Dec2004*/][g])/ (TwoTempR));
        sum_of_probabilities += w[i];
        a[i] = 0;
    }

    a[0] = w[0] / sum_of_probabilities;
    for (i=1; i<8; i++){
        a[i] = a[i-1] + w[i] / sum_of_probabilities;
    }


    k = drand48();
```

```
    k = ((float)gen_rand32()/4294967295.0f);    // A random number
which determines which NN to jump to.


    found=0;

    // Identification of which NN to jump to.
    for(u=0; u<8; u++)
    {
        if(0 <= k &&<=a[u])
        {
            found=1;        //this shows that k <= a[0]){has been
found between a[u-1] and a[u] and u determines the location of the NN
to jump to.
            break;
        }
    }

    if(found){
#if VACANCY_NUMBER > 1          // if there is more than one vacancy
this checks we're not doing a Vancancy-Vancancy jump.
        if(atom[p_[0u]][q_[0u]][r_[0]] != 5u]]!=-1){
#endif
            ASSERT(p!=p_[u] || q !=q_[u] || r!=r_[u]);
            Periodic_Boundary_Conditions(p, q, r,
atom[p_[0u]][q_[0u]][r_[0]]);u]]);   //moves the atom to the vacancy
position.

            if(atom[p][q][r] != 0){
                if(Atom_Tracker(p,q,r) != 0){
                    printf("Error outputting atoms for atom tracking
on line: %d\n",__LINE__);
                    return 1;
                }
                countmoves(atom[p][q][r]);
            }

            l = p_[0u]; m = q_[0]; n = r_[0];}
        else {label = 1;};}
    else if(a[0] < k && k <= a[1]){
        if(atom[p_[1]][q_[1]][r_[1]] != 5){
            Periodic_Boundary_Conditions(p, q, r,
atom[p_[1]][q_[1]][r_[1]]);
            l = p_[1]; m = q_[1u]; n = r_[1];}u];
            else {label = 1;};}
            else if(a[1] < k && k <= a[2]){
        if(atom[p_[2]][q_[2]][r_[2]] != 5){
            Periodic_Boundary_Conditions(p, q, r,l][m][n]=-1;   //
moves the vacancy to the atom[p_[2]][q_[2]][r_[2]]); position.
                l = p_[2]; m = q_[2]; n = r_[2];}
        else {label = 1;};}
    else if(a[2] < k && k <= a[3]){
        if(atom[p_[3]][q_[3]][r_[3]] != 5){
            Periodic_Boundary_Conditions(p, q, r,
atom[p_[3]][q_[3]][r_[3]]);
            l = p_[3]; m = q_[3]; n = r_[3];}
        else {label = 1;};}
    else if(a[3] < k && k <= a[4]){
        if(atom[p_[4]][q_[4]][r_[4]] != 5){
            Periodic_Boundary_Conditions(p, q, r,
atom[p_[4]][q_[4]][r_[4]]);
```

```
            l = p_[4]; m = q_[4]; n = r_[4];}
        else {label = 1;};}
    else if(a[4] < k && k <= a[5]){
        if(atom[p_[5]][q_[5]][r_[5]] != 5){
            Periodic_Boundary_Conditions(p, q, r,
atom[p_[5]][q_[5]][r_[5]]);
            l = p_[5]; m = q_[5]; n = r_[5];}
        else {label = 1;};}
    else if(a[5] < k && k <= a[6]){
        if(atom[p_[6]][q_[6]][r_[6]] != 5){
            Periodic_Boundary_Conditions(p, q, r,
atom[p_[6]][q_[6]][r_[6]]);
            l = p_[6]; m = q_[6]; n = r_[6];}
        else {label = 1;};}
    else if(a[6] < k && k <= a[7]){
        if(atom[p_[7]][q_[7]][r_[7]] != 5){
            Periodic_Boundary_Conditions(p, q, r,
atom[p_[7]][q_[7]][r_[7]]);
            l = p_[7]; m = q_[7]; n = r_[7];}
        else {label = 1;};}

    if (label == 0){
        if(l == 1){l = l + AXIAL_ATOMS_NUMBER;}
            else if(l == AXIAL_ATOMS_NUMBER + 2){l = l -
AXIAL_ATOMS_NUMBER;}

        if(m == 1){m = m + AXIAL_ATOMS_NUMBER;}
            else if(m == AXIAL_ATOMS_NUMBER + 2){m = m -
AXIAL_ATOMS_NUMBER;}

        if(n == 1){n = n + AXIAL_ATOMS_NUMBER;}
            else if(n == AXIAL_ATOMS_NUMBER + 2){n = n -
AXIAL_ATOMS_NUMBER;}

        Periodic_Boundary_Conditions(l, m, n, 5);
        Vacancy_Coordinates(l, m, n, 5, h); // updates the position of
the vacancy in Vacancy_Coordinates.
            vacancyprofile[h][l][m][n] +=1; // outputs the new
position of the vacancy i to the the array VancancyProfile

            *real_time += 1 / sum_of_probabilities; // increments the
real time.
    }

#if VACANCY_NUMBER > 1
        }   // closes the if statement needed if there is more than
one vanancy.
#endif
    }

    return 0;
}


/*********************************************************************
*****/
/* Periodic boundary conditions */
/*********************************************************************
*****/
void Periodic_Boundary_Conditions(int p, int q, int r, int h)
{
```

```
    int i, j, k;
    int xmirror = 1, ymirror = 1, zmirror = 1;
    int x[2];
    int y[2];
    int z[2];

    x // this replaced the original periodic boundary conditions and
simply uses the modulus to remap in [0] = p;
    y[0] = q;
    z[0] = r;

    if(1 < p && p <= 3){
        xmirror += 1;
        x[1] = p + ,AXIAL_ATOMS_NUMBER;}).
    else if( //REQUIRES THAT AXIAL_ATOMS_NUMBER <= p && p <BE EVEN
SUCH THAT AXIAL_ATOMS_NUMBER + 2){+1 IS EQUIVALENT TO LAYER 0
        xmirror += 1;
        x[1] = p - // +AXIAL_ATOMS_NUMBER;} serves only to avoid
negative modulus errors and does not affect the positions of atoms.

    if(1 < q && q <= 3){
        ymirror += 1;
        y[1] = q + atom[(p+AXIAL_ATOMS_NUMBER;}
    else if()%AXIAL_ATOMS_NUMBER <= ][(q && q < +AXIAL_ATOMS_NUMBER +
2){
        ymirror += 1;
        y[1] = q - )%AXIAL_ATOMS_NUMBER;}

    if(1 < r && r <= 3){
        zmirror += 1;
        z[1] = r + ][(r+AXIAL_ATOMS_NUMBER;}
    else if()%AXIAL_ATOMS_NUMBER <= r && r < AXIAL_ATOMS_NUMBER + 2){
        zmirror += 1;
        z[1] = r - AXIAL_ATOMS_NUMBER;}

    for (i=0; i<xmirror; i++)
        for (j=0; j<ymirror; j++)
            for (k=0; k<zmirror; k++){
                atom[(x[i])][(y[j])][(z[k])]] = h;
    }

}


/*********************************************************************
*****/
/* Allocaton of coordinates of vacancies at new positions */
/*********************************************************************
*****/
void Vacancy_Coordinates(int l, int m, int n, int h, int i)
{
    Coordinates_of_Vacancy[i][0] = l;
    Coordinates_of_Vacancy[i][1] = m;
    Coordinates_of_Vacancy[i][2] = n;

}


/*****************************************************************/
/* Cluster analysis */
/*****************************************************************/
```

```
voidint Cluster_Analysis()(unsigned long long monte_carlo_steps,
double *real_time, int file_number, int* the_value_of_e)
{
    FILE *fp;
    float output[8];

    int solute_number[AXIAL_ATOMS_NUMBER + 2][AXIAL_ATOMS_NUMBER + 2]
        [AXIAL_ATOMS_NUMBER + 2];
        /* Three-dimensional array indicating a solute number */
    int pointer[TOTAL_SOLUTE_ATOMS_NUMBER + 1];
        /* Pointer for solute numbers */
    int accomm[8+1];  /* Variable for the accommodation of solute
numbers
        of nearest neighbor solute atoms. 8 is the coordinate number
*/

    int Coordinates_of_Atoms_for_Clusters[TOTAL_SOLUTE_ATOMS_NUMBER +
1][3];
    int Coordinates_of_Solute_Atoms[TOTAL_SOLUTE_ATOMS_NUMBER + 1][3];
    int isolated_solute_atoms[5];  /* 5 means the number of atom types
*/

    int indicater;  /* Indicater of the existence of solute atoms at
nearest neighbor positions */
    int isolated_Cu_atoms=0;
    int solute_atoms_inside_cluster=0;
    int cluster_size[TOTAL_SOLUTE_ATOMS_NUMBER +
1isolated_solute_atoms[6];
    int number_of_clusters[TOTAL_SOLUTE_ATOMS_NUMBER + 1];
        /* Number of clusters havind size[] */
    int total_number_of_clusters = 0;
    float average_size_of_clusters=0;
    int max_size=0;     // largest cluster size in terms of no. of
atoms.
    int position = 0;   //holds the positon in the array
cluster_contents where clusters start for use when outputting the
contents of clusters.
    int l, m, n, a, b, c;
    int e,f,i, j, k, r, s,t,u;
    int delta_l[9];
    /*-------------------------------------------------------------*/
    /* Clearance of atomic information on     int delta_m[9];
    int delta_n[9];
    int** partial_cluster;//notes if this cluster crosses the periodic
boundary layers */
    /*-------------------------------------------------------------*/
    for (m=1;     int** cluster_pos_sum;
    float cluster_pos_average[3];
    int l_av,m<=AXIAL_av, n_av;

    partial_cluster = allocatememory2d(TOTAL_SOLUTE_ATOMS_NUMBER + 2;
m++)+1,3);
    if(!atom){
        printf("Failed to allocate memory for (n=partial_cluster on
line %d.\n",__LINE__);
        return 1; n<=AXIAL
    }

    cluster_pos_sum = allocatememory2d(TOTAL_SOLUTE_ATOMS_NUMBER + 2;
n++){+1,3);
        atom[1][m][n] = 0;
```

```
            if(!atom[n][1][m] = 0;){
        atom[m][n][1] = 0;
    }
    printf("Failed to allocate memory for (m=1; m<=AXIAL_ATOMS_NUMBER +
2; m++)cluster_pos_sum on line %d.\n",__LINE__);
        for (n=return 1; n<=AXIAL_ATOMS_NUMBER + 2; n++){
            atom[AXIAL_ATOMS_NUMBER + 2][m][n] = 0;
            atom[n][AXIAL_ATOMS_NUMBER + 2][m] = 0;
            atom[m][n][AXIAL_ATOMS_NUMBER + 2] = 0;
    }
        }


    /*---------------------------------------------------------*/
    /* Counting the number of solute atoms inside clusters */
    /*---------------------------------------------------------*/
    //i = 1;
    for (l=20; l<AXIAL_ATOMS_NUMBER + 2; l++)++){
        for (m=20; m<AXIAL_ATOMS_NUMBER + 2; m++)++){
            for (n=20; n<AXIAL_ATOMS_NUMBER + 2; n++){
                if(atom[l][m][n] != 0 && atom[l][m][n] != 5-1){
                    solute_number[l][m][n] = atom[l][m][n];  // was
solute_number[l][m][n] = i;

Coordinates_of_Atoms_for_Clusters[(atom[l][m][n])][0] = l;  // was
Coordinates_of_Atoms_for_Clusters[i][0] =]= l;
                    Coordinates_of_Atoms_for_Clusters[i][1] = m;

Coordinates_of_Atoms_for_Clusters[(atom[l][m][n])][1] = m;  // was
Coordinates_of_Atoms_for_Clusters[i][0]= m

Coordinates_of_Atoms_for_Clusters[(atom[l][m][n])][2] = n;  // was
Coordinates_of_Atoms_for_Clusters[i][2] =0]= n;
                    pointer[(atom[l][m][n])] = atom[l][m][n];  // was
pointer[i] = i;
                i = i + 1;                }
            }
        }
    }


    for(j=1; j <= TOTAL_SOLUTE_ATOMS_NUMBER; j++){

        for(k=1; k<=8; k++){
            accomm[k] = 0;}

        for(k=0; k<8; k++){  // finds out where the neighbours of a
given solute atom are
            a = Coordinates_of_Atoms_for_Clusters[j][0] +

NN_vector[Coordinates_of_Atoms_for_Clusters[j][2]%2]&1][k][0];
            b = Coordinates_of_Atoms_for_Clusters[j][1] +

NN_vector[Coordinates_of_Atoms_for_Clusters[j][2]%2]&1][k][1];
            c = Coordinates_of_Atoms_for_Clusters[j][2] +

NN_vector[Coordinates_of_Atoms_for_Clusters[j][2]%2]&1][k][2];

            a = a + AXIAL_ATOMS_NUMBER;          //This does not change
the result but removes negative Modulus errors
            b = b + AXIAL_ATOMS_NUMBER;
```

```
            c = c + AXIAL_ATOMS_NUMBER;

            a%=AXIAL_ATOMS_NUMBER; // applies periodic boundary
conditions
            b%=AXIAL_ATOMS_NUMBER;
            c%=AXIAL_ATOMS_NUMBER;

            delta_l[k+1] = abs(Coordinates_of_Atoms_for_Clusters[j][0]
- a);
            delta_m[k+1] = abs(Coordinates_of_Atoms_for_Clusters[j][1]
- b);
            delta_n[k+1] = abs(Coordinates_of_Atoms_for_Clusters[j][2]
- c);

            if(atom[a][b][c] != 0 && atom[a][b][c] != 5-1){
                accomm[k + 1] = solute_number[a][b][c];}          ];
// records the identities of neighbours which are solute atoms
            }
        }

        for(r=1; r<=8; r++){
            //If the neighbouring atom is not a vacancy or matrix
            if(accomm[r] != 0){ && pointer[j] != pointer[accomm[r]]){
// checks neighbour is not a vacancy or Fe and that we've not already
encountered this atom before.
                //If the "pointer" value for this atom is less than
our neighbour
                if(pointer[j] < pointer[accomm[r]]){
                    //Set all atoms in the dataset that are equal to
the neighbour's ID
                    //to this new lower ID
                    if(delta_l[r] > 1){
                        partial_cluster[j][0] = 1;
                        partial_cluster[accomm[r]][0] = 1;
                    }
                    if(delta_m[r] > 1){
                        partial_cluster[j][1] = 1;
                        partial_cluster[accomm[r]][1] = 1;
                    }
                    if(delta_n[r] > 1){
                        partial_cluster[j][2] = 1;
                        partial_cluster[accomm[r]][2] = 1;
                    }
                    for(s=1; s <= TOTAL_SOLUTE_ATOMS_NUMBER; s++){
                        if(pointer[s] == pointer[accomm[r]]){
                            pointer[s] = pointer[j];}];
                            for(t=0;t<3;t++){
                                partial_cluster[s][t] =
partial_cluster[j][t];
                            }
                        }
                    }
                }
                else if (pointer[j] > pointer[accomm[r]]){
                    //If the "pointer" value is greater than our
neighbour, then set every one
                    //with our number to our neighbour's lower number
                    if(delta_l[r] > 1){
                        partial_cluster[j][0] = 1;
                        partial_cluster[accomm[r]][0] = 1;
                    }
```

```
                    if(delta_m[r] > 1){
                        partial_cluster[j][1] = 1;
                        partial_cluster[accomm[r]][1] = 1;
                    }
                    if(delta_n[r] > 1){
                        partial_cluster[j][2] = 1;
                        partial_cluster[accomm[r]][2] = 1;
                    }
                    for(s=1; s <= TOTAL_SOLUTE_ATOMS_NUMBER; s++){
                        if(pointer[s] == pointer[j]){
                            pointer[s] = pointer[accomm[r]];}}];
                }                       for(t=0;t<3;t++){
            }
        }

    }
                                partial_cluster[s][t] =
partial_cluster[accomm[r]][t];
                            }
                        }
                    }
                }
            }
        }

    }
    for(j=1;j<=TOTAL_SOLUTE_ATOMS_NUMBER;j++){
        for(s=1;s<=TOTAL_SOLUTE_ATOMS_NUMBER;s++){
            if(pointer[j]==pointer[s]){
                for(t=0;t<3;t++){
                    if(partial_cluster[s][t] != partial_cluster[j][t]
&& partial_cluster[j][t] != 1){
                        //We should adopt the value of
partial_cluster[s][t]
                        //and we need to go back and change all the
ones we've just passed
                        partial_cluster[j][t] = partial_cluster[s][t];
                        for(u=1; u<s;u++){
                            if(pointer[s] == pointer[j]){
                                partial_cluster[s][t] =
partial_cluster[j][t];
                            }
                        }
                    }
                    else{
                        partial_cluster[s][t] = partial_cluster[j][t];
                    }
                }
            }
        }
    }

    #ifdef DEBUG
        int *debugPtr;

        debugPtr=(int *)malloc(TOTAL_SOLUTE_ATOMS_NUMBER*sizeof(int));

memcpy(debugPtr,pointer,TOTAL_SOLUTE_ATOMS_NUMBER*sizeof(int));
        debugPtr[0]=0;
        qsort(debugPtr,TOTAL_SOLUTE_ATOMS_NUMBER,sizeof(int),int_cmp);
```

```
        int numUniq=1;
        for(j=1; j<TOTAL_SOLUTE_ATOMS_NUMBER; j++)
        {
            if(debugPtr[j]!=debugPtr[j-1])
                numUniq++;
        }
        printf("Num unique :%d", numUniq);

        free(debugPtr);
    #endif

    /*-------------------------------------------------------------------
------*/
    /* Counting the numbers of isolated solute atoms surrounded by Fe
atoms */
    /*-------------------------------------------------------------------
------*/
    i = 1;
    isolated_soluteCu_atoms[ = isolated_solute_atoms[2] =
isolated_solute_atoms[3] = isolated_solute_atoms[4] = 0;
    for (l=20; l<AXIAL_ATOMS_NUMBER + 2; l++)++){
        for (m=20; m<AXIAL_ATOMS_NUMBER + 2; m++)++){
            for (n=20; n<AXIAL_ATOMS_NUMBER + 2; n++){
                indicater = 0;
                //If we are a non-copper solute, lets do stuff
                if(atom[l][m][n] == 2 ||>= CU_ATOMS_NUMBER+1 &&
atom[l][m][n] == 3 || atom[l][m][n] == 4<= TOTAL_SOLUTE_ATOMS_NUMBER){
                    Coordinates_of_Solute_Atoms[i][0] = l;
                    Coordinates_of_Solute_Atoms[i][1] = m;
                    Coordinates_of_Solute_Atoms[i][2] = n;

                    for(k=0; k<8; k++){
                        a = Coordinates_of_Solute_Atoms[i][0] +

NN_vector[Coordinates_of_Solute_Atoms[i][2]%2]&1][k][0];
                        b = Coordinates_of_Solute_Atoms[i][1] +

NN_vector[Coordinates_of_Solute_Atoms[i][2]%2]&1][k][1];
                        c = Coordinates_of_Solute_Atoms[i][2] +

NN_vector[Coordinates_of_Solute_Atoms[i][2]%2]&1][k][2];

                        a = a + AXIAL_ATOMS_NUMBER;          //This
does not change the result but removes negative Modulus errors
                        b = b + AXIAL_ATOMS_NUMBER;
                        c = c + AXIAL_ATOMS_NUMBER;

                        a%=AXIAL_ATOMS_NUMBER;
                        b%=AXIAL_ATOMS_NUMBER;
                        c%=AXIAL_ATOMS_NUMBER;

                        if(atom[a][b][c] != 0 && atom[a][b][c] != 5-
1){
                            indicater += 1;};
            }            }
                    }

                    //Indicator tells us if there is another solute
around this
                    //particular solute or not.
                    if(indicater == 0){
```

```
isolated_solute_atoms[getAtomType(atom[l][m][n])]+=1; // getAtomType
returns the chemical identidy of the atom[ at l][,m][,n]] += 1; from
its unique solute number
                    }

                    i = i + 1;++;
                }
            }
        }
    }

    /*-----------------------------------------------------------------
----*/
    /* Quantitative estimation of obtained simulation microstructures
*/
    /*-----------------------------------------------------------------
----*/

    f = e = 0;

    const int mid_point = (int)(AXIAL_ATOMS_NUMBER/2.)-1;
    printf("The mid_point is %d\n",mid_point);
    for(i=1; i <=TOTAL_SOLUTE_ATOMS_NUMBER; i++){
        solute_atoms_inside_cluster = 0;
    //  printf("This is cluster %d\n\n",e);
        for(j=i; j <= TOTAL_SOLUTE_ATOMS_NUMBER; j++){
            if(pointer[j] == i){
                solute_atoms_inside_cluster += 1;};
        }
                ASSERT(f < TOTAL_SOLUTE_ATOMS_NUMBER && f>=0);
                cluster_size[i] =contents[f] = j;    // records the
identities of the solute atoms which are in a given cluster.
                f++;
                for(t=0;t<3;t++){
                    //printf("%d Co-ordinate is %d\n", t,
Coordinates_of_Atoms_for_Clusters[j][t]);
                    if(partial_cluster[j][t] == 0){
                        cluster_pos_sum[e+1][t] +=
Coordinates_of_Atoms_for_Clusters[j][t];
                    //  printf("Cluster_pos_sum[%d][%d] is
%d\n",e+1,t,cluster_pos_sum[e+1][t]);
                    }
                    else{
                        //FIX THIS BUT MIGHT GET AWAY WITH IT FOR NOW
                        if(Coordinates_of_Atoms_for_Clusters[j][t] <=
mid_point){
                            cluster_pos_sum[e+1][t] +=
Coordinates_of_Atoms_for_Clusters[j][t]+AXIAL_ATOMS_NUMBER;
                        //  printf("Cluster_pos_sum[%d][%d] is
%d\n",e+1,t,cluster_pos_sum[e+1][t]);
                        }
                        else{
                            cluster_pos_sum[e+1][t] +=
Coordinates_of_Atoms_for_Clusters[j][t];
                        //  printf("Cluster_pos_sum[%d][%d] is
%d\n",e+1,t,cluster_pos_sum[e+1][t]);
                        }
                    }
                }
            }
```

```
        }
        ASSERT(i < TOTAL_SOLUTE_ATOMS_NUMBER+1 && i>=0);
        if(solute_atoms_inside_cluster;          != 0){
    }       e++;
            cluster_size[e] = solute_atoms_inside_cluster;  // holds
the size of a given cluster, e. This is needed to compute which atoms
in cluster_contents belong to which cluster.
        }

        // finds the maximum size of the clusters.
        if(cluster_size[e] > max_size){
            max_size = cluster_size[e];
        }
    }

    printf("The maximum cluster size is %i atoms.\n", max_size);

    for(k=1; k <= TOTAL_SOLUTE_ATOMS_NUMBER; k++){
        number_of_clusters[k] = 0;};
    }

    for(r=1; r <= TOTAL_SOLUTE_ATOMS_NUMBER;e; r++){       //now runs
up to & inlcuding e as 0 atom clusters no longer included
        ASSERT(r <= e && r>=0);
        ASSERT(cluster_size[r] < TOTAL_SOLUTE_ATOMS_NUMBER+1 &&
cluster_size[r] >= 0);
        number_of_clusters[cluster_size[r]] += 1;};
    }
    for(s=2; s <= TOTAL_SOLUTE_ATOMS_NUMBER; s++){
        ASSERT(cluster_size[r] < TOTAL_SOLUTE_ATOMS_NUMBER+1 &&
cluster_size[r] >= 0);
        total_number_of_clusters += number_of_clusters[s];};];
    }

    average_size_of_clusters = (TOTAL_SOLUTE_ATOMS_NUMBER -
number_of_clusters[1])*(1.0f)
            / )/total_number_of_clusters;

    printf("Number of 1 atom clusters is %i.\n",
number_of_clusters[1]);
    isolated_Cu_atoms = number_of_clusters[1] -
isolated_solute_atoms[2]
        ]- isolated_solute_atoms[3] ]- isolated_solute_atoms[4];

    /*                                                          */
    /*    //----------------------------------------------------------*/
    // Writing of obtained structural parameters to files     */
    /*----------------------------------------------------------*/
    fp = fopen("    //-----------------------------------------------
--------*/

    char filename[100];
    sprintf(filename, "analyticalresults", "a");-%dK-
%d.txt",(int)TEMP,VERSION_NO);
    fp = fopen(filename, "a");
    if(!fp){
        printf("File: %s not opened correctly for output of cluster
search results.\n",filename);
        return 1;
    }
    output[0] = (floatunsigned long long)monte_carlo_steps;
```

```
    output[1] = (float))*real_time;
    output[2] = (float)isolated_Cu_atoms;
    output[3] = (float)isolated_solute_atoms[2];  /*// number of
isolated Ni atoms */
    output[4] = (float)isolated_solute_atoms[3];  /*// number of
isolated Mn atoms */
    output[5] = (float)isolated_solute_atoms[4];  /*// number of
isolated Si atoms */
    output[6] = (float)total_number_of_clusters;
    output[7] = average_size_of_clusters;

    //comma separation replaced with tab separation for ease of
opening file in excel.
    if(fprintf(fp, "%.1e,\t%.7f,\t%.0f,\t%.0f,\t%.0f,\t%.0f,
\t%.0f,\t%6.4f\n", output[0],
        output[1], output[2], output[3], output[4], output[5],
output[6],
        output[7]));]) < 0){
        printf("Error writing cluster search results to:
%s.\n",filename);
        fclose(fp);

    /*-------------------------------------------------------------------
*/
    /* Reproduction of atomic information on periodic boundary layers
*/
    /*-------------------------------------------------------------------
*/
    for (l=         return 1;
    }

    fclose(fp);

    // outputs the identities of solute atoms in a clusters to a file
"Atoms in Clusters.txt"
    FILE *fp2;
    char filename2[100];
    sprintf(filename2, "Atoms in clusters[%"FMT_LLU"]-%dK-
%d.txt",time_for_analysis[file_number],(int)TEMP,VERSION_NO);
    fp2 = fopen(filename2, "w");
    if(!fp2){
        printf("File: %s not opened correctly.\n",filename2);
        return 0;
    }

    int nl=0; //decides whether a newline character is needed.


    for(f=1; f <= e; f++){
        if(cluster_size[f] >= 4){           //sets the cut off for the
minimum cluster size to output

            if(nl != 0){
                if(fprintf(fp2,"\nCluster Number %d\t",f) < 0){
                    printf("Error writing atoms in clusters to file %s
on line %d.\n", filename2,__LINE__);
                    fclose(fp2);
                    return 1;
                }
            }
            else{
```

```
                if(fprintf(fp2,"Cluster Number %d\t",f) < 0){
                    printf("Error writing atoms in clusters to file %s
on line %d.\n", filename2,__LINE__);
                    fclose(fp2);
                    return 1;
                }
                nl = 1;
            }


cluster_pos_average[0]=cluster_pos_sum[f][0]/(float)cluster_size[f];

cluster_pos_average[1]=cluster_pos_sum[f][1]/(float)cluster_size[f];

cluster_pos_average[2];]=cluster_pos_sum[f][2]/(float)cluster_size[f];

            l_av=(int)(cluster_pos_average[0]+0.5+FLT_EPSILON);
//rounds to the nearest int
            m_av=(int)(cluster_pos_average[1]+0.5+FLT_EPSILON);
//rounds to the nearest int
            n_av=(int)(cluster_pos_average[2]+0.5+FLT_EPSILON);
//rounds to the nearest int

            l<_av%=AXIAL_ATOMS_NUMBER + 2; l++) ; //Applies periodic
boundary conditions
           for (m=2; m<_av%=AXIAL_ATOMS_NUMBER + 2; m++);
            for (n=2; n<_av%=AXIAL_ATOMS_NUMBER +;

            if(fprintf(fp2,"%d\t%d\t%d",l_av,m_av,n_av) < 0){
                printf("Error writing atoms in clusters to file %s on
line %d.\n", filename2,__LINE__);
                fclose(fp2);
                return 1;
            }


            for(i=position ;i < (position + cluster_size[f]); i++){
// works out where in the cluster contents array the ID's of the atoms
in cluster f are.
                if(fprintf(fp2,"\t%i",cluster_contents[i]) < 0){
                    printf("Error writing atoms in clusters to file %s
on line %d.\n", filename2,__LINE__);
                    fclose(fp2);
                    return 1;
                }
            }
        }

        position += cluster_size[f];        //increments position to
the stat of the next cluster.
    }
    *the_value_of_e = e;
    freememory2d(TOTAL_SOLUTE_ATOMS_NUMBER+1,3,cluster_pos_sum);
    freememory2d(TOTAL_SOLUTE_ATOMS_NUMBER+1,3,partial_cluster);
    fclose(fp2);

    return 0;
}

/*****************************************************************/
/* Diffusion analysis */
```

```
/*****************************************************************/
int diffusion(int* the_value_of_e){

    int type, denom, i,j,found;
    int l,m,n;
    int p,q,r;
    int clustered_atoms[5];
    int diff_length_jump[5];
    int diff_length_jump_clustered[5];
    int diff_length_jump_unclustered[5];
    int diff_length_pos[5][3];
    int diff_length_pos_clustered[5][3];
    int diff_length_pos_unclustered[5][3];
    int diff_count[5];
    int delta_l = 0;
    int delta_m = 0;
    int delta_n = 0;
    int diff_count_dl[5];
    int diff_count_dm[5];
    int diff_count_dn[5];
    int diff_count_dl_clustered[5];
    int diff_count_dm_clustered[5];
    int diff_count_dn_clustered[5];
    int diff_count_dl_unclustered[5];
    int diff_count_dm_unclustered[5];
    int diff_count_dn_unclustered[5];
    char ID[3];
    int** atom_initial;
    int** atom_final;
    int Atom_ID;
    FILE *fin;
    FILE *fout;
    gzFile gzfin;
    char filename[100];
    char gz_filename[100];
    char buffer[50];
    int check;

    printf("Doing Diffusion Analysis.\n");

    int* all_clustered_atoms;
    int e;
    int f;
    int k=0;
    int position = 0;
    int min;
    int max;
    int mid;

    e = *the_value_of_e;
    printf("The value of e is: %d.\n",e);

    unsigned long long No_of_Moves_clustered[5];
    unsigned long long  No_of_Moves_unclustered[5];

    for(i=0;i<5;i++){
        clustered_atoms[i] = 0;
        No_of_Moves_clustered[i] = 0;
        No_of_Moves_unclustered[i] = 0;
    }
```

```
    all_clustered_atoms =
malloc(TOTAL_SOLUTE_ATOMS_NUMBER*sizeof(int));
    if(!all_clustered_atoms){
        printf("Failed to allocate memory for
all_clustered_atoms.\n");
        return 1;
    }

    //Identifies all atoms which have ended up in clusters and sorts
them
    for(f=1; f <= e; f++){
        if(cluster_size[f] >= 10){
            fflush(stdout);
            for(i=0;i<cluster_size[f];i++){
                all_clustered_atoms[k+i] =
cluster_contents[position+i];
            }
            k += cluster_size[f];
        }
        position +=cluster_size[f];
    }

    all_clustered_atoms =
(int*)realloc(all_clustered_atoms,k*sizeof(int));
    if(!all_clustered_atoms){
        printf("Failed to reallocate memory for
all_clustered_atoms.\n");
        return 1;
    }

    qsort(all_clustered_atoms,k,sizeof(int),int_cmp);
    //-------------------------------------------------------------/

    for(i=0;i<k;i++){
        clustered_atoms[getAtomType(all_clustered_atoms[i])] += 1;
    }

    sprintf(gz_filename,"Tracked Atom Positions-%dK-
%d",(int)TEMP,VERSION_NO);
    gzfin = gzopen(gz_filename,"rb");
    #ifndef NOERROR
    if(!gzfin){
        printf("Input file not opened correctly on line: %d.
Exiting\n",__LINE__);
        free(all_clustered_atoms);
        return 1;
    }
    #endif

    while(!gzeof(gzfin) && i<TOTAL_SOLUTE_ATOMS_NUMBER){
        check = gzread(gzfin,&Atom_ID,sizeof(int));
        #ifndef NOERROR
        if(check != sizeof(int)){
            printf("gzread error on line: %d. Exiting.\n",__LINE__);
            gzclose(gzfin);
            free(all_clustered_atoms);
            return 1;
        }
        #endif
        i++;
```

```
        p = gzgetc(gzfin);
        #ifndef NOERROR
        if(p == -1){
            printf("gzgetc error on line: %d. Exiting.\n",__LINE__);
            gzclose(gzfin);
            free(all_clustered_atoms);
            return 1;
        }
        #endif

        q = gzgetc(gzfin);
        #ifndef NOERROR
        if(q == -1){
            printf("gzgetc error on line: %d. Exiting.\n",__LINE__);
            gzclose(gzfin);
            free(all_clustered_atoms);
            return 1;
        }
        #endif

        r = gzgetc(gzfin);
        #ifndef NOERROR
        if(r == -1){
            printf("gzgetc error on line: %d. Exiting.\n",__LINE__);
            gzclose(gzfin);
            free(all_clustered_atoms);
            return 1;
        }
        #endif
    }

    while(!gzeof(gzfin)){
        check = gzread(gzfin,&Atom_ID,sizeof(int));
        #ifndef NOERROR
        if(check != sizeof(int)){
            printf("gzread error on line: %d. Exiting.\n",__LINE__);
            gzclose(gzfin);
            free(all_clustered_atoms);
            return 1;
        }
        #endif

        p = gzgetc(gzfin);
        #ifndef NOERROR
        if(p == -1){
            printf("gzgetc error on line: %d. Exiting.\n",__LINE__);
            gzclose(gzfin);
            free(all_clustered_atoms);
            return 1;
        }
        #endif

        q = gzgetc(gzfin);
        #ifndef NOERROR
        if(q == -1){
            printf("gzgetc error on line: %d. Exiting.\n",__LINE__);
            gzclose(gzfin);
            free(all_clustered_atoms);
            return 1;
        }
        #endif
```

```
        r = gzgetc(gzfin);
        #ifndef NOERROR
        if(r == -1){
            printf("gzgetc error on line: %d. Exiting.\n",__LINE__);
            gzclose(gzfin);
            free(all_clustered_atoms);
            return 1;
        }
        #endif

        min = 0;
        max = k- 1;
        mid = (max + min) / 2;
        found = 0;

        while((min < max) && (Atom_ID != all_clustered_atoms[mid])){

            if(Atom_ID > all_clustered_atoms[mid]){
                min = mid+1;
                mid = (max + min) / 2;
            }
            else if(Atom_ID < all_clustered_atoms[mid]){
                max = mid-1;
                mid = (max + min) / 2; n++){
            }

            if(Atom_ID == all_clustered_atoms[mid]){
                found = 1;
                type = getAtomType(Atom_ID);
                if(type == -1){
                    printf("Error in obtaining atom type.
Exiting.\n");
                    gzclose(gzfin);
                free(all_clustered_atoms);
                    return 1;
                }
                No_of_Moves_clustered[type] += 1;
                if(No_of_Moves_clustered[type] >= ULLONG_MAX){
                    printf("Max value of No_of_Moves_clustered[%d]
reached",type);
                    gzclose(gzfin);
                    free(all_clustered_atoms);
                    return 1;
                }

            }

        }

        if(found == 0){
            type = getAtomType(Atom_ID);
            if(type == -1){
                printf("Error in obtaining atom type. Exiting. The ID
i tried to obtain was:%d\n", Atom_ID);
                gzclose(gzfin);
                free(all_clustered_atoms);
                return 1;
            }
            No_of_Moves_unclustered[type] += 1;
            if(No_of_Moves_unclustered[type] >= ULLONG_MAX){
```

```
                printf("Max value of No_of_Moves_unclustered[%d]
reached",type);
                gzclose(gzfin);
                free(all_clustered_atoms);
                return 1;
            }
        }

    }

    gzclose(gzfin);

    atom_initial = allocatememory2d(TOTAL_SOLUTE_ATOMS_NUMBER+1,3);
    if(!atom_initial){
        printf("Error allocating memory for atom_initial.\n");
        free(all_clustered_atoms);
        return 1;
    }
    atom_final = allocatememory2d(TOTAL_SOLUTE_ATOMS_NUMBER+1,3);
    if(!atom_final){
        printf("Error allocating memory for atom_final.\n");
        free(all_clustered_atoms);
        freememory2d(TOTAL_SOLUTE_ATOMS_NUMBER+1,3,atom_initial);
        return 1;
    }

    for(i=0;i<5;i++){
        diff_count[i] = 0;
        diff_length_jump[i] = 0;
        diff_count_dl[i]=0;
        diff_count_dm[i]=0;
        diff_count_dn[i]=0;
        diff_count_dl_clustered[i]=0;
        diff_count_dm_clustered[i]=0;
        diff_count_dn_clustered[i]=0;
        diff_count_dl_unclustered[i]=0;
        diff_count_dm_unclustered[i]=0;
        diff_count_dn_unclustered[i]=0;
    }

    sprintf(filename,"Initial-solute-positions-%dK-
%d.txt",(int)TEMP,VERSION_NO);
    fin = fopen(filename,"r");
    if(fin == NULL){
        printf("File %s not opened correctly on line
%d.",filename,__LINE__);
        free(all_clustered_atoms);
        freememory2d(TOTAL_SOLUTE_ATOMS_NUMBER+1,3,atom_initial);
        freememory2d(TOTAL_SOLUTE_ATOMS_NUMBER+1,3,atom_final);
        return 1;
    }

    while(!feof(fin)){
        if(!fgets(buffer,50,fin) && !feof(fin)){
            printf("Error reading from file: %s on line
%d.\n",filename,__LINE__);
            free(all_clustered_atoms);
            freememory2d(TOTAL_SOLUTE_ATOMS_NUMBER+1,3,atom_initial);
            freememory2d(TOTAL_SOLUTE_ATOMS_NUMBER+1,3,atom_final);
            fclose(fin);
            return 1;
```

```
        }
        if(sscanf(buffer,"%i\t%i\t%i\t%i\n", &Atom_ID,&l,&m,&n) != 4){
            printf("Error converting buffer (%s) to Atom_ID, l, m and
n on line %d.\n",buffer,__LINE__);
            free(all_clustered_atoms);
            freememory2d(TOTAL_SOLUTE_ATOMS_NUMBER+1,3,atom_initial);
            freememory2d(TOTAL_SOLUTE_ATOMS_NUMBER+1,3,atom_final);
            fclose(fin);
            return 1;
        }
        atom_initial[Atom_ID][0] = l;
        atom_initial[Atom_ID][1] = m;
        atom_initial[Atom_ID][2] = n;
    }

    fclose(fin);

    sprintf(filename,"final-solute-positions-%dK-
%d.txt",(int)TEMP,VERSION_NO);
    fin = fopen(filename,"r");
    if(fin == NULL){
        printf("File %s not opened correctly on line
%d.",filename,__LINE__);
        free(all_clustered_atoms);
        freememory2d(TOTAL_SOLUTE_ATOMS_NUMBER+1,3,atom_initial);
        freememory2d(TOTAL_SOLUTE_ATOMS_NUMBER+1,3,atom_final);
        return 1;
    }

    while(!feof(fin)){
        if(!fgets(buffer,50,fin) && !feof(fin)){
            printf("Error reading from file: %s on line
%d.\n",filename,__LINE__);
            free(all_clustered_atoms);
            freememory2d(TOTAL_SOLUTE_ATOMS_NUMBER+1,3,atom_initial);
            freememory2d(TOTAL_SOLUTE_ATOMS_NUMBER+1,3,atom_final);
            fclose(fin);
            return 1;
        }
        if(sscanf(buffer,"%i\t%i\t%i\t%i\n", &Atom_ID,&l,&m,&n) != 4){
            printf("Error converting buffer (%s) to Atom_ID, l, m and
n on line %d.\n",buffer,__LINE__);
            free(all_clustered_atoms);
            freememory2d(TOTAL_SOLUTE_ATOMS_NUMBER+1,3,atom_initial);
            freememory2d(TOTAL_SOLUTE_ATOMS_NUMBER+1,3,atom_final);
            fclose(fin);
            return 1;
        }
        atom_final[Atom_ID][0] = l;
        atom_final[Atom_ID][1] = m;
        atom_final[Atom_ID][2] = n;
    }

    fclose(fin);

    for(i=1; i <= TOTAL_SOLUTE_ATOMS_NUMBER; i++){

        type = getAtomType(i);
        if(type == -1){
            printf("Error in getting atom type for atom %d on line %d.
Exiting.\n",i,__LINE__);
```

```
            free(all_clustered_atoms);
            freememory2d(TOTAL_SOLUTE_ATOMS_NUMBER+1,3,atom_initial);
            freememory2d(TOTAL_SOLUTE_ATOMS_NUMBER+1,3,atom_final);
            return 1;
        }

        // Diffusion based on number of jumps
        diff_count[type] += No_of_Moves[i];
        if(diff_count[type] >= ULLONG_MAX){
            printf("Max value of diff_count[%d] reached",type);
            free(all_clustered_atoms);
            freememory2d(TOTAL_SOLUTE_ATOMS_NUMBER+1,3,atom_initial);
            freememory2d(TOTAL_SOLUTE_ATOMS_NUMBER+1,3,atom_final);
            return 1;
        }

        //Diffusion based on distance from initial position
        delta_l = abs(atom_initial[i][0] - atom_final[i][0]);
        delta_m = abs(atom_initial[i][1] - atom_final[i][1]);
        delta_n = abs(atom_initial[i][2] - atom_final[i][2]);

        if(delta_l > AXIAL_ATOMS_NUMBER/2){
            delta_l = AXIAL_ATOMS_NUMBER - delta_l;
        }
        if(delta_m > AXIAL_ATOMS_NUMBER/2){
            delta_m = AXIAL_ATOMS_NUMBER - delta_m;
        }
        if(delta_n > AXIAL_ATOMS_NUMBER/2){
            delta_n = AXIAL_ATOMS_NUMBER - delta_n;
        }

        diff_count_dl[type] += delta_l;
        diff_count_dm[type] += delta_m;
        diff_count_dn[type] += delta_n;

        min = 0;
        max = k- 1;
        mid = (max + min) / 2;
        found = 0;

        while((min < max) && (i != all_clustered_atoms[mid])){

            if(i > all_clustered_atoms[mid]){
                min = mid+1;
                mid = (max + min) / 2;
            }
            else if(i < all_clustered_atoms[mid]){
                max = mid-1;
                mid = (max + min) / 2;
            }

            if(i == all_clustered_atoms[mid]){
                found = 1;
                diff_count_dl_clustered[type] += delta_l;
                diff_count_dm_clustered[type] += delta_m;
                diff_count_dn_clustered[type] += delta_n;
            }

        }

        if(found == 0){
```

```
            diff_count_dl_unclustered[type] += delta_l;
            diff_count_dm_unclustered[type] += delta_m;
            diff_count_dn_unclustered[type] += delta_n;
        }
    }

    for(j=1;j<5;j++){
        ASSERT(diff_count[j] = No_of_Moves_clustered[j] +
No_of_Moves_unclustered[j]);
        ASSERT(diff_count_dl[j] = (diff_count_dl_clustered[j] +
diff_count_dl_unclustered[j]));
        ASSERT(diff_count_dm[j] = (diff_count_dm_clustered[j] +
diff_count_dm_unclustered[j]));
        ASSERT(diff_count_dn[j] = (diff_count_dn_clustered[j] +
diff_count_dn_unclustered[j]));
    }

    // Diffusion based on number of jumps
    diff_length_jump[1] =
(int)((float)diff_count[1]/(float)CU_ATOMS_NUMBER);
    if(diff_length_jump[1] > INT_MAX){
        printf("Error. diff_length_jump greater than the maximum value
for an Int.\n");
        free(all_clustered_atoms);
        freememory2d(TOTAL_SOLUTE_ATOMS_NUMBER+1,3,atom_initial);
        freememory2d(TOTAL_SOLUTE_ATOMS_NUMBER+1,3,atom_final);
        return 1;
    }
    diff_length_jump[2] =
(int)((float)diff_count[2]/(float)NI_ATOMS_NUMBER);
    if(diff_length_jump[2] > INT_MAX){
        printf("Error. diff_length_jump greater than the maximum value
for an Int.\n");
        free(all_clustered_atoms);
        freememory2d(TOTAL_SOLUTE_ATOMS_NUMBER+1,3,atom_initial);
        freememory2d(TOTAL_SOLUTE_ATOMS_NUMBER+1,3,atom_final);
        return 1;
    }
    diff_length_jump[3] =
(int)((float)diff_count[3]/(float)MN_ATOMS_NUMBER);
    if(diff_length_jump[3] > INT_MAX){
        printf("Error. diff_length_jump greater than the maximum value
for an Int.\n");
        free(all_clustered_atoms);
        freememory2d(TOTAL_SOLUTE_ATOMS_NUMBER+1,3,atom_initial);
        freememory2d(TOTAL_SOLUTE_ATOMS_NUMBER+1,3,atom_final);
        return 1;
    }
    diff_length_jump[4] =
(int)((float)diff_count[4]/(float)SI_ATOMS_NUMBER);
    if(diff_length_jump[4] > INT_MAX){
        printf("Error. diff_length_jump greater than the maximum value
for an Int.\n");
        free(all_clustered_atoms);
        freememory2d(TOTAL_SOLUTE_ATOMS_NUMBER+1,3,atom_initial);
        freememory2d(TOTAL_SOLUTE_ATOMS_NUMBER+1,3,atom_final);
        return 1;
    }

    diff_length_jump_clustered[1] =
(int)((float)No_of_Moves_clustered[1]/(float)clustered_atoms[1]);
```

```
    diff_length_jump_clustered[2] =
(int)((float)No_of_Moves_clustered[2]/(float)clustered_atoms[2]);
    diff_length_jump_clustered[3] =
(int)((float)No_of_Moves_clustered[3]/(float)clustered_atoms[3]);
    diff_length_jump_clustered[4] =
(int)((float)No_of_Moves_clustered[4]/(float)clustered_atoms[4]);

    diff_length_jump_unclustered[1] =
(int)((float)No_of_Moves_unclustered[1]/(float)(CU_ATOMS_NUMBER -
clustered_atoms[1]));
    diff_length_jump_unclustered[2] =
(int)((float)No_of_Moves_unclustered[2]/(float)(NI_ATOMS_NUMBER -
clustered_atoms[2]));
    diff_length_jump_unclustered[3] =
(int)((float)No_of_Moves_unclustered[3]/(float)(MN_ATOMS_NUMBER -
clustered_atoms[3]));
    diff_length_jump_unclustered[4] =
(int)((float)No_of_Moves_unclustered[4]/(float)(SI_ATOMS_NUMBER -
clustered_atoms[4]));

    sprintf(filename,"Diffusion-%dK-%d.txt",(int)TEMP,VERSION_NO);
    fout = fopen(filename,"w");
    if(!fout){
        printf("Could not open file %s to out diffusion
data.\n",filename);
        free(all_clustered_atoms);
        freememory2d(TOTAL_SOLUTE_ATOMS_NUMBER+1,3,atom_initial);
        freememory2d(TOTAL_SOLUTE_ATOMS_NUMBER+1,3,atom_final);
        return 1;
    }

    //Diffusion based on distance from initial position
    for(i=1;i<=4;i++){
        switch(atom[l][m][n]){i){
            case 1: Periodic_Boundary_Conditions(l, m, n, 1);denom =
CU_ATOMS_NUMBER; sprintf(ID,"Cu"); break;
            case 2: Periodic_Boundary_Conditions(l, m, n, 2);denom =
NI_ATOMS_NUMBER; sprintf(ID,"Ni"); break;
            case 3: Periodic_Boundary_Conditions(l, m, n, 3);denom =
MN_ATOMS_NUMBER; sprintf(ID,"Mn"); break;
            case 4: Periodic_Boundary_Conditions(l, m, n, 4);denom =
SI_ATOMS_NUMBER; sprintf(ID,"Si"); break;
            case 5: Periodic_Boundary_Conditions(l, m, n,
5);default: printf("I should not be here line %d.\n",__LINE__);
                    free(all_clustered_atoms);

freememory2d(TOTAL_SOLUTE_ATOMS_NUMBER+1,3,atom_initial);

freememory2d(TOTAL_SOLUTE_ATOMS_NUMBER+1,3,atom_final);
                    fclose(fout); return 1; break;
        }}
        }

}

        diff_length_pos[i][0] =
(int)((float)diff_count_dl[i]/(float)denom);
        diff_length_pos[i][1] =
(int)((float)diff_count_dm[i]/(float)denom);
        diff_length_pos[i][2] =
(int)((float)diff_count_dn[i]/(float)denom);
```

```
        diff_length_pos_clustered[i][0] =
(int)((float)diff_count_dl_clustered[i]/(float)(clustered_atoms[i]));
        diff_length_pos_clustered[i][1] =
(int)((float)diff_count_dm_clustered[i]/(float)(clustered_atoms[i]));
        diff_length_pos_clustered[i][2] =
(int)((float)diff_count_dn_clustered[i]/(float)(clustered_atoms[i]));

        diff_length_pos_unclustered[i][0] =
(int)((float)diff_count_dl_unclustered[i]/(float)(denom -
clustered_atoms[i]));
        diff_length_pos_unclustered[i][1] =
(int)((float)diff_count_dm_unclustered[i]/(float)(denom -
clustered_atoms[i]));
        diff_length_pos_unclustered[i][2] =
(int)((float)diff_count_dn_unclustered[i]/(float)(denom -
clustered_atoms[i]));

        ASSERT(diff_length_pos[i][0] <= AXIAL_ATOMS_NUMBER/2 &&
diff_length_pos[i][1] <= AXIAL_ATOMS_NUMBER/2 && diff_length_pos[i][2]
<= AXIAL_ATOMS_NUMBER/2);
        ASSERT(diff_length_pos_clustered[i][0] <= AXIAL_ATOMS_NUMBER/2
&& diff_length_pos_clustered[i][1] <= AXIAL_ATOMS_NUMBER/2 &&
diff_length_pos_clustered[i][2] <= AXIAL_ATOMS_NUMBER/2);
        ASSERT(diff_length_pos_unclustered[i][0] <=
AXIAL_ATOMS_NUMBER/2 && diff_length_pos_unclustered[i][1] <=
AXIAL_ATOMS_NUMBER/2 && diff_length_pos_unclustered[i][2] <=
AXIAL_ATOMS_NUMBER/2);

        fprintf(fout,"All atoms.\n");
        fprintf(fout,"Average diffusion length for %2s is:\n%d based
on No. of jumps.",ID,diff_length_jump[i]);
        fprintf(fout,"\n(%d,%d,%d) based on distance from initial
position.\n",diff_length_pos[i][0],diff_length_pos[i][1],diff_length_p
os[i][2]);
        fprintf(fout,"Clustered atoms\n");
        fprintf(fout,"Average diffusion length for %2s is:\n%d based
on No. of jumps.",ID,diff_length_jump_clustered[i]);
        fprintf(fout,"\n(%d,%d,%d) based on distance from initial
position.\n",diff_length_pos_clustered[i][0],diff_length_pos_clustered
[i][1],diff_length_pos_clustered[i][2]);
        fprintf(fout,"Matrix atoms\n");
        fprintf(fout,"Average diffusion length for %2s is:\n%d based
on No. of jumps.",ID,diff_length_jump_unclustered[i]);
        fprintf(fout,"\n(%d,%d,%d) based on distance from initial
position.\n\n",diff_length_pos_unclustered[i][0],diff_length_pos_unclu
stered[i][1],diff_length_pos_unclustered[i][2]);
    }

    fclose(fout);
    free(all_clustered_atoms);
    freememory2d(TOTAL_SOLUTE_ATOMS_NUMBER+1,3,atom_initial);
    freememory2d(TOTAL_SOLUTE_ATOMS_NUMBER+1,3,atom_final);

    return 0;
}

/*************************************************************/
/* Counts number of times a solute has jumped */
/*************************************************************/
int countmoves(int Atom_ID){
```

```
No_of_Moves[Atom_ID] += 1;

return 0;
}

/*****************************************************************/
/* Saving of atoms arrangement */
/*****************************************************************/
voidint Saving_Atoms_Arrangement(int file_number)
{
    FILE *fp;
    float output[4];
    char filename[100];
    int l, m, n;
    int i;
    const doublefloat a = 0.287;      /* Lattice constant of alfa-iron
*/

    sprintf(filename, ","atomsarrangement[%.1e].[%"FMT_LLU"]-%dK-
%d.pos", time_for_saving[file_number]);],(int)TEMP,VERSION_NO);

    fp = fopen(filename, "w");wb");
    if(!fp){
        printf("Could not open file: %s for output of pos
file.\n",filename);
        return 1;
    }

    for (l=0; l<AXIAL_ATOMS_NUMBER + 2; l++)++){
        for (m=0; m<AXIAL_ATOMS_NUMBER + 2; m++)++){
            for (n=0; n<AXIAL_ATOMS_NUMBER + 2; n++){
                switch(n%2&1){
                    case 0: output[0] = (float)((l - 2) * a);
                            output[1] = (float)((m - 2) * a);
                            output[2] = (float)((n - 2) / 2. * a);
                            output[32] = (float)(atom[l][m][n] + 10.);
/ 2. * a);
                            break;
                    case 1: output[0] = (float)((l - 2) * a + a /
2.);
                            output[1] = (float)((m - 2) * a + a /
2.);
                            output[2] = (float)((n - 2) / 2. * a);
                            output[3] = (float)(atom[l][m][n] + 10.);
                            break;
                }

                switch(atom[l][m][n]){
                    case -1: output[3] = (float)15.; break; // case of
Vacancy
                    case 0:  output[3] = (float)10.; break;
                    default: output[3] =
(float)(getAtomType(atom[l][m][n])+ 10.);
                        if(getAtomType < 0){
                            printf("Could not obtain Atom Type for
atom %d on line %d.\n",atom[l][m][n],__LINE__);
                            fclose(fp);
                            return 1;
                        };
                        break;
```

```
                }

                //Swap output bytes order, such that we are outputting
a big-endian formatted
                //binary file.
                //Note: This assumes that we are in a little endian
system.
                for(i=0;i<4;i++){
                    floatSwapBytes(output+i);
                }

                if(fwrite(output, sizeof(float), 4, fp);) != 4){
            }       printf("Error writing pos file.\n");
                    fclose(fp);

}
                    return 1;
                }
            }
        }
    }

    fclose(fp);

    return 0;
}

/*****************************************************************/
//Saves a cumulative total of the No. of time the vacancy has been at
a given lattice site.
/*****************************************************************/
int savevacancypositions(int file_number, int**** vacancyprofile,
double *real_time, unsigned long long monte_carlo_steps)
{
char filename[100];

int i=0;
int l,m,n;

    for(i=0;i<VACANCY_NUMBER;i++){
        FILE *VacProfout;

        sprintf(filename, "vacancypositions-%d-[%"FMT_LLU"]-%dK-
%d.txt",i, time_for_saving[file_number],(int)TEMP,VERSION_NO);

        VacProfout = fopen(filename,"w");
        if(!VacProfout){
            printf("Unable to open file to output vacancy info.\n");
            fclose(VacProfout);
            return 1;
        }

        fprintf(VacProfout,"Monte Carlo Steps = %"FMT_LLU"\nReal Time
= %f\n",monte_carlo_steps, *real_time);
        fputs("l\tm\tn\tNo. of times",VacProfout);

        for(l=0; l<AXIAL_ATOMS_NUMBER; l++){
            for(m=0; m<AXIAL_ATOMS_NUMBER; m++){
                for(n=0; n<AXIAL_ATOMS_NUMBER; n++){
                    if(fprintf(VacProfout,"\n%i\t%i\t%i\t%i",
l,m,n,vacancyprofile[i][l][m][n]) < 0){
```

```
                        printf("Error outputting vacancy position info
for l = %d, m = %d, n = %d to file.\n", l,m,n);
                        fclose(VacProfout);
                        return 1;
                    }

                }
            }
        }
        fclose(VacProfout);
    }
    return 0;
}

/*****************************************************************/
/* Saves positions of tracked atoms each time they are changed */
/*****************************************************************/
int Atom_Tracker(int l, int m, int n){

    if(gzwrite(Atom_track_filename,&atom[l][m][n],sizeof(int)) !=
sizeof(int)){
        printf("gzwrite error on line: %d.\n", __LINE__);
        return 1;
    }
    gzputc(Atom_track_filename,l);
    gzputc(Atom_track_filename,m);
    gzputc(Atom_track_filename,n);

    return 0;
}
/*****************************************************************/
/* Binary search of Atoms to track for atom[l][m][n]             */
/*****************************************************************/
int binary_search(int l, int m, int n){

int min = 0;
int max = Number_of_atoms_to_track - 1;
int mid;

    mid = (max + min) / 2;

    if(atom[l][m][n] == Atoms_to_track[mid]){
        return 1;
    }

    while((min < max) && (atom[l][m][n] != Atoms_to_track[mid])){

        if(atom[l][m][n] > Atoms_to_track[mid]){
            min = mid+1;
            mid = (max + min) / 2;
            //break;
        }
        else if(atom[l][m][n] < Atoms_to_track[mid]){
            max = mid-1;
            mid = (max + min) / 2;
            //break;
        }

        if(atom[l][m][n] == Atoms_to_track[mid]){
            return 1;
        }
```

```
    }

return 0;
}

//Compares two integers. Used only when debugging enabled.
int int_cmp(const void *a, const void *b)
{
    const int *ia = (const int *)a; // casting pointer types
    const int *ib = (const int *)b;
    return *ia  - *ib;
    /* integer comparison: returns negative if b > a
    and positive if a > b */
}


// Converts pos file from litte endian to big endian.
void floatSwapBytes(float *inFloat) // Added 13/6/11
{
    FloatSwapUnion fa,fb;
    fa.f = *inFloat;

    fb.c[0] = fa.c[3];
    fb.c[1] = fa.c[2];
    fb.c[2] = fa.c[1];
    fb.c[3] = fa.c[0];

    *inFloat=fb.f;
}


int print_positions(unsigned long long monte_carlo_steps){

    int l,m,n;
    int nl=0;
    FILE *fout;
    char filename[100];

    if(monte_carlo_steps == 0){
        sprintf(filename,"Initial-solute-positions-%dK-
%d.txt",(int)TEMP,VERSION_NO);
        fout = fopen(filename,"w");
        if(fout == NULL){
            printf("File not opened correctly on line
%d.\n",__LINE__);
            return 1;
        }
    }
    else{
        sprintf(filename,"final-solute-positions-%dK-
%d.txt",(int)TEMP,VERSION_NO);
        fout = fopen(filename,"w");
        if(fout == NULL){
            printf("File not opened correctly on line
%d.\n",__LINE__);
            return 1;
        }
    }
```

```
    for(l=0; l<AXIAL_ATOMS_NUMBER; l++){
        for(m=0; m<AXIAL_ATOMS_NUMBER; m++){
            for(n=0; n<AXIAL_ATOMS_NUMBER; n++){
                if(atom[l][m][n] != 0 && atom[l][m][n] != -1){
                    switch(nl){
                        default:
                            if(fprintf(fout,"\n%i\t%i\t%i\t%i",
atom[l][m][n],l,m,n) < 0){
                                printf("Positons not written to file
correctly on line %d.\n", __LINE__);
                                fclose(fout);
                                return 1;
                            }; break;
                        case 0:
                            if(fprintf(fout,"%i\t%i\t%i\t%i",
atom[l][m][n],l,m,n) < 0){
                                printf("Positons not written to file
correctly on line %d.\n", __LINE__);
                                fclose(fout);
                                return 1;
                            }
                            nl = 1; break;
                    }
                }
            }
        }
    }

    fclose(fout);
    return 0;
}
```

## E.2 Additional Analysis Code

### E.2.1 Linked Clustering

```
#ifdef DEBUG
    #include <assert.h>
    #define ASSERT(f) {if(!(f)){ printf("Assertion failed: %s - %d
",__FILE__,__LINE__);getchar();}}
#else
    #define ASSERT(f) {}
#endif

#include <stdio.h>
#include <stdlib.h>
#include <string.h>
#include <math.h>
#include <float.h>
#include "GSsimulation_parameters.h"

int Read_Tracked_Atoms(int number_analysis_times, int T,int
version_no, float* final_clusters_vol, int DISTMAXMIN);
int binary_search(int i, int* buffer);
void writefile(int*** linked_clusters, int*** linked_clusters_comp,
int** linked_clusters_count,int no_analysis_times_run,int T,int
version_no);
int int_cmp(const void *a, const void *b) ;
int*** allocatememory3d(int imax, int jmax,int kmax);
int freememory3d(int imax,int jmax,int kmax, int ***buffer);
int** allocatememory2d(int jmax, int imax);
int freememory2d(int imax,int jmax, int **buffer);
int compositions(int Number_of_atoms_in_cluster, int***
linked_clusters_comp, int l, int h);
int summary(int*** linked_clusters, int*** linked_clusters_comp, int*
no_unlinked_clusters, int** unlinked_clusters_comp, int**
linked_clusters_count, int no_analysis_times_run, int version_no, int
T, float final_clusters_vol);
int getAtomType(int i);

int Number_of_atoms_to_track;
int Number_of_clusters_to_track;
int *Atoms_to_track;
int *cluster_sizes;
int cluster_ID;
int *atoms_in_cluster;
int *atoms_of_interest=0;
float *cluster_position;
int *cluster_IDs_of_interest;


int main(void){


    FILE *fin;

    int number_analysis_times =
sizeof(time_for_analysis)/sizeof(unsigned long long);
    int no_analysis_times_run;
    char filename[50];
    char *string;
    char *buffer;
    int h=0,i=0,l=0;
    int a,b,c;
    float x,y,z;
    const float a0=0.287;
    int f;
```

```
    int T;
    int version_no;
    int Number_of_atoms_in_cluster;
    float file_size;
    int check;
    int tmpInt;
    int*** linked_clusters;
    int*** linked_clusters_comp;
    int** linked_clusters_count;
    int* no_unlinked_clusters;
    int** unlinked_clusters_comp;
    int found=0;
    float final_clusters_vol=0.0;

    const int BUFFER_SIZE=1000*1000;
    const int DISTMAXMIN=2;
    int ATOMS_IN_CLUSTER_MAX;
    int MAX_NO_OF_LINKED_CLUSTERS=1000;
    version_no = VERSION_NO;
    T = TEMP;

    no_analysis_times_run =
Read_Tracked_Atoms(number_analysis_times,T,version_no,
&final_clusters_vol,DISTMAXMIN); // Reads in the clustered atoms of
interest
    if(no_analysis_times_run == -1){ //Checks that Read_Tracked_Atoms
did not fail
        printf("Error reading Atoms_in_clusters. Exiting");
        exit(1);
    }

    //allocate memory for the atoms we will read in.
    linked_clusters =
allocatememory3d(Number_of_clusters_to_track,no_analysis_times_run,MAX
_NO_OF_LINKED_CLUSTERS);
    if(linked_clusters == NULL){
        printf("Failed to allocate memory for linked_clusters on line:
%d.\n",__LINE__);
        exit(1);
    }
    linked_clusters_comp =
allocatememory3d(Number_of_clusters_to_track,no_analysis_times_run,5);
    if(linked_clusters_comp == NULL){
        printf("Failed to allocate memory for linked_clusters on line:
%d.\n",__LINE__);

freememory3d(Number_of_clusters_to_track,no_analysis_times_run,MAX_NO_
OF_LINKED_CLUSTERS,linked_clusters);
        exit(1);
    }
    linked_clusters_count =
allocatememory2d(Number_of_clusters_to_track,no_analysis_times_run);
    if(linked_clusters_count == NULL){
        printf("Failed to allocate memory for linked_clusters on line:
%d.\n",__LINE__);

freememory3d(Number_of_clusters_to_track,no_analysis_times_run,MAX_NO_
OF_LINKED_CLUSTERS,linked_clusters);

freememory3d(Number_of_clusters_to_track,no_analysis_times_run,5,linke
d_clusters_comp);
```

```
        exit(1);
    }

    buffer = malloc(BUFFER_SIZE); // allocate memory for the buffer
for reading in lines from the input file.
    if(!buffer){
        printf("Malloc failed on line: %d\n",__LINE__);

freememory3d(Number_of_clusters_to_track,no_analysis_times_run,MAX_NO_
OF_LINKED_CLUSTERS,linked_clusters);

freememory3d(Number_of_clusters_to_track,no_analysis_times_run,5,linke
d_clusters_comp);

freememory2d(Number_of_clusters_to_track,no_analysis_times_run,linked_
clusters_count);
    }

    no_unlinked_clusters=calloc(no_analysis_times_run,sizeof(int));
    if(!no_unlinked_clusters){
        printf("Calloc failed on line: %d\n",__LINE__);

freememory3d(Number_of_clusters_to_track,no_analysis_times_run,MAX_NO_
OF_LINKED_CLUSTERS,linked_clusters);

freememory3d(Number_of_clusters_to_track,no_analysis_times_run,5,linke
d_clusters_comp);

freememory2d(Number_of_clusters_to_track,no_analysis_times_run,linked_
clusters_count);
        free(buffer);
    }

    unlinked_clusters_comp=allocatememory2d(no_analysis_times_run,5);
    if(!unlinked_clusters_comp){
        printf("Failed to allocate memory for unlinked_clusters_comp
on line: %d\n",__LINE__);

freememory3d(Number_of_clusters_to_track,no_analysis_times_run,MAX_NO_
OF_LINKED_CLUSTERS,linked_clusters);

freememory3d(Number_of_clusters_to_track,no_analysis_times_run,5,linke
d_clusters_comp);

freememory2d(Number_of_clusters_to_track,no_analysis_times_run,linked_
clusters_count);
        free(buffer);
        free(no_unlinked_clusters);
    }

    for(h = 0; h < no_analysis_times_run-1; h++){   //for all the
files which contain the IDs of atoms in clusters at a given time

        sprintf(filename,"Atoms in clusters[%llu]-%iK-
%d.txt",time_for_analysis[h],T,version_no);

        printf("The current file being analysed is: %s\n",filename);

        fin = fopen(filename,"r");
        if(fin == NULL){
```

```
            printf("File not opened correctly on line
%d.\n",__LINE__);

freememory3d(Number_of_clusters_to_track,no_analysis_times_run,MAX_NO_
OF_LINKED_CLUSTERS,linked_clusters);

freememory3d(Number_of_clusters_to_track,no_analysis_times_run,5,linke
d_clusters_comp);

freememory2d(Number_of_clusters_to_track,no_analysis_times_run,linked_
clusters_count);
            free(buffer);
            exit(1);
        }

        fseek(fin,0,SEEK_END);
        file_size = ftell(fin); //find out the file size
        fseek(fin,0,SEEK_SET); // return to the beginning of the file

        printf("The file size is %f.\n",file_size);

        if(file_size != 0){ //if the file size is not zero then do
something
            while(!feof(fin)){ //while we're not at the end of the
file
                atoms_in_cluster = calloc(1000,sizeof(int)); //Alloc
memory to store the IDs of the atoms in the cluster we are reading in
                if(!atoms_in_cluster){
                    printf("Calloc failed on line: %d.\n",__LINE__);

freememory3d(Number_of_clusters_to_track,no_analysis_times_run,MAX_NO_
OF_LINKED_CLUSTERS,linked_clusters);

freememory3d(Number_of_clusters_to_track,no_analysis_times_run,5,linke
d_clusters_comp);

freememory2d(Number_of_clusters_to_track,no_analysis_times_run,linked_
clusters_count);
                    free(buffer);
                    fclose(fin);
                    exit(1);
                }

                ATOMS_IN_CLUSTER_MAX = 1000; //Set the inital maximum
to be 1000 atoms


                if(!fgets(buffer,BUFFER_SIZE,fin)){ //Read in a line
from the file and store it in buffer
                    printf("Buffer read failure on line %d. Proabably
an EOL error.\n",__LINE__);
                    fclose(fin);

freememory3d(Number_of_clusters_to_track,no_analysis_times_run,MAX_NO_
OF_LINKED_CLUSTERS,linked_clusters);

freememory3d(Number_of_clusters_to_track,no_analysis_times_run,5,linke
d_clusters_comp);

freememory2d(Number_of_clusters_to_track,no_analysis_times_run,linked_
clusters_count);
```

```
                    free(atoms_of_interest);
                    free(atoms_in_cluster);
                    free(buffer);
                    exit(1);
                }
                //printf(buffer);

                string = strtok(buffer," "); //read in the word
Cluster - Don't care about this
                if(!string){
                    printf("Error on line %d.\n",__LINE__);
                    fclose(fin);

freememory3d(Number_of_clusters_to_track,no_analysis_times_run,MAX_NO_
OF_LINKED_CLUSTERS,linked_clusters);

freememory3d(Number_of_clusters_to_track,no_analysis_times_run,5,linke
d_clusters_comp);

freememory2d(Number_of_clusters_to_track,no_analysis_times_run,linked_
clusters_count);
                    free(atoms_of_interest);
                    free(atoms_in_cluster);
                    free(buffer);
                    exit(1);
                }

                string = strtok(NULL, " "); //read in the word Number
- Don't care about this
                if(!string){
                    printf("Error on line %d.\n",__LINE__);
                    fclose(fin);

freememory3d(Number_of_clusters_to_track,no_analysis_times_run,MAX_NO_
OF_LINKED_CLUSTERS,linked_clusters);

freememory3d(Number_of_clusters_to_track,no_analysis_times_run,5,linke
d_clusters_comp);

freememory2d(Number_of_clusters_to_track,no_analysis_times_run,linked_
clusters_count);
                    free(atoms_of_interest);
                    free(atoms_in_cluster);
                    free(buffer);
                    exit(1);
                }

                string = strtok(NULL, "\t"); //read in the cluster ID
- Don't care about this
                if(!string){
                    printf("Error on line %d.\n",__LINE__);
                    fclose(fin);

freememory3d(Number_of_clusters_to_track,no_analysis_times_run,MAX_NO_
OF_LINKED_CLUSTERS,linked_clusters);

freememory3d(Number_of_clusters_to_track,no_analysis_times_run,5,linke
d_clusters_comp);

freememory2d(Number_of_clusters_to_track,no_analysis_times_run,linked_
clusters_count);
```

```
                    free(atoms_of_interest);
                    free(atoms_in_cluster);
                    free(buffer);
                    exit(1);
                }

                check = sscanf(string,"%d",&cluster_ID);  //Reads in
cluster_ID and checks it's correctly read
                if(check != 1){
                    printf("sscanf read failure. I read %d
things.\n",check);
                    fclose(fin);

freememory3d(Number_of_clusters_to_track,no_analysis_times_run,MAX_NO_
OF_LINKED_CLUSTERS,linked_clusters);

freememory3d(Number_of_clusters_to_track,no_analysis_times_run,5,linke
d_clusters_comp);

freememory2d(Number_of_clusters_to_track,no_analysis_times_run,linked_
clusters_count);
                    free(atoms_of_interest);
                    free(atoms_in_cluster);
                    free(buffer);
                    exit(1);
                }

                string = strtok(NULL, "\t"); //read in the x position
                if(!sscanf(string,"%d",&a)){
                    printf("Error on line %d.\n",__LINE__);
                    fclose(fin);

freememory3d(Number_of_clusters_to_track,no_analysis_times_run,MAX_NO_
OF_LINKED_CLUSTERS,linked_clusters);

freememory3d(Number_of_clusters_to_track,no_analysis_times_run,5,linke
d_clusters_comp);

freememory2d(Number_of_clusters_to_track,no_analysis_times_run,linked_
clusters_count);
                    free(atoms_of_interest);
                    free(atoms_in_cluster);
                    free(buffer);
                    exit(1);
                }

                string = strtok(NULL, "\t"); //read in the y position
                if(!sscanf(string,"%d",&b)){
                    printf("Error on line %d.\n",__LINE__);
                    fclose(fin);

freememory3d(Number_of_clusters_to_track,no_analysis_times_run,MAX_NO_
OF_LINKED_CLUSTERS,linked_clusters);

freememory3d(Number_of_clusters_to_track,no_analysis_times_run,5,linke
d_clusters_comp);

freememory2d(Number_of_clusters_to_track,no_analysis_times_run,linked_
clusters_count);
                    free(atoms_of_interest);
                    free(atoms_in_cluster);
```

```
                    free(buffer);
                    exit(1);
                }

                string = strtok(NULL, "\t"); //read in the z position
                if(!sscanf(string,"%d",&c)){
                    printf("Error on line %d.\n",__LINE__);
                    fclose(fin);

freememory3d(Number_of_clusters_to_track,no_analysis_times_run,MAX_NO_
OF_LINKED_CLUSTERS,linked_clusters);

freememory3d(Number_of_clusters_to_track,no_analysis_times_run,5,linke
d_clusters_comp);

freememory2d(Number_of_clusters_to_track,no_analysis_times_run,linked_
clusters_count);
                    free(atoms_of_interest);
                    free(atoms_in_cluster);
                    free(buffer);
                    exit(1);
                }

                //Convert a,b,c to actual bcc co-ordinates

                switch(c&1){ //Converts to real bcc co-ordinates
                    case 0: x = (float)(a * a0);
                            y = (float)(b * a0);
                            z = (float)(c / 2. * a0);
                            break;
                    case 1: x = (float)(a  * a0 + a0 / 2.);
                            y = (float)(b  * a0 + a0 / 2.);
                            z = (float)(c / 2. * a0);
                            break;
                }

                found=0;

                for(f=0;f<Number_of_clusters_to_track-1;f++){ //Loop
through the clusters identified in Read_Tracked_Atoms
                    l=f; //identifes which of the clusters we are in
(those read in in read tracked atoms - 0 is the first cluster)
                    if(x>cluster_position[3*f]-DISTMAXMIN &&
x<cluster_position[3*f]+DISTMAXMIN){ //If the cluster is within the
min/max of the centre of this then check the y co-ords
                        if(y>cluster_position[3*f+1]-DISTMAXMIN &&
y<cluster_position[3*f+1]+DISTMAXMIN){ //If the cluster is within the
min/max of the centre of this then check the z co-ords
                            if(z>cluster_position[3*f+2]-DISTMAXMIN &&
z<cluster_position[3*f+2]+DISTMAXMIN){ //If the cluster is within the
min/max of the centre of this then we are interested in it
                                i = 0; // iterator for the number of
atoms in the current cluster
                                found=1;
                                string = strtok(NULL,"\t"); //read in
the first Atom_ID in the matching cluster
                                while(string != NULL){ //Check we
haven't got to the end of the Atoms in the cluster

                                    if(sscanf(string,"%d",&tmpInt)){
//Check we read in the Atom_ID correctly
```

```
                                        atoms_in_cluster[i] = tmpInt;
//Store it in atoms_in_cluster

//printf("%d\n",atoms_in_cluster[i]);
                                        i++;
                                        if(i == ATOMS_IN_CLUSTER_MAX){
//If we reach the maximum number of atoms we can store increase the
size of atoms_in_cluster by 1000
                                            atoms_in_cluster =
realloc(atoms_in_cluster,(i+1000)*sizeof(int));
                                            ATOMS_IN_CLUSTER_MAX +=
1000; //Set ATOMS_IN_CLUSTER_MAX to the new maximum no of atoms
                                        }
                                    }
                                    string = strtok(NULL,"\t"); //
read in the next entry
                                }

                                Number_of_atoms_in_cluster = i;
//store the number of atoms that were in the cluster we've just read
in

compositions(Number_of_atoms_in_cluster, linked_clusters_comp, l, h);
//Add the composition of this cluster to the array
linked_clusters_comp


linked_clusters[l][h][linked_clusters_count[l][h]] = cluster_ID;
//Store the cluster ID of the cluster in linked clusters by l (ID of
the cluster it is linked to) and h (the time step at which it was
linked)
                                linked_clusters_count[l][h] += 1; //
Increase the count of the number of clusters linked to cluster l at
time h by one
                                ASSERT(linked_clusters_count[l][h] <
MAX_NO_OF_LINKED_CLUSTERS);
                                if(linked_clusters_count[l][h] ==
MAX_NO_OF_LINKED_CLUSTERS){ //Check we've not reached the max number
of clusters we can store
                                    printf("Out of memory in
linked_clusters, please increase value of MAX_NO_OF_LINKED_CLUSTERS to
greater than %d.\n", MAX_NO_OF_LINKED_CLUSTERS);

freememory3d(Number_of_clusters_to_track,no_analysis_times_run,MAX_NO_
OF_LINKED_CLUSTERS,linked_clusters);

freememory3d(Number_of_clusters_to_track,no_analysis_times_run,5,linke
d_clusters_comp);

freememory2d(Number_of_clusters_to_track,no_analysis_times_run,linked_
clusters_count);
                                    free(atoms_of_interest);
                                    free(atoms_in_cluster);
                                    free(buffer);
                                    fclose(fin);
                                    exit(1);
                                }

                                //printf("I am now in cluster
%d.\n",cluster_IDs_of_interest[l]);
```

```
                                f = Number_of_clusters_to_track; //
we've finished with this l so set it to its max value to exit the loop
                                //think this should be f!
                            }
                        }
                    }
                }

                if(found==0){
                    no_unlinked_clusters[h]+=1;

                    string = strtok(NULL,"\t"); //read in the first
Atom_ID in the matching cluster
                    while(string != NULL){ //Check we haven't got to
the end of the Atoms in the cluster

                        if(sscanf(string,"%d",&tmpInt)){ //Check we
read in the Atom_ID correctly

unlinked_clusters_comp[h][getAtomType(tmpInt)]+=1;
                        }
                        string = strtok(NULL,"\t"); // read in the
next entry
                    }

                }


                free(atoms_in_cluster);
            }
            printf("All finished for now.\n");
        }
        fclose(fin);
    }

    writefile(linked_clusters,
linked_clusters_comp,linked_clusters_count,no_analysis_times_run,T,ver
sion_no);
    summary(linked_clusters, linked_clusters_comp,
no_unlinked_clusters, unlinked_clusters_comp, linked_clusters_count,
no_analysis_times_run, version_no, T, final_clusters_vol);


freememory3d(Number_of_clusters_to_track,no_analysis_times_run,MAX_NO_
OF_LINKED_CLUSTERS,linked_clusters);

freememory3d(Number_of_clusters_to_track,no_analysis_times_run,5,linke
d_clusters_comp);

freememory2d(Number_of_clusters_to_track,no_analysis_times_run,linked_
clusters_count);
    free(atoms_of_interest);
    free(buffer);

    printf("cluster tracking complete.\n");
    return 0;
}

int compositions(int Number_of_atoms_in_cluster, int***
linked_clusters_comp, int l, int h){
```

```
int i;

    for(i = 0; i < Number_of_atoms_in_cluster; i++){
        linked_clusters_comp[l][h][getAtomType(atoms_in_cluster[i])]
+= 1;
    }

    return 0;
}

int summary(int*** linked_clusters, int*** linked_clusters_comp,int*
no_unlinked_clusters, int** unlinked_clusters_comp, int**
linked_clusters_count, int no_analysis_times_run, int version_no, int
T, float final_clusters_vol){

int i, j;
int tot_atoms = 0;
int tot_Cu_atoms = 0;
int tot_Ni_atoms = 0;
int tot_Mn_atoms = 0;
int tot_Si_atoms = 0;
int tot_clusters = 0;
float Cu_Conc;
float Ni_Conc;
float Mn_Conc;
float Si_Conc;
float Av_size;
int tot_unlinked_atoms=0;
float unlinked_Cu_Conc=0;
float unlinked_Ni_Conc=0;
float unlinked_Mn_Conc=0;
float unlinked_Si_Conc=0;
float linked_Nd;
float unlinked_Nd;

FILE *fout;
char filename[100];

    sprintf(filename,"Linked-atoms_positions-Summary-%dK-%d.txt",T,
version_no);
    fout = fopen(filename, "w");
    fprintf(fout,"Linked clusters summrary.\n");
    fprintf(fout,"File Name\tAv. Cu Conc\tAv. Ni Conc\tAv. Mn
Conc\tAv. Si Conc\tNo. Cu Atoms\tNo. Ni Atoms\tNo. Mn Atoms\tNo. Si
Atoms\tAv. Size\tNumber of Clusters\t\tUnlinked Cu. Conc\tUnlinked Ni.
Conc\tUnlinked Mn. Conc\tUnlinked Si. Conc\tUnlinked Cu
Atoms\tUnlinked Ni Atoms\tUnlinked Mn Atoms\tUnlinked Si Atoms\tNo.
Unlinked Clusters\t\tLinked Nd.\tUnlinked Nd.\n");

    for(i =0; i < no_analysis_times_run; i++){
        for(j = 0; j < Number_of_clusters_to_track; j++){
            tot_Cu_atoms += linked_clusters_comp[j][i][1];
            tot_Ni_atoms += linked_clusters_comp[j][i][2];
            tot_Mn_atoms += linked_clusters_comp[j][i][3];
            tot_Si_atoms += linked_clusters_comp[j][i][4];
            tot_clusters += linked_clusters_count[j][i];
        }

        linked_Nd=(float)tot_clusters/final_clusters_vol;
```

```
        tot_atoms = tot_Cu_atoms + tot_Mn_atoms + tot_Ni_atoms +
tot_Si_atoms;

        Cu_Conc = (float)tot_Cu_atoms/(float)tot_atoms;
        Ni_Conc = (float)tot_Ni_atoms/(float)tot_atoms;
        Mn_Conc = (float)tot_Mn_atoms/(float)tot_atoms;
        Si_Conc = (float)tot_Si_atoms/(float)tot_atoms;
        Av_size = (float)tot_atoms/(float)tot_clusters;


tot_unlinked_atoms=unlinked_clusters_comp[i][1]+unlinked_clusters_comp
[i][2]+unlinked_clusters_comp[i][3]+unlinked_clusters_comp[i][4];

unlinked_Cu_Conc=(float)unlinked_clusters_comp[i][1]/(float)tot_unlink
ed_atoms;

unlinked_Ni_Conc=(float)unlinked_clusters_comp[i][2]/(float)tot_unlink
ed_atoms;

unlinked_Mn_Conc=(float)unlinked_clusters_comp[i][3]/(float)tot_unlink
ed_atoms;

unlinked_Si_Conc=(float)unlinked_clusters_comp[i][4]/(float)tot_unlink
ed_atoms;

unlinked_Nd=(float)no_unlinked_clusters[i]/((128.0*128.0*128.0/85.0)-
final_clusters_vol);

        fprintf(fout,"\nFile-Atoms in clusters[%llu]-%dK-
%d.txt\t%f\t%f\t%f\t%f\t%i\t%i\t%i\t%i\t%f\t%i\t\t%f\t%f\t%f\t%f\t%i\t
%i\t%i\t%i\t%i\t\t%f\t%f",time_for_analysis[i], T, version_no,

Cu_Conc,Ni_Conc,Mn_Conc,Si_Conc,tot_Cu_atoms,tot_Ni_atoms,tot_Mn_atoms
,tot_Si_atoms,Av_size,tot_clusters,unlinked_Cu_Conc,unlinked_Ni_Conc,u
nlinked_Mn_Conc,unlinked_Si_Conc,unlinked_clusters_comp[i][1],

unlinked_clusters_comp[i][2],unlinked_clusters_comp[i][3],unlinked_clu
sters_comp[i][4],no_unlinked_clusters[i],linked_Nd,unlinked_Nd);

        tot_Cu_atoms = 0;
        tot_Ni_atoms = 0;
        tot_Mn_atoms = 0;
        tot_Si_atoms = 0;
        tot_atoms = 0;
        tot_clusters = 0;
        tot_unlinked_atoms=0;
    }

    fclose(fout);
    return 0;
}


/*****************************************************************/
//Returns the identidy of a solute atom from it's unique ID.
/*****************************************************************/
int getAtomType(int i){
    if (i <= CU_ATOMS_NUMBER)
        return 1;
```

```
    if(i >= CU_ATOMS_NUMBER+1 && i <=
(CU_ATOMS_NUMBER+NI_ATOMS_NUMBER))
        return 2;

    if(i >= (CU_ATOMS_NUMBER+NI_ATOMS_NUMBER+1)&& i <=
(CU_ATOMS_NUMBER+NI_ATOMS_NUMBER+MN_ATOMS_NUMBER))
        return 3;

    if(i >= (CU_ATOMS_NUMBER+NI_ATOMS_NUMBER+MN_ATOMS_NUMBER+1) && i
<= TOTAL_SOLUTE_ATOMS_NUMBER)
        return 4;

    ASSERT(0);
    return -1;
}

void writefile(int*** linked_clusters, int*** linked_clusters_comp,
int** linked_clusters_count, int no_analysis_times_run, int T,int
version_no){

FILE *fout;
int i,j,k;
char filename[100];
float Cu_Conc, Ni_Conc, Mn_Conc, Si_Conc, tot_atoms;

    sprintf(filename,"Linked-Clusters_positions-%dK-
%d.txt",T,version_no);
    fout = fopen(filename,"w");

    for(i = 0; i < Number_of_clusters_to_track; i++){
        fprintf(fout,"Cluster Number %d\t(Size: %d
Atoms)\n",cluster_IDs_of_interest[i],cluster_sizes[i]);
        for(j = 0; j < no_analysis_times_run-1; j++){
            tot_atoms = linked_clusters_comp[i][j][1] +
linked_clusters_comp[i][j][2] +linked_clusters_comp[i][j][3]
+linked_clusters_comp[i][j][4];
            Cu_Conc = (float)linked_clusters_comp[i][j][1]/tot_atoms;
            Ni_Conc = (float)linked_clusters_comp[i][j][2]/tot_atoms;
            Mn_Conc = (float)linked_clusters_comp[i][j][3]/tot_atoms;
            Si_Conc = (float)linked_clusters_comp[i][j][4]/tot_atoms;

            fprintf(fout,"\tFile-Atoms in clusters[%llu]-%dK-
%d.txt\t%f\t%f\t%f\t%f\t",time_for_analysis[j], T, version_no,
Cu_Conc, Ni_Conc, Mn_Conc, Si_Conc);
            for(k = 0; k < linked_clusters_count[i][j]; k++){
                //FIXME: Off by one error (0 bytes after).
                fprintf(fout,"%d\t",linked_clusters[i][j][k]);
            }
            if(i != Number_of_clusters_to_track-1 || j !=
no_analysis_times_run-2){
                fprintf(fout,"\n");
            }
        }
        if(i != Number_of_clusters_to_track-1){
            fprintf(fout,"\n");
        }
    }

    fclose(fout);
}
```

```
int Read_Tracked_Atoms(int number_analysis_times, int T,int
version_no, float* final_clusters_vol, int DISTMAXMIN){

    FILE *fin;

    int j = 1;
    int k = 0;
    int d = 0;
    int a,b,c;
    float x,y,z;
    int l,m,n;
    int l_min,l_max,m_min,m_max,n_min,n_max;
    int sum=0;
    const float a0=0.287;
    int check;
    int found=0;
    char filename[100];
    char* buffer;
    char* string;
    const int BUFFER_SIZE=1000*1000;
    int*** atoms_for_volume;
    int periodic_l, periodic_m, periodic_n;
    const int distmax_sites = (int)((float)DISTMAXMIN/a0); //for x-y,
double for z

    buffer = malloc(BUFFER_SIZE);


atoms_for_volume=allocatememory3d(AXIAL_ATOMS_NUMBER,AXIAL_ATOMS_NUMBE
R,AXIAL_ATOMS_NUMBER);
    if(!atoms_for_volume){
        printf("Failed to allocate memory for atoms_for_volume on
line: %d.\n",__LINE__);
        return -1;
    }

    k = number_analysis_times-1; // Array Starts from zero so last
entry is size - 1

    printf("k is: %d\n",k);

    while(found != 1 && k >= 0){

        sprintf(filename,"Atoms in clusters[%llu]-%dK-
%d.txt",time_for_analysis[k],T,version_no);

        found=0; // Assume file does not exist and is cannot be opened
correctly
        fin = fopen(filename,"r");
        if(fin != NULL){ //Checks file exists and is opened correctly
            found=1; // Set found to 1 as the file was opened and we
no longer need test for files
            printf("The opened file is: %s\n",filename);
            break;
        }
        else{
            printf("File not opened, %s.\n",filename);
            k--; //file k doesn't exist so set k to be the next
highest file.
        }
    }
```

```
    printf("k is: %d\n",k); // print the value of k on which the while
loop exited.

    while(!feof(fin)){  //Sets the clusters from the file fin and the
atoms contained within them.

        if(fgets(buffer,BUFFER_SIZE,fin) == NULL){ // Reads in the
first line from the file fin to buffer
            printf("Buffer read failure on line %d. Probably an EOL
error.\n",__LINE__);
            free(buffer);

freememory3d(AXIAL_ATOMS_NUMBER,AXIAL_ATOMS_NUMBER,AXIAL_ATOMS_NUMBER,
atoms_for_volume);
            fclose(fin);
            return -1;
        }
        //printf(buffer);

        string = strtok(buffer," "); //read in the word Cluster -
Don't care about this
        if(!string){
            printf("Error on line %d.\n",__LINE__);
            free(buffer);

freememory3d(AXIAL_ATOMS_NUMBER,AXIAL_ATOMS_NUMBER,AXIAL_ATOMS_NUMBER,
atoms_for_volume);
            fclose(fin);
            return -1;
        }

        string = strtok(NULL, " "); //read in the word Number - Don't
care about this
        if(!string){
            printf("Error on line %d.\n",__LINE__);
            free(buffer);

freememory3d(AXIAL_ATOMS_NUMBER,AXIAL_ATOMS_NUMBER,AXIAL_ATOMS_NUMBER,
atoms_for_volume);
            fclose(fin);
            return -1;
        }

        string = strtok(NULL, "\t"); //read in the cluster ID
        if(!string){
            printf("Error on line %d.\n",__LINE__);
            free(buffer);

freememory3d(AXIAL_ATOMS_NUMBER,AXIAL_ATOMS_NUMBER,AXIAL_ATOMS_NUMBER,
atoms_for_volume);
            fclose(fin);
            return -1;
        }

        check=sscanf(string,"%d",&cluster_ID); //Reads in cluster_ID
and checks it's correctly read
        if(check != 1){
            printf("sscanf read failure. I read %d things.\n",check);
            free(buffer);
```

```
freememory3d(AXIAL_ATOMS_NUMBER,AXIAL_ATOMS_NUMBER,AXIAL_ATOMS_NUMBER,
atoms_for_volume);
            fclose(fin);
            return -1;
        }

        string = strtok(NULL, "\t"); //read in the x position
        if(!sscanf(string,"%d",&a)){
            printf("sscanf read failure on line %d.\n",__LINE__);
            free(buffer);

freememory3d(AXIAL_ATOMS_NUMBER,AXIAL_ATOMS_NUMBER,AXIAL_ATOMS_NUMBER,
atoms_for_volume);
            fclose(fin);
            return -1;
        }

        string = strtok(NULL, "\t"); //read in the y position
        if(!sscanf(string,"%d",&b)){
            printf("sscanf read failure on line %d.\n",__LINE__);
            free(buffer);

freememory3d(AXIAL_ATOMS_NUMBER,AXIAL_ATOMS_NUMBER,AXIAL_ATOMS_NUMBER,
atoms_for_volume);
            fclose(fin);
            return -1;
        }

        string = strtok(NULL, "\t"); //read in the z position
        if(!sscanf(string,"%d",&c)){
            printf("sscanf read failure on line %d.\n",__LINE__);
            free(buffer);

freememory3d(AXIAL_ATOMS_NUMBER,AXIAL_ATOMS_NUMBER,AXIAL_ATOMS_NUMBER,
atoms_for_volume);
            fclose(fin);
            return -1;
        }

        //Convert a,b,c to actual bcc co-ordinates

        switch(c&1){ //Converts to real bcc co-ordinates
            case 0: x = (float)(a * a0);
                    y = (float)(b * a0);
                    z = (float)(c / 2. * a0);
                    break;
            case 1: x = (float)(a  * a0 + a0 / 2.);
                    y = (float)(b  * a0 + a0 / 2.);
                    z = (float)(c / 2. * a0);
                    break;
        }

        j = 0; // iterator to count the number of atoms in the cluster
being read

        string = strtok(NULL,"\t"); // Read in the Atom_ID of the next
atom in the cluster
        while(string != NULL){ //Check that we've read something and
not hit the end of the list of atoms in that cluster
```

```
            j++; //Keeps track of the current cluster size so that the
correct atoms can be retrived from Atoms_to_track
            string = strtok(NULL,"\t"); // Read in the Atom_ID of the
next atom in the cluster
        }


        if(j >= 10){ //if we are a cluster i.e we have more than 10
atoms note down our size in cluster_sizes
            d++; // iterator to keep track of the number of clusters
in cluster_sizes
            cluster_position =
realloc(cluster_position,d*3*sizeof(float)); // Increase the size of
cluster_position to accomodate the new entry
            cluster_IDs_of_interest =
realloc(cluster_IDs_of_interest,d*sizeof(int)); // Increase the size
of cluster_position to accomodate the new entry
            cluster_sizes = realloc(cluster_sizes,d*sizeof(int)); //
Increase the size of cluster_sizes to accomodate the new entry
            cluster_position[3*(d-1)] = x; // stores cluster x pos
            cluster_position[3*(d-1)+1] = y; // stores cluster y pos
            cluster_position[3*(d-1)+2] = z; // stores cluster z pos
            cluster_IDs_of_interest[d-1] = cluster_ID; // stores the
cluster_ID
            cluster_sizes[d-1] = j; // stores cluster size


            //a,b,c are the psuedo-bcc co-ordinates of the centre
            l_min=a-distmax_sites;
            l_max=a+distmax_sites;
            m_min=b-distmax_sites;
            m_max=b+distmax_sites;
            n_min=c-(2*distmax_sites);
            n_max=c+(2*distmax_sites);

            for(l=l_min;l<=l_max;l++){
                periodic_l=(l+AXIAL_ATOMS_NUMBER)%AXIAL_ATOMS_NUMBER;

                for(m=m_min;m<=m_max;m++){

periodic_m=(m+AXIAL_ATOMS_NUMBER)%AXIAL_ATOMS_NUMBER;

                    for(n=n_min;n<=n_max;n++){


periodic_n=(n+AXIAL_ATOMS_NUMBER)%AXIAL_ATOMS_NUMBER;


if(atoms_for_volume[periodic_l][periodic_m][periodic_n]!= 1){ //check
we've not already noted this site.

atoms_for_volume[periodic_l][periodic_m][periodic_n]= 1; // this site
is within DISTMAXMIN of the centre of a CU ppt and not previously
found.
                        }

                    }
                }
            }

        }
```

```
    }

    for(l=0;l<AXIAL_ATOMS_NUMBER;l++){
        for(m=0;m<AXIAL_ATOMS_NUMBER;m++){
            for(n=0;n<AXIAL_ATOMS_NUMBER;n++){

                sum+=atoms_for_volume[l][m][n]; //sum all the sites
which were within 3nm of any cluster centre;

            }
        }
    }

    *final_clusters_vol=(float)sum/85.0; //volume containing all the
linked clusters

    // All clusters have been read so note down how many clusters we
are interested in
    Number_of_clusters_to_track = d;

    printf("There were %i clusters at the end of the
simulation.\n",Number_of_clusters_to_track);
    fclose(fin); //Close the input file
    free(buffer);   //Free the memory allocated to read in the
clusters.

freememory3d(AXIAL_ATOMS_NUMBER,AXIAL_ATOMS_NUMBER,AXIAL_ATOMS_NUMBER,
atoms_for_volume);
    return k+1; // Return the number of analysis times run
}

int binary_search(int i, int* buffer){

int min = 0;
int max = Number_of_atoms_to_track - 1;
int mid;

    mid = (max + min) / 2;

    if(i == buffer[mid]){
        return 1;
    }

    while((min < max) && (i != buffer[mid])){

        if(i > buffer[mid]){
            min = mid+1;
            mid = (max + min) / 2;
            //break;
        }
        else if(i < buffer[mid]){
            max = mid-1;
            mid = (max + min) / 2;
            //break;
        }

        if(i == buffer[mid]){
            return 1;
        }
    }
```

```
return 0;
}

//Compares two integers.
int int_cmp(const void *a, const void *b)
{
    const int *ia = (const int *)a; // casting pointer types
    const int *ib = (const int *)b;
    return *ia  - *ib;
    /* integer comparison: returns negative if b > a
    and positive if a > b */
}

/*************************************************************/
// allocates memory for an j*k*i array and returns the location of the
memory
/*************************************************************/
int*** allocatememory3d(int imax, int jmax, int kmax) //k=cols/x
j=rows/y  i=height/z
{
int j=0;
int k=0;
int ***buffer;

printf("Allocating Memory\n");
buffer = (int***) calloc(imax , sizeof(int**)); // memory for the
hieght
if(!buffer){
    printf("Failed allocation");
    return NULL;
}
    for (j=0; j<imax; j++){
        buffer[j] = (int**) calloc(jmax , sizeof(int*)); // memory for
the rows
        if(!buffer[j]){
            printf("Failed allocation");
            return NULL;
        }
        for(k=0;k<jmax;k++){
            buffer[j][k] = (int*) calloc(kmax, sizeof(int));  //memory
for the columns
            if(!buffer[j][k]){
                printf("Failed allocation");
                return NULL;
            }
        }
    }

return buffer;
}

/*************************************************************/
// frees the memory allocated for an i*j*k array
/*************************************************************/
int freememory3d(int imax,int jmax,int kmax, int ***buffer)
//k=cols/x  j=rows/y  i=height/z  buffer is memory location to be
cleared
{
int j=0;
int k=0;
```

```
printf("freeing memory\n");
    for(j=0; j < imax; j++){
        for(k=0; k < jmax; k++){
            free(buffer[j][k]);   // frees memory for the columns
        }
        free(buffer[j]);    // frees memory for the rows
    }

free(buffer); // frees memory for the height.

printf("I have freed the memory\n");
return 0;
}

/*****************************************************************/
// allocates memory for an i*j array and returns the location of the
memory
/*****************************************************************/
int** allocatememory2d(int imax, int jmax) //j=cols/x  i=rows/y
{
    int j=0;
    int** buffer;

    printf("Allocating Memory.\n");
    buffer = (int**) calloc(imax , sizeof(int*)); // memory for the
cols
    if(!buffer){
        printf("Failed allocation");
        return NULL;
    }
    for (j=0; j<imax; j++){
        buffer[j] = (int*) calloc(jmax , sizeof(int)); // memory for
the rows
        if(!buffer[j]){
            printf("Failed allocation");
            return NULL;
        }
    }

return buffer;
}

/*****************************************************************/
// frees the memory allocated for an i*j array
/*****************************************************************/
int freememory2d(int imax,int jmax, int **buffer)  //j=cols/x
i=rows/y  buffer is memory location to be cleared
{
    int j=0;

    printf("Freeing memory.\n");
    for(j=0; j < imax; j++){
        free(buffer[j]);    // frees memory for the rows
    }

    free(buffer); // frees memory for the height.

    printf("I have freed the memory.\n");
return 0;
}
```

### E.2.2 Cluster Formation Videos

```
#include<stdio.h>
#include<stdlib.h>
#include"GSsimulation_parameters.h"
#include"zlib.h"
#include"zconf.h"

//functions
int Read_Tracked_Atoms(int T, int version_no);
int readline(gzFile fin, FILE *fout, int *counter, int xmin, int xmax,
int ymin, int ymax, int zmin, int zmax);
int Read_Atoms_Simulation(int T, int version_no, int *counter);
//-------------------------------------

//Global variables
int *Atoms_to_track;
int Number_of_atoms_to_track;
//-----------------------------------

int main(void){

int check;
int T=TEMP;
int version_no=VERSION_NO;
int counter=0;

    check = Read_Atoms_Simulation(T, version_no,&counter);
    #ifndef NOERROR
    if(check !=1){
        printf("Error in Read_Atoms_Simulation on line %d.
Exiting.\n",__LINE__);
    }
    #endif

    printf("Read Tracked Atoms complete. There are %d movements in the
output file.\n",counter);
return 0;
}

/*****************************************************************/
/* Reads in the list Atom positions output from the Simulation  */
/*****************************************************************/
int Read_Atoms_Simulation(int T, int version_no,int *counter){
    gzFile fin;
    FILE *fout;
    FILE *fout_initial;

    int i=0;
    int check;
    char filename[100];
    char filename_out[100];
    char filename_out_intitial[100];
    int xmin, xmax, ymin, ymax, zmin, zmax;

    sprintf(filename,"Tracked Atom Positions-%dK-%d",T,version_no);
    printf("file name is %s\n",filename);

    printf("Please enter the min and max x values as (xmin-xmax)\n");
    check = scanf("%3d-%3d",&xmin,&xmax);
    while(xmin < 0 || xmin > 127 || xmax < 0 || xmax > 127 || check !=
2 || xmin >= xmax){
        printf("xmin or xmax not valid, please re-enter.\n");
```

```
        scanf("%3d-%3d",&xmin,&xmax);
    }

    printf("Please enter the min and max y values as (ymin-ymax)\n");
    scanf("%3d-%3d",&ymin,&ymax);
    while(ymin < 0 || ymin > 127 || ymax < 0 || ymax > 127 || check !=
2 || ymin >= ymax){
        printf("ymin or ymax not valid, please re-enter.\n");
        scanf("%3d-%3d",&ymin,&ymax);
    }

    printf("Please enter the min and max z values as (zmin-zmax)\n");
    scanf("%3d-%3d",&zmin,&zmax);
    while(zmin < 0 || zmin > 127 || zmax < 0 || zmax > 127 || check !=
2 || zmin >= zmax){
        printf("zmin or zmax not valid, please re-enter.\n");
        scanf("%3d-%3d",&zmin,&zmax);
    }

    fin = gzopen(filename,"rb");
    #ifndef NOERROR
    if(fin == NULL){
        printf("Input file not opened correctly on line: %d.
Exiting\n",__LINE__);
        return 0;
    }
    #endif

    sprintf(filename_out,"Atoms-of-interest-positions-%dK-
%d.txt",T,version_no);
    fout = fopen(filename_out,"w");
    #ifndef NOERROR
    if(fout == NULL){
        printf("Output file not opened correctly on line: %d.
Exiting\n",__LINE__);
        gzclose(fin);
        return 0;
    }
    #endif

    sprintf(filename_out_intitial,"Atoms-of-interest-intitial-
positions-%dK-%d.txt",T,version_no);
    fout_initial = fopen(filename_out_intitial,"w");
    #ifndef NOERROR
    if(fout_initial == NULL){
        printf("Output file for intitial-positions not opened
correctly on line: %d. Exiting\n",__LINE__);
        gzclose(fin);
        fclose(fout);
        return 0;
    }
    #endif


fprintf(fout_initial,"%d\t%d\t%d\t%d\t%d\t%d\n",xmin,xmax,ymin,ymax,zm
in,zmax);

    while(!gzeof(fin) && i<TOTAL_SOLUTE_ATOMS_NUMBER){  //reads in all
the initial positions of solutes in the ROI.
```

```
        check = readline(fin,fout_initial,counter,xmin, xmax, ymin,
ymax, zmin, zmax);
        #ifndef NOERROR
        if(check != 1){
            printf("Error in readline on line %d.
Exiting.\n",__LINE__);
            gzclose(fin);
            fclose(fout);
            fclose(fout_initial);
            return 0;
        }
        #endif
        i++;
    }
    fclose(fout_initial);

    while(!gzeof(fin)){ //reads in all solute-vacancy swaps in the
ROI.
        check = readline(fin,fout,counter,xmin, xmax, ymin, ymax,
zmin, zmax);
        #ifndef NOERROR
        if(check != 1){
            printf("Error in readline on line %d.
Exiting.\n",__LINE__);
            gzclose(fin);
            fclose(fout);
            return 0;
        }
        #endif
    }

    gzclose(fin);
    fclose(fout);
    return 1;
}


int readline(gzFile fin, FILE *buffer, int *counter, int xmin, int
xmax, int ymin, int ymax, int zmin, int zmax){

int check;
char p=0,q=0,r=0;
int l=0,m=0,n=0;
int Atom_ID;

    check = gzread(fin,&Atom_ID,sizeof(int));
    #ifndef NOERROR
    if(check != sizeof(int)){
        printf("gzread error on line: %d. Exiting.\n",__LINE__);
        return 0;
    }
    #endif

    p = gzgetc(fin);
    #ifndef NOERROR
    if(p == -1){
        printf("gzgetc error on line: %d. Exiting.\n",__LINE__);
        return 0;
    }
    #endif
```

```
    q = gzgetc(fin);
    #ifndef NOERROR
    if(q == -1){
        printf("gzgetc error on line: %d. Exiting.\n",__LINE__);
        return 0;
    }
    #endif

    r = gzgetc(fin);
    #ifndef NOERROR
    if(r == -1){
        printf("gzgetc error on line: %d. Exiting.\n",__LINE__);
        return 0;
    }
    #endif

    l = (int)p;
    m = (int)q;
    n = (int)r;

    if(l >= xmin && l <= xmax && m >= ymin && m <= ymax && n >= zmin
&& n <= zmax){
        fprintf(buffer,"%d\t%d\t%d\t%d\n",Atom_ID,l,m,n);
        *counter += 1;
    }

    return 1;
}
```

```
#include <stdio.h>
#include <stdlib.h>
#include <math.h>
#include "GSsimulation_parameters.h"

int OUTPUT_BIN; //Number of movements between file outputs
long int OUTPUT_BIN_LIMIT; //
int OUTPUT_BIN_NEW;
int COLOUR;
int xmax,xmin,ymax,ymin,zmax,zmin;
int *Atoms_to_track;
int Number_of_atoms_to_track;

int writefile(int step_no, int ***atom, int T, int version_no);
int getAtomType(int atomID);
void get_No_of_atoms(int T, int version_no);
int*** allocatememory3d(int imax, int jmax,int kmax);
int freememory3d(int imax,int jmax,int kmax, int ***buffer);
int** allocatememory2d(int jmax, int imax);
int freememory2d(int imax,int jmax, int **buffer);
int Read_Tracked_Atoms();
int binary_search(int buffer);

int main(void){

    int i=0;
    int p,q,r;  //psuedo cubic lattice positions
    int version_no = VERSION_NO;
    int T = TEMP;
    int ***atom;
    int **atom_coords;
    int x=0,y=0,z=0;
    int check=0;
    int k;
    int atomID=0;
    int counter;
    int step_no = 0;
    long int file_size;
    char filename[100];
    char filename_initial[100];
    char in_buffer[100];
    long int number_entries_read=0;

    FILE *fin;
    FILE *fin_initial;

    printf("Please enter the number of atom movements between file
outputs.\n");
    scanf("%10d",&OUTPUT_BIN);
    printf("Would you like to increase this after X number of steps?
y=1/n=0\n");
    scanf("%1d",&k);
    if(k==1){
        printf("After how many steps do you want to increase the
number of movements between file outputs?\n");
        scanf("%10ld",&OUTPUT_BIN_LIMIT);
        printf("What is the new number of atom movements you would
like between file outputs?\n");
        scanf("%10d",&OUTPUT_BIN_NEW);
    }
    else{
```

```
        OUTPUT_BIN_NEW = OUTPUT_BIN;
        sprintf(filename,"Atoms-of-interest-positions-%dK-
%d.txt",T,version_no);
        fin = fopen(filename,"r");

        fseek(fin,0,SEEK_END);
        file_size = ftell(fin); //find out the file size
        fseek(fin,0,SEEK_SET); // return to the beginning of the file

        OUTPUT_BIN_LIMIT = (long int)((float)file_size/4.0); //Set bin
limit to the number of entries in the file
        printf("There are %ld movements in the output file. The file
size was %ld.\n",OUTPUT_BIN_LIMIT,file_size);
        fclose(fin);
    }

    printf("Would you like to colour atoms which end up in clusters a
different colour? y=1/n=0\n");
    scanf("%1d",&COLOUR);

    counter = OUTPUT_BIN;

    sprintf(filename_initial,"Atoms-of-interest-intitial-positions-
%dK-%d.txt",T,version_no);

    fin_initial = fopen(filename_initial,"r");

    fgets(in_buffer,100,fin_initial);

sscanf(in_buffer,"%d\t%d\t%d\t%d\t%d\t%d",&xmin,&xmax,&ymin,&ymax,&zmi
n,&zmax);

    atom = allocatememory3d(xmax-xmin-1,ymax-ymin-1,zmax-zmin-1);
    atom_coords = allocatememory2d(TOTAL_SOLUTE_ATOMS_NUMBER,3);

    if(COLOUR == 1){
        check = Read_Tracked_Atoms();
        if(check != 0){
            printf("Error reading tracked atoms. Exiting. Check file
'IDs_of_clustered_atoms.txt' is present.\n");
            fclose(fin_initial);
            freememory3d(xmax-xmin-1 ,ymax-ymin-1,zmax-zmin-1,atom);
            freememory2d(TOTAL_SOLUTE_ATOMS_NUMBER,3,atom_coords);
            exit(1);
        }
    }

    while(!feof(fin_initial)){  //Sets up the initial positions of the
solute atoms of interest.
        i++;

        fgets(in_buffer,100,fin_initial);
        if(fgets != NULL){
            sscanf(in_buffer,"%d\t%d\t%d\t%d",&atomID,&p,&q,&r);

            if( p != xmin && p != xmax && q != ymin && q != ymax && r
!= zmin && r != zmax ){
                atom[p-xmin-1][q-ymin-1][r-zmin-1] = atomID;

                atom_coords[atomID][0] = p;
                atom_coords[atomID][1] = q;
```

```
                atom_coords[atomID][2] = r;
            }
        }
    }


    writefile(step_no,atom,T,version_no);

    fclose(fin_initial);

    sprintf(filename,"Atoms-of-interest-positions-%dK-
%d.txt",T,version_no);
    fin = fopen(filename,"r");

    while(!feof(fin)){

        fgets(in_buffer,100,fin);   //reads line and stores in buffer

        check = sscanf(in_buffer,"%d\t%d\t%d\t%d",&atomID,&p,&q,&r);
        if(check == 4){

            if( p != xmin && p != xmax && q != ymin && q != ymax && r
!= zmin && r != zmax ){ //if we're not off the edge then move the atom
to it's new position

                atom[p-xmin-1][q-ymin-1][r-zmin-1] = atomID;


                if(atom_coords[atomID][0] !=0 &&
atom_coords[atomID][1] != 0 && atom_coords[atomID][2] != 0){ //you're
moving from a site in the ROI to a new one in the ROI
                    x = atom_coords[atomID][0]-xmin-1;
                    y = atom_coords[atomID][1]-ymin-1;
                    z = atom_coords[atomID][2]-zmin-1;

                    atom[x][y][z] = 0;
                }

                atom_coords[atomID][0] = p;
                atom_coords[atomID][1] = q;
                atom_coords[atomID][2] = r;

            }
            else{   // if we're off the edge then delete the old
position info.

                if(atom_coords[atomID][0] !=0 &&
atom_coords[atomID][1] != 0 && atom_coords[atomID][2] != 0){
                    x = atom_coords[atomID][0]-xmin-1;
                    y = atom_coords[atomID][1]-ymin-1;
                    z = atom_coords[atomID][2]-zmin-1;

                    atom[x][y][z] = 0;

                    atom_coords[atomID][0] = 0;
                    atom_coords[atomID][1] = 0;
                    atom_coords[atomID][2] = 0;
                }
            }
```

```
            counter--;
            number_entries_read++;

            if(counter == 0){
                step_no++;
                writefile(step_no, atom, T, version_no);

                switch(k){
                    case 1: if(number_entries_read >=
OUTPUT_BIN_LIMIT){
                                counter = OUTPUT_BIN_NEW;
                            }
                            else{
                                counter = OUTPUT_BIN;
                            }
                        break;
                    default:  counter = OUTPUT_BIN; break;
                }
            }
        }
    }

    freememory3d(xmax-xmin-1,ymax-ymin-1,zmax-zmin-1,atom);
    freememory2d(TOTAL_SOLUTE_ATOMS_NUMBER,3,atom_coords);
    fclose(fin);
    printf("vtk-output complete.\n");
    return 0;
}

int writefile(int step_no, int ***atom, int T, int version_no){

    int p=0,q=0,r=0;
    const float a = 0.287;      //alpha-Fe lattice constant
    FILE *fout;
    char filename[100];
    float l=0,m=0,n=0;
    int NO_OF_ATOMS=0;
    int found = 2;

    sprintf(filename,"Cluster-Atoms-%d-%d-Step-
%i.vtk",T,version_no,step_no);

    fout = fopen(filename,"w");

    for(p=0;p<xmax-xmin-1;p++){
        for(q=0;q<ymax-ymin-1;q++){
            for(r=0;r<zmax-zmin-1;r++){
                if(atom[p][q][r] != 0){
                    NO_OF_ATOMS += 1;
                }
            }
        }
    }

    fputs("# vtk DataFile Version 2.0\n",fout);
    fprintf(fout,"Cluster_Atoms_Step_%i\n",step_no);
    fputs("ASCII\n",fout);
    fputs("DATASET UNSTRUCTURED_GRID\n",fout);
    fprintf(fout,"POINTS %i float\n",NO_OF_ATOMS);

    for(p=0;p<xmax-xmin-1;p++){
```

```
        for(q=0;q<ymax-ymin-1;q++){
            for(r=0;r<zmax-zmin-1;r++){
                if(atom[p][q][r] != 0){
                    //Converts the l,m,n values from their psuedo
cubic lattice positions to their correct bcc lattice positions
                    switch((r+xmin+1)&1){
                    case 0: l = (float)((p+xmin+1) * a);
                            m = (float)((q+xmin+1) * a);
                            n = (float)((r+xmin+1) / 2. * a);
                            break;
                    case 1: l = (float)((p+xmin+1) * a + a / 2.);
                            m = (float)((q+xmin+1)* a + a / 2.);
                            n = (float)((r+xmin+1) / 2. * a);
                            break;
                    }

                    fprintf(fout,"%f %f %f\n",l,m,n);
                }
            }
        }
    }

    fputs("\nCELLS 0 0\n\n",fout);
    fprintf(fout,"POINT_DATA %i\n", NO_OF_ATOMS);
    fputs("SCALARS scalars float 1\n",fout);
    fputs("LOOKUP_TABLE default\n",fout);

    for(p=0;p<xmax-xmin-1;p++){
        for(q=0;q<ymax-ymin-1;q++){
            for(r=0;r<zmax-zmin-1;r++){
                if(atom[p][q][r] != 0){
                    switch(COLOUR){
                        case 0:
fprintf(fout,"%f\n",(float)getAtomType(atom[p][q][r])); break; //
COLOURING OF ATOMS IN CLUSTERS IS DISABLED
                        case 1: // COLOURING OF ATOMS ENABLED
                            found = binary_search(atom[p][q][r]);
                            switch(found){
                                case 2: printf("Error in Binary
Search.\n"); break;
                                case 0:
fprintf(fout,"%f\n",(float)getAtomType(atom[p][q][r])); break; //Atom
not being tracked - given usual colour
                                case 1: fprintf(fout,"%f\n",5.0f);
break; //Atom being tracked - given a separate colour (5).
                            };
                        found = 2; break;
                    }
                }
            }
        }
    }
    fclose(fout);

    return 0;

}

int getAtomType(int i)
{
    if (i <= CU_ATOMS_NUMBER)
```

```
        return 1;

    if(i >= CU_ATOMS_NUMBER+1 && i <=
(CU_ATOMS_NUMBER+NI_ATOMS_NUMBER))
        return 2;

    if(i >= (CU_ATOMS_NUMBER+NI_ATOMS_NUMBER+1)&& i <=
(CU_ATOMS_NUMBER+NI_ATOMS_NUMBER+MN_ATOMS_NUMBER))
        return 3;

    if(i >= (CU_ATOMS_NUMBER+NI_ATOMS_NUMBER+MN_ATOMS_NUMBER+1) && i
<= TOTAL_SOLUTE_ATOMS_NUMBER)
        return 4;

    //ASSERT(0);
    return -1;
}

/*****************************************************************/
/* Reads in the list of Atom IDs to track                        */
/*****************************************************************/
int Read_Tracked_Atoms(){

    FILE *fin;
    char filename[100];

    int i = 0;
    int j = 1;
    char in_buffer[100];

    sprintf(filename,"IDs_of_clustered_atoms.txt");

    fin = fopen(filename,"r");
    if(fin == NULL){
        printf("File not opened correctly. Exiting.\n");
        return 1;
    }

    while(!feof(fin)){  //Sets up the initial positions of the solute
atoms of interest.
        Atoms_to_track =  realloc(Atoms_to_track,j*sizeof(int));
        fgets(in_buffer,100,fin);
        sscanf(in_buffer,"%d",Atoms_to_track+i);
        i++;
        j++;
    }
    Number_of_atoms_to_track = i;

    fclose(fin);

    return 0;
}

/*****************************************************************/
/* Binary search of Atoms to track for atom[l][m][n]             */
/*****************************************************************/
int binary_search(int buffer){

int min = 0;
int max = Number_of_atoms_to_track - 1;
int mid;
```

```
    mid = (max + min) / 2;

    if(buffer == Atoms_to_track[mid]){
        return 1;
    }

    while((min < max) && (buffer != Atoms_to_track[mid])){

        if(buffer  > Atoms_to_track[mid]){
            min = mid+1;
            mid = (max + min) / 2;
            //break;
        }
        else if(buffer < Atoms_to_track[mid]){
            max = mid-1;
            mid = (max + min) / 2;
            //break;
        }

        if(buffer == Atoms_to_track[mid]){
            return 1;
        }

    }

return 0;
}


/*****************************************************************/
// allocates memory for an j*k*i array and returns the location of the
memory
/*****************************************************************/
int*** allocatememory3d(int imax, int jmax, int kmax) //k=cols/x
j=rows/y  i=height/z
{
int j=0;
int k=0;
int ***buffer;

printf("Allocating Memory\n");
buffer = (int***) calloc(imax , sizeof(int**)); // memory for the
hieght

    for (j=0; j<imax; j++)
    {
        buffer[j] = (int**) calloc(jmax , sizeof(int*)); // memory for
the rows
        for(k=0;k<jmax;k++)
        {
            buffer[j][k] = (int*) calloc(kmax, sizeof(int));  //memory
for the columns


            if(!buffer[j][k])
            {
                printf("Failed allocation");
                exit(1);
            }
        }
```

```
    }

return buffer;
}

/*************************************************************/
// frees the memory allocated for an i*j*k array
/*************************************************************/
int freememory3d(int imax,int jmax,int kmax, int ***buffer)
//k=cols/x  j=rows/y  i=height/z  buffer is memory location to be
cleared
{
int j=0;
int k=0;
printf("freeing memory\n");
    for(j=0; j < imax; j++)
    {
        for(k=0; k < jmax; k++)
        {
            free(buffer[j][k]);   // frees memory for the columns
        }
    free(buffer[j]);    // frees memory for the rows
    }

free(buffer); // frees memory for the height.

printf("I have freed the memory\n");
return 0;
}

/*************************************************************/
// allocates memory for an i*j array and returns the location of the
memory
/*************************************************************/
int** allocatememory2d(int imax, int jmax) //j=cols/x  i=rows/y
{
int j=0;
int** buffer;

printf("Allocating Memory.\n");
buffer = (int**) calloc(imax , sizeof(int*)); // memory for the cols

    for (j=0; j<imax; j++)
    {
        buffer[j] = (int*) calloc(jmax , sizeof(int)); // memory for
the rows
        if(!buffer[j])
        {
            printf("Failed allocation");
            exit(1);
        }
    }

return buffer;
}

/*************************************************************/
// frees the memory allocated for an i*j array
/*************************************************************/
int freememory2d(int imax,int jmax, int **buffer)  //j=cols/x
i=rows/y  buffer is memory location to be cleared
```

```
{
int j=0;

printf("Freeing memory.\n");
    for(j=0; j < imax; j++)
    {
    free(buffer[j]);    // frees memory for the rows
    }

free(buffer); // frees memory for the height.

printf("I have freed the memory.\n");
return 0;
}
```